On the Climatology of Orographic Precipitation in the Mid-Latitudes

Justin R. Minder

A dissertation
submitted in partial fulfillment of
the requirements for the degree of

Doctor of Philosophy

University of Washington

2010

Program Authorized to Offer Degree: Department of Atmospheric Sciences

University of Washington
Graduate School

This is to certify that I have examined this copy of a doctoral dissertation by

Justin R. Minder

and have found that it is complete and satisfactory in all respects,
and that any and all revisions required by the final
examining committee have been made.

Co-Chairs of the Supervisory Committee:

Dale R. Durran

Gerard H. Roe

Reading Committee:

Dale R. Durran

Gerard H. Roe

Mark T. Stoelinga

Date:

In presenting this dissertation in partial fulfillment of the requirements for the doctoral degree at the University of Washington, I agree that the Library shall make its copies freely available for inspection. I further agree that extensive copying of this dissertation is allowable only for scholarly purposes, consistent with "fair use" as prescribed in the U.S. Copyright Law. Requests for copying or reproduction of this dissertation may be referred to Proquest Information and Learning, 300 North Zeeb Road, Ann Arbor, MI 48106-1346, 1-800-521-0600, to whom the author has granted "the right to reproduce and sell (a) copies of the manuscript in microform and/or (b) printed copies of the manuscript made from microform."

Signature______________________________

Date__________________________________

University of Washington

Abstract

On the Climatology of Orographic Precipitation in the Mid-Latitudes

Justin R. Minder

Co-Chairs of the Supervisory Committee:
Professor Dale R. Durran
Department of Atmospheric Sciences

Professor Gerard H. Roe
Department of Earth and Space Science

For mountainous regions, and regions downstream, the climatology of mid-latitude orographic precipitation determines the susceptibility to hazards such as flooding and landslides while also cotrolling the volume and timing of streamflow and fresh water resources. However, due to modeling and observational challenges, many aspects of the climatology of mountain precipitation remain poorly understood. This thesis uses a synthesis of numerical models, theory, and field observations, loosely focused on the Cascade and Olympic Mountains of western North America, to investigate in detail a number of general aspects of mid-attitude orographic precipitation.

First, the climatology of ridge-valley scale precipitation patterns is investigated by analysis of several years of data from the Olympic Mountains, both from archived operational mesoscale numerical model forecasts and a special dense observing network of precipitation gauges. By simulating and analyzing case studies, the physical processes responsible for the mean pattern and variations in the pattern are diagnosed. Large ($> 50\%$) enhancement of precipitation over ridges relative to valleys a few kilometers away is found to be a very robust feature of the region's climate, and the climatological patterns are surprisingly well-simulated by a mesoscale model (despite frequent errors for individual storms).

The impact of large climatological gradients in mountain precipitation, such as those

found in the Olympic mountains, on patterns of landslide susceptibility is also investigated. This is accomplished using an idealized model of shallow landslides, forced by the climatology developed from mesoscale model forecasts. Results suggest that small-scale maxima in climatological precipitation may play an important role in making certain regions more susceptible to slope failure. Furthermore, the use of unadjusted lowland precipitation data to characterize conditions on nearby mountain slopes may lead to a substantial underestimate of landslide hazard.

Next, the controls on the sensitivity of mountain snowpack accumulation to climate warming are investigated using two idealized physically based models. Results suggest that the relationship between the climatological melting-level distribution and the topography is the principle control on the sensitivity of snowpack accumulation to climate warming. It is also shown that, while thermodynamically driven increases in precipitation with warming may moderate the loss of snowfall somewhat, for large amounts of warming increases in precipitation become unimportant, as the loss of accumulation area is too substantial.

Finally, the physical mechanisms acting on the mesoscale to control the mountainside snow line are investigated. On the mountainside, the snow line is often located at an elevation hundreds of meters different from its elevation in the free air upwind. The processes responsible for this behavior are examined in semi-idealized simulations with a mesoscale numerical weather prediction model. Spatial variations in latent cooling from melting precipitation, adiabatic cooling from vertical motion, and the melting distance of frozen hydrometeors are all shown to make important contributions. The relative importance of these processes depends on properties of the incoming flow and terrain geometry. Results suggest an increased depression of the snow line below the upstream 0°C level with increasing temperature, a relationship that, if present in nature, could act to buffer mountain hydroclimate against the impacts of climate warming.

TABLE OF CONTENTS

Page

List of Figures . . . iii

List of Tables . . . xiii

Chapter 1: Introduction . . . 1
  1.1 Motivation . . . 1
  1.2 Challenges . . . 2
  1.3 Previous work . . . 3
  1.4 An example: The Olympic and Cascade mountains . . . 5
  1.5 Outline . . . 10

Chapter 2: The climatology of small-scale orographic precipitation: Patterns and processes . . . 13
  2.1 Introduction and Background . . . 13
  2.2 Precipitation in the Olympic Mountains . . . 16
  2.3 Case studies . . . 29
  2.4 Composite analysis of precipitation climatology . . . 49
  2.5 Discussion . . . 52
  2.6 Conclusions . . . 55

Chapter 3: Spatial patterns of orographic rainfall and shallow landslide susceptibility . . . 57
  3.1 Introduction and Background . . . 57
  3.2 Rainfall and Landslides over the Western Olympic Mountains . . . 60
  3.3 Methods . . . 63
  3.4 Results . . . 67
  3.5 Sensitivity Analysis . . . 74
  3.6 Conclusions . . . 77

Chapter 4: The sensitivity of climatological mountain snowpack accumulation to climate warming . . . 79
4.1 Introduction and background . . . 79
4.2 Focus and strategy . . . 80
4.3 Linear Theory (LT) Orographic Snowfall Model . . . 83
4.4 Melting-Level (ML) Model . . . 95
4.5 Experiments: Controls on λ_S . . . 98
4.6 Conclusions . . . 107

Chapter 5: Mesoscale controls on the climatology of the mountainside snow line . . . 110
5.1 Introduction and background . . . 110
5.2 Numerical Model . . . 119
5.3 Results: physical mechanisms . . . 123
5.4 Results: 2-D sensitivity experiments . . . 140
5.5 Results: 3D effects . . . 151
5.6 Discussion . . . 156
5.7 Summary and Conclusions . . . 159

Chapter 6: Summary and conclusions . . . 161

Bibliography . . . 165

LIST OF FIGURES

Figure Number Page

1.1 Figure caption 6

2.1 Rainfall observations in the Olympic Mountains. (a) shows the terrain of the Olympic Peninsula (grayscale shading), with a maximum elevation of 2.43 km. The locations which regularly report hourly precipitation (from the RAWS, ASOS, and the SNOTEL networks) are shown with stars. Location of the Quillayute (KUIL) sounding, and the COOP stations (Forks and Sequim) discussed in the text are also denoted. (b) shows a detailed view of the Queets-Quinault gauge network. Mixed precipitation gauges are shown with white circles, while rain-only gauges are shown with black circles. The Queets and Quinault Valleys, and the Black Knob (BKBW) RAWS station are also denoted. 17

2.2 MM5 annual precipitation climatology (color shading, in units of mm yr^{-1}), and model topography (contours every 250 m) over Olympic, Cascade, and Coastal mountain ranges (water years 2001–2006). 18

2.3 Precipitation weighted wind roses from water years 2004–2006. The length of each radial line is proportional to the amount of precipitation falling at the BKBW station when winds are from each direction. (a) uses 6 hr 850 hPa winds from the gridpoint in the NCEP-NCAR reanalysis upwind of the site during average flow, (b) uses 6 hr averaged 10 m winds from the BKBW station. 21

2.4 Observed and modeled precipitation totals at sites along Queets-Quinault gauge transect for four rainy seasons (dates given in Table 2.1). Accumulated precipitation is plotted as a function of approximate distance along transect. Black lines and circles show observations from the gauges that were continually operational for the entire season. Gray lines and circles show archived MM5 forecasts interpolated to gauge locations. Elevations of the gauges deployed each year are given by shaded topographic profile at the bottom of each plot. The MM5 terrain interpolated to the gauge locations is given by the dashed line in the first column of figures. The columns (left to right) show season total precipitation, precipitation from the largest events, and precipitation from the remaining events (method for defining events is described in the text). (Note: the use of a different interpolation scheme resulted in somewhat different MM5 values than those shown in Anders et al. (2007)). 24

2.5 Top rainfall events for the water year 2005 gauge season. The top three rows show the individual top events, determined as described in the text, together responsible for approximately 50% of the observed precipitation during the field season. The bottom row shows the sum of the top events, the sum of the season's remaining precipitation, and the season total. Note that large errors present for individual events show a tendency to average out when events are summed. 25

2.6 Outermost model domain and large-scale flow for 28 Nov case study. Extent of nested MM5 domains (12, 4, and 1.33 km) are shown with boxes. Simulated 850 hPa heights at 12 UTC on 20 Oct 2003 (time of the beginning of rainfall) are shown with contours (heights are extrapolated below the topography in regions of high terrain). 33

2.7 Modeled and observed time series from 20 Oct 2003 storm. Black lines and points show observations, while grey lines and points show MM5 hindcast. (a) 1hr precipitation totals at gauge network sites. Solid lines are for the average of all high elevation sites ($>$ 200 m), while dashed lines are for low elevations ($<$ 200 m). (b) Modeled and observed windspeed (solid) and observed wind gusts (dashed) at BKBW station. (c) Wind direction. (d) Temperatures (solid) and dew-point (dashed) at BKBW, and temperature at ridge-top site (dotted). Note, the observations show saturation throughout the period, thus the dew point is not visible as it is plotted atop the temperature. 35

2.8 Skew-T Log-P plots of observed and modeled soundings at KUIL at 12 UTC, 20 Oct 20 2003. The observed sounding is shown in black (solid line for temperature, dashed line for dew-point). A profile of winds is shown on the right, with each full barb representing 5 m s^{-1}. The model sounding is shown in gray, and is taken 1 hr previous to the observation time to account for the error in the model timing of the storm passage. 36

2.9 Storm total precipitation for case studies. (a) Storm total precipitation for 20 Oct 2003 event as modeled by MM5 with 1.33 km horizontal resolution and Reisner2 microphysics. Tick marks along the perimeter of the map show model grid spacing. (b) Observed and modeled precipitation at gauge network sites as function of distance along the transect. Observations are shown with the bold black line. Output from MM5 simulations with varied resolution and microphysical parameterizations are shown with line-styles denoted by the legend. Elevation of gauge sites is represented by the shaded terrain profile. (c) and (d) are analogous to (a) and (b) for the 28 Nov event. (e) and (f) are analogous to (a) and (b) for the 17 Jan event. The time interval used for the storm total transects and maps are given in Table 2.3. 37

2.10 Precipitation patterns and processes at time of peak modeled rainfall (14 UTC on 20 Oct 2003). (a) Map view of 1 hr accumulated precipitation (gray shading), with elevation (contours, 200 m interval), and 10 m winds (wind barbs, full barb = 10 kts). Location of the gauge network (thin NW-SE line), and the following cross-sections (bold N-S line) are also shown. (b) Vertical cross-section parallel to near-surface winds, precipitation rates are contoured for rain (fine dashes) every 2 mm hr^{-1}, and for graupel (solid) and snow (long dashes) every 1 mm hr^{-1}. (c) Cloud water mixing ratio (gray shading, scale shown on the right), and vertical velocity (black contours every 40 cm s^{-1}, with negative values denoted by dashed contours). (d) Contours of Reisner2 precipitation source terms including the collection of cloud water by: rain (fine dashes), graupel (solid black), and snow (medium dashes), and the sink of precipitation by evaporation (solid gray) (interval of 2.5×10^{7} s^{-1}). Characteristic hydrometeor back-trajectories (as described in the text) are shown with thick black lines in (b) and (d). 39

2.11 Wave structure, stability and directional critical level. (a) Winds at time of maximum rainfall (14 UTC) for 20 Oct case are shown with barbs at 1 km (gray) and 3 km (black) (full barb= 10 kts). (b) Cross-section (at location of bold line in (a)) of vertical velocities, and cross-ridge circulation. Contours of equivalent potential temperature are also shown (light gray lines, interval of 1.5 K). Note that the mountain wave decays as it passes through the warm front aloft, where the stability drops and the cross-ridge component of the wind approaches zero. (c) and (d) are the same as (a) and (b), but for a time during the 28 Nov case. 42

2.12 Modeled and observed rainfall distribution for early portion of 28 Nov storm, with low freezing-level. (a) Accumulated precipitation over western Olympic Mountains between 05 and 10 UTC in MM5 1.33 km simulation with Reisner2 microphysics. (b) Accumulated precipitation for the same period as in (a) for sites along gauge transect, from observations and 1.33 km MM5 domain for different microphysical parameterizations. 44

2.13 Cross section of modeled precipitation sources (contours, interval of 1×10^7 s^{-1}) and trajectories at 10 UTC on 28 Nov 2003. The section is taken parallel to the low level flow (along bold line shown in figure2.12). Plotting conventions are as for figure 2.10d. Note the shallower slopes of the hydrometeor trajectories as compared to those in Figure 2.10d. 45

2.14 Modeled and observed rainfall distribution for stable and unstable portions of 17 Jan storm. (a) shows accumulated precipitation simulated over western Olympic Mountains between 00 and 16 UTC on 17 Jan 2005 (stable period). (b) Precipitation for sites along gauge transect from observations and 1.33 km MM5 domain using different microphysical parameterization during same period as in (a). (c) Shows accumulated precipitation simulated between 22 UTC on 17 Jan, and 12 UTC on 18 Jan (convective period). (d) Precipitation for sites along gauge transect from observations and 1.33 km MM5 during same period as in (c). 47

2.15 Observed average 12hr precipitation patterns composited based upon 2 m temperature at BKBW station for the water year 2006 field season. Each figure shows the average 12 hr accumulated precipitation at the gauge sites during periods when the lowland temperatures are within the labeled intervals. The number of events used for each composite is noted as "samples". Rainfall events with gauge network averaged precipitation rates of less than 6 mm / 12 hrs were excluded from the analysis. 50

2.16 MM5 average 12 hr precipitation patterns composited based upon 2 m temperature simulated at site of BKBW station for Oct 2005 through Dec 2007. Methods and conventions used are equivalent to those for Figure 2.15. 51

3.1 Topography and mapped slides for the Queets and Quinault basins (location of the basins within Washington State are shown in inset map). Elevation is shaded in grayscale and ranges from 0 – 2.2 km. Shallow slides are shown in red, and deep-seated slides are green. Mapped slides include scar and runout, and complete mapping has only been done for the Quinault basin. The white line indicates the divide between the two basins. The blue box indicates the location of Figure 3.5. 61

3.2 Total modeled and observed precipitation at locations along the transect of gauges shown in Figure 3.3, for November–April of 2004–2005. Elevations of gauge sites are shown by the shaded terrain profile (the model elevations interpolated to the gauge sites are shown with the dashed line). Gauge observation are shown in black and model climatology interpolated to gauge locations is shown in gray (figure adapted from Minder et al. (2008)). 62

3.3 Maximum 24 hr averaged rainfall rate from 7 yrs of MM5 high-resolution atmospheric model iterations (reinterpolated from the 4 km MM5 grid to 1 km). The location of the Black Knob weather station (BKBW) is indicated with a star, and the location of the gauge network of Anders et al. (2007) and Minder et al. (2008) is shown with circles. 63

3.4 Critical cohesion as predicted by SHALSTAB (equation 3.1) using the MM5 rainfall climatology shown in Figure 3.3. Gray areas represent locations classified as unconditionally stable or with $C_{crit} = 0$. 68

3.5 Mapped slides and SHALSTAB modeled C_{crit} for the individual hillside indicated by the blue box in Figure 3.1. Elevation are shown with gray-scale shading (shading interval of 100 m). Regions of high C_{crit} are color-shaded according to the inset key. The perimeters of several mapped slides are delineated in cyan. 69

3.6 Number of mapped landslides per km^2 in each C_{crit} category (calculated as described in text) for slides mapped in the Queets and Quinault basins and SHALSTAB calculated values of C_{crit}. 70

3.7 Change in critical cohesion between the SHALSTAB run using the MM5 rainfall pattern and the run using uniform precipitation equal to the region average of the MM5 rainfall (pattern - average). 71

3.8 Change in critical cohesion between the SHALSTAB run using the MM5 rainfall pattern and run using uniform precipitation equal to the MM5 rainfall at the location of the lowland station BKBW (pattern - lowland). The location of BKBW is indicated with a star. 72

3.9 (a) Frequency distribution of C_{crit} for SHALSTAB runs with MM5 patterned rainfall (dashed black line), uniform region average rainfall (solid gray line) and lowland rainfall (solid black line). The distributions have been normalized by the total area of the basins, and cells with $C_{crit} = 0$ are omitted. (b) Frequency distribution of changes in C_{crit} between run with patterned and the runs with uniform rainfall (gray line for uniform average rainfall, black line for uniform lowland rainfall). Distributions have been normalized as in (b), and cells with change in $C_{crit} = 0$ are omitted. (c) Fractional area of the region exceeding various values of C_{crit} for patterned and uniform rainfall runs (line styles as in (a)). (d) Fractional change in area exceeding various values of C_{crit} between SHALSTAB runs with patterned and uniform rainfall (line styles as in (b)). 73

3.10 Critical cohesion (contoured and labeled every 1 kPa) as a function of tan(θ) and a/b using the parameters in Table 3.3 and uniform rainfall of 260 mm/day. The most unstable DEM grid cell in each mapped shallow slide (i.e. those shown in Figure 3.1) is plotted as a point based on its tan(θ) and a/b values. Regions above the arching bold line are predicted to become saturated in the model. Locations to the left of the vertical bold line are unconditionally stable. Note, limitations of our DEM dataset cause underestimation of steep slopes, thus the slopes for points to the right of the figure are best considered as representing minimum values. 75

3.11 Sensitivity of C_{crit} to variations in different parameters. (a)–(b) sensitivity to modeled spatial variations in rainfall (± 160 mm/day). (c)-(h) sensitivity to variations in soil parameters (z,tanϕ,ρ_s). The magnitudes of variations in soil parameters (given above the figure panels) are chosen to give changes in C_{crit} comparable to those due to precipitation variations shown in (a)–(b). . . 76

4.1 Map of study region. Topography of the Cascades and Olympic Mountains is shown in grayscale (maximum elevation is 4392 m at Mount Rainier). The boundary of the catchment that drains the Cascades into the Puget Sound (with the exception of a small section in Canada) is shown with a bold line. Major catchments within that basin are delineated with narrow lines (those used for Figure 4.12 are labeled A-G). The location of the Quillayute sounding (KUIL) is shown with a star, and the locations of SNOTEL stations used in Figure 4.4 are shown with white circles 82

4.2 Comparison of maps of precipitation, P, and snow water accumulation, S, from MM5 and LT models for Oct-Mar of 2005-2006 and 2006-2007: (a) MM5 modeled P, (b) LT modeled P, (c) MM5 modeled S, (d) LT modeled S. Thick black line shows the Puget Sound catchment. The MM5 model elevation is contoured with thin black lines every 500 m. 87

4.3 Comparison of LT model and MM5. Profiles of (a) $A(z)$, (b) $P(z)$, (c) $S(z)$, and (d) $\Sigma(z)$ from MM5 (black line) and LT snowfall model (grey line) for the accumulation seasons of water years 2006 and 2007. Profiles are evaluated for the entire domain shown in Figure 4.2. 88

4.4 Comparison of LT snowfall model with SNOTEL observations. Average fractional error in LT modeled Oct-Apr (a) P and (b) S accumulation, and (c) S/P relative to SNOTEL stations as a function of elevation for 1980-2007. . . 90

4.5 Profiles of LT snowfall model variables for the Puget Sound catchment (Figure 4.1) from the *climo_control* run: (a) topographic area, $A(z)$, (b) average accumulated precipitation, $P(z)$, (c) average snow water accumulation $S(z)$, and (d) integrated snow water accumulation $\Sigma(z)$. Control simulation is shown in black, and grey lines are for simulation with 1.5 km level warmed by 1°C (surface warming of 0.83 °C). 93

4.6 Maps of LT model change in (a) precipitation and (b) snow water accumulation for *climo_control* simulation. Smoothed topography (from the MM5 model) is contoured every 500 m. 94

4.7 Profiles of ML model variables for the Puget Sound catchment (Figure 4.1) from the $climo\_\Delta Tunif$ run: (a) topographic area, $A(z)$, (b) ML frequency distribution, $f(ML; z)$, (c) average snow water accumulation $S(z)$, and (d) integrated snow water accumulation $\Sigma(z)$. Control simulation is shown in black, warmed simulation is in gray. 96

4.8 Profile of change in average snow water accumulation, $\Delta S(z)$, under climate warming from the ML model (grey) compared with LT model (black). To facilitate comparison the $\Delta S(z)$ values from each model are normalized by dividing by the average of $S(z)$ from 0-2500 m for that model. 98

4.9 LT model simulated precipitation patterns (mm yr^{-1}) for acc0607 period from runs with (a) more westerly wind direction ($exp\_\Delta wdir50$), and (b) decreased microphysical time delay ($exp\_\tau 850$). MM5 topography is contoured every 500 m. 100

4.10 (a)-(c) Profiles of LT snowfall model $P(z)$, $S(z)$, and $\Sigma(z)$ for acc0607 period from: (black) $exp\_control$, (light gray) $exp\_\tau 850$ experiment, and (dark gray) Δ_wdir50 experiment. (d)-(f) same as for (a)-(c) but for: (black) $exp\_control$, (light gray) $exp\_\Delta ML\_0$, and (dark gray) ΔML_400. 101

4.11 Values of λ_S estimated as a function of average sea level temperature during storms. Temperatures are relative to current KUIL climatology ($[T_s]_{avg} - [T_s]_{KUIL}$, with $[T_s]_{KUIL} = 8.5$ °C). Bold line is for LT model and thin line is for ML model. 103

4.12 Sensitivity of snowfall to warming predicted by the LT snowfall model ($(\lambda_S)_{LT}$) versus sensitivity from the ML ($(\lambda_S)_{ML}$) for various catchments draining into Puget Sound (indicated with letters in Figure 4.1). The dashed line has a slope of unity for comparison. Note the large basin to basin variability of λ_S exhibited by both models. 104

4.13 Percentage change in snow accumulation as a function of surface warming as estimated by LT snowfall model (black solid line, with circles showing individual model runs). Gray solid line and dashed lines show the changes that would occur if only ML's or precipitation intensity were to change with warming. Black dashed line shows the sum of the two gray lines. The fine dashed line show the linear extrapolation of the λ_S values calculated from the $\Delta T = 1$ °C case. The shaded region shows the range of GCM projected warmings (for 2080's minus 1980's) for the Pacific Northwest region (Climate Impacts Group, 2009). Projections come from the IPCC AR4 models with emissions scenario A1B. Vertical line shows the best GCM estimate attained from a weighted average of the AR4 models (Climate Impacts Group, 2009). 109

5.1 Schematic illustration of how the main quantities considered in this study are defined. (a) Determination of Z_{0C} from a temperature profile, $T(z)$. (b) Determination of Z_S from a profile of frozen hydrometeor mixing ratio , $(q_s+q_g)(z)$. (c) Determination of ΔZ_{0C}, ΔZ_S, and ΔZ_{0CtoS} from upwind and mountainside values of Z_{0C} and Z_S. Dashed lines are drawn at the elevation of the upstream Z_{0C} and the mountainside Z_S. 112

5.2 Figures from previous observational studies showing drop in Z_{0C} and Z_{BB}. (a) Isotherms (^{o}C, with Z_{0C} in red) analyzed from aircraft *in situ* measurements over the northern Sierra Nevada on 25 Feb 1983 (adapted from Marwitz, 1987). (b) Equivalent radar reflectivity (dBZ_e) from RHI scans with the NOAA CP-3 radar over the northern Sierra Nevada on 15 Feb 1980 (from Marwitz, 1983). (c) Reflectivity (dBZ_e) from P-3 airborne radar analysis over the Lago Maggiore region of the Italian Alps on 21 Oct 1999 (from Medina et al., 2005). (d) Reflectivity (dBZ_e) from RHI scans with the S-Pol radar over the Oregon Cascades on 28 Nov 2001 (from Medina et al., 2005). In all panels winds are impinging from the left. 114

5.3 Domains for the WRF simulations: (a) 2D simulation domain showing the terrain profile with a bold line. The location of the troposphere, stratosphere, and damping layer are denoted, as are the initial atmospheric conditions for the control simulation; (b) 3D simulation domains showing the inner two of three nested domains (d2-d3) and their horizontal grid spacing ($\Delta x, y$). The terrain elevation for the 3D control simulation is contoured every 300 m. . . . 120

5.4 Skew-T log-p plot showing soundings of temperature (solid) and dew-point (dashed) used to initialize the control simulation. 124

5.5 Wind and cloud for control simulation. (a) Cross-mountain winds (u, filled contours every 1 m s^{-1}, with bold grey line at $u = U$ =15 m s^{-1}) and along-mountain winds (v, contoured every 1 m s^{-1}, with bold line at v=0, and dashed lines for v <0). (b) Vertical winds (w, contoured every 10 cm s^{-1}, with bold line at w=0, and dashed lines for w <0), and cloud liquid water mixing ratio (q_c, shaded every 5×10^{-5} kg kg^{-1}). 125

5.6 (a) Mixing ratios of cloud and hydrometeor species for control simulation. q_c is shaded every shaded every 5×10^{-5} kg kg^{-1}. Hydrometeor mixing ratios are contoured every 5×10^{-5} kg kg^{-1}: rain (q_r, blue), snow (q_s, green), graupel (q_g, red). Cloud ice (q_i, cyan) is contoured every 2.5×10^{-6} kg kg^{-1}. (b) Detail of melting region. Isotherms are contoured with thin lines every 1°C. Bold lines show: Z_{0C} (red), Z_S (blue), and Z_{RS} (cyan). The mesoscale modification of Z_{0C} and Z_S are noted (ΔZ_{0C}, ΔZ_S, and ΔZ_{0CtoS}). 126

5.7 Surface precipitation rates (at $z = h$) for total precipitation (pcp), rain, (pcp_r), snow (pcp_s), and graupel (pcp_g). Also shown are the frozen precipitation rate ($pcp_{s,g}$) at $z = Z_{0C}$ and the terrain profile (h) (in gray). 127

5.8 Microphysical profiles at x=-66 km from WRF control simulation (solid) and simplified column model (dashed) as a function of distance below Z_{0C}. (a) Mixing ratios: q_s (green), q_g (red), q_r (blue). (b) Fraction of frozen hydrometeor mass from Z_{0C} remaining, $\frac{(q_s+q_g)(z)}{(q_s+q_g)(z=Z_{0C})}$ (black), and ratio of frozen precipitation to total precipitation rate, $\frac{pcp_s+pcp_g}{pcp}$ (cyan). Horizontal lines denote Z_S (black) and Z_{RS} (cyan) from each model. (c) Precipitation rates: pcp_s (green), pcp_g (red), pcp_r (blue). 128

5.9 Sensitivity of column model Z_S and Z_{RS} to variations in frozen precipitation rate $(pcp_s + pcp_g)$ at Z_{0C}. All simulations use the same lapse rate and w as in Figure 5.8. Distance is measured from Z_{0C}. 130

5.10 Schematic diagram showing how the contributions of various physical processes to ΔZ_{0CtoS} are quantified in the WRF simulation. Solind lines represent Z_{0C} (red) and Z_S (blue) from a control simulation, while dashed lines represent Z_{0C} and Z_S from a simulation where LCpmelt is suppressed. Denoted on the right are contributions from: microphysical melting distance, $(\Delta Z_{0CtoS})_{micro.}$; LCpmelt, $(\Delta Z_{0CtoS})_{LC}$); adiabatic cooling, $(\Delta Z_{0CtoS})_{Ad.}$. . . 131

5.11 (a) As in figure 5.6, but Z_{0C} and Z_S are also shown for the experiment in which LCpmelt is suppressed (dashed lines) and Z_{RS} is omitted. (b) Back trajectory analysis for the control simulation. One-hour air parcel back trajectories ending at Z_{0C} are plotted (green lines, with circles every 5 min). Also shown are: $(q_s + q_g)$ (shaded every $1{\times}10^{-4}$) and Z_{0C} (red line) 132

5.12 Schematics showing how ΔZ_{0C} is determined by adiabatic cooling in the parcel model. (a) $x - z$ section showing environmental temperature profile and flow along lowest streamline. (b) Idealized profiles of environmental temperature (with lapse rate Γ) and parcel temperature (with lapse rates Γ_d and Γ_m) showing how lapse rate differences lead to ΔZ_{0C} (shown in red). (c) Profiles (in black) showing how a decrease in T_s decreases ΔZ_{0C}. (d) Profiles (in black) showing how an increase in Γ (and decrease in N_m) decreases ΔZ_{0C}. 134

5.13 Results from idealized parcel model showing ΔZ_{0C} (contours) as a function of upstream surface temperature, T_s, and moist stability, N_m^2, for RH =95 %. Negative contours are dashed. Red dot shows the parameters used for the control WRF simulation. 135

5.14 Figure caption 138

5.15 Cross-sections from T_s simulations. (a) For T_s=3°C simulation: q_c (shaded every 5×10^{-5} kg kg^{-1}), Z_{0C} and Z_S from simulations with (solid) and without (dashed) LCpmelt. (b) As in (a), but for T_s=7°C. (c) Precipitation rates (see key) and terrain profile (gray). 142

5.16 (a) ΔZ_S, ΔZ_{0C}, and ΔZ_{0CtoS} as a function of T_s (see key). (b) Contributions of mechanisms discussed in text to ΔZ_{0CtoS} as a function T_s (see key). Also included is the prediction from the parcel model discussed in section 5.3.4. . . 142

5.17 (a) As in figure 5.15a, but for $N_m = 0.002\ \mathrm{s}^{-1}$ simulation. (b) As in figure 5.15a, but for $N_m = 0.007\ \mathrm{s}^{-1}$. (c) As in figure 5.15c, for N_m simulations. . . 143

5.18 As in figure 5.16, but for N_m experiments. 143

5.19 (a) As in figure 5.15a, but for $U = 10\ \mathrm{m\ s}^{-1}$ simulation. (b) As in figure 5.15a, but for $U = 20\ \mathrm{m\ s}^{-1}$. (c) As in 5.15c, but for U simulations. 145

5.20 As in figure 5.16, but for U experiments. 145

5.21 (a) As in figure 5.15a, but for $RH = 85\%$ simulation. (b) As in figure 5.15a, but for $RH = 98\%$. (c) As in figure 5.15c, but for RH simulations. 147

5.22 As in figure 5.16, but for RH experiments. 147

5.23 (a) As in figure 5.15a, but for $a = 15$ km simulation. (b) As in figure 5.15a, but for $a = 65$ km. (c) As in figure 5.15c, but for a simulations. 148

5.24 As in figure 5.16, but for a experiments. 148

5.25 (a) As in figure 5.15a. (b) As in figure 5.15a, but for $h_m = 3$ km. (c) As in figure 5.15c, but for h_m simulations. 150

5.26 As in figure 5.16, but for h_m experiments. 150

5.27 Horizontal winds at lowest model level (vectors), precipitation rate (filled contours), and terrain height (gray contours, every 300 m) from intermediate domain ($\Delta x, y$ =6 km) for 3D experiments: (a) for control case (precipitation contoured every 0.5 mm h^{-1}), (b) for blocked case (precipitation contoured every 0.1 mm h^{-1}). Dashed lines show locations of the cross sections shown in figures 5.28 and 5.29 152

5.28 Cross sections at $y = 0$ for 3D version of control simulation: (a) w (contoured) and q_c (shaded), as in figure 5.5b; (b) Mixing ratios: q_r, q_s, q_g, and q_i (contoured) and q_c (shaded), as in figure 5.6a; (c) Z_{0C} (red) and Z_S (blue), with (solid) and without (dashed) LCpmelt, and q_c (shaded), as in figure 5.11a; (d) surface precipitation rate compared between 3D and 2D control simulations (see key) with terrain profile (gray). 153

5.29 $x - z$ cross sections from blocked simulation. As in figure 5.28, but vertical velocities in (a) are contoured every 2 cm s^{-1}. 155

LIST OF TABLES

Table Number Page

2.1 Statistics from each observational field-season. The dates of each season are given, as are the modeled and observed measures of ridge-valley enhancement (as defined in the text) for the season-total precipitation. Also shown are the normalized root-mean-squared-error (RMSE) and bias of the model forecasts over the network (also defined in the text). 23

2.2 Percent of 12hr periods during each season showing enhanced precipitation (i.e. $R/V > 1$) at the high elevation ($>$ 200 m) gauge sites relative to the low elevation ($<$ 200 m) sites . Percentages were calculated for medium-to-heavy rainfall periods ($>$ 4 mm / 12 hrs) and heavy rainfall periods ($>$ 24 mm / 12 hrs). Periods of sub-zero temperatures when one or more gauges was frozen are excluded from the analysis. The sample size of medium-and-heavy periods ranged from 65–199, while the sample size for heavy periods ranged from 11–23. 28

2.3 Conditions for case studies discussed in text. The time period of event included in first section. The second section includes modeled and observed surface conditions. $\mathbf{R/V}$ and $\mathbf{R_{max}/V_{min}}$ give the ridge-valley enhancement as described in the text. **Pcp**, gives the storm-total precipitation at the BKBW station. **Temp, Wspd, Wdir** denote the range of 2 m temperature, and 10 m wind speeds and directions at BKBW. **Wgst** denotes the observed wind gusts. The third section provides metrics from the modeled KUIL sounding. **FL** gives the range of freezing levels. $\mathbf{N^2_{m,\,0--2km}}$, $\mathbf{WSPD_{(0-2km)}}$, and, $\mathbf{WDIR_{(0-2km)}}$, give the range of moist static stabilities, wind speeds, and wind directions, averaged between 0 and 2 km. 30

3.1 Uniform values for soil parameters used in SHALSTAB modeling (symbols defined in text). 65

4.1 Sensitivity of snow accumulation to warming for various runs of LT and ML models. The top section of the table gives results for the two long simulations (1980-2007), with and without vertical structure to the warming, discussed in Sections 4.3 and 4.4. The lower section is for simulations of Oct.-Apr. of 2005-06 and 2006-07 (acc0607) used for the experiments discussed in Section 4.5. All values are in units of % change in snow accumulation per degree C of surface warming. ML model entries that are left blank have the same value as *exp_control*. 92

ACKNOWLEDGMENTS

I am indebted to my advisors Gerard Roe and Dale Durran for their sage guidance throughout my graduate career. I've had great fun working with them on many problems that I find compelling. By words and example they have taught me how to be a scientist. The freedom and support they afforded me has allowed me to dabble in the broad range of topics contained in this thesis.

This thesis also benefited greatly from the input of my other committee members: Robert Houze, Mark Stoelinga, Jessica Lundquist, and Luanne Thompson. Special thanks go to Jessica Lundquist, whose Snow Hydrology class provided me the opportunity and motivation to develop the ideas contained in chapter 4.

The field work in the Olympic mountains that provides the backbone of chapters 2 and 3 would not have been possible without the generous help of many. Alison Anders is responsible for the establishment of the network in 2003. The original set of mixed precipitation gauges were built by Pascal Stork and made available to by Clifford Mass at the University of Washington. Steve Domonkos played a crucial role in the redesign and improvement of the precipitation gauges. Help installing and maintaining the gauges each year in the field benefited from the help of countless friends and colleagues. Particular gratitude goes to Nic Wayand, Aaron Donahoe, Kat Huybers, Lucas Harris, Nils Napp, Carrie Lee, Angie Pendergrass, and Sandra Penny. I have much gratitude for the following organizations that allowed the deployment of instrumentation on their lands: Olympic National Forest, Olympic National Park, Washington State Department of Transportation, Quinault Indian Nation, Quinault River Inn, and Lake Quinault High School.

Thanks to Cliff Mass and the Northwest Regional Modeling Consortium for providing the operational MM5 model output and Neil Johnson for assistance in dearchiving it. These data played an important role in chapters 2,3, and 4. Joe Casola assisted in the processing of the SNOTEL data used in chapter 4.

The excellent computer support in the Departments of Atmospheric Science and Earth and Space science has been invaluable. Harvey Greenburg provided substantial technical assistance in the GIS analysis used in chapter 3. David Warren provided expert support for the high performance computing required to run the MM5 and WRF. Rick Steed assisted in setting up the MM5 simulations used in chapter 2.

Conversations with Ronald Smith and Bill Dietrich helped improve the work in chapters 2 and 3. Conversations with and proofreading from Sandra Penny were also valuable.

This work would not have been completed without financial support from a University of Washington (UW) Program on Climate Change (PCC) first year fellowship, a National Science Foundation (NSF) Graduate Research Fellowship, and NSF grants: EAR-0642835 and ATM-0506589.

Finally, Sandra and Gustopher Penny have provided invaluable emotional support and companionship for the past 3 years.

DEDICATION

To my family who instilled in me the importance of education and a passion for learning. To my Pop-pop, Paul Aubry, who lead me through many many musemes (scientific and otherwise) and provided me, at the age of 5, my first "scientific" position as an assistant in his basement invention lab. To my Grandpa, Joe Minder, who lead me through the woods, streams, and mountains, showing me wonder and beauty in nature.

Chapter 1

INTRODUCTION

1.1 Motivation

The climatology of orographic precipitation — precipitation that has been generated or modified by topography — strongly affects both natural and human systems in and around mountainous regions. It is well established that major mountain ranges extract moisture from the prevailing winds, in the form of precipitation, as air is lifted over the terrain. This provides water for the growth of vegetation and human settlements on the windward slopes, while downwind regions are deprived of water. This is the most familiar scenario, however many other climatological patterns and impacts also occur. For instance, mean precipitation may be enhanced well upwind, along the crest, or even in the lee of topographic barriers. Also, robust climatological patterns exist not just on the scale of entire ranges; individual ridges and valleys can control rain and snowfall patterns down to scales of just a few kilometers. Furthermore, prevailing winds are not required for strong topographic controls on rainfall climatologies; mountains can play a central role in initiating airmass convection by acting as elevated heat sources. Reviews in Smith (1979); Banta (1990); Houze (1993); Roe (2005); and Smith (2006) cover the wide range of possible orographic precipitation patterns and mechanisms that have been identified.

The climatology of orographic precipitation is the statistics (including the mean, variability, and extremes) of a long-term distribution of precipitation amount and type occurring at various space and time scales. Different aspects of the climatology are important for different natural and human systems. For instance, climatological extremes in hourly to weekly orographic rainfall and snowfall determine the susceptibility of regions to natural hazards such as landslides, avalanches, and flooding (e.g., Caine, 1980; Conway and Raymond, 1993; Javier et al., 2007). At longer timescales the mean and year-to-year variability of wintertime frozen precipitation is crucial in many regions because the annual melting of mountain snowpacks provides water resources in dry summer months (e.g., Serreze et al., 1999; Barnett et al., 2005). Over still longer timescales, the runoff and landslides caused by orographic precipitation act to erode the topography itself, and precipitation patterns that are robust over very long time scales may exert significant control on how the form of a mountain range evolves (e.g., Stolar et al., 2007; Anders et al., 2008). Understanding these and other impacts of orographic precipitation requires both an understanding of climatological distributions and the responsible physical mechanisms.

1.2 Challenges

The study of orographic precipitation is often hampered by sparsity of observations, hard to measure mixed precipitation, small spatial scales of variability, remoteness, and radar beam blockage by terrain. When attempting to study the *climatology* of mountain precipitation these challenges grow larger. For example, observational datasets suitable for detailed climate studies seldom exist. In the western US the most extensive networks of mountain stations — Remote Automated Weather Stations (RAWS,http://www.fs.fed.us/raws/) and Snowpack Telemetry (SNOTEL,http://www.wcc.nrcs.usda.gov/snow/)— have been collecting data only for a few decades at most. Furthermore, these stations are narrowly engineered for specific applications (monitoring fire hazard and water resources respectively) and thus the quality and availability of the data can be poor for seasons and variables not important to these purposes.

One strategy for achieving better observational data over mountains has been to undertake intensive field campaigns during which aircraft and state of the art instrumentation are deployed (e.g., Bougeault et al., 2001). While the data from these campaigns are invaluable, they are only of limited use for climatological studies since they typically cover just a few weeks, and thus sample a modest portion of the climatological distribution of weather. Numerical models are a core tool in studies of climate, particularly Global Climate Models (GCMs). Unfortunately the finest resolution GCMs used for the 4th IPCC assessment report have effective grid scales of about 1 degree (Randall et al., 2006), too coarse to adequately resolve even some of the largest mountain ranges on the planet (such as the Andes). Since global simulations at scales that resolve mountain weather (and other mesoscale phenomena) are not practical, regional climate models (RCMs) — complete dynamical models run over a limited domain with a horizontal resolutions of 10's of kms or less, supplied with boundary conditions from global models — have become important tools for studies of mountain climate. Still, challenges remain since the dominant scales of atmospheric variability over complex mountainous terrain can be on the order of a few kilometers, a scale that is still too fine for extensive RCM simulations to be practical, and results from RCM's can be strongly sensitive to how subgridscale physical processes are parameterized.

1.3 Previous work

Most advances in understanding the climatology of orographic precipitation have occurred when new methods, tools, and datasets have appeared, allowing researchers to overcome some of the above-mentioned challenges. Early work largely focused on characterizing the distribution of mountain precipitation and relating it to synoptic conditions (e.g., prevailing winds) or precipitation type (e.g., convective versus stratiform). Much of this pioneering work used rain gauges, and the development of dense networks of simple and inexpensive gauges was key to providing sufficient spatial resolution (e.g., Bergeron, 1960, 1968; Wilson and Atwater, 1972; Huff et al., 1975). Among the most interesting results of these early gauge-based studies was the realization that topography can control precipitation at surprisingly small spatial scales. This realization lead to development of the seeder-feeder conceptual model for orographic enhancement of precipitation (Bergeron, 1960, 1968). Later on, the development of remote sensing with ground-based radar and satellites lead to further advances as these technologies were able to provide high spatial and temporal resolution data in regions with sparse observations, data that were particularly useful for identifying topographic controls on summertime convection (e.g., Kuo and Orville, 1973; Biswas and Jayaweera, 1976).

The past decade or so has seen substantial activity and progress in climatological studies of orographic precipitation. A number of advances were due to new datasets of surface observations. These include both new syntheses of existing observations that have produced high-resolution gridded datasets (e.g., Frei and Schär, 1998; Daly et al., 2002), and analysis of data from relatively new networks (e.g., SNOTEL (Serreze et al., 1999, 2001)).

Advances in remote sensing have also been important, yielding climatologies from ground-based Doppler radars (e.g., Houze et al., 2001; James and Houze, 2005), and satellite-borne radars (e.g, the Tropical Rainfall Measuring Mission (Anders et al., 2006; Giovannettone and Barros, 2009)). Finally, long-term field campaigns, wherein intensive observations are taken over the course of several years, have created very detailed datasets of sufficient length to be useful for climate-related questions. A prime example of this is the Hydrometeorlogical Testbed (HMT) deployment in the northern Sierra Nevada and Coastal mountains of California where an extensive network of radar profilers, GPS integrated water vapor sensors, precipitation gauges, temperature sensors, distrometers, and stream gauges have been deployed every winter since 2005-2006 (e.g., Ralph et al. (2005), http://hmt.noaa.gov/), and built off of the previous PACJET and CALJET field campaigns. Extended HMT observations have helped give climatological perspective on: the importance of narrow jets of moisture flux for intense mountain precipitation (e.g., Neiman et al., 2002), the importance of "nonbrightband" rain (e.g., Neiman et al., 2005), the relationship of barrier jet winds to variations in the precipitation pattern over the Sierra (Neiman et al., 2010; Lundquist et al., 2010), and the mesoscale structure of the snow line (Lundquist et al., 2008; Kingsmill et al., 2008).

Advances in numerical modeling have also aided recent progress. The development of mesoscale models that are high-resolution, non-hydrostatic, and include sophisticated physical parameterizations (all made possible by advances in computing resources) has been key. Using these as RCMs to simulate regional climate over the past decades has been useful for better understanding mountain climates and their variability (e.g., Leung et al., 2003a,b). Additionally, using RCMs to make projections of future climate change has been useful for assessing climate impacts and for identifying mesoscale responses to climate change in mountainous regions (e.g., Giorgi et al., 1997; Leung et al., 2004; Salathé et al., 2008). However, it appears that the vast majority of RCM simulations are still run at too coarse of a resolution to accurately simulate the climatology of a number of important processes such as summertime convective storms (e.g., Hohenegger et al., 2008). Mesoscale models have also been used to study the climatology of mountain precipitation by simulating moist flow over idealized topography. This has been done both with experiments exploring wide ranges of parameter space (e.g., Colle, 2004), and with experiments focused on testing hypotheses arising from climatological observations (e.g., Zängl, 2008). Such simulations have been useful for identifying the mechanisms that act to shape orographic precipitation over the wide range of storm conditions that determine a climatology.

Finally, the development of idealized models and theories has also proven useful. For instance, the Linear Theory (LT) model of Smith and Barstad (2004) is a simple and efficient physically based model that incorporates most of the fundamental processes controlling orographic precipitation during stably-stratified unblocked flow. For instance, the model's speed has made it a useful tool for simulating climatological precipitation at high spatial resolution and over long time scales (e.g., Anders et al., 2008; Schuler et al., 2008).

1.4 An example: The Olympic and Cascade mountains

The studies in this thesis aim to draw general conclusions about the climatology of mountain precipitation. However, they do so largely by considering specific mountains. Throughout the following chapters the Olympic and Cascade mountains (Figure 1.1a), or idealizations thereof, are used as illustrative climatological case studies. These mountains reside on the west coast of North America in the mid-latitudes ($\sim 47°$N). The Cascades are a linear range oriented in the north-south direction, with mean crest elevation around 2 km, but with several volcanic peaks rising above 3 km. The Olympic mountains are a coastal range that is dome shaped, and rises to a maximum elevation of 2.4 km. Both ranges are deeply incised by river valleys that have created numerous ridges and valleys roughly 10-20 km in width and 0.5 km in relief.

Annual mean precipitation in the Olympics and Cascades is dominated by rain and snowfall events associated with mid-latitude cyclones of the Pacific storm track from Oct-Apr. The synoptic-scale flow during these storms is relatively simple compared to other mountain ranges due to the location of the Olympics and Cascades downwind of the a large expanse of open ocean. Orographic precipitation processes during these storms change as a function of storm sector (e.g., Hobbs, 1978; Medina et al., 2007). Warm sector and frontal precipitation occurring during steady neutral-to-stably stratified flow from the southwest sector provides much of the annual accumulation. The most extreme precipitation intensities

Figure 1.1: (overleaf) Topography and precipitation for the Olympic and Cascade Mountains of the northwestern Washington, USA (From Minder and Roe (2010)). (a) shows elevation in grayscale (black corresponds to 3.5 km) and the location of regularly reporting precipitation gauges located above 150 m elevation (white dots).(b)-(d) shows precipitation from October 2000 to September 2007 in gray shading, and smoothed contours of elevation every 250 m. (b) is from the PRISM analysis of gauge observations (Daly et al., 2008). (c) is from the operational MM5 numerical weather predictions (e.g., Minder et al., 2008). (d) is from the LT model of (Smith and Barstad, 2004) forced with data taken from atmospheric soundings at KUIL (shown in (a)). (e) compares the observed (gray) and MM5 (black) precipitation for a gauge transect in the southwestern Olympics (location shown with white line in (c)) for the winter of 2004-2005. The topographic profile (peak elevation of 800 m) is shaded (modified from Minder et al., 2008).

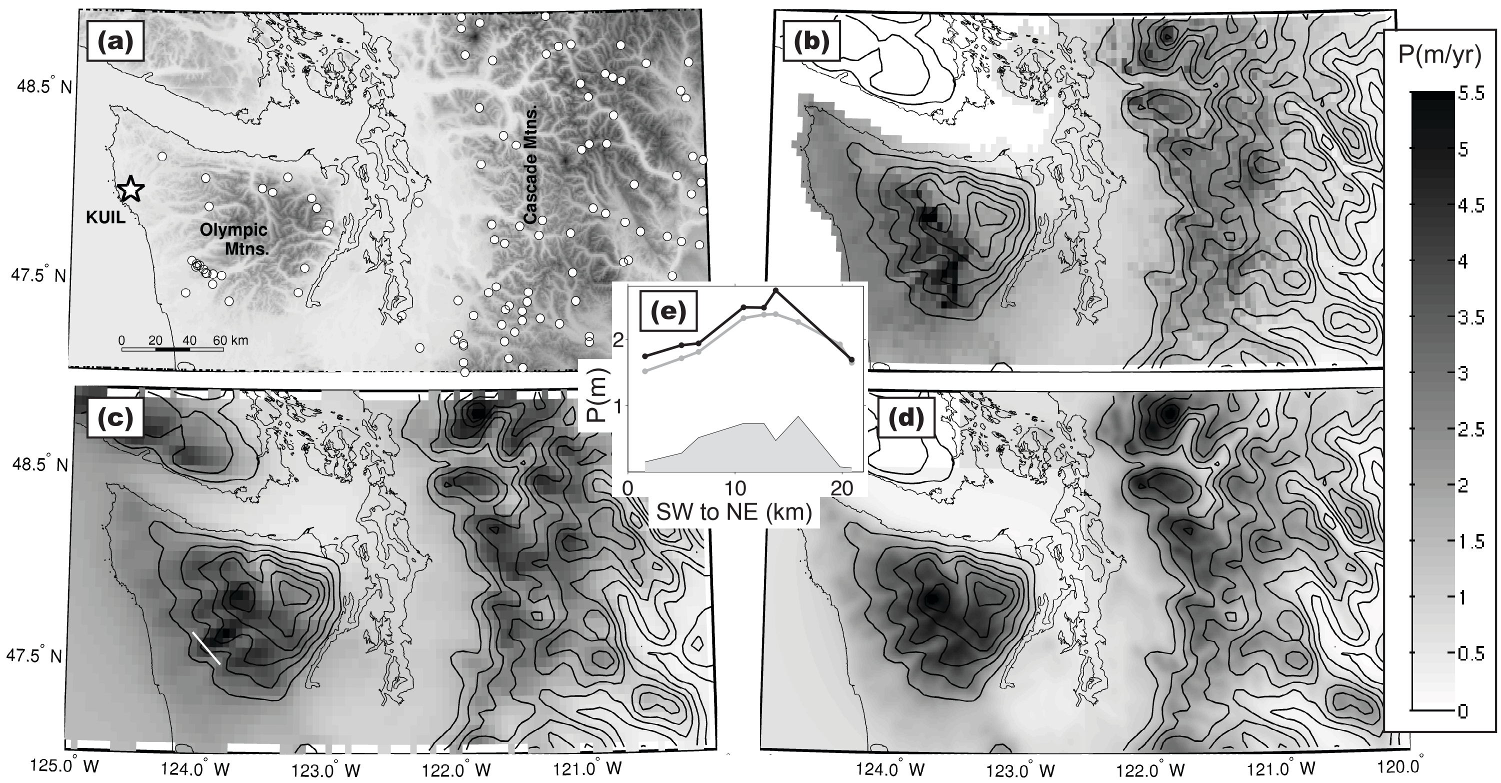
(a)
48.5° N
47.5° N
KUIL
Olympic Mtns.
Cascade Mtns.
0 20 40 60 km
(b)
(c)
(d)
(e)
P(m)
2
1
0
10
20
SW to NE (km)
P(m/yr)
5.5
5
4.5
4
3.5
3
2.5
2
1.5
1
0.5
0
125.0° W
124.0° W
123.0° W
122.0° W
121.0° W
120.0°

in the region occur when narrow bands of intense water vapor flux preceding cold fronts, so called "atmospheric rivers", impinge against the terrain (e.g., Neiman et al., 2008). Intense convective precipitation can occur in the lee (to the east) of the Olympics after the passage of surface cold fronts, due to the convergence of winds diverted around the range (Mass, 1981). During wintertime storms the 0°C isotherm and the rain-snow line typically occur at mid-elevations, around 1000 m, on the Cascades and Olympics, but there is large variability, with snow sometimes extending to sea level and rain sometimes reaching the highest peaks. Year-to-year variability in wet-season precipitation over the Olympics and Cascades is quite large; standard deviations are about 16% of the mean for precipitation, and 34% for snowfall (Serreze et al., 1999). This innerannual variability is related, in part, to hemispheric patterns of climate variability such as El Nino Southern Oscillation, and the Pacific Decadal Oscillation.

A rich body of data and literature exists that gives insight into precipitation patterns and processes in the region. Twice-daily atmospheric soundings, taken from Quillayute (KUIL) on the coast (Figure 1.1a), have been characterizing the flow approaching from the Pacific since 1966. Intensive observations from aircraft and radars during numerous field campaigns (e.g., CASCADE (Hobbs et al., 1971), CYCLES (Hobbs, 1978), COAST (Bond et al., 1997), and IMPROVE (Stoelinga et al., 2003)) detailed the airflow, thermodynamics, and microphysics associated with storms in the region, and illuminated many of the important processes controlling the orographic precipitation distribution. Operational mesoscale numerical weather prediction (NWP) model forecasts have been run at 4 km horizontal resolution over both the Olympics and the Cascades since 1999 ((Mass et al., 2003),www.atmos.washington.edu/mm5rt/), providing output that allows for the construction of detailed model-based climatologies of precipitation patterns and processes. Long-term climatological observations of mountain precipitation in the region come from a variety of networks, mainly: the Cooperative Observer Program (COOP), RAWS, and SNOTEL). To objectively analyze these point observations into gridded maps the Parameter Regression on Independent Slopes Model (PRISM, (Daly et al., 2008)) is often used. The best observations of mountain snow in the region measure accumulated snow water equivalent (SWE). Daily measurements for the past few decades come from SNOTEL, while manual measurements back to 1950 come from snow-course measurements, and indirect measurements of basin integrated SWE derived from streamflow extend the record back to 1930. These SWE record have been used to characterize trends and variability in the region's mountain snowpack and investigate their physical causes (e.g., Serreze et al., 1999, 2001; Hamlet et al., 2005; Mote et al., 2005; Mote, 2006; Mote et al., 2008; Casola et al., 2009; Stoelinga et al., 2009).

Figure 1.1 gives an overview the annual mean precipitation over both the Olympics and Cascades using several of the main datasets and models used in this study. Regularly reporting precipitation gauges are shown in Figure 1.1a. Many stations exist, but they are distributed largely in the foothills and valleys of the mountains, leaving large regions unsampled and providing insufficient coverage to characterize variations on the scale of ridges and valleys.

Analysis of data from these stations using the PRISM algorithm is shown in Figure 1.1b. Apparent in this panel are the dramatic variations in annual precipitation that occur across the ranges. The southwestern slopes of the Olympics and the western slopes of the Cascades receive upward of 4 m yr^{-1} accumulated precipitation as they force impinging winds during storms to rise, expand, and cool. To the lee of the mountains (northeast of the Olympics, and west of the Cascades) far less precipitation falls as winds, having deposited much of their moisture on the windward slopes, descend and dry. Figure 1.1b also suggests large variations on the scale of major ridges and valleys (about 20 km), with ridges receiving much more accumulation, however the sparse nature of the gauge network and the assumptions included in PRISM makes these features questionable.

Models can offer further insight into the precipitation patterns. Climatologies from the sophisticated MM5 mesoscale NWP model (discussed further in Chapter 2), and the idealized LT model (discussed further in Chapter 4) are shown in Figures 1.1c-d. These both agree quite well with the PRISM analysis in term of the range-scale patterns, but also exhibit the ridge-valley scale variations in precipitation found in PRISM, suggesting even larger ridge-top enhancement. The MM5 is a more sophisticated tool which is able to capture features such as the enhancement of precipitation well upwind of the Olympics that is absent in the Linear Theory model, however the Linear Theory model is also a powerful tool since it compares generally very well with MM5, may be run efficiently at very high resolution, and its results are much more straightforward to interpret.

The distribution of annual precipitation across an individual ridge in the southwest Olympics is shown in Figure 1.1e using data from from a dense gauge network (see Figure 1.1a) and the MM5 (see white line Figure 1.1c). This transect of high resolution observations shows that the ridge-top enhancement of precipitation found in the models and PRISM gauge analyses is very much a real feature. Chapter 2 characterizes this small-scale orographic enhancement in detail and examines its physical causes and variability. Chapter 3 deals with the impacts of such small-scale orographic precipitation patterns on the triggering of landslides.

1.5 Outline

The remainder of this thesis presents four distinct studies that investigate different aspects of the climatology of mid latitude orographic precipitation. These studies characterize precipitation patterns, investigate the responsible physical mechanisms, examine the impacts on hillslope failure and snowpack accumulation, and look into the effects of climate change. The tools used in these studies vary from field observations by precipitation gauges, to state-of-the-art NWP models, to simplified theoretical models. Common threads in these studies include: (1) a focus on the small spatial scale patterns that have only been recently modeled and observed, (2) a synthesis of data from observations and models of varying complexity to gain a fuller picture, (3) an extension of understanding from previous studies of individual storms to climatological scales.

Chapter 2 begins by characterizing the small-scale (10 km) patterns of precipitation that occur over the ridges and valleys of the Olympic Mountains. This work is conducted by collecting and analyzing several years of data, both from archived MM5 model forecasts and a special observing network of about 15 mixed precipitation gauges. By using the MM5 to simulate and analyze case studies, the physical processes responsible for the mean pattern and variations in the pattern are diagnosed. Major results of this work included the finding that large ($> 50\%$) enhancement of precipitation over ridges relative to valleys is a very robust feature of the region's climate, and the finding that these climatological patterns are surprisingly well-simulated by a mesoscale model (despite frequent errors for individual storms). Content of this chapter comes from the published paper: Minder et al. (2008).

Chapter 3 builds off the results from Chapter 2 by investigating how large climatological gradients in precipitation, such as those found in the Olympics, may influence patterns of landslide susceptibility. To do so an idealized model of shallow landslides is used, applied over a region in the Olympics as a case study. Using the climatology developed from MM5 forecasts the model is forced both with a climatological pattern of extreme precipitation and with characteristic uniform values of precipitation to isolate the role of spatial rainfall variations in controlling landslide susceptibility. Sensitivity calculations are also conducted to compare the relative importance of spatial variations in rainfall with spatial variations in soil properties. Results of this work suggest that small-scale maxima in climatological precipitation may play an important role — comparable with some landscape factors (such as soil thickness and vegetation) — in making certain regions more susceptible to slope failure. Also, the use of unadjusted lowland precipitation data to characterize conditions on nearby mountain slopes may lead to a substantial underestimate of landslide hazard. Content of this chapter comes from the published paper: Minder et al. (2009).

Chapter 4 deals with climate-related changes in mountain snowpack. Much previous work on the subject has focused on analyzing the past using observations, or making future projections using sophisticated models. While these studies have explained much about how snowpack changes with climate, they have generally not focused on isolating the underlying physical processes responsible for the changes. As a step in that direction this work uses two idealized physically based models to investigate controls on the sensitivity of mountain snowpack accumulation to climate warming. One of the models includes only the distribution of storm melting-levels, while the other model (based on the LT model of Smith and Barstad, 2004) also includes the basic physics of orographic precipitation. Results suggest that the relationship between the climatological melting-level distribution and the topography is the principle control on the sensitivity of snowpack accumulation to climate warming. Additionally, the results show that, while thermodynamically driven increases in precipitation with warming may moderate the loss of snowfall somewhat, for large amounts of warming precipitation increases have an insignificant effect because the loss of snow accumulation area is too substantial. The content of this chapter comes from the following published paper: Minder (2010).

Chapter 5 investigates the physical processes that control the climatology of the snow line, the elevation at which precipitation transitions between rain and snow, over mountains. Recent multi-year observations reveal that during storms the snow line on the windward slopes of mountains is typically at much lower elevations (several 100 m's lower) than in the free air upwind of the mountain. The mesoscale modification of the snow line is poorly understood, is not resolved by global models, and is large enough to have major impacts on a variety of natural and human systems. Semi-idealized simulations with a mesoscale NWP model (WRF) are used to simulate the rain-snow boundary over mountains for stably stratified orographic precipitation. These simulations allow the identification of the physical mechanisms responsible for mesoscale structure of the snow line. Results reveal that latent cooling from melting precipitation, adiabatic cooling from vertical motion, and spatial variations in microphysical timescales all play important roles. However, the relative importance of these processes depends on the properties of the incoming flow and the terrain geometry. The content of this chapter is in preparation for submission as a full length journal article.

Chapter 6 will present a brief summary and some general conclusions.

Chapter 2

THE CLIMATOLOGY OF SMALL-SCALE OROGRAPHIC PRECIPITATION: PATTERNS AND PROCESSES[1]

2.1 Introduction and Background

The effect of small-scale topographic features on the distribution of precipitation was first recognized in the 1960's due to observations by Tor Bergeron's "Project Pluvius" rain-gauge network showing a 50% enhancement of precipitation over ∼50 m high, ∼10 km wide hills in Uppsala Sweden (Bergeron, 1968). Advancement in understanding orographic precipitation on scales smaller than entire mountain ranges (scales of 10's of km or less) has been slow in the decades following Bergeron's work, and major gaps in understanding still persist, particularly with respect to the climatology of precipitation patterns. Progress has been impeded in large part due to insufficient observations of mountain precipitation: gauge networks seldom have the spatial density required to sample subrange-scale variations in precipitation; the distribution of stations tends to be biased towards valley sites (Groisman and Legates, 1994); and the frozen precipitation often present at high mountain sites is notoriously challenging to measure accurately (e.g., Yang et al., 1998). Radar data is also sparse over mountains due to blocking of the beam by topographic features. Furthermore, only in the past decade or so have observations been augmented with operational numerical weather prediction (NWP) models, run regularly with sufficient spatial resolution to simulate orographic precipitation on scales of 10 km and less (e.g., see discussion in Alpert et al., 1994).

The distribution of precipitation over mountains is critically important for a range of applications. For instance, landslides and avalanches are triggered by intense and/or persistent precipitation at particular locations within mountainous terrain (Caine, 1980; Conway and Raymond, 1993). The evolution of mountain snow pack, a crucial and changing water resource in regions such as the American West (Mote et al., 2005), is also influenced by precipitation distribution. Additionally, the successful prediction of flood events has been shown to be sensitive to the proper simulation of small-scale precipitation features (Westrick and Mass, 2001). Furthermore, if mountain precipitation patterns remain persistently tied to topography over thousands of years, they can be translated into patterns of erosion that shape the mountains themselves, resulting in a coupled co-evolution between precipitation and topography (e.g., Willett, 1999; Roe et al., 2002; Anders et al., 2008; Stolar et al., 2007).

---

[1] The contents of this chapter are published in Minder et al. (2008), © 2008 Royal Meteorlogical Society. The published version may be found at: http://www3.interscience.wiley.com/journal/119816998/abstract.

Recently, advances in model resolution, remote sensing, and observations have begun to illuminate the distribution of small-scale orographic precipitation, and the responsible processes. In particular, several field campaigns have produced extremely detailed analyses of individual orographic precipitation events (e.g., the CASCADE (Hobbs, 1975), SCPP (Marwitz, 1987), COAST (Colle and Mass, 1996), MAP (Bougeault et al., 2001), and IMPROVE (Stoelinga et al., 2003) projects), but only recently have small-scale patterns been a focus. Many of these case studies have involved scenarios with stable flow impinging upon topography, and recent work has shown that small-scale mountain waves, forced by individual ridges, may play a central role in shaping the precipitation distribution. Over the slopes of the Oregon Cascades, airborne dual-Doppler radar data and *in situ* measurements were collected as part of phase-two of the Improvement of Microphysical Parameterization through Observational Verification Experiment (IMPROVE-2) field campaign. Using these data Garvert et al. (2007) found vertical velocity signatures from gravity waves forced by ∼10 km wide and ∼1 km high ridges and valleys perpendicular to the crest on the windward side of the range during a storm with stably stratified flow. Associated with these waves were enhancements in cloud liquid water, radar reflectivity, and hydrometeor mixing ratios, all centered roughly over the ridges. These anomalies were reproduced in a high resolution (1.33 km in the horizontal) NWP model, and were found to enhance the precipitation over the windward slope of the range by up to 14%. Colle (2007) looked at the effect of windward ridges on precipitation during stable flow using a NWP model in a two-dimensional, idealized context. He found that for a range of upstream conditions, the addition of ridge-valley relief on the upwind side of a barrier can lead to a local enhancement of precipitation on ridge-tops, ranging from 200–300%, and a net 10–35% enhancement over the windward slopes as a whole. Similar enhancement of precipitation during stable flow over narrow topographic features has been observed and/or modeled for storms over ridges in the Sierra Nevada (Grubisic et al., 2005), the Mongolian Rim of Arizona (Bruintjes et al., 1994), and the modest hills of Long Island, NY (Colle and Yuter, 2007).

In the presence of unstable impinging flow, stationary and transient convective features triggered by small-scale topography can strongly control the pattern and efficiency of precipitation (e.g., Kirshbaum and Durran, 2004; Fuhrer and Schär, 2005). Such processes represent modes of orographic precipitation which are distinctly different from those found during stable flow. For instance, narrow (2–4 km wide), stationary, convective rain bands have been observed with NEXRAD radar over the coastal mountains of Oregon. These bands of convection are triggered by lee waves associated with ascent over small-scale topographic features, and align themselves parallel to the low-level flow, at times cutting across ridges and valleys (Kirshbaum et al., 2007).

A variety of storms, with varying degrees of stability, were studied during the Mesoscale Alpine Programme (MAP) in the European Alps, and across a range of conditions observations showed precipitation patterns and processes linked to topographic features on scales as small as 10 km (Rotunno and Houze, 2007; Smith et al., 2003). Under conditions with potentially unstable impinging flow, convective cells embedded within stratiform precipitation were associated with intense riming and precipitation over the first narrow range of the Alpine massif (Smith et al., 2003; Medina and Houze, 2003).

The above-noted studies offer detailed accounts of individual storm events, but little is known about storm-to-storm variations in precipitation patterns and how they combine to form a climatological average. Studies which have focused on such issues suggest that small-scale patterns can be pronounced in the climatology and persistent over timescales of years. Frei and Schär (1998) constructed a gridded precipitation analysis from the dense gauge networks present over the European Alps, and observed ∼40-km scale patterns tied to small ranges. A transect of climatological mean radar reflectivity over the Alps (Houze et al., 2001) shows persistent features on 10-km scales (attributable in part to convection). Anders et al. (2006) examined Tropical Rainfall Measuring Mission (TRMM) data over the Himalaya, finding 10-km scale precipitation patterns, persistent for several years, with major valleys penetrating into the range receiving a great excess of precipitation relative to adjacent ridges. In contrast, Anders et al. (2007) found a 60–100% enhancement of precipitation over ∼10 km wide ridges relative to adjacent valleys by analyzing seven years of model output and three years of gauge observations from the Olympic Mountains of Washington State, USA.

While the above studies have demonstrated that small-scale terrain features exert a strong influence on mountain precipitation both for individual storms and in the climatological mean, they also show that the nature of this influence can vary markedly depending upon geographic location and atmospheric conditions. Here we extend the analysis of the small-scale distribution of precipitation over the Olympic Mountains. The availability of long sets of both observational data and NWP output at high spatial resolution allows us to address in detail the following:

1. *What are the dominant physical processes responsible for the observed precipitation patterns?*
2. *How sensitive are the patterns to changes in atmospheric factors such as winds, stability, temperature and frontal regime?*

Answers to these questions help extend the understanding of small-scale orographic precipitation in midlatitudes to climatological time scales. The results have important applications for natural hazards assessments, and ultimately, for the evolution of landscapes over geologic time.

2.2 Precipitation in the Olympic Mountains

The Olympic Mountains of Washington State, shown in Figure 2.1, are a roughly dome-shaped coastal mountain range, rising to approximately 2.4 km at the peak of Mount Olympus. The western side of the range, exposed to the prevailing southwesterly winds, receives plentiful annual precipitation (Forks, on the northwestern side of the range receives 3.0 m of annual precipitation); whereas locations in the lee of the mountains are affected by a

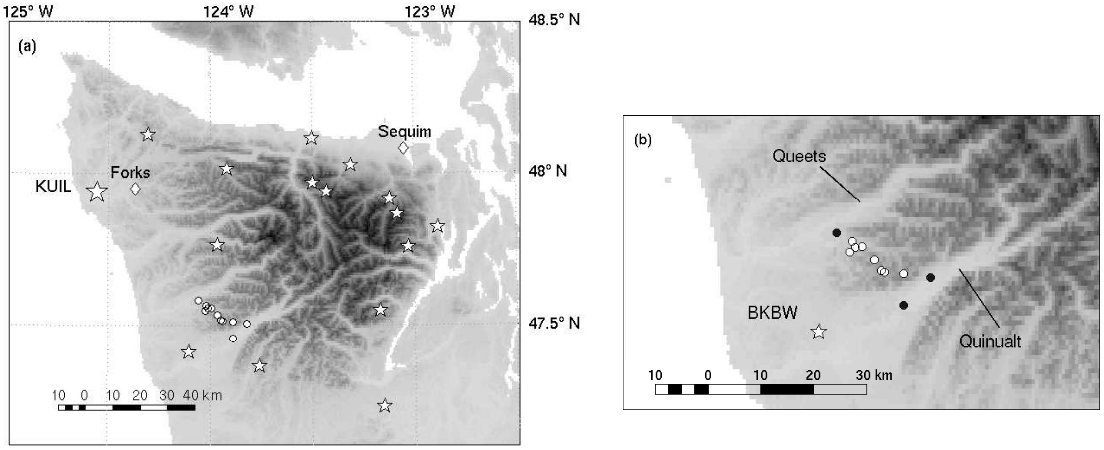

Figure 2.1: Rainfall observations in the Olympic Mountains. (a) shows the terrain of the Olympic Peninsula (grayscale shading), with a maximum elevation of 2.43 km. The locations which regularly report hourly precipitation (from the RAWS, ASOS, and the SNOTEL networks) are shown with stars. Location of the Quillayute (KUIL) sounding, and the COOP stations (Forks and Sequim) discussed in the text are also denoted. (b) shows a detailed view of the Queets-Quinault gauge network. Mixed precipitation gauges are shown with white circles, while rain-only gauges are shown with black circles. The Queets and Quinault Valleys, and the Black Knob (BKBW) RAWS station are also denoted.

strong rain shadow (Sequim, on the Northeastern side receives 0.4 m annually). The vast majority of the precipitation falls from October through April, within the warm sectors of mid-latitude cyclones. (At Forks, for example, only 16% of the annual total falls from May through September). The current stations which report hourly precipitation over the Olympics, shown with stars in Figure 2.1, are arrayed mainly around the perimeter of the mountains, and are far too sparsely distributed to characterize patterns on a ridge-valley scale. Upper air conditions are measured via rawindsone at Quillayute (also indicated in Figure 2.1) at 00 and 12 UTC.

2.2.1 Mesoscale Modeling over the Olympics

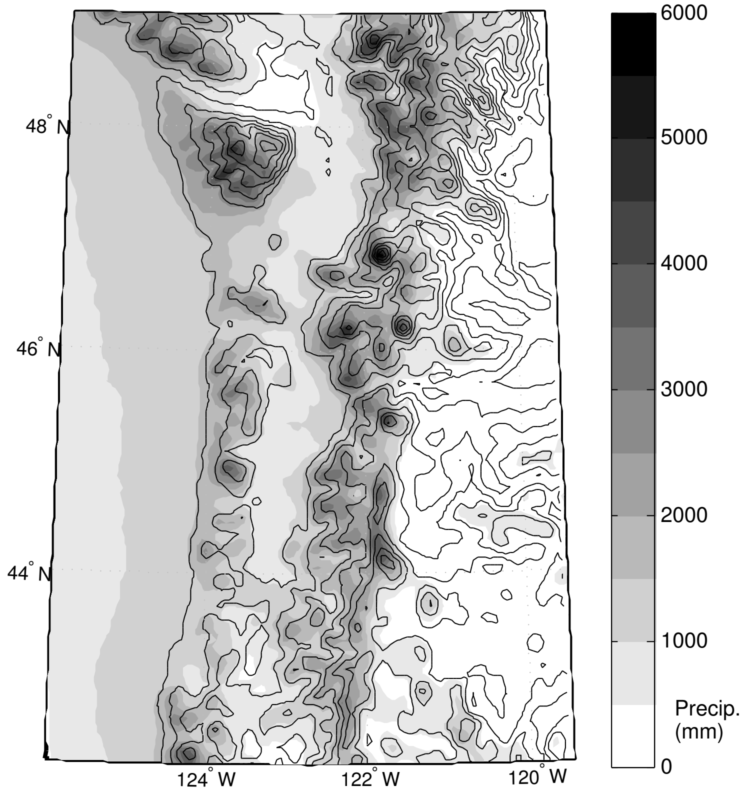

Figure 2.2: MM5 annual precipitation climatology (color shading, in units of mm yr^{-1}), and model topography (contours every 250 m) over Olympic, Cascade, and Coastal mountain ranges (water years 2001–2006).

Since 1997 the fifth generation Penn State-National Center for Atmospheric Research Mesoscale model (known as the MM5, (Grell et al., 1995)) has been run (by the Northwest Regional Modeling Consortium at the University of Washington) at 4 km horizontal resolution over the Pacific Northwest (Mass et al., 2003, , http://www.atmos.washington.edu/mm5rt/). The model is run twice daily (initialized at 00 and 12 UTC), forced with initial and lateral boundary conditions supplied by the National Center for Environmental Prediction (NCEP) Global Forecast System (GFS) model (runs before mid-2002 were forced with the

NCEP's "Eta" model). A variety of changes have been made to the MM5 model grid, initialization, and parameterizations schemes since 1997. Most notable for this study are the changes in microphysical scheme from Simple Ice (Dudhia, 1989) to Reisner2 V.3.6 (Reisner et al., 1998; Thompson et al., 2004) occurring in February of 2004, and to Reisner2 V.3.7 microphysics starting in May of 2006. A full listing of model changes can be found at: http://www.atmos.washington.edu/mm5rt/log.html.

To test for biases in the MM5 simulation of the flow impinging on the Western Olympics, we have compared 24 hr model forecasts at 850 hPa to those observed via the Quillayute sounding during conditions characteristic of major precipitation events (flow from the southwest quadrant, 850 hPa wind speeds > 15 ms^{-1}) by calculating the mean error (forecast minus observed) over 203 soundings from two rainy seasons (2005–2006 and 2006–2007). The mean error in the temperature is quite small, +0.18 K. MM5 water vapor mixing ratios have a moist error of $+5 \times 10^{-4}$ kg/kg (about a 12% bias relative to the mean value), but due to documented dry biases in the Vaisala radiosondes (e.g., Wang et al., 2002) it is unclear if this reflects a deficiency in the model or the observations. The model winds are biased to be somewhat weak and too westerly, with a mean error of -1.1 ms^{-1} (a 5.6% bias relative to the mean) for wind speed and $+8.4°$ for wind direction. Based on the scale of these biases, we expect them to result in only modest errors in the incoming vapor flux available for orographic precipitation. The detailed structures of airflow and precipitation over the Olympics can also be well simulated by MM5, as shown by Colle and Mass (1996) through comparison of airborne radar observations with model output. Results from their work also showed evidence for an enhancement of precipitation over the major ridges on the windward side of the range. Colle et al. (2000) compared 1997–1999 cool-season, 4 km-MM5 precipitation forecasts to observations and found relatively small biases over the Olympics, which contrasted with significant over-prediction of precipitation over the windward slopes of the Cascade Mountains. However, when only heavy precipitation events were considered a bias towards significant under-prediction was observed over the Olympics, with biases approaching 50% at some locations.

The work of Colle et al. (2000) also revealed that the climatology of precipitation on the 4 km model domain exhibits significant enhancement over the ~10 km wide ridges on the windward side of the Olympics. This feature is pronounced, amounting to a 50–300% enhancement on the ridges relative to the valleys, and it has appeared with remarkable consistency in the MM5 annual precipitation totals for over six years (Anders et al., 2007). A climatology of MM5 annual precipitation is shown in Figure 2.2, for water years 2001–2006 (A water year in this Pacific Northwest is defined to begin on October 1st and end on September 30th, designated by the calendar year in which it ends), revealing that the modeled ridge-valley pattern of enhancement is not confined to the Olympic Mountains; similar patterns are found over the Cascade, Coastal, and Vancouver Island mountain ranges.

2.2.2 Queets-Quinault Gauge Network

Motivated by the remarkable ridge-valley precipitation difference in the MM5 forecasts, we established a high-density network of data-logging precipitation gauges in a transect across one of the major ridges in the Southwestern Olympics (Figure 2.1a-b). The network of gauges cuts across the topographic ridge that experiences the greatest enhancement of precipitation in the MM5 climatology, from the Queets river valley in the northwest to the Quinault river valley in the southeast. The gauge network has been deployed for water years 2004–2007 during each wet season from early October until late April. The gauge elevations range from approximately 50–900 m (Figure 2.4).The lowest elevation (< 200 m) gauge sites were equipped with traditional tipping bucket rain gauges with 0.2 mm/tip resolution, whereas higher elevation sites (> 200 m) were equipped with gauges capable of measuring both frozen and liquid precipitation (Figure 2.1b). These mixed precipitation gauges have a resolution of 1 mm/tip, and are similar in design to the gauges described by McCaughey and Farnes (1996) and later produced by Campbell Scientific as snow adaptor CS705. During our field seasons, the percentage of lowland precipitation occurring when the ridge-top temperatures were $> 0.5°$ C ranged from 74–87 %, suggesting that much of the precipitation atop the ridge fell as rain. Thus, we do not expect the undercatch of frozen precipitation to introduce large biases into our observations of season-total precipitation. Further discussion of the gauge network can be found in Anders et al. (2007).

The incident wind speed and direction influence the pattern and strength of ascent, and

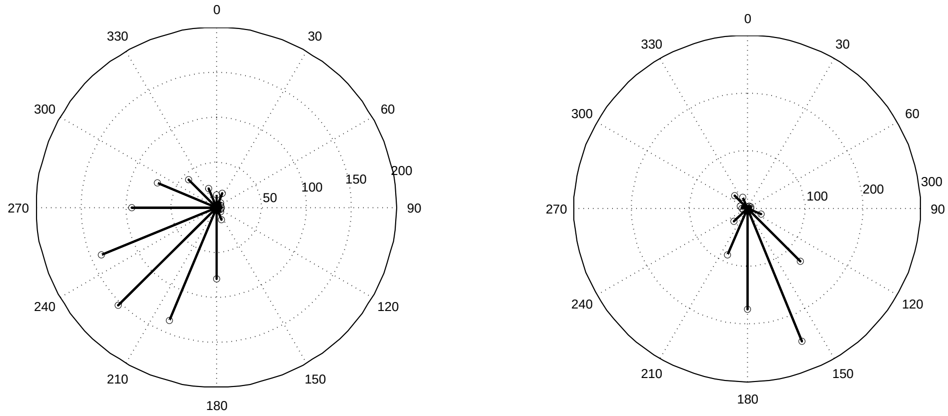

(a) (b)

Figure 2.3: Precipitation weighted wind roses from water years 2004–2006. The length of each radial line is proportional to the amount of precipitation falling at the BKBW station when winds are from each direction. (a) uses 6 hr 850 hPa winds from the gridpoint in the NCEP-NCAR reanalysis upwind of the site during average flow, (b) uses 6 hr averaged 10 m winds from the BKBW station.

hence the resulting pattern of condensation and precipitation (e.g., Hill et al., 1981; Smith and Barstad, 2004). We therefore examine the climatological distribution of winds near our study site. Figure 2.3a is a precipitation-weighted wind rose for the 850 hPa winds from the NCEP-NCAR reanalysis (Kalnay et al., 1996, , http://www.cdc.noaa.gov/), weighted by precipitation observations from the Black Knob (BKBW) Remote Automated Weather Station, the nearest station to our study area (Figure 2.1b). At 850 hPa, the winds are almost entirely southerly to southwesterly during periods of significant rainfall. In contrast, the same exercise performed with the 10 m winds measured at BKBW (Figure 2.3b) shows mainly southeasterly to southerly winds during precipitation events. These low-level winds are characteristic of topographic blocking, which occurs when nonlinear dynamics lead to deceleration, and often deflection, of the low-level incident flow (e.g., Pierrehumbert and Wyman, 1985). Thus, from Figure 2.3, we find that a nearly 90° climatological veering of winds with height occurs during precipitation events, from surface SE winds that are approximately perpendicular to the major sub-range-scale topographic ridges and valleys, to 850 hPa SW winds that are parallel to the ridges and valleys. Blocking of low-level flow has been shown to have strong influence on orographic precipitation, both in idealized simulations (e.g., Jiang, 2003), and in observations (e.g., Medina and Houze, 2003), and may be, in part, responsible for the extension of the Olympic Mountain precipitation maximum upstream over the coastal lowlands and the Pacific (see Figure 2.2).

Table 2.1: Statistics from each observational field-season. The dates of each season are given, as are the modeled and observed measures of ridge-valley enhancement (as defined in the text) for the season-total precipitation. Also shown are the normalized root-mean-squared-error (RMSE) and bias of the model forecasts over the network (also defined in the text).

Season		**wy2004**	**wy2005**	**wy2006**	**wy2007**
Dates		10/17/2003 -5/1/2004	11/08/2004 -4/4/2005	10/10/2005 -2/15/2006	10/28/2006 -4/17/2007
R/V	*Obs.*	1.40	1.35	1.29	1.57
	MM5	1.48	1.38	1.30	1.37
$\mathbf{R_{max}/V_{min}}$	*Obs.*	1.61	1.61	1.63	1.78
	MM5	1.60	1.59	1.45	1.46
RMSE (normalized)	*Season*	0.22	0.10	0.11	0.11
	Top-Events	0.20	0.20	0.26	0.13
Bias	*Season*	1.16	0.93	0.90	1.04
	Top-Events	1.08	0.82	0.76	0.97

We compare the annual precipitation observed by our gauge network with that from the archived 4 km-MM5 output by linearly interpolating the 24–36 hr forecasts, summed over entire field seasons, to the gauge locations. MM5 forecast hours 24–36 are used to assure that precipitation has been spun-up on the innermost domain (Colle et al., 2000). The apparent long spin-up time on the 4km domain occurs, in part, because it has been initialized later into the MM5 forecasts, at times which have ranged from fhr 6 to 12. The left column of panels in Figure 2.4 show the field-season totals at each of the continuously operating gauge sites for the past four field-seasons from the MM5 forecasts and the observations. The range of dates defining each field-season are given in Table 2.1. Precipitation totals are plotted as a function of approximate distance along the cross-ridge transect. We find the skill of

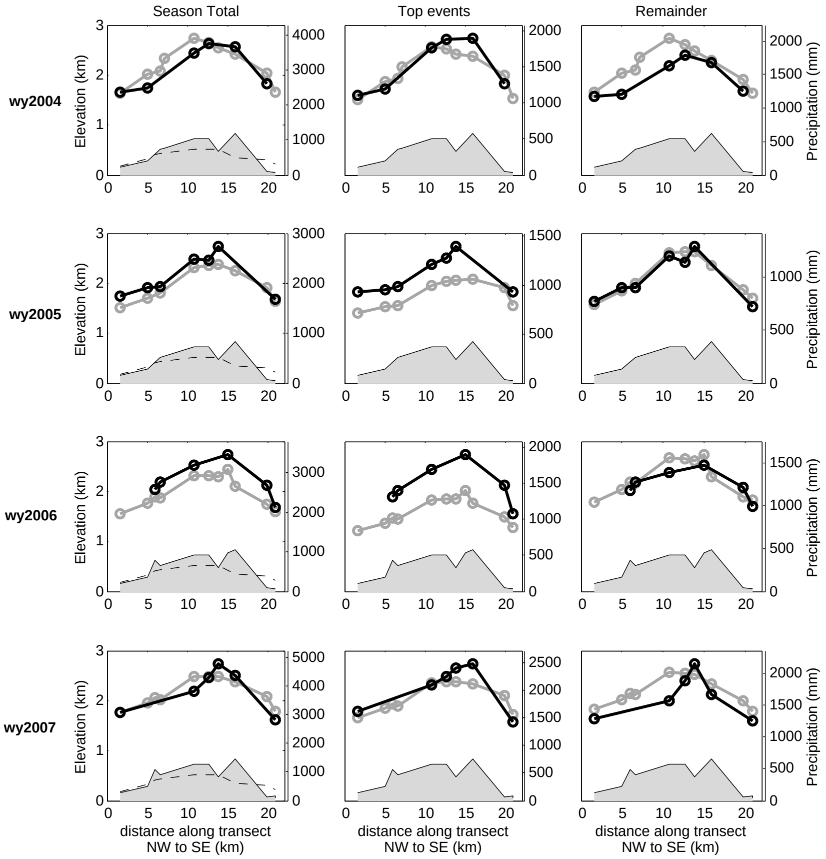

Figure 2.4: Observed and modeled precipitation totals at sites along Queets-Quinault gauge transect for four rainy seasons (dates given in Table 2.1). Accumulated precipitation is plotted as a function of approximate distance along transect. Black lines and circles show observations from the gauges that were continually operational for the entire season. Gray lines and circles show archived MM5 forecasts interpolated to gauge locations. Elevations of the gauges deployed each year are given by shaded topographic profile at the bottom of each plot. The MM5 terrain interpolated to the gauge locations is given by the dashed line in the first column of figures. The columns (left to right) show season total precipitation, precipitation from the largest events, and precipitation from the remaining events (method for defining events is described in the text). (Note: the use of a different interpolation scheme resulted in somewhat different MM5 values than those shown in Anders et al. (2007)).

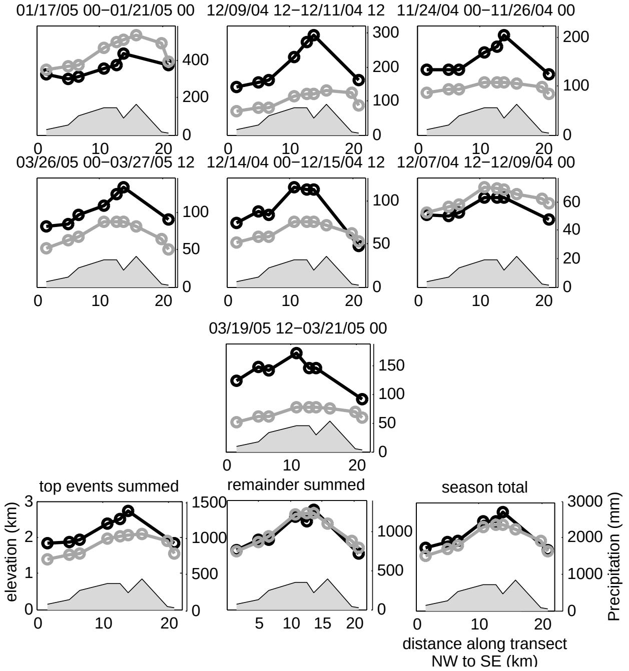

Figure 2.5: Top rainfall events for the water year 2005 gauge season. The top three rows show the individual top events, determined as described in the text, together responsible for approximately 50% of the observed precipitation during the field season. The bottom row shows the sum of the top events, the sum of the season's remaining precipitation, and the season total. Note that large errors present for individual events show a tendency to average out when events are summed.

the model at reproducing the pattern and amount of precipitation at the gauge sites to be remarkable, considering the observational uncertainties associated with the gauging of mixed precipitation, the coarseness of the model resolution (4 km) relative to the width of the ridge (∼10 km), and the representiveness error associated with interpolating relatively coarsely gridded precipitation fields to point locations (e.g., Tustison et al., 2001). These results affirm that the ridge-valley enhancement is a very consistent and pronounced feature, occurring year-after-year in both the model and observations.

We consider two measures of the ridge-valley precipitation enhancement:

- **R/V**: The ratio of the average precipitation at the high elevation sites (> 200 m) to that measured at the low elevation sites (< 200 m).

- $\mathbf{R_{max}/V_{min}}$: The ratio of the maximum precipitation among the high elevation sites (> 200 m) to the minimum among the low elevation sites (< 200 m).

The values of these two enhancement metrics for each season are shown in Table 2.1. The same sites are used to calculate the modeled and observed enhancement. However, vandalism and gauge malfunctions disrupted the collection of continuous data at some sites, thus a slightly different network of gauge sites was used for each year (note the different gauge sites shown in Figure 2.4). Hence, care must be taken in comparing the enhancement between years. On average the MM5 shows a somewhat weaker $\mathbf{R_{max}/V_{min}}$ enhancement (ranging from 1.45–1.60), than the gauges (which range from 1.61–1.78). However, even if MM5 were perfectly representing the precipitation processes over the Olympics, we might expect a smaller spatial variability (and hence enhancement) in the interpolated model output solely due to the differences in scale between the point observations of the gauges and the model forecasts of 16 km^2 spatial averages (e.g., Tustison et al., 2001).

For the season totals, the average values of model bias:

$$Bias = \frac{1}{N}\sum_{i=1}^{N}\frac{F_i}{O_i} \quad , \tag{2.1}$$

and root-mean-squared error:

$$RMSE = \sqrt{\frac{\sum_{i=1}^{N}(F_i - O_i)^2}{N}}, \tag{2.2}$$

are both calculated over the gauge network. F_i and O_i are the forecast and observed precipitation at the ith gauge site, and N is the number of gauge sites. The $RMSE$ values are normalized by dividing by the network averaged precipitation to give a fractional error. These values are shown in Table 2.1. The model does not show a systematic bias towards over- or under-prediction of the season total, in agreement with the relatively small biases Colle et al. (2000) found in the MM5 over the Western Olympics for the 1997–1999 rainy seasons.

We have also considered the skill of the model at representing precipitation patterns for individual major storm events appearing in either the gauge observations or MM5 forecasts. We define the top MM5 events by ranking all MM5 24–36 hr precipitation forecasts based upon an areal mean of the accumulated precipitation over the region of our gauge network. We define the top gauged events by ranking our gauge observations based on network averaged precipitation. The top storm events are formed by separately aggregating the adjacent top MM5 and gauged events into single extended events, and then further combining any extended MM5 and gauge events that overlap. Lastly, the 12 hr periods preceding and succeeding a storm event were also included in that event. This method was chosen to assure that precipitation events forecast by MM5 with a timing error are compared with the appropriate event in the observations. We define the top storm events to be those storm events which together make up ∼50% of the observed rainfall. The top storm events, chosen in this manner, range in length from 1.5 to 6 days, with a mean length of 2.2 days. The number of top events in a water year varied between 7 and 12.

Figure 2.5 shows the modeled and observed precipitation for the top events of the water year 2005 field season. Note the large errors apparent for many of the individual events. These storms include events with and without convective instability present in the Quillayute sounding. Also shown are the sum of the top events, the remaining events, and the season total precipitation. The aggregated top events are much better simulated than most of the individual events, and the sum of the many smaller events is simulated even more skillfully. Large model errors for individual storms, contrasting with an excellent modeled climatology, are found for each year (not shown). The sum of the large events and remaining rainfall are plotted in the right two columns of Figure 2.4. For the large events of water years 2005 and 2006 there is a significant under-prediction of precipitation (approaching 25% for water year 2006) over the region, which is largely masked by the inclusion of the smaller events in the season total. Such under-prediction during heavy rainfall is in agreement with the findings of Colle et al. (2000) for the rainy seasons of 1997–1999, but does not appear in water years 2004 and 2007. For the remaining smaller rainfall events the model shows little to no systematic bias.

Thus, the integrated effect of a range of over- and under-predicted events is a very re-

Table 2.2: Percent of 12hr periods during each season showing enhanced precipitation (i.e. $R/V > 1$) at the high elevation (> 200 m) gauge sites relative to the low elevation (< 200 m) sites . Percentages were calculated for medium-to-heavy rainfall periods (> 4 mm / 12 hrs) and heavy rainfall periods (> 24 mm / 12 hrs). Periods of sub-zero temperatures when one or more gauges was frozen are excluded from the analysis. The sample size of medium-and-heavy periods ranged from 65–199, while the sample size for heavy periods ranged from 11–23.

Season	% **ridge-enhanced**		% **ridge-enhanced**	
	(> 4 mm /12 hrs)		(> 24 mm /12 hrs)	
	Obs	*MM5*	*Obs*	*MM5*
wy2004	80	99	91	100
wy2005	94	96	88	100
wy2006	66	92	72	94
wy2007	83	94	91	100

alistic model climatology. This suggests that the model is capturing the essential physics controlling precipitation over our study area, however the errors for individual events may be indicative of some deficiency in the model representation of precipitation processes, or the result of random errors. Deficiencies in microphysical parameterizations have been extensively studied as a source of error in the simulation of mountain precipitation (e.g., Stoelinga et al., 2003). Recent work has begun to examine the sensitivity of orographic precipitation forecasts to initial conditions. Walser and Schär (2004) used an ensemble of model runs to show that "even if the NWP model and synoptic forcing are assumed to be perfect", precipitation forecasts over mountainous terrain may "on occasions be critically affected by predictability limitations". Therefore, we hypothesize that errors in the specification of initial conditions (particularly over the observation-sparse Pacific Ocean), may be responsible for some of the large model errors that occur for individual storms.

Lastly, we have also examined the storm-to-storm distribution of enhancements found in the gauge and the model data. For each 00–12 and 12–24 UTC period we calculated the **R/V** enhancement metric. We consider 12 hr periods where greater than 4 mm of precipitation occurred over our gauge network, (since at lower precipitation rates, the ability of our 1 mm/tip gauges to adequately resolve the ridge-valley difference is suspect). We also consider heavy rainfall periods with above 24 mm in 12 hrs. As shown in Table 2.2, in majority of events the ridge-valley enhancement is present. It seems, however, to be a more persistent feature in the model than in the observations. This may point to a real difference between the modeled and actual precipitation patterns during some events. Alternatively, this may be an artifact of observational errors. While snow at the lowland sites is very rare, during cold storms a significant amount of precipitation may fall as snow atop the ridge. Gauges are much more vulnerable to under-catch errors during snowfall (e.g., Yang et al., 1998), so greater under-catch at ridge-top compared to valley sites during cold events may lead to an underestimate of the enhancement for some events in the gauges. Limiting the analysis to periods of heavy rainfall shows the enhancement to be a more persistent feature during such events.

2.3 Case studies

The excellent agreement between the modeled and observed precipitation climatology over the Queets-Quinault region, combined with the verification, on 10-km scales, of modeled dynamical and microphysical fields during observing campaigns (Garvert et al., 2007; Colle and Mass, 1996), gives us confidence that MM5 simulations capture the fundamental physical processes responsible for the ridge-valley enhancement over the southwestern Olympics. We have therefore conducted a detailed analysis of several case studies to diagnose the mechanism for precipitation enhancement in the model and the factors controlling the storm-to-storm variations in the small-scale pattern of precipitation.

Based on archived MM5 forecasts, gauge network observations, and soundings taken from Quillayute, we chose five major precipitation events to simulate, three of which we shall discuss (Table 2.3). In selecting these events we focused upon intense precipitation events, as these matter the most for flooding, landsliding, and erosion. The 28 Nov 2003 and 21 Oct 2003 events contained the largest 12 hr rainfall totals over the network in water year 2004

Table 2.3: Conditions for case studies discussed in text. The time period of event included in first section. The second section includes modeled and observed surface conditions. **R/V** and $\mathbf{R_{max}/V_{min}}$ give the ridge-valley enhancement as described in the text. **Pcp**, gives the storm-total precipitation at the BKBW station. **Temp, Wspd, Wdir** denote the range of 2 m temperature, and 10 m wind speeds and directions at BKBW. **Wgst** denotes the observed wind gusts. The third section provides metrics from the modeled KUIL sounding. **FL** gives the range of freezing levels. $\mathbf{N^2_{m,\,0--2km}}$, $\mathbf{WSPD_{(0-2km)}}$, and, $\mathbf{WDIR_{(0-2km)}}$, give the range of moist static stabilities, wind speeds, and wind directions, averaged between 0 and 2 km.

Case	**28 Nov**		**20 Oct**		**17 Jan**	
Dates-Times (UTC)	11/28/2003 05 – 11/29/2003 06		10/20/2003 06 – 10/20/2003 18		01/17/2005 00 – 01/18/2005 12	
	Obs.	*MM5*	*Obs.*	*MM5*	*Obs.*	*MM5*
Pcp. (mm)	173	131	70	64	241	170
R/V	1.3	1.4	1.6	2.2	1.1	1.3
$\mathbf{R_{max}/V_{min}}$	2.0	1.8	2.6	4.5	1.5	2.8
Temp (C)	5.6 – 10	4.4 – 11.7	12.2 – 15.6	12.8 – 17.2	9.2 – 10.6	7.2 – 12.8
Wspd *Wgst* **(m s^{-1})**	1.8 *3.6* – 5.8 *11.6*	2.6 – 10.3	3.1 *5.3* – 7.4 *13.8*	4.1 – 11.9	3.1 *6.6* – 4.5 *9.8*	5.5 – 7.2
Wdir (deg.)	130 – 340	140 – 320	120 – 190	100 – 210	187 – 240	210 – 171
FL (km)		1.0 – 3.0		2.5 – 3.8		2.2 – 3.1
$\mathbf{N^2_{m,\,(0-2km)}}$($\times10^{-5}$ **s**$^{-2}$)		2.5 – 15		-10 – 7.3		2.3 – 11
$\mathbf{WSPD_{(0-2km)}}$ **(m s^{-1})**		6.0 – 32		11 – 32		11 – 28
$\mathbf{WDIR_{(0-2km)}}$**(deg.)**		173 – 316		157 – 213		173 – 244

according to the archived forecasts, and the Jan 17, 2005 event was the largest for water year 2005. We also sampled events with a range of atmospheric conditions to learn if variations in certain atmospheric factors exert significant control on the precipitation pattern. Table 2.3 shows the range of stability, windspeeds, wind directions, temperatures, and freezing-levels observed during each precipitation event. Lastly, we sought events with atypical precipitation patterns in the gauges and the model, in an effort to better understand the mechanisms that can alter the pattern. The Jan 17, 2005 event had an unusual precipitation pattern with minimal ridge-valley enhancement (storm-total ridge-valley enhancements are also given in Table 2.3).

For each case we have re-run the MM5, with an additional nested 1.33 km resolution domain (not included in the operational runs), so as to better resolve the ridges and valleys of interest. We will focus on describing a single canonical example, the 20 Oct 2003 storm, since the basic processes contributing to the pattern were found to be very similar between events. We will then refer to two other case studies primarily to discuss how variations in the pattern occur.

2.3.1 Model Setup

For each case study hindcasts were completed with MM5 version 3.7.2 in non-hydrostatic mode. Four one-way nested domains were included in the simulation, with horizontal resolutions of 36, 12, 4, and 1.33 km (locations of these domains are shown in Figure 5.3). 33 unevenly-spaced, terrain-following, full sigma levels were used, with increased horizontal resolution in the boundary layer, and a top level located at 100 hPa. A radiative upper boundary condition (Klemp and Durran, 1983) was applied to prevent unrealistic reflections of gravity waves off the model top. The atmospheric initial and boundary conditions were supplied by interpolation from the NCEP-NCAR reanalyzes (2.5° × 2.5° horizontal resolution) (Kalnay et al., 1996). The model terrain and land-use data were formed by interpolating U.S. Geological Survey data (with 5 min resolution on the 36 km domain, and 30 sec resolution on the inner domains), via a Cressman-type analysis scheme and a two-pass smoother-desmoother. Initial conditions for snow cover as well as subsurface soil temperature and moisture were provided by analysis grids from NCEP's Eta 221 model (with 40 km horizontal spacing), while sea surface temperatures were provided from the U.S. Navy Optimum Interpolation System (OTIS) (with 0.25 ° horizontal resolution).

As we are interested in the small-scale precipitation processes during given large-scale conditions, we nudged the outermost domain towards the reanalysis grid to force the large-scale flow to evolve similarly to our best estimate of what actually occurred. This nudging was accomplished via the Four Dimensional Data Assimilation scheme, using Newtonian relaxation of temperature, zonal and meridional winds, and moisture towards the values from the reanalysis grids (Stauffer and Seaman, 1990). Within the boundary layer, moisture was not nudged.

The MRF Planetary Boundary Layer (PBL) scheme was used on all domains to account for turbulent processes in the PBL (Hong and Pan, 1996). Short and long wave radiative transfer were parameterized via the CCSM radiation scheme (Hack et al., 1993). Consistent with the current setup of the operational Pacific Northwest MM5, Kain-Fritsch convective parameterization was used on all but the innermost (1.33 km) domain, to parameterize unresolved convective motions and associated precipitation (Kain, 2004). Parameterized convective precipitation was minimal during the events simulated. Our principle case study was run with and without convective parameterization on the 4 km domain, which only resulted in very minimal changes in storm total precipitation.

All runs were completed with three different microphysical schemes. The schemes vary widely in complexity and number of physical processes included, thus we use them to determine relevant processes controlling the observed pattern, and to roughly assess the sensitivity of the simulated precipitation distribution to the microphysical parameterization used. The Reisner2 scheme (version 3.7) (Reisner et al., 1998; Thompson et al., 2004) was used as our best representation of the microphysical processes taking place in the atmosphere. It is a bulk microphysical scheme which predicts mixing ratios of water vapor, cloud liquid water, cloud ice, snow, rain, and graupel, as well as the number concentration of cloud ice. The Simple Ice scheme (Dudhia, 1989) predicts the same mixing ratios as Reisner2, except for graupel, which is omitted. Liquid and frozen water do not coexist in this scheme, and there are many fewer interactions between different species of condensed and frozen water.

It was used in part to determine the importance of the complex interactions between frozen and liquid water species included in Reisner2 for determining the precipitation pattern. The Warm Rain scheme has a formulation that is very similar to Simple Ice, except all water is assumed to be in the liquid (or vapor) phase. It is quite physically unrealistic for the events we consider, since frozen precipitation processes are certainly occurring, but was used to test the range of responses in the small-scale precipitation pattern to changes in microphysical parameterization.

For comparison to gauge and station data, the MM5 forecasts were interpolated to point locations using bilinear interpolation.

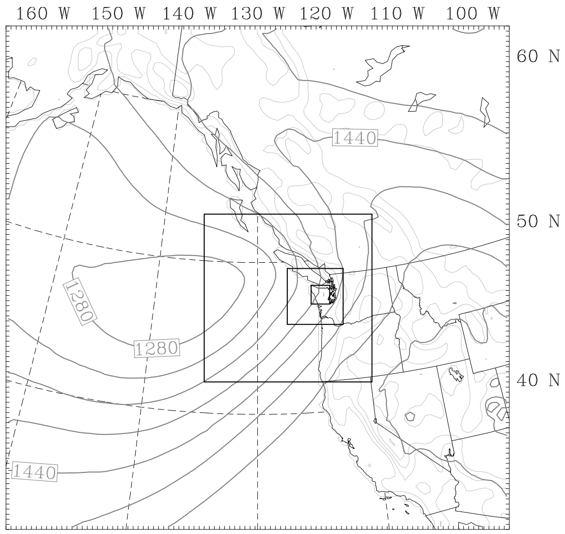

Figure 2.6: Outermost model domain and large-scale flow for 28 Nov case study. Extent of nested MM5 domains (12, 4, and 1.33 km) are shown with boxes. Simulated 850 hPa heights at 12 UTC on 20 Oct 2003 (time of the beginning of rainfall) are shown with contours (heights are extrapolated below the topography in regions of high terrain).

2.3.2 Fundamental Mechanisms: 20 Oct 2003

On 20 Oct 2003 a surface low tracked up the Pacific Northwest coast, accompanied by heavy rainfall over the Olympics. The 850 hPa heights modeled by the 36 km domain of our MM5 hindcast at the time rainfall commenced are contoured in Figure 5.3, showing southwesterly flow off of the Pacific impinging upon the Olympics. Warm surface temperatures ($> 10^o$ C) persisted throughout the storm. Near 19 UTC a second period of heavy rainfall began, with moisture supplied by a relatively narrow band of vapor flux originating in the tropics which impacted the Olympics. The feature was simulated by the model, but was displaced to the south, causing the MM5 precipitation to end too early. Thus, we consider only the well-simulated first half of the storm in our analysis.

Comparison of MM5 simulation and observations

Time series of modeled and observed surface variables at BKBW are given in Figure 2.7 (all model output is from runs using Reisner2 microphysics unless otherwise noted). There was a minor timing error in the forecast, thus all MM5 time series are shifted in by 1 hr so that the changes in rainfall rate match the timing in the observations. Both MM5 and observations show the rainfall occurring within a broad warm frontal zone with rising temperatures and southeasterly flow veering to southerly with time. The model represents well the changes in wind direction and temperature that occur over the course of the event, although the simulated surface windspeeds are closer to the observed gusts than the observed sustained winds. One-hour average precipitation rates for ridge and valley sites are shown in Figure 2.7a. Peak 1 hr averaged rainfall rates in the model and gauges exceeded 16 mm hr^{-1}, and rates greater than 8 mm hr^{-1} were sustained for over 5 hrs. The overall duration and intensity of the event are well modeled. Both observations and the model show a ridge-top enhancement of precipitation throughout the event and the magnitude of the enhancement is well simulated during the periods of significant rainfall.

The 12 UTC 20 Oct 2003 sounding at Quillayute (black line in Figure 2.8) gives a profile of conditions upwind of the mountains at the beginning of the heavy rainfall. Very strong low-level winds were observed, veering with height (as expected in the pre-frontal

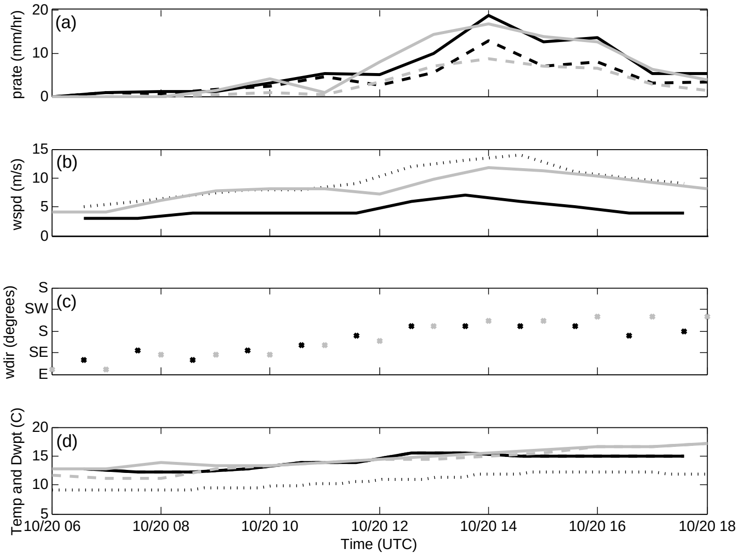

Figure 2.7: Modeled and observed time series from 20 Oct 2003 storm. Black lines and points show observations, while grey lines and points show MM5 hindcast. (a) 1hr precipitation totals at gauge network sites. Solid lines are for the average of all high elevation sites (> 200 m), while dashed lines are for low elevations (< 200 m). (b) Modeled and observed windspeed (solid) and observed wind gusts (dashed) at BKBW station. (c) Wind direction. (d) Temperatures (solid) and dew-point (dashed) at BKBW, and temperature at ridge-top site (dotted). Note, the observations show saturation throughout the period, thus the dew point is not visible as it is plotted atop the temperature.

region of warm advection) from S-SE near the surface to SW around 800 hPa. Near-neutral stratification was present throughout much of the sounding. However, a stable layer occurred between 900 and 800 hPa associated with the warm-frontal zone aloft, and was capped by a slightly unstable layer (with respect to saturated vertical displacements). The freezing-level at this time was above the topography, near 625 hPa. The model sounding (shown in gray, shifted 1 hr in time as for Figure 2.7) captures the basic vertical structure well, but the MM5 exhibits an upward displacement of the warm front, and lacks the unstable layer.

The simulated storm-total (20 Oct 06–18 UTC) pattern of precipitation is shown in

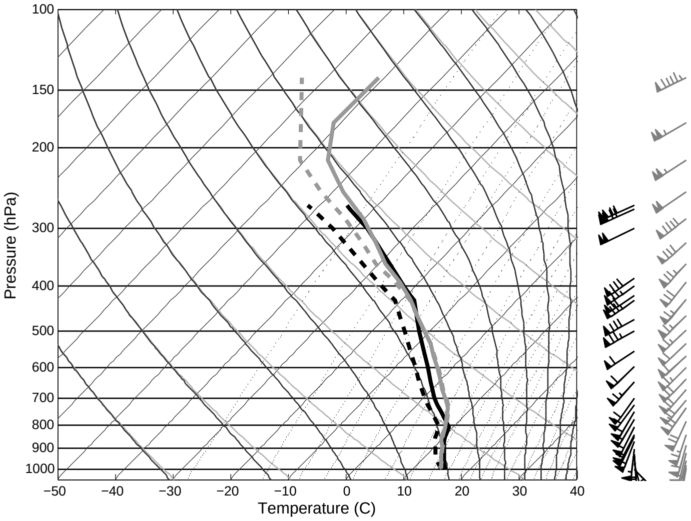

Figure 2.8: Skew-T Log-P plots of observed and modeled soundings at KUIL at 12 UTC, 20 Oct 20 2003. The observed sounding is shown in black (solid line for temperature, dashed line for dew-point). A profile of winds is shown on the right, with each full barb representing 5 m s^{-1}. The model sounding is shown in gray, and is taken 1 hr previous to the observation time to account for the error in the model timing of the storm passage.

Figure 2.9a. The same pattern of enhancement found in the archived 4 km-MM5 climatology (i.e. Figure 2.2) is reproduced for this case. Ridge-valley enhancement during this case was particularly strong: within the Queets river valley storm total precipitation was as low as 30 mm, whereas a few km to the southeast, atop the adjacent ridge, precipitation totals exceed 160 mm.

In Figure 2.9b, observed and modeled storm total precipitation at our gauge sites are plotted. Totals are shown from the 1.33 km domain of our MM5 Reisner2 hindcast, as well as the 4 km domain, and for runs of using less sophisticated microphysical schemes, allowing us to assess the impact of changes in horizontal resolution and physical parameterization on the simulation. All these simulations capture the basic shape and magnitude of the enhancement. However, the location of the observed precipitation maximum is shifted upwind over the first prominent peak on the southwest side of the ridge, whereas, the

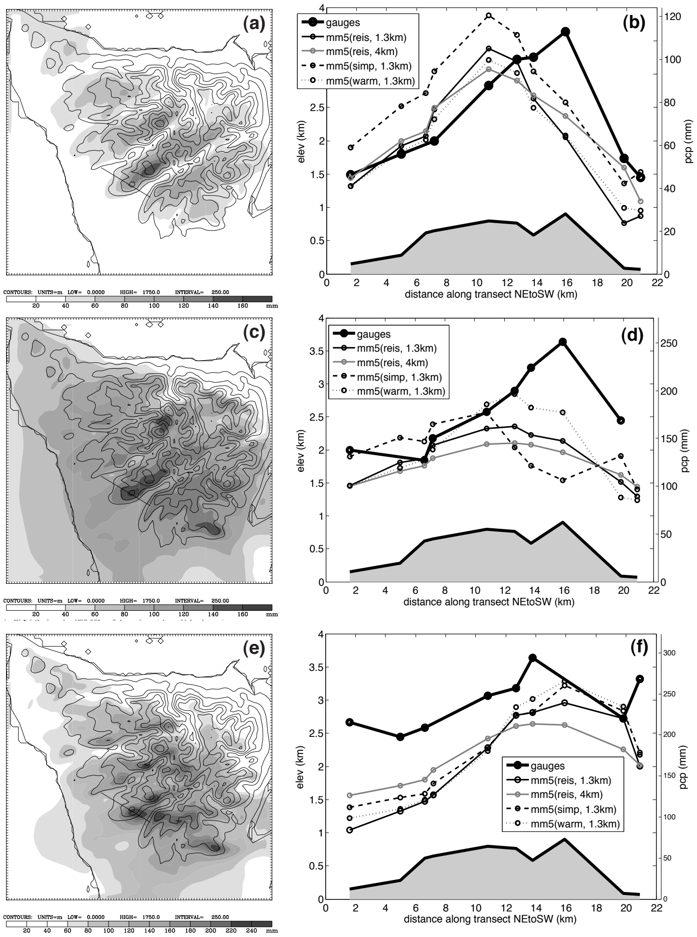

Figure 2.9: Storm total precipitation for case studies. (a) Storm total precipitation for 20 Oct 2003 event as modeled by MM5 with 1.33 km horizontal resolution and Reisner2 microphysics. Tick marks along the perimeter of the map show model grid spacing. (b) Observed and modeled precipitation at gauge network sites as function of distance along the transect. Observations are shown with the bold black line. Output from MM5 simulations with varied resolution and microphysical parameterizations are shown with line-styles denoted by the legend. Elevation of gauge sites is represented by the shaded terrain profile. (c) and (d) are analogous to (a) and (b) for the 28 Nov event. (e) and (f) are analogous to (a) and (b) for the 17 Jan event. The time interval used for the storm total transects and maps are given in Table 2.3.

modeled precipitation is centered over the crest. Over-prediction of cross-ridge winds (see Figure 2.7) may have contributed to this error in location of the modeled maximum by the excess downwind advection of falling rain. The simulations with various microphysical schemes show only minor differences in precipitation over the ridge, with the intermediate complexity scheme (Simple Ice) producing the most skillful representation of the rainfall totals. The insensitivity to choice of parameterization for this storm is perhaps unsurprising, considering the high freezing-level, which implies the dominance of warm microphysical processes (which are represented quite similarly between the considered schemes).

Mechanism for Precipitation Enhancement

Having gained confidence that the MM5 is faithfully representing the basic characteristics of this event, we now proceed to investigate the mechanisms responsible for the ridge-valley enhancement in the model. We will focus upon the time of heaviest precipitation in the model (forecast hour 27, or 14 UTC on 20 Oct). Shown in Figure 2.10a is the 1 hr precipitation total over the western Olympics for the hour previous to this time, as well as the 10 m modeled winds. Low-level winds are southerly and impinge obliquely upon the NE-SW oriented ridges. Figure 2.10b-d show vertical cross sections taken parallel to the low-level winds across the ridge from N to S. Figure 2.10b shows contours of precipitation rates (i.e. vertical flux of precipitation) for the modeled species of hydrometeors. The majority of the enhancement in the precipitation rate over the ridges takes place at low-levels, with much of it occurring in the rain water field at less than 1 km above the ridge crest. A signature of the enhancement is also found higher up, above the freezing level, in the graupel and snow fields.

Vertical velocity and cloud water mixing ratio are plotted along the transect in Figure 2.10c. Strong ascent (descent), exceeding 2 m s^{-1}, is found over the windward (leeward) slopes, extending up to 4 km elevation, with indication of a slight upstream tilt with height of the vertical velocity fields. Such patterns of vertical motion are expected from the theory of mountain waves in stably-stratified flow (e.g., Smith, 1979). The cloud water field shows an intense maximum (> 0.75 g kg^{-1}) located between the maximum and the node in the

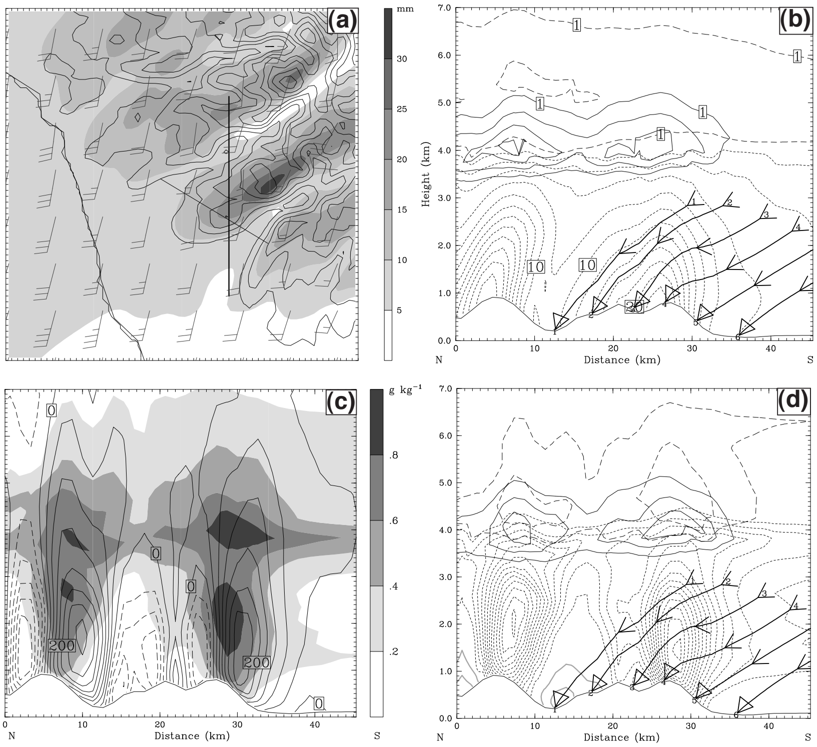

Figure 2.10: Precipitation patterns and processes at time of peak modeled rainfall (14 UTC on 20 Oct 2003). (a) Map view of 1 hr accumulated precipitation (gray shading), with elevation (contours, 200 m interval), and 10 m winds (wind barbs, full barb = 10 kts). Location of the gauge network (thin NW-SE line), and the following cross-sections (bold N-S line) are also shown. (b) Vertical cross-section parallel to near-surface winds, precipitation rates are contoured for rain (fine dashes) every 2 mm hr^{-1}, and for graupel (solid) and snow (long dashes) every 1 mm hr^{-1}. (c) Cloud water mixing ratio (gray shading, scale shown on the right), and vertical velocity (black contours every 40 cm s^{-1}, with negative values denoted by dashed contours). (d) Contours of Reisner2 precipitation source terms including the collection of cloud water by: rain (fine dashes), graupel (solid black), and snow (medium dashes), and the sink of precipitation by evaporation (solid gray) (interval of 2.5×10^7 s^{-1}). Characteristic hydrometeor back-trajectories (as described in the text) are shown with thick black lines in (b) and (d).

vertical velocity. The presence of this dense cloud is due to the ascent in the mountain wave, but its downwind displacement from the location of maximum vertical velocity, and its detailed structure are set by the balance of condensation, downwind advection, and loss of cloud water due to precipitation (e.g., Smith and Barstad, 2004).

To understand the pathways by which condensed water over the ridges is converted into precipitation we examined the source terms for precipitation in the Reisner2 microphysical scheme. We focus on the conversion terms in the scheme that create precipitation, and not those which transfer water between the various species of hydrometeors. We average these terms over the windward slopes of the Olympics for this time, from the surface to 200 hPa (using the methods described by Colle et al. (2005)). This analysis shows that about eight times more water vapor is condensed into cloud liquid water than is deposited onto ice particles, underscoring the importance of liquid phase microphysics for this event. Furthermore, the largest sources of precipitation, by at least an order of magnitude, are found in the terms involving collection of cloud liquid water. These include the collection of cloud water by rain, graupel, and snow (contoured in Figure 2.10d). All of these terms have maxima in the regions of thick cloud and intense rain over the ridge, and the largest source by far is the collection of cloud water by rain, maximizing at low levels. For this case, evaporation of rain within the sub-saturated valleys appears to also make a contribution towards the ridge-valley precipitation differential (gray contours in Figure 2.10d), but this effect was modest and was not observed in other cases. Thus, low-level collection of cloud droplets in wave-induced clouds appears to be the dominant control on the ridge-valley precipitation pattern during this storm, whereas auto-conversion of cloud water, depositional growth of snow, and evaporation of rain in sub-saturated valleys have relatively minor roles in directly determining the rainfall distribution.

The downwind drift of precipitation can play a key role in determining the rainfall pattern (e.g., Hobbs et al., 1973). To illuminate this effect we determine characteristic back-trajectories of hydrometeors that land at various locations along the cross-section (plotted on Figure 2.10b and d). These trajectories are calculated using the mass-weighted fall speed of hydrometeors as represented in the microphysical scheme, as well as the model fields of horizontal and vertical motion. The trajectories are integrated back in time with a time step of 10 s, using winds interpolated from the hourly model output (we justify the use of hourly winds by the steadiness of the modeled winds at this time). The plotted trajectories trace the path of hydrometeors back 10 min in time, with the middle arrow head showing the position at 5 min. From these plots we see that trajectories ending on the ridges (in the valleys) where rainfall rates are high (low), spend the longest (shortest) period of time in the region of thick cloud and extensive collection. Downwind drift spreads the enhanced precipitation beyond the region of enhanced condensation and collection. For instance at 17.5 km along the transect high precipitation rates are found, despite relatively modest cloud water mixing ratio and collection sources overhead, since the trajectory ending there passes through the region of enhanced collection.

Since condensation in the ascending branch of the ridge-induced mountain wave is the source of the enhanced precipitation, it is important to understand the wave structure. Figure 2.10c shows the mountain waves signature over the ridges decays near 3–4 km. A model sounding upstream of the ridge at 14 UTC shows average low-level (surface to 1 km) stability (moist buoyancy frequency) of 0.008 s^{-1} (Durran and Klemp (1982)'s eqn. 36) and cross-ridge wind speed of 15 m s^{-1}. If we idealize the impinging flow as uniform and two-dimensional, linear mountain wave theory (e.g., Smith, 1979) would predict that, under these conditions, 20 km wide undulations in the topography would produce mountain waves that would propagate vertically, whereas waves forced by 10 km undulations would decay with a vertical scale of 3.0 km. Thus for this case, the waves triggered over the major ridges are near the limit for vertical propagation, so decay of the waves is not entirely surprising. In contrast, during the 28 Nov case, waves are observed at times when linear theory (with uniform impinging flow) predicts propagation even for 10-km scale waves, and model output shows notable upstream tilt suggesting that the waves are indeed propagating, nonetheless model output shows them decaying near 3 km.

Therefore, simple (2-D, uniform impinging flow) linear theory predicts the presence of standing waves rising above the major ridges of the Olympics, but not always the decay of these structures which is simulated in MM5. The vertical structure of the impinging flow offers two explanations why waves might decay even when simple linear theory predicts propagation. Figure 2.11b and d show a vertical cross-sections of the flow, taken perpen-

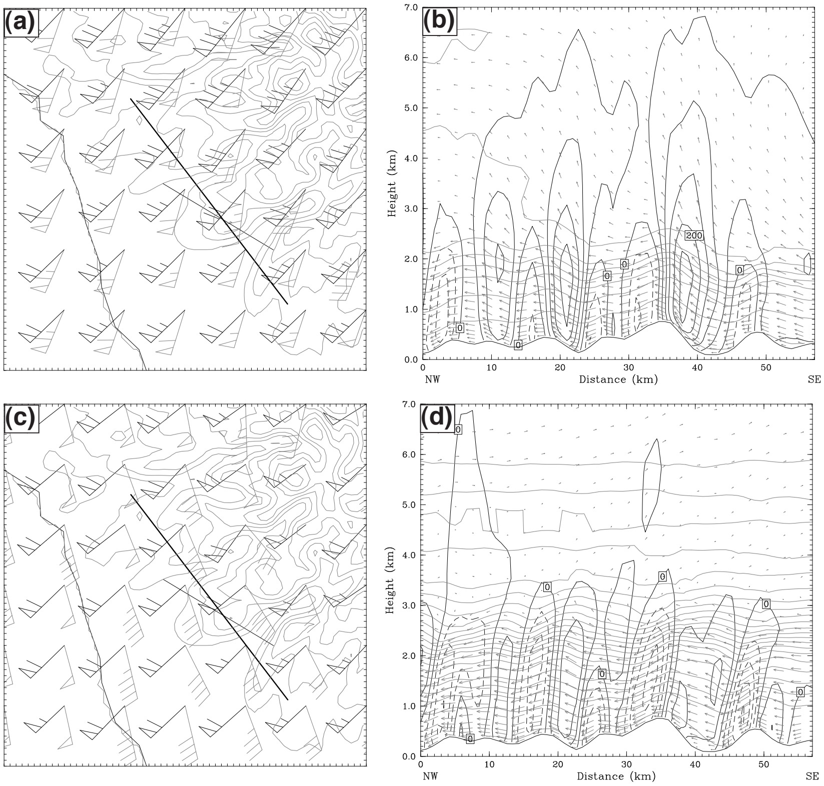

Figure 2.11: Wave structure, stability and directional critical level. (a) Winds at time of maximum rainfall (14 UTC) for 20 Oct case are shown with barbs at 1 km (gray) and 3 km (black) (full barb= 10 kts). (b) Cross-section (at location of bold line in (a)) of vertical velocities, and cross-ridge circulation. Contours of equivalent potential temperature are also shown (light gray lines, interval of 1.5 K). Note that the mountain wave decays as it passes through the warm front aloft, where the stability drops and the cross-ridge component of the wind approaches zero. (c) and (d) are the same as (a) and (b), but for a time during the 28 Nov case.

dicular to the ridge, with contours of vertical velocity and equivalent potential temperature (θ_e) as well as velocity vectors in the plane of the cross-section. The θ_e lines coincide with stream lines for moist pseudo-adiabatic flow, and their vertical spacing is a rough indicator of moist stability. Decay of the waves in the vertical velocity field occurs near the height where the θ_e lines become much more widely spaced, above the warm frontal boundary. The drop in stability which this implies represents a change in the propagation characteristics of the atmosphere (namely the index of refraction of the gravity waves), which may cause a vertically propagating wave to become evanescent and decay with height (e.g., Smith, 1979). But, directional shear in the profile of impinging winds also occurs near this height (associated with the warm advection beneath the front), forming a directional critical layer where the winds become parallel to the phase lines of the waves forced by the topography. Gravity waves are unable to propagate through such a level as their energy is absorbed or advected downstream (Shutts, 1998; Doyle and Jiang, 2006). Figure 2.11a and c show the 1 km and 3 km winds. As expected from the theory of critical levels, the height at which the mountain wave vertical motions decay to near zero coincides with the height at which the cross-ridge winds become negligible due to the veering with height. Examining the time evolution of the wind and stability profiles and wave structure throughout this and other simulated storms reveals that the vertical extent of the mountain wave co-varies with the height of the warm front aloft, however it is unclear if this is due to the changes in wind direction or stability across the front.

While the above-described mechanisms are the predominate control on the rainfall distribution for each case, distinctly different patterns and processes dominated during a few periods of our case studies. These departures are interesting in that they lend insight into what processes can lead to an unexpected rainfall pattern, and may be the rule rather than the exception either in other geographical regions or in past or future climates. We will explore the two principal exceptions we encountered in the following two subsections.

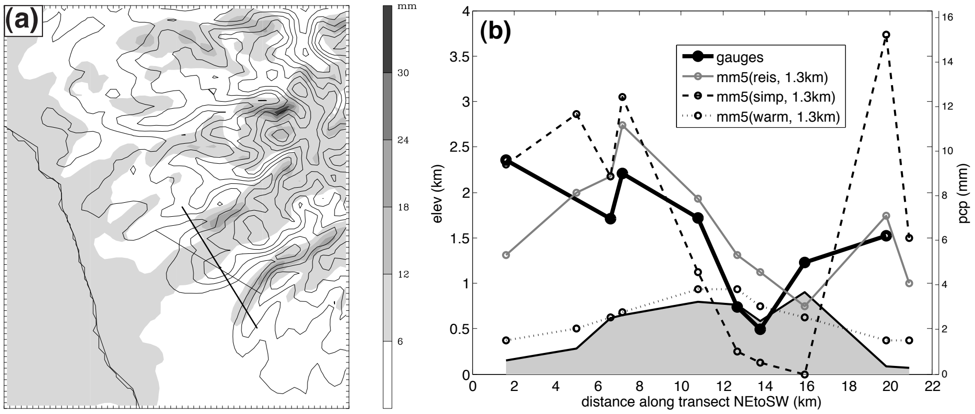

Figure 2.12: Modeled and observed rainfall distribution for early portion of 28 Nov storm, with low freezing-level. (a) Accumulated precipitation over western Olympic Mountains between 05 and 10 UTC in MM5 1.33 km simulation with Reisner2 microphysics. (b) Accumulated precipitation for the same period as in (a) for sites along gauge transect, from observations and 1.33 km MM5 domain for different microphysical parameterizations.

2.3.3 Influence of the freezing level : 28 Nov 2003

The synoptic forcing leading to the 28 Nov 2003 event included the passage of a mature surface low pressure center to the north of the Olympic peninsula. Heavy precipitation ($>$ 10 mm hr^{-1}) occurred throughout an 8 hr period of warm advection and rainfall quickly dropped off after a cold-frontal passage. Both observations and model output of storm-total precipitation for this event, shown in Figure 2.9, show enhancement over the ridge, however the enhancement is not as strong or well-simulated as in the 20 Oct case. There was a timing error in the simulation of the storm, so all model output has been shifted forward in time by 6 hrs.

Throughout the main portion of the storm, steady mountain waves occurred over the ridges and the mechanisms discussed for the 20 Oct storm dominated the precipitation pattern. However, early in the storm a distinctly different precipitation pattern occurred,

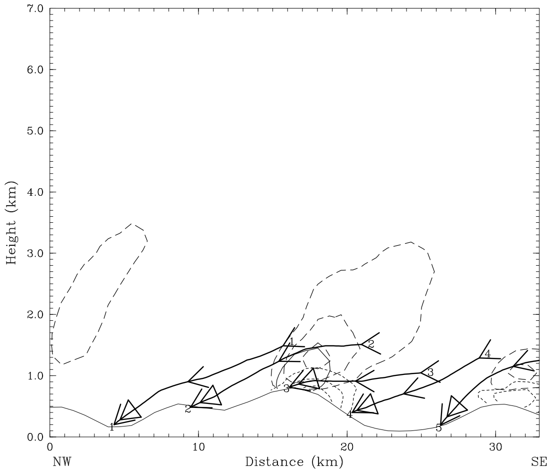

Figure 2.13: Cross section of modeled precipitation sources (contours, interval of 1×10^7 s^{-1}) and trajectories at 10 UTC on 28 Nov 2003. The section is taken parallel to the low level flow (along bold line shown in figure2.12). Plotting conventions are as for figure 2.10d. Note the shallower slopes of the hydrometeor trajectories as compared to those in Figure 2.10d.

which is masked in the storm total by the more voluminous rainfall that followed.

During the beginning of the 28 Nov event (05-14 UTC), observed ridge-top temperatures were near freezing, and the modeled KUIL soundings showed a low freezing level (near 800 hPa). The MM5 matches the basic structure of the 12 UTC Nov 28 KUIL sounding, but under predicts the freezing level by over 1 km (since it misforecast the altitude of the front aloft). During the hours immediately before and after the sounding the MM5 significantly under-predicts the precipitation rates at high elevation sites. This may be due to the low simulated freezing-level which could have led to excess advection of snow into the lee. Nevertheless, during the earliest hours of the storm (06-10 UTC) observations and the simulation agree better and both show an atypical pattern of precipitation. Figure 2.12a shows a map of simulated precipitation totals over the Olympics during this period. Precipitation does not maximize on the crests of the southwestern Olympic ridges, but rather over their lee slopes (the wind being from the SSE). The transect in 2.12b shows that while the details of the precipitation distribution are not all captured by the MM5 Reisner2 run, both model and the gauges portray a pronounced maximum shifted away from the ridge crest into the lee.

Due to the much slower fall-speed of snow compared to rain, periods with low freezing-level and strong cross-barrier flow can be associated with enhanced spillover of orographic precipitation onto lee slopes (e.g., Sinclair et al., 1997). Figure 2.13a shows a cross-section of cloud water, precipitation source terms, and hydrometeor back-trajectories analogous to Figure 2.10d. The hydrometeor trajectories shown are significantly shallower than those depicted in 2.10d (as well as those simulated during the peak of the 28 Nov rainfall), and trajectories ending in the lee valley pass through the region of enhancement while those ending on the windward slope do not, suggesting that advection of slow falling snow into the lee is responsible for the abnormal pattern. The exaggeration of the lee maxima in the Simple Ice run (Figure 2.12b) is consistent with prior results showing that the scheme advects too much precipitation (in the form of snow) onto the lee slopes due to the neglect of supercooled water and faster-falling graupel (e.g., Colle et al., 2005). The more typical ridge-top enhancement pattern found in the Warm Rain simulation supports the notion that the lee-side maxima is due to processes involving frozen hydrometeors. Our findings are in agreement with those of Zängl (2007), who presented observations of enhancement in the lee of narrow mountains in the Alps during storms with low freezing levels. His simulations of these Alpine storms suggest that when the freezing-level is located near the crest of a narrow mountain, lee-side enhancement is produced via a combination of downwind advection of frozen hydrometers generated in the orographic cloud, and by the flux of frozen hydrometeors through the freezing-level associated with mountian wave descent.

2.3.4 Influence of convection: 17 Jan 2005

The 17 Jan event was part of a prolonged period of several days of heavy rains that occurred as a mid-level short wave passed, and a low level baroclinic zone was maintained over the region. There was no passage of distinct surface fronts during this case, only a diffuse frontal zone of warm advection. As with the 20 Oct case, the freezing level remained more than

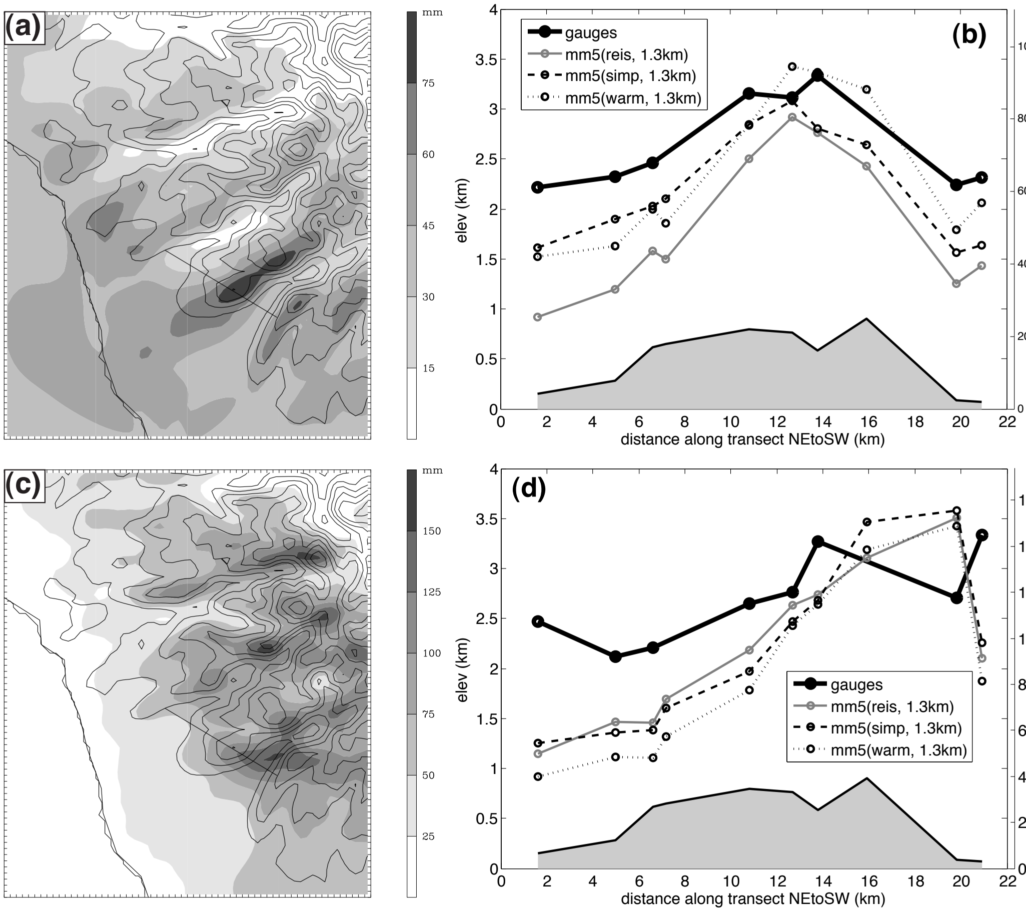

Figure 2.14: Modeled and observed rainfall distribution for stable and unstable portions of 17 Jan storm. (a) shows accumulated precipitation simulated over western Olympic Mountains between 00 and 16 UTC on 17 Jan 2005 (stable period). (b) Precipitation for sites along gauge transect from observations and 1.33 km MM5 domain using different microphysical parameterization during same period as in (a). (c) Shows accumulated precipitation simulated between 22 UTC on 17 Jan, and 12 UTC on 18 Jan (convective period). (d) Precipitation for sites along gauge transect from observations and 1.33 km MM5 during same period as in (c).

1 km above the ridges. Early in the storm, collection in stable orographic clouds over the ridges dominated the rainfall pattern as detailed for the 20 Oct event. Near 17 UTC on 17 Jan, a transition to unstable conditions occurred. The MM5 accumulated precipitation for this event showed a typical pattern of ridge-crest enhancement over the northernmost ridges of the western Olympics, but an atypical valley maxima over the Quinault valley (Figure 2.9e). The transect of gauge observations (Figure 2.9f) also shows some indication of a valley maximum, in addition to a subdued maximum over the crest.

Near 18 UTC on 17 Jan 2005, both observed and simulated soundings from KUIL showed a transition from stable/neutral to neutral/unstable conditions at low-to-middle levels (the simulated squared moist buoyancy frequency between 1 and 3 km (Durran and Klemp, 1982) changed from 8.7×10^{-5} s^{-2} at 14 UTC to -3.9×10^{-5} s^{-2} at 22 UTC). Accompanying this was the disappearance of the steady waves of cloudwater and vertical motion over the ridges, and the appearance of individual transient cells of which began precipitating offshore and were advected across the mountains (apparent in 10 min model output (not shown)). These features consisted of elevated cores of upward motion, with flanks of subsidence, indicative of cellular convection. The precipitation rates associated with these features more than doubled as they encountered the topographic barriers of the Olympics.

Simulated precipitation totals from before and after the transition to unstable conditions are depicted in Figure 2.14a and c. After the transition to cellular convection, the pattern of rainfall over the region of our field study was less tightly tied to the topography, and included a rainfall maximum in the Quinault valley which occurred as a result of transient cells which tracked over the valley. Channeling of flow into the valley did not appear to play a role. Gauge observations also exhibit an abnormal pattern during this period, with a valley rainfall maximum, in contrast to the more typical ridge-top maximum seen in the earlier portion of the storm (Figure 2.14b). These results suggest that during times of convection, the absence of mountain wave generated cloud water over topographic ridges and the scattered tracks of individual convective cells may lead to precipitation patterns which are fundamentally distinct from typical storm totals and the climatological mean.

Stationary bands of of convection were briefly simulated late in the 20 Oct case (not shown). Like those examined by Kirshbaum et al. (2007) these rainbands were only a few kilometers wide, triggered over topography, and aligned parallel to the low-level flow. These bands were not modeled on the 4 km domain, as they were too small to be resolved by such a grid; thus they represent a feature of mountain precipitation not captured by the operational forecasts, and may account for some of the discrepancies between the models and observations. However, the excellent agreement between the 4-km MM5 and our gauge network over the Western Olympics suggests that, at least in that region, such banded convection is not a dominant mechanism shaping the precipitation climatology.

2.4 Composite analysis of precipitation climatology

The above-analyzed case studies yield suggestions as to the importance of various atmospheric factors in controlling the small-scale distribution and enhancement of mountain precipitation. For instance, changes in wind direction during the course of storm events (e.g. those shown in Figure 2.7) did not result in noteworthy changes in the spatial structure of precipitation, whereas changes in the height of the freezing-level appeared to drastically reshape the pattern.

We have already shown that the pattern of ridge-valley enhancement found in our case studies dominates for the majority of storms and in the climatological mean. We now use our gauge observations and the archived MM5 forecasts to test hypotheses about what factors are responsible for variations in the ridge-valley precipitation pattern. To do so we composite rainfall totals at sites within our field study area based upon upwind atmospheric conditions.

Figure 2.15 shows 12 hr accumulated precipitation, composited based upon 12 hr averaged 2-m temperatures measured at BKBW, as a function of distance along the gauge transect for the water year 2006 field season. For warm temperatures ($> 5^o$ C) the enhancement of rainfall over the ridge is pronounced. However, for colder temperatures, the ridge-valley enhancement is minimal. Each year of gauge data was analyzed separately, since very few gauges were continuously operational for the full duration of all four field seasons. However, similar results of reduced enhancement at low temperatures were found for all but one field seasons (water year 2005). This relationship between surface temperature and enhancement could be associated with changes in the height of the freezing-level,

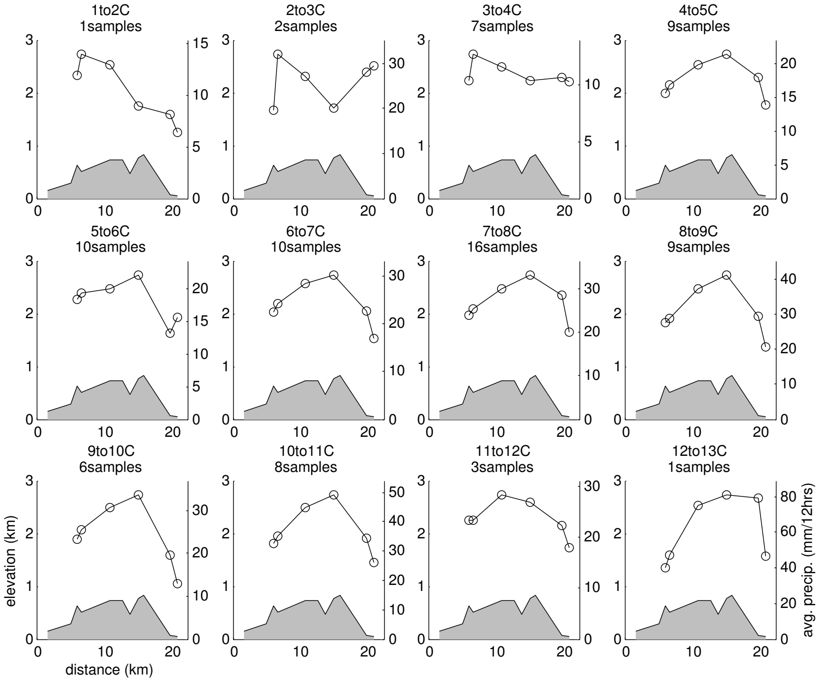

Figure 2.15: Observed average 12hr precipitation patterns composited based upon 2 m temperature at BKBW station for the water year 2006 field season. Each figure shows the average 12 hr accumulated precipitation at the gauge sites during periods when the lowland temperatures are within the labeled intervals. The number of events used for each composite is noted as "samples". Rainfall events with gauge network averaged precipitation rates of less than 6 mm / 12 hrs were excluded from the analysis.

and downwind drift of frozen hydrometeors as discussed in the section 2.3.3. Alternatively, this relationship may be an artifact of measurement errors, since under-catch during periods of ridge-top snow and valley rain (as discussed in section 2.2.2) may distort the observed pattern and lead to the false appearance of reduced enhancement during cold periods.

Figure 2.16 is equivalent to Figure 2.15, but was constructed using the archived MM5 output from October 2005–December 2007. Using the model output avoids the observational uncertainties associated with undercatch of snow, and offers a more continuous dataset resulting in a larger sample size. As for the observations, the pattern shows a

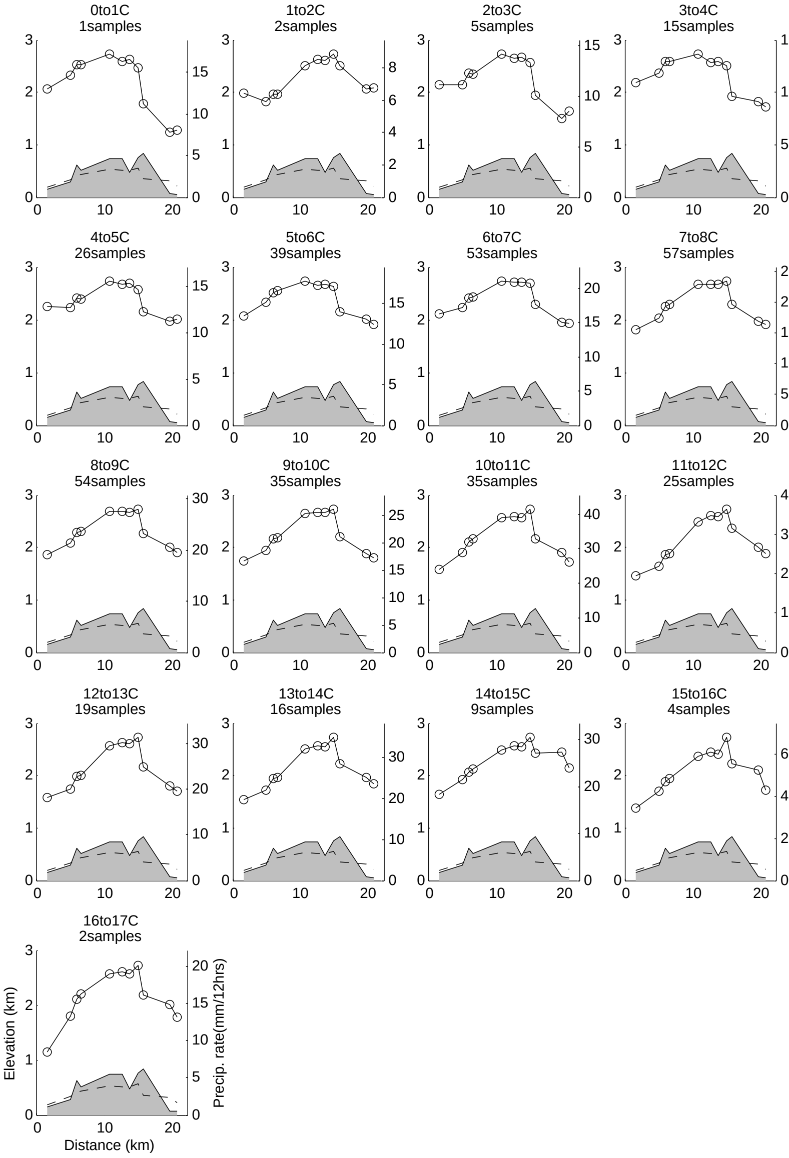

Figure 2.16: MM5 average 12 hr precipitation patterns composited based upon 2 m temperature simulated at site of BKBW station for Oct 2005 through Dec 2007. Methods and conventions used are equivalent to those for Figure 2.15.

temperature dependence, albeit less pronounced. While all temperature bins exhibit the same fundamental pattern of enhanced precipitation on the ridge-top relative to the valleys, this enhancement becomes more subdued with decreasing temperature. Although there is a modest suggestion of increase in lee-side precipitation at low temperature, there is not evidence of a distinct lee-side peak in enhancement (as shown in Figure 2.12 and Zängl (2007)). This may be absent because it is not a dominant and persistent feature of the climatology. Alternatively, it may be an important feature that requires a finer grid spacing than 4–km to be properly resolved.

We have conducted the same compositing using other upwind metrics that would be expected to have bearing upon the pattern of orographic precipitation including 10 m wind speed and wind direction, precipitation rate, and low-level water vapor flux at BKBW. Results (not shown) indicate that, both in MM5 and observations, the basic form and amplitude of the ridge-valley precipitation pattern are remarkably insensitive to changes in the considered parameters. The ridge-top maxima is a pronounced feature both during events with ridge-parallel and ridge-perpendicular winds, for events with a range of wind speeds, and during events with both light and heavy upstream rainfall rates. While there are significant variations in the precipitation pattern, they do not appear to be systematically related to these other parameters in a simple way.

2.5 Discussion

The consistent pattern of observed ridge-top enhancement, coupled with results from our case study analysis (and backed-up by aircraft observations during the IMPROVE II field campaign (Garvert et al., 2007)) point to the collection of cloud droplets in low-level wave clouds forced by ascent over individual ridges as the dominant control on precipitation patterns over the western Olympics. Bergeron's conceptual model of the seeder-feeder mechanism aids in explaining the enhancement occurring over the ridges of the Olympics. However, in our simulations, as found in previous work (e.g., Browning et al., 1974), there is no clear separation between synoptically forced clouds and orographically-forced clouds, both of which seed and feed the collection process. We also find that the sloping trajectories of hydrometeors play an important role, and during periods of low freezing-level the slow fallspeeds of frozen hydrometeors can drastically alter the pattern. The cross-ridge flow, which is a major feature of the climatology in the southwestern Olympics (Figure 2.3), plays a key-role in determing the regions of enhancement, and may be related to the blocking of the low-level air on the scale of the entire range. Variations in microphysical parameterizations do not fundamentally alter the the ridge-valley enhancement pattern, suggesting it does not depend on complex microphysical interactions for its existence.

Previous studies have identified other physical mechanisms as potentially important components of orographic enhancement, including: small-scale turbulence (e.g., Houze and Medina, 2005), banded convection (e.g., Kirshbaum et al., 2007), and lee-side stratification (e.g., Zängl, 2005). While these may be key components of some individual storms, we find that over the western Olympic Mountains they do not need to be invoked in order to understand the basic climatological precipitation pattern on the ridge-valley scale.

In model simulations the enhancement occurs at very low levels (<1km) over the terrain. This suggests that it would be difficult to fully characterize the rainfall using traditional ground-based scanning radar, which must scan at significantly high elevation angles to avoid terrain blockage and ground clutter. Therefore, unless optimally placed, ground-based radar may tend to greatly underestimate surface rainfall over the Oylmpics (e.g., Kitchen and Blackall, 1992).

The structure of small-scale mountain waves may represent a fundamental control on both precipitation patterns and the efficiency of orographic precipitation. Smith and Barstad (2004) have already examined how linear mountain wave dynamics control orographic precipitation for the case of uniform, stable upstream flow, and their model can be tuned to reproduce well the patterns of precipitation observed over the Western Olympics (Anders et al., 2007). However, Smith's model does not represent the inherent nonlinearity associated with the collection processes which constitute the principal source for precipitation over the ridges of the Olympics. Thus, while the linear model provides a simple and elegant representation of the precipitation processes, care must be taken in the physical interpretion of its results since the neglect of nonlinear cloud processes can mask important threshold behaviors (Jiang and Smith, 2003). Directional shear and changes in stability with height may limit the vertical extent of mountain waves and associated orographic clouds. We do not expect the vertical extent of the small-scale wave clouds to have a major bearing upon the small-scale patterns of surface rainfall, since these patterns must be most strongly controlled by the cloud structure in the lowest kilometer or so (since, due to downwind advection, rainfall originating from higher levels cannot consistently translate into patterns as tightly tied to narrow terrain features as we have observed (Bergeron, 1968)). However, the depth of the cloud forced by the ridge may affect the amount of enhancement that occurs (e.g., Carruthers and Choularton, 1983; Choularton and Perry, 1986) and present a strong control on the efficiency with which moisture is extracted from the incident flow and converted to precipitation (as represented by the "drying-ratio" metric (Smith et al., 2003)).

The robustness of the patterns we have observed in the Olympics lead us to believe that they can likely be generalized to other mountain regions with significant ridge-valley relief, that receive much of their precipitation as rain under stable conditions during the passage of mid-latitude cyclones. Despite the presence of similar simulated patterns over the Cascades (Figure 2.2) we have less confidence in generalizing the observed patterns to colder regions. During heavy rainfall in the Olympics the freezing level is often situated above the height of the windward ridges, and accordingly, the low-level collection responsible for the ridge-valley pattern is not strongly controlled by ice-phase processes. Relative to the Olympics, large biases have been identified in MM5 forecasts over the higher Cascades, perhaps due to the increased importance of ice-phase microphysics. Also, the downwind drift of snow (e.g. Figure 2.12 and Zängl (2007)) may drastically alter the pattern during cold events. In regions where rainfall from convective events plays a major role we expect that small-scale patterns may differ notably, as the lack of steady wave clouds, and the presence of features such as banded convection (e.g., Kirshbaum et al., 2007), and transient cells (as discussed in section 2.3.4) can lead to fundamentally different patterns.

The persistence of the small-scale precipitation patterns in the Olympics provides potential for strong interactions between surface processes and mountain climates. For instance, Anders et al. (2008) have coupled a model of surface erosion and a linear model of orographic precipitation (Smith and Barstad, 2004) to show how small-scale patterns of rainfall and topography can co-evolve on geological time scales. Stolar et al. (2007) have examined how the spatial pattern of Olympic-Mountain precipitation influences uplift, erosion rates, and the shape of the range. Moreover, small-scale patterns of mountain rainfall may act as a control on the pattern of shallow landslide hazard in the Olympic mountains, since soil saturation due to extended and/or heavy rainfall is a prime trigger for such landslides (e.g., Caine, 1980).

Key questions remain in regards to the importance of various factors in limiting the predictability of mountain precipitation. Deficiencies in model parameterizations (particularly microphysics), horizontal resolution, and initialization have all been cited as major contributors. The excellent agreement between the modeled and observed climatology implies it is unlikely that there are major systematic biases in the model's representation of the fundamental precipitation processes over the region. Yet, major shortcomings are present in the model's representation of individual events. For major Olympic mountain storms, the relatively small differences in simulated precipitation between microphysical parameterizations of various complexity suggest that microphysics alone are not the largest source of forecast error in this region. We posit that initial condition errors may impose an important limit on precipitation predictability for many storms. To test this hypothesis requires further work using tools such as ensemble methods to quantify mesoscale predictability limitations arising from uncertainties in upstream initial conditions (e.g., Torn and Hakim, 2007).

2.6 Conclusions

Analysis of case studies and climatologies from both dense gauge observations and high-resolution mesoscale model output over the western Olympic Mountains has revealed the following:

- Persistent small-scale patterns of precipitation occur over the ∼10 km wide, ∼800 m high ridges and valleys of the western Olympic Mountains. These patterns are characterized by a 50–60% excess accumulation over the ridges relative to the adjacent valleys in the annual mean.

- The MM5 shows excellent skill in simulating these patterns at seasonal time scales, however major errors exist for individual storms. These errors are not obviously related to deficiencies in model resolution or microphysics alone, and may be due in part to initial condition errors.

- The mechanism responsible for the ridge-top enhancement of precipitation is similar to Bergeron's conceptual seeder-feeder model. Regions of enhanced condensation of cloud water are produced by ascent in stable flow over the windward slopes of major ridges. Within these clouds precipitation generated on the synoptic and mesoscale grows by collection of, leading to enhanced precipitation which is advected by the prevailing winds.

- Under atypical conditions, fundamental changes in small-scale patterns may occur. During periods of low freezing-level, advection of falling snow over the major ridges may lead to a lee-side or valley maximum of precipitation. During unstable conditions the tracks of individual convective cells can play a major role in determining the rainfall pattern.

- Case studies and composite analysis suggest that departures from the pattern of ridge-top enhancement are rare; the basic patterns and processes appear robust to changes in temperature, winds, and background rainfall rates.

Chapter 3

SPATIAL PATTERNS OF OROGRAPHIC RAINFALL AND SHALLOW LANDSLIDE SUSCEPTIBILITY [1].

3.1 Introduction and Background

One of the primary triggers for shallow landslides on soil mantled landscapes is high intensity and/or long duration rainfall (e.g., Caine, 1980; Guzzetti et al., 2008). Over mountainous regions, where slides tend to occur, atmospheric circulations forced by the topography lead to distinct rainfall patterns that may include greater than two-fold differences in accumulation over horizontal distances of a few kilometers (e.g., Bergeron, 1968; Smith et al., 2003; Roe, 2005; Kirshbaum and Durran, 2005). However, it is not generally known how strongly such spatial variations of rainfall control slope stability. If the influence is sizable, and the rainfall patterns are predictable, then climatologies and/or forecasts of kilometer-scale rainfall patterns may prove valuable for landslide hazard assessment and forecasting.

In this study we will distinguish between different timescales on which rainfall characteristics affect the spatially variable likelihood of landslide occurrence over a region. Landslide probability on storm timescales will refer to the likelihood of slope failure during a single storm or series of storms that may last from hours to weeks. This may be strongly influenced by the detailed features of a given storm such as its intensity, duration, track, structure, and interaction with the topography. This contrasts with landslide susceptibility on climatological timescales, which will refer to the spatially variable likelihood of failure given the distribution of storms that occur in a region over the course of years to millennia. This depends on the statistical properties of the climatological distribution of storms, including the average, variability, and extremes of storm intensity, duration, etc.

Previous work on rainfall patterns and slope stability is limited and almost exclusively has focused on the storm timescale. Some of these studies have used slope aspect and wind direction in an attempt to empirically relate the pattern of wind driven rainfall to the locations of slope failures (e.g., Pike and Sobieszczyk, 2008), but these studies typically neglect horizontal variations in rainfall rate (the vertical flux of rain), variations which, as mentioned above, can be quite large. Recently researchers have begun to use small-scale rainfall patterns in modeling slides triggered by individual storms. In New Zealand a landslide forecasting system is being developed using physically based models of hydrology and slope stability forced by rainfall from a numerical weather prediction model on a 12 km horizontal grid (Schmidt et al., 2008). However, while small-scale rainfall forecasts have been used in this modeling efforts, the authors stopped short of quantifying the effect of the spatial rainfall variations or the value added to their predictions by considering them.

---

[1] The contents of this chapter are published in Minder et al. (2009), © 2009 American Geophysical Union. The published version may be found at: http://www.agu.org/journals/wr/wr0904/2008WR007027/

Other studies have used ground- and space-based radar measurements to estimate the rainfall distribution and relate it to slide locations (Campbell, 1975; Wieczorek et al., 2001; MacLeod, 2006; Chang et al., 2008). Uncertainties with estimating surface rainfall from radar can limit the effectiveness of such methods (e.g., Wieczorek et al., 2001; MacLeod, 2006), however a combination of radar and gauge observations can be use to make a more confident analysis of the rainfall pattern (e.g., Chang et al., 2008). Using NEXRAD radar Wieczorek et al. (2001) found that a localized (∼5 km radius) region of particularly heavy rainfall was colocated with many of the slope failures occurring during an extreme convective storm on June 27, 1995 in the Blue Ridge Mountains of Madison County, Virginia. Using a physically based transient model of slope stability forced by radar derived rainfall from this event, Morrissey et al. (2004) found significant "spatial and temporal variations of the factor of safety" (a measure of slope instability) correlated with the movement of individual convective storm cells, just a few kilometers in width, across the landscape. Results from this event suggest an important role for small-scale rainfall features in determining where slide are triggered on the storm timescale. Yet, if the rainfall from such convective cells is distributed randomly across a region from storm to storm they will have no net influence on the pattern of susceptibility over climatological timescales. For spatial variations in mountain rainfall to influence the climatological pattern of landslide susceptibility they must be both large and persistent enough. Whether this is the case on small (10 km or less) scales remains an open question.

In mapping landslide susceptibility over climatological timescales, spatial distributions of various parameters (e.g. slope, drainage area, vegetation, bedrock geology) are often used. Quantitative hazard assessment is typically accomplished either through the use of empirical models (e.g., Gupta and Joshi, 1990; Baeza and Corominas, 2001; Lee et al., 2003; Saha et al., 2005), or spatially distributed physically based models of slope stability and hydrology (e.g., Montgomery and Dietrich, 1994; Wu and Sidle, 1995; Casadel et al., 2003; Morrissey et al., 2004). Information on 10 km scale spatial variability of rainfall is very seldom considered in long-term susceptibility analysis, in part because mountain rainfall patterns have not been well observed or understood on those scales. However, in recent years it has become clear that large variations in precipitation occurring on spatial scales of 10 km or less are a persistent and predictable feature of mountain climates in a variety of regions (James and Houze, 2005; Anders et al., 2006, 2007; Minder et al., 2008). A better understanding of the impact of these variations may have important applications. For instance, researchers have been developing techniques to use intensity-duration thresholds for slope failure, and satellite-borne radar estimates of precipitation at 0.25° × 0.25° horizontal resolution to issue near real-time assessment of landslide hazard (Hong et al., 2006). However, the effects of subgridscale variations in rainfall on such a system have not been determined. Furthermore, observations of precipitation in mountainous regions are usually sparse. As a result, studies of landslides often are forced to rely upon gauge observations from a single point to characterize the rainfall over an entire study region (e.g., Casadel et al., 2003; Gorsevski et al., 2006, provide recent examples). Available gauges tend to be sited in accessible lowlands and valleys (Groisman and Legates, 1994), locations that may poorly represent conditions at the locations where slides occur. Yet the errors in hazard assessments due to the distance between gauge observations and landslide locations have not been well quantified.

We aim to better characterize the influence of small-scale rainfall patterns on climatological shallow landslide susceptibility. To do so we consider two adjacent watersheds in the Olympic Mountains of Washington state and use a modeled rainfall climatology (supported by observations) to force a simple model of slope stability in order to address the following:

What effect on landslide susceptibility may be expected from rainfall variations occurring over spatial scales of 10 km? How large of a bias in hazard assessment may occur if a lowland station is used to characterize precipitation across a mountainous catchment? How does spatial variability of precipitation compare to spatial variability in soil properties for determining variations in slope stability?

3.2 Rainfall and Landslides over the Western Olympic Mountains

The Olympic Mountains of Washington State receive copious amounts of precipitation over their western (windward) slopes. Most of this rainfall occurs during midlatitude cyclones as stably stratified moist air from over the Pacific is forced over the topography by southwesterly winds. Precipitation at locations in the Olympics can amount to over 5 m in the annual total. Using 6 years of forecasts from the MM5, a high-resolution (4 km in the horizontal) weather model used for operational forecasts in the Pacific Northwest (Mass et al., 2003, and http://www.atmos.washington.edu/mm5rt/mm5info.html), a small-scale precipitation climatology was developed over the region (Anders et al., 2007). This climatology suggests that substantial enhancement of storm total and annual mean precipitation occurs over 10–20 km scale ridges relative to the adjacent valleys (Anders et al., 2007; Minder et al., 2008). The most pronounced enhancement in the model occurs over a 15 km wide, 1 km high topographic ridge separating the Queets and Quinault basins (Fig. 3.1 shows the topography of the basins).

Four years of observations from a high density network of precipitation gauges in the region support the model climatology, with MM5 and gauges both showing 60 to 80 % more rainy-season (October-May) precipitation atop the ridge than in the valleys that flank it. Figure 3.2 shows a comparison of annual total precipitation from the MM5 and observations at gauge locations in a transect across the ridge for most of one rainy season (locations of the gauges are shown in Figure 3.3). The model captures well both the amount and spatial distribution of precipitation across the gauge network, with the model's normalized route mean squared error in rainy season total precipitation at the gauge sites ranging from 10–22 % (Minder et al., 2008). Favorable performance of the MM5 is found despite the coarseness of its 4 km mesh relative to the ridge-valley topography, and MM5 case studies

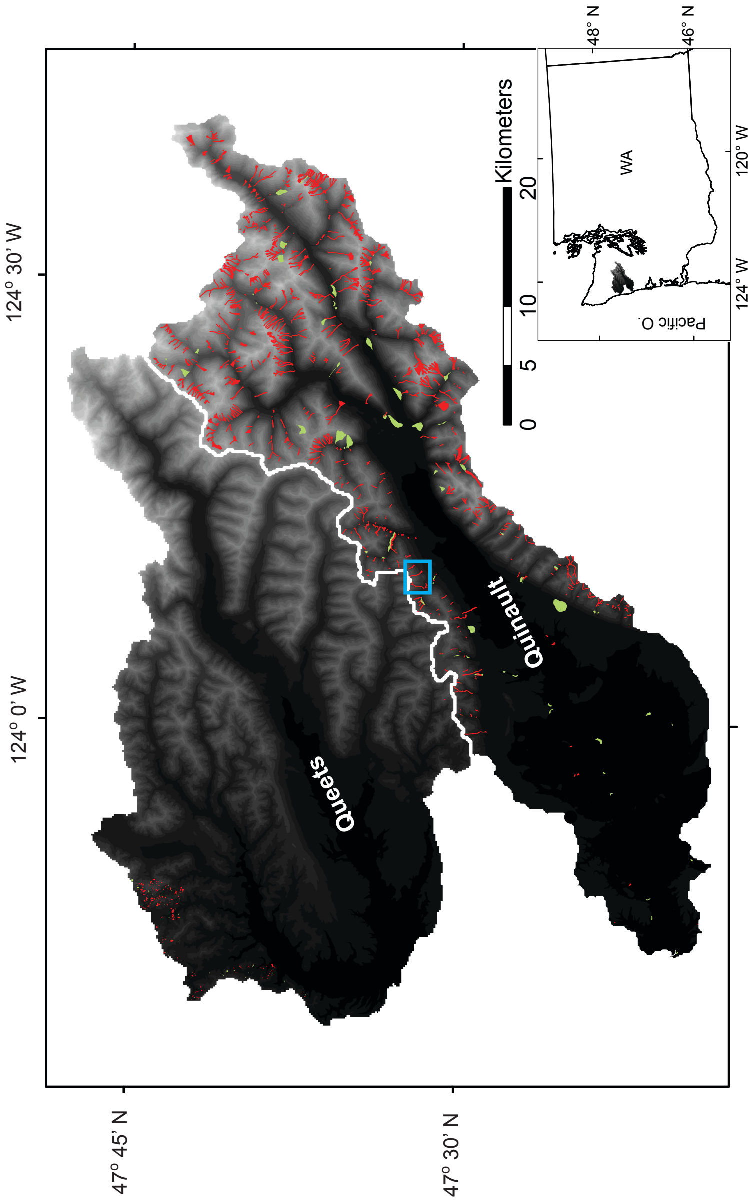
124° 30' W
124° 0' W
47° 45' N
47° 30' N
Kilometers
0
5
10
20
Queets
Quinault
48° N
46° N
WA
120° W
124° W
Pacific O.

Figure 3.1: Topography and mapped slides for the Queets and Quinault basins (location of the basins within Washington State are shown in inset map). Elevation is shaded in grayscale and ranges from 0 – 2.2 km. Shallow slides are shown in red, and deep-seated slides are green. Mapped slides include scar and runout, and complete mapping has only been done for the Quinault basin. The white line indicates the divide between the two basins. The blue box indicates the location of Figure 3.5.

with higher (1.33 km) resolution produce similar rainfall (Minder et al., 2008). The pattern of ridge-top enhancement is a particularly robust feature of heavy rainfall events (Minder et al., 2008), during which the ridge can receive over three times the rainfall of adjacent valleys (Anders et al., 2007). While individual major storms are frequently misforecast by the model, on average the precipitation modeled for major storms is quite realistic (Anders et al., 2007; Minder et al., 2008).

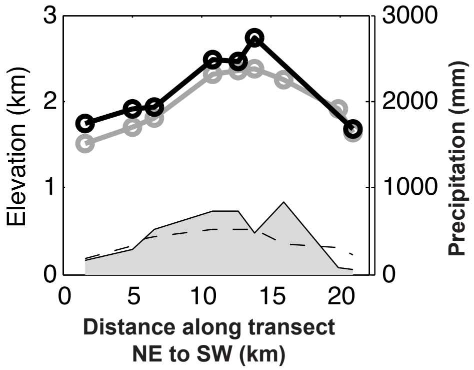

Figure 3.2: Total modeled and observed precipitation at locations along the transect of gauges shown in Figure 3.3, for November–April of 2004–2005. Elevations of gauge sites are shown by the shaded terrain profile (the model elevations interpolated to the gauge sites are shown with the dashed line). Gauge observation are shown in black and model climatology interpolated to gauge locations is shown in gray (figure adapted from Minder et al. (2008)).

Shallow landslides are a pervasive feature in the western Olympic Mountains. Mapped shallow and deep-seated landslides in the Queets and Quinault basins are shown in Figure 3.1. These were primarily surveyed by Lingley (1999) using areal photography and made available as a digital coverage by the Washington State Department of Natural Resources Landslide Hazard Zonation Project (http://www.dnr.wa.gov/forestpractices/lhzproject/).

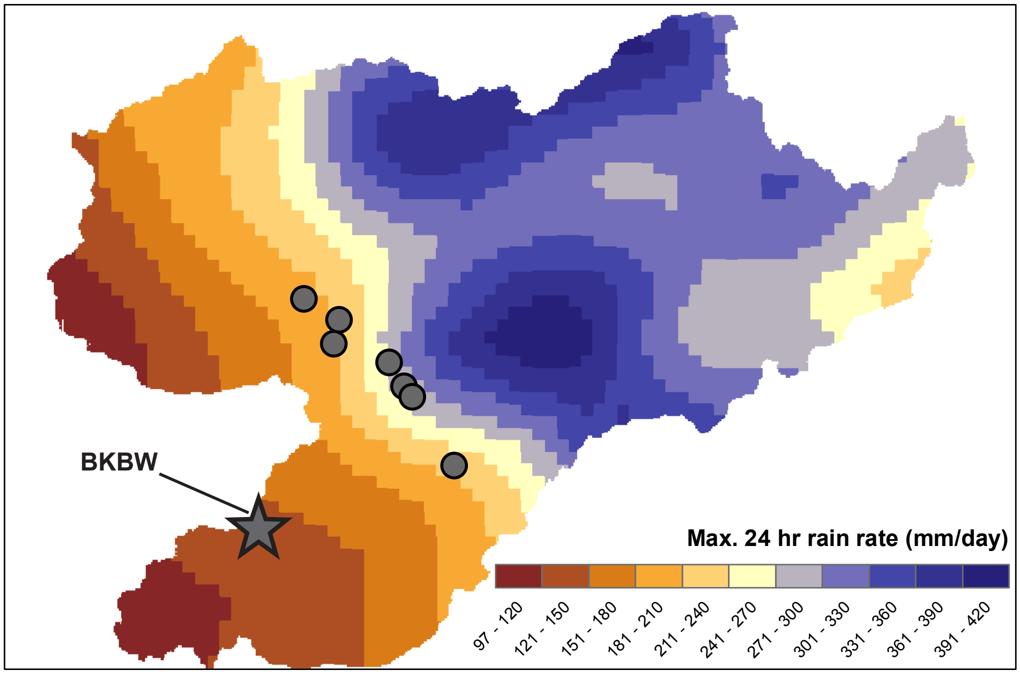
BKBW
Max. 24 hr rain rate (mm/day)
97 - 120
121 - 150
151 - 180
181 - 210
211 - 240
241 - 270
271 - 300
301 - 330
331 - 360
361 - 390
391 - 420

Figure 3.3: Maximum 24 hr averaged rainfall rate from 7 yrs of MM5 high-resolution atmospheric model iterations (reinterpolated from the 4 km MM5 grid to 1 km). The location of the Black Knob weather station (BKBW) is indicated with a star, and the location of the gauge network of Anders et al. (2007) and Minder et al. (2008) is shown with circles.

This region has a variety of land cover, with vegetation ranging from mature forest (> 50 yrs old) to clear-cuts. The surface geology is also variable, including Quaternary alpine glacial deposits as well as Tertiary marine sedimentary and volcanoclastic rocks (broken by a number of faults, shearing, and bedding structures) (Lingley, 1999).

3.3 Methods

We wish to quantify the effect that spatial variations in climatological precipitation may have on shallow landslide susceptibility. To this end we will use the rainfall pattern from the MM5 as a best estimate of the rainfall distribution over the region, and the SHALSTAB model of slope stability (Montgomery and Dietrich, 1994) as a representation of the fundamental physics governing landslide triggering by rainfall. Our aim is to determine, in a semi-idealized context, if climatological rainfall patterns similar to those found in the Olympic mountains represent a large enough physical signal to play an important role in determining landslide susceptibility. It is not our intent to directly test whether considering rainfall patterns improves prediction of landslide locations, as uncertainties in our datasets (e.g. rainfall climatology, landslide mapping, and soil properties) make such a task intractable.

The SHALSTAB model (Montgomery and Dietrich, 1994), utilizes GIS software to couple an "infinite-slope" stability model with a steady-state model of rainfall infiltration and topographic-driven flow of water within the soil. The only detailed spatial information required by the model is a high resolution digital elevation model (DEM) of the topography. By assigning spatially-uniform mean values to other, often poorly mapped, parameters the model can be used to indicate where topographic factors make slopes prone to failure, with steep, convergent slopes identified as the most unstable (Montgomery and Dietrich, 1994). Since root strength offers significant reinforcement in forested regions, we consider a formulation of SHALSTAB that includes the effective soil cohesion due to vegetation (Montgomery et al., 2000). However to avoid making assumptions about landslide size we consider only basal cohesion and not cohesion around the perimeter of the slide. SHALSTAB may be applied by solving, at each DEM grid cell, for the critical value of a chosen parameter at which failure should occur. In principle any parameter may be used. We choose to solve for critical soil cohesion as our measure of slope instability:

$$\begin{aligned} C_{crit} &= z\rho_w g\cos^2(\theta)\tan(\phi) \\ &\quad\times\left[\frac{a}{b}\frac{q}{T}\frac{1}{\sin(\theta)} - \frac{\rho_s}{\rho_w}(1-\frac{\tan(\theta)}{\tan(\phi)})\right], \end{aligned} \tag{3.1}$$

where q is a steady-state precipitation flux, g the is acceleration due to gravity, T is the saturated soil transmissivity, a/b is the contributing drainage area per gridcell length (calculated as in Montgomery et al. (2000)), ρ_s is the wet bulk density of the soil, ρ_w is the density of water, θ is the angle of the topographic slope, ϕ is the angle of internal friction, z is the soil depth, and C_{crit} is the critical cohesion of the soil. Actual soil cohesion likely varies greatly across our study area due to variations in vegetation and land use, however solving for C_{crit} means we need not make assumptions about the actual cohesion. Note that in the model slopes that become saturated have their critical cohesion set to the value occurring at saturation, as excess water is assumed to run off as overland flow. For given topography and soil parameters, locations predicted to remain stable under saturated conditions, even without soil cohesion, are termed "unconditionally stable".

In our SHALSTAB simulations we use a 10 m DEM grid, the highest resolution available for our study area. To isolate the effects of spatial variability in rainfall we assume uniform values for soil depth and material properties (Table 3.3). These values were mostly taken from previous studies in the Oregon Coast Range (e.g., Montgomery et al., 2000), and are only meant to represent reasonable mean values for illustration.

Table 3.1: Uniform values for soil parameters used in SHALSTAB modeling (symbols defined in text).

Parameter	**Value**
ρ_w/ρ_s	2
z	$1\ m$
ϕ	33°
T	$65\ m^2/day$

SHALSTAB models the response of soil pore pressures to steady rainfall of infinite duration. This is an approximation to the pseudo-steady state response of actual soils to prolonged rainfall, which occurs on a timescale of about 1 day for small slides in diffusive soils (Iverson, 2000). Many slides are actually triggered by the transient response of pore pressures to bursts of intense rainfall, which occurs on a timescale of tens of minutes for shallow slides in diffusive soils (Iverson, 2000). However, we focus on the pseudo-steady response since it is less dependent upon high-frequency variations in rain-rate (which are poorly characterized), and since regions of increased saturation due to this slow response will be more prone to failure due to transient forcing.

We first run SHALSTAB to calculate the critical cohesion using equation (3.1), including the spatially varying pattern of rainfall ($(q(x, y))$) predicted by MM5. For this we use the 7 year maximum 24 hr average rainfall rate at each MM5 grid point (Figure 3.3). The 7 year maximum rainfall rate is used to determine the most hazardous conditions at each location that would be expected over a climatological timescale. Ideally a period longer than 7 years would be used to develop a proper rainfall climatology, but we are limited by the extent of the MM5 dataset and the semi-idealized nature of our study only requires a plausible climatology. Furthermore, based on the storm-to-storm robustness of the rainfall pattern we expect a longer climatology would look similar, except perhaps with larger extreme rainfall rates. A 24 hr averaging period is used since this is the timescale over which pseudo-steady-state adjustment of groundwater flow occurs (Iverson, 2000). To calculate the 24 hr rain rates we first construct a time series of 0–12 UTC and 12–24 UTC forecast rainfall from forecast hours 24–36 of the MM5 runs (initialized twice daily at 0 and 12 UTC). For practical reasons the 24 hr averages are obtained by using a 24 hr running mean window that shifts forward in time by 12 hr increments rather than by 1 hr increments, thus the actual maximum rate is potentially underestimated. Before feeding the rainfall pattern into SHALSTAB we linearly reinterpolate it to a 1 km grid to smooth out some of the sharpest gradients introduced by the coarseness of the MM5 mesh.

The pattern of 24 hr maximum rainfall rate shown in Figure 3.3 exhibits both a steady increase in rainfall towards the interior of the Olympic mountains, as well as variations in rainfall associated with the major ridges and valleys. This pattern is somewhat different than the pattern of rainy season total precipitation (shown with the transect in Figure 3.2 and in Anders et al. (2007) and Minder et al. (2008)). While both the season-total and extreme rainfall patterns exhibit large variations associated with the ridge-valley relief, for the extreme rainfall the maximum appears to be shifted away from the ridge crest towards the southeastern slopes of the ridge. Case studies analyzed by Minder et al. (2008) suggest that such a shift in the rainfall pattern is reasonable.

We consider the results from our first SHALSTAB simulation, using the MM5 rainfall pattern, as our best estimate of the true slope stability. We then rerun SHALSTAB twice, both times with uniform rainfall forcing. For the first of these runs we choose an uniform rain rate representative of the spatially averaged maximum 24 hr rain rate over the basins: 256 mm/day. Comparison of the output from this run with the original patterned rainfall run is used to determine how much the rainfall pattern affects landslide susceptibility. For the second run we use the MM5 rainfall to choose a uniform rain rate representative of the maximum 24 hr value that would be measured at the location of the Black Knob (BKBW, shown in Figure 3.3), the nearest weather station with precipitation data for multiple years that would be readily available for hazard assessment: 141 mm/day. Comparison of the output from this run with the patterned rainfall run is used to determine the biases that may occur if lowland observations are used to characterize the rainfall and landslide susceptibility across a mountainous catchment.

3.4 Results

Figure 3.4 shows C_{crit} calculated across the basin using the MM5 precipitation pattern. The highest values of critical cohesion are greater than 6 kPa, suggesting that those slopes would fail under the most extreme 7 yr rainfall unless they had significant stabilization associated with vegetation and root strength. Many of the mapped slides initiate in steep topographic hollows, and SHALSTAB does qualitatively well at identifying these locations as regions of high C_{crit} (e.g. Figure 3.5). We make a cursory check on the ability of SHALSTAB to identify the locations prone to failure using methods analogous to Montgomery et al. (1998). More specifically, for each of the shallow landslides mapped in Figure 3.1 we associate the slide with the location within the mapped slide polygon where the critical cohesion is a maximum (this is done to better associate the mapped slide, which include both scar and run-out, with the location of of failure). We bin the frequency of slide occurrence by the slide's maximum critical cohesion, and then normalize each bin by the total area in the study region with that value of critical cohesion. The results from this, plotted in Figure 3.6, show a clear tendency for slides to occur much more frequently with high values of C_{crit}, as should be expected if the model is skillful at identifying the locations where failures tend to occur. While this analysis does not definitively demonstrate SHALSTAB's skill, the combination of these results with more rigorous evaluations of the model in settings similar to our study region (e.g., Montgomery et al., 1998) give us confidence in its appropriateness for this study.

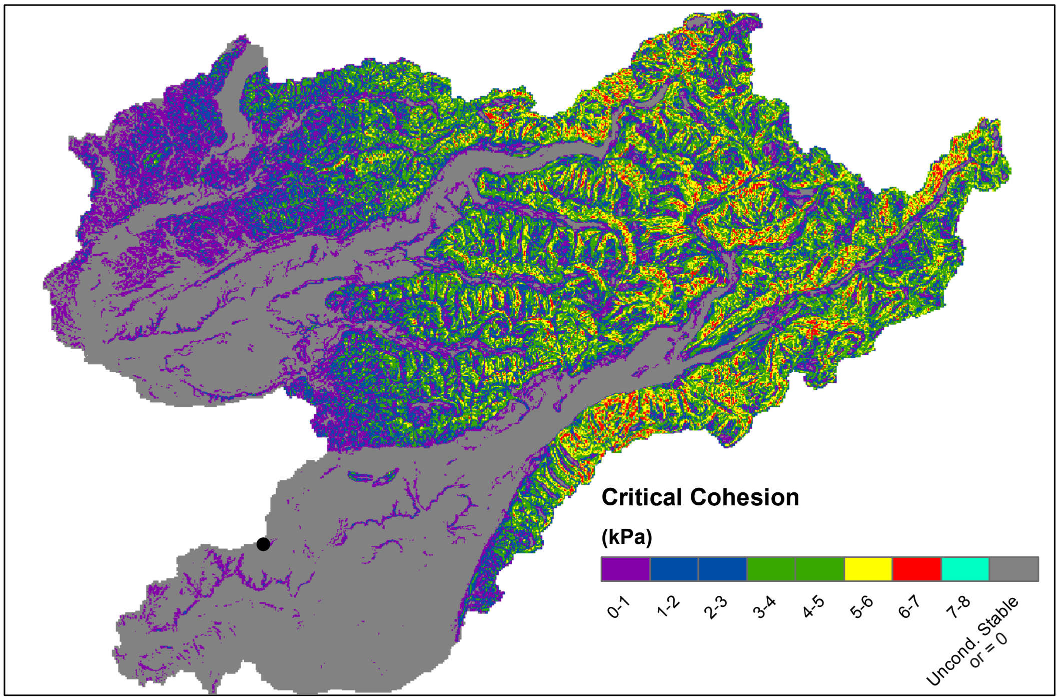

Figure 3.4: Critical cohesion as predicted by SHALSTAB (equation 3.1) using the MM5 rainfall climatology shown in Figure 3.3. Gray areas represent locations classified as unconditionally stable or with $C_{crit} = 0$.

Figure 3.7 shows the difference in C_{crit} that occurs when patterned rainfall is used relative to when uniform rainfall equal to the region average is used. As should be expected, it shows that neglecting the rainfall pattern causes an overestimate (underestimate) of slope stability in regions that receive more (less) than the area average rainfall. The change in C_{crit} is modest over most of the study region (< 0.5 kPa), but can be more substantial near the locations of the minima and maxima in the precipitation pattern (> 1 kPa). A larger fraction

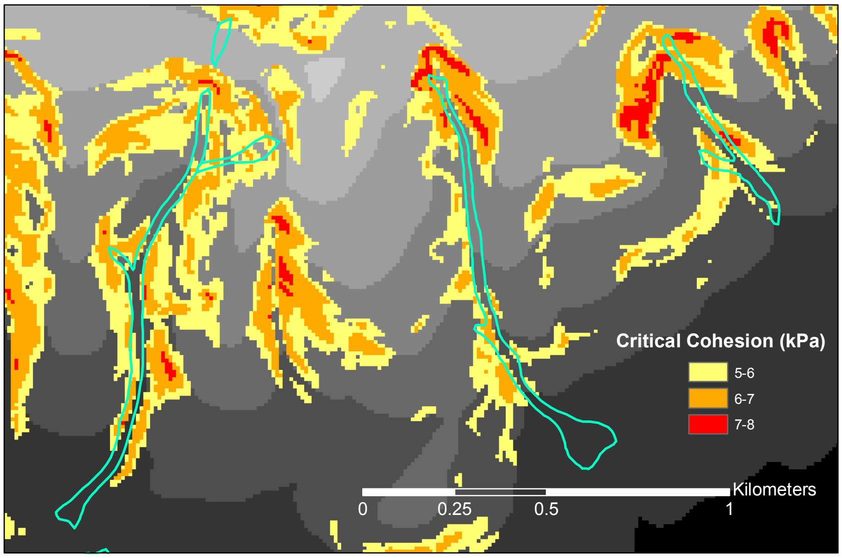

Figure 3.5: Mapped slides and SHALSTAB modeled C_{crit} for the individual hillside indicated by the blue box in Figure 3.1. Elevation are shown with gray-scale shading (shading interval of 100 m). Regions of high C_{crit} are color-shaded according to the inset key. The perimeters of several mapped slides are delineated in cyan.

of the study region experiences an overestimate than an underestimate of the stability when the pattern is neglected since the most gentle slopes, which are unconditionally stable, tend to reside in the lowlands and valleys where rainfall rates tend to be more modest.

Figure 3.8 shows the difference in C_{crit} that occurs when patterned rainfall is used relative to when uniform rainfall from the lowland station BKBW is used. Since nearly all locations where slides may occur (locations that are not unconditionally stable) receive more rainfall than the BKBW's lowland location, C_{crit} is found to increase, and the stability is overestimated, almost everywhere when the rainfall pattern is considered, and by upwards of 3 kPa in the center of the ridge's rainfall maximum. In other words, considering the

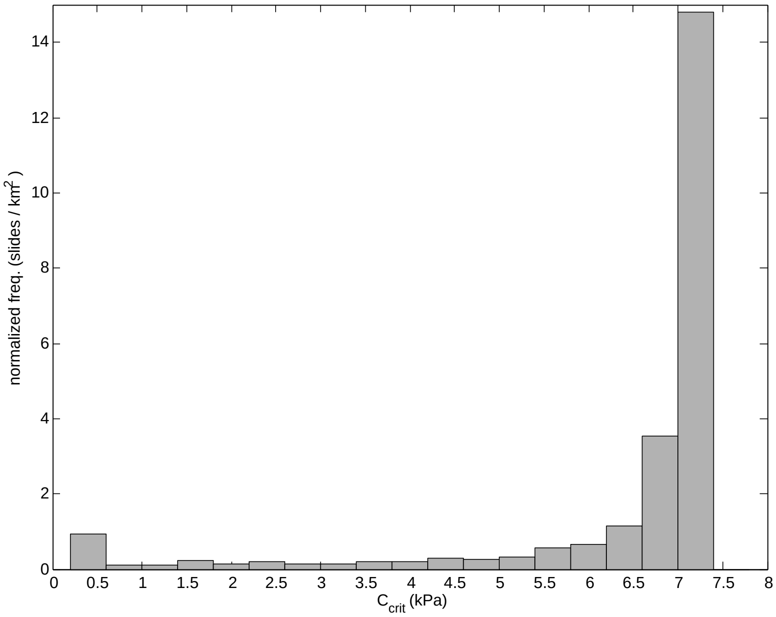

Figure 3.6: Number of mapped landslides per km^2 in each C_{crit} category (calculated as described in text) for slides mapped in the Queets and Quinault basins and SHALSTAB calculated values of C_{crit}.

rainfall pattern instead of just the lowland precipitation reveals a larger number of slopes that require significant reinforcement from root strength to resist failure.

We further analyze the results of these experiments by considering bulk statistics from the runs. Figure 3.9a shows a frequency distribution of C_{crit} values for the patterned and uniform rainfall cases. When the rainfall pattern is neglected in favor of the average rainfall, the distribution of C_{crit} is shifted towards somewhat lower (more stable) values, corresponding to an overall modest overestimate of the stability of slopes in the study region. When the rainfall pattern is neglected in favor of the lowland rainfall a much more substantial shift in the distribution and overestimate of the stability occurs.

Figure 3.9b shows the frequency distribution of the changes in critical cohesion experienced between the uniform and patterned case (patterned - uniform). Figure 3.9b again shows that using the rainfall pattern instead of the uniform average precipitation increases

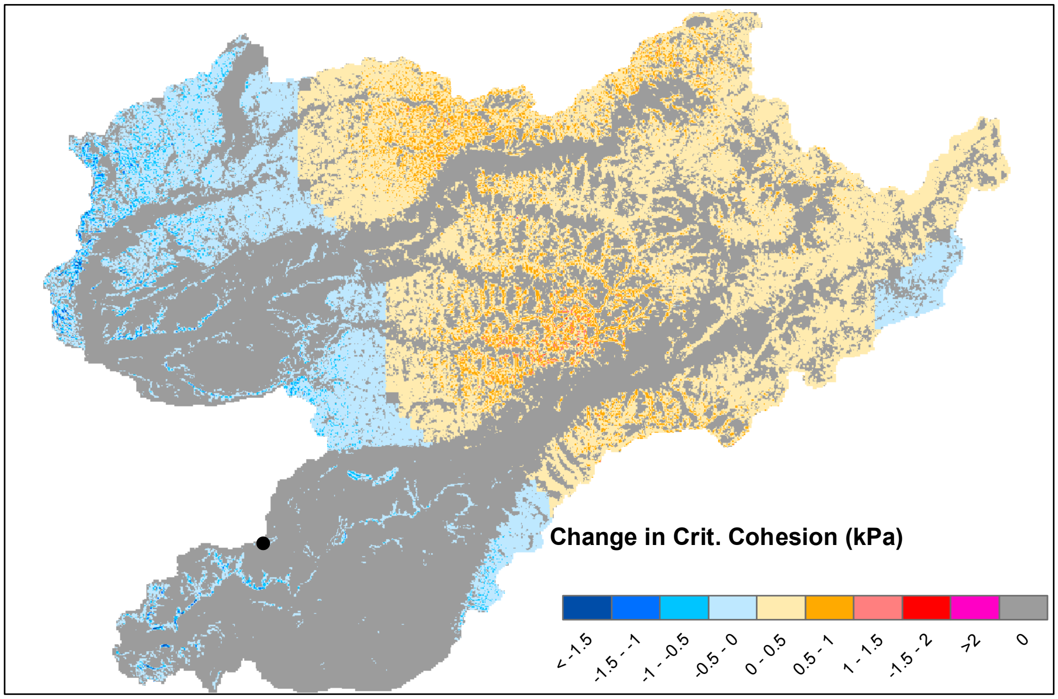

Figure 3.7: Change in critical cohesion between the SHALSTAB run using the MM5 rainfall pattern and the run using uniform precipitation equal to the region average of the MM5 rainfall (pattern - average).

C_{crit} for some slopes and decreases it for others, indicating that neglecting rainfall patterns under or over estimates the stability depending upon location. In contrast, using the rainfall pattern instead of the uniform lowland precipitation increases C_{crit} nearly everywhere, indicating that uniform lowland rainfall results in a very widespread overprediction of slope stability.

The scale of the differences in C_{crit} can be used to place the impact of spatial rainfall variations in context. For instance, direct measurements of cohesive reinforcement by roots in Pacific Northwest forests (collected from the Oregon Coast Range) reveal that typical cohesion from roots ranges from 6.8–23.2 kPa for industrial forests, and from 1.5–6.7 kPa

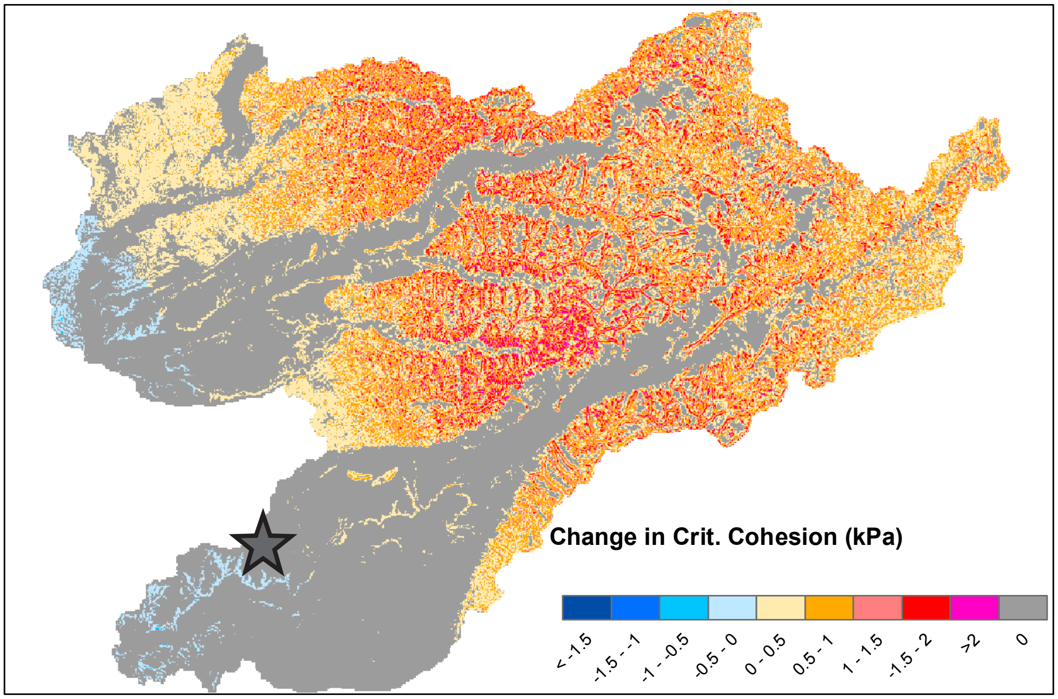

Figure 3.8: Change in critical cohesion between the SHALSTAB run using the MM5 rainfall pattern and run using uniform precipitation equal to the MM5 rainfall at the location of the lowland station BKBW (pattern - lowland). The location of BKBW is indicated with a star.

for clear-cuts <11 yrs old (Schmidt et al., 2001). Therefore, particularly for heavily logged basins, the maximum biases in the estimate of C_{crit} due to use of uniform lowland rainfall (~ 3 kPa) are equivalent to a substantial portion of the net reinforcement provided by tree roots, suggesting that such biases are indeed relevant. Even the seemingly modest changes in the estimate of C_{crit} introduced by using uniform averaged precipitation (as much as 1 kPa) may appear non-trivial in this context.

Figure 3.9c shows the fractional area of the landscape exceeding various values of C_{crit}. This can be used to determine the fraction of the landscape that would be considered

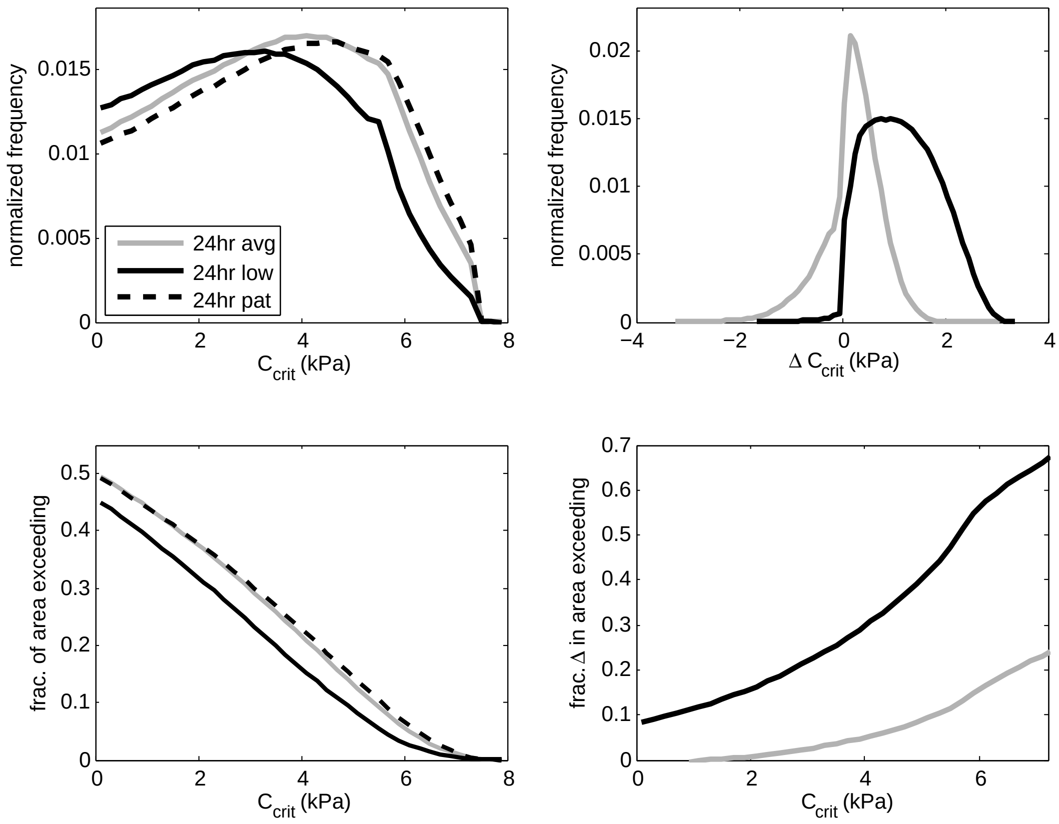

Figure 3.9: (a) Frequency distribution of C_{crit} for SHALSTAB runs with MM5 patterned rainfall (dashed black line), uniform region average rainfall (solid gray line) and lowland rainfall (solid black line). The distributions have been normalized by the total area of the basins, and cells with $C_{crit} = 0$ are omitted. (b) Frequency distribution of changes in C_{crit} between run with patterned and the runs with uniform rainfall (gray line for uniform average rainfall, black line for uniform lowland rainfall). Distributions have been normalized as in (b), and cells with change in $C_{crit} = 0$ are omitted. (c) Fractional area of the region exceeding various values of C_{crit} for patterned and uniform rainfall runs (line styles as in (a)). (d) Fractional change in area exceeding various values of C_{crit} between SHALSTAB runs with patterned and uniform rainfall (line styles as in (b)).

unstable if a given value of cohesion were present everywhere. For instance, if all soils on the landscape had a cohesion of 6 kPa, the model would predict that about 7% of our study region would fail. Figure 3.9d shows the fractional change in the curves of Figure 3.9c that occurs when the precipitation pattern is neglected. For example, if a critical cohesion threshold of 6 kPa is used, 15% fewer slopes would be identified as unstable when the uniform average rainfall is used instead of the rainfall pattern, indicating a significant underestimate of the area in danger of failure. When the uniform lowland rainfall is used instead of the rainfall pattern 55% fewer slopes would be identified as unstable, indicating a very substantial underestimate of the area in danger of failure. A higher (lower) percentage increase in the number of unstable slopes is found if a higher (lower) C_{crit} threshold is used, and the underestimate reaches 64% for the use of lowland rainfall when a 7 kPa is used. We thus conclude that in regions with large spatial variability in rainfall (such as the Olympic Mountains) the spatial pattern of rainfall acts to moderately increase the area prone to shallow landsliding by focusing rainfall on the mountain ridges where slopes are steep relative to the lowlands and valleys. Additionally, the use of lowland rainfall data alone to estimate hazard throughout even a relatively small mountainous catchment, may result in a substantial underestimate of the landslide susceptibility.

3.5 Sensitivity Analysis

Certainly, hillslope properties that we have considered to be uniform in our analysis so far actually vary significantly on real landscapes. Even if there is a sizable effect on slope stability associated with rainfall variations, it may be largely overwhelmed by the effect of variations in other factors. We investigate the relative importance of spatial variability in different factors by first quantifying the sensitivity of slope stability to characteristic small-scale rainfall variations, and then comparing this to the sensitivity to variations in soil properties.

Figure 3.10 shows contours of C_{crit} predicted by SHALSTAB as a function of θ and a/b for the parameters listed in Table 3.3 and uniform rainfall of 260 mm/day (roughly the mean value from the MM5 rainfall pattern). The stability of any site on the landscape may be determined by locating the point on such a plot. Note that steeper slopes lead to

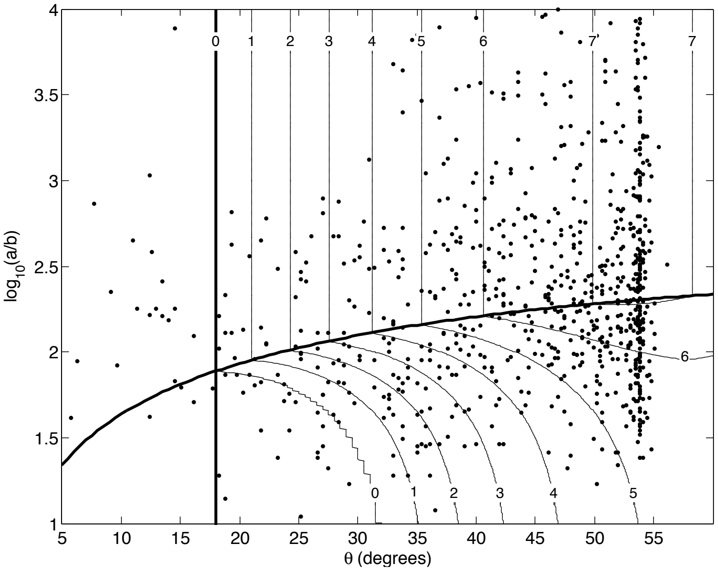

Figure 3.10: Critical cohesion (contoured and labeled every 1 kPa) as a function of tan(θ) and a/b using the parameters in Table 3.3 and uniform rainfall of 260 mm/day. The most unstable DEM grid cell in each mapped shallow slide (i.e. those shown in Figure 3.1) is plotted as a point based on its tan(θ) and a/b values. Regions above the arching bold line are predicted to become saturated in the model. Locations to the left of the vertical bold line are unconditionally stable. Note, limitations of our DEM dataset cause underestimation of steep slopes, thus the slopes for points to the right of the figure are best considered as representing minimum values.

increased C_{crit}, as does greater topographic convergence (a/b). However, increases in a/b only increase C_{crit} until the soil reaches saturation (this occurs along the arching bold line in Figure 3.10), at which point overland flow is assumed to occur and pore pressures do not increase further. The most unstable point (as predicted by value of C_{crit}) within each mapped shallow landslide polygon is shown as a dot on this figure. As already shown in Figure 3.6, the distribution of points illustrates that while slides occur in many settings on the landscape, they are concentrated in the regions of high θ and a/b that SHALSTAB identifies as particularly unstable.

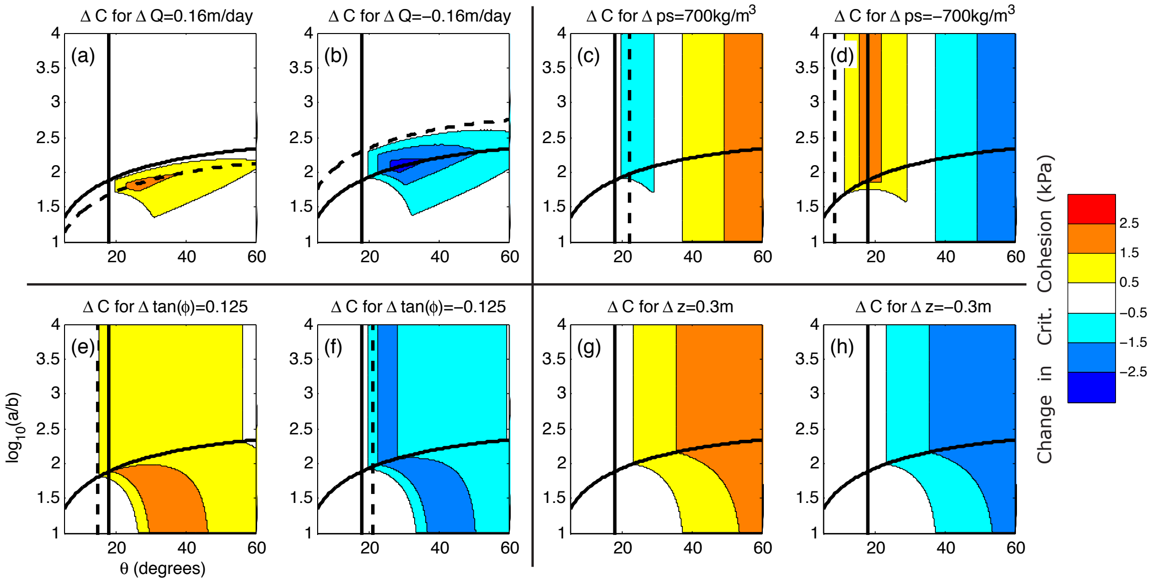

Figure 3.11: Sensitivity of C_{crit} to variations in different parameters. (a)–(b) sensitivity to modeled spatial variations in rainfall (± 160 mm/day). (c)-(h) sensitivity to variations in soil parameters (z,tanϕ,ρ_s). The magnitudes of variations in soil parameters (given above the figure panels) are chosen to give changes in C_{crit} comparable to those due to precipitation variations shown in (a)–(b).

Increasing or decreasing the value of q in equation (3.1) by an amount characteristic of the maximum basin-scale rainfall variations (± 160 mm/day, the difference between the maximum and minimum MM5 rainfall values) changes the value of critical cohesion at each point on the landscape by the amount shown in Figure 3.11a–b. As found for our case study, changes in C_{crit} reach over 2.5 kPa. Additionally, this analysis illustrates that the sensitivity to rainfall variability is felt on a specific part of the landscape, namely near-saturated, relatively modest slopes with convergent topography, as this is where groundwater transport is focused and soils are poorly drained.

Figure 3.11c–h shows the analogous results for changes in three of the soil properties included in SHALSTAB (z,tanϕ,ρ_s). For comparison we choose the magnitude of changes in the soil properties so that they result in stability changes of roughly the same scale as those arising from precipitation variations in Figure 3.11a–b. Due to the form of equation (3.1) the sensitivity of C_{crit} to changes in both soil properties and rainfall is linear, meaning a change in any of the parameters will lead to a linearly proportional change in stability (except in regions that reach saturation or unconditional stability). Note that different regions of the landscape show sensitivity depending on which parameter is varied. For each of the soil parameters, variations of significant amplitude are required to match the effect of precipitation variations, showing that climatological patterns in extreme precipitation on the basin-scale can be of comparable importance with variations in soil properties for determining the pattern of landslide hazard. The position of mapped slides on Figure 3.10 reveals that a significant number of slides occur in the region of large precipitation sensitivity as predicted from Figure 3.11a-b, however it is the scale of variations in precipitation relative to variations in soil properties that determines their importance in shaping the spatial distribution of hazard. For instance, Figures 3.10 and 3.11g-h suggest that if ± 30 % variations in soil thickness were to occur, they would have more impact than the observed precipitation variability in the locations where most slides are found.

3.6 Conclusions

We have analyzed the relationship between spatial patterns of rainfall and patterns of landslide susceptibility using high-resolution atmospheric model output (supported by gauge observations) and a physically based model of slope stability. We find that the climatological spatial variations in intense rainfall for a pair of basins in the Olympic Mountains are large enough to cause non-trivial variations in slope stability. For our study area we find that the use of area-averaged precipitation to estimate landslide susceptibility at a mountain site results in an underestimate of the area prone to failure from intense rainfall events that can exceed 20%, whereas use of lowland precipitation data can result in an underestimate of as much as 64%.

The destabilizing effects of the increase in precipitation from its lowland minimum to its mountain maximum may be expressed in terms of soil cohesion. In this framework we find that the enhancement of hazard at chronically rainy locations is equivalent to a substantial fraction of the actual soil cohesion supplied by vegetation in industrial and recently logged forests. This implies that the same land-use produces a different level of risk in the wetter uplands than one would assume from considering lowland rainfall data and assuming spatially uniform rainfall. In particular, forestry practices that reduce root strength can carry a greater danger of slope failure in forested upland areas than in the surrounding lowlands – even for the same local slope gradients and soil properties. Furthermore, the impact of the spatial variations of rainfall observed in locations such as the Olympic Mountains may be comparable to the effect of significant variations in soil parameters (e.g. ±30% variations soil depth).

We expect our results should generalize to a variety of regions. Similar patterns of precipitation are expected to be a common feature for midlatitude mountain ranges that receive their heaviest rainfall under convectively stable conditions. Less is known about the climatology of mountain precipitation on small scales produced by convective storms. In part due to the stochastic nature of convection, it is possible that the extreme rainfall patterns and their importance for landslide susceptibility are very different in regions that receive their heavy rainfall from such storms. As shown in Figure 3.11 unsaturated, relatively modest slopes with convergent topography are most sensitive to variations in rainfall, so our results are particularly pertinent for locations where many slides occur on such slopes. However, if large variations in soil properties exist, the effects of rainfall variability may be masked. Taken together, our results suggest that, for many regions, persistent spatial patterns in precipitation should be one of the factors considered in analyses of mass wasting by shallow landslides and in hazard assessments. High-resolution and high-quality datasets for mountain precipitation can be hard to come by, but strategically placed gauge networks and high-resolution atmospheric model output may prove valuable resources for the study of slope stability.

Chapter 4

THE SENSITIVITY OF CLIMATOLOGICAL MOUNTAIN SNOWPACK ACCUMULATION TO CLIMATE WARMING [1]

4.1 Introduction and background

Mountain snowfall maintains glaciers, sets the extent of ecosystems, provides for recreation, and produces major hazards in the form of avalanches. Mountain snowpack is crucial for many communities, since it preserves the precipitation that falls during wintertime storms and releases it as runoff which provides water resources during dry summer months. Globally about one-sixth of the world's population relies on glaciers and seasonal snow and ice for water resources, much of which resides in mountainous terrain (Barnett et al., 2005).

The importance of mountain snow and its intimate connections to climate have spurred recent research into how it is affected by climate change and variability. A focal point for these studies has been the mountains of the western United States (US) where snowpack makes a large contribution to regional hydrology and is heavily relied upon for water resources (e.g., Serreze et al., 1999; Barnett et al., 2005). Observations show a region-wide decline in spring snowpack since the mid-1900s, dominated by loss at low elevations where wintertime temperatures are near-freezing (Mote et al., 2005). These losses have been attributed to increased temperatures (Mote et al., 2005; Hamlet et al., 2005; Mote, 2006; Mote et al., 2008), which lead to snow loss via some combination of increased frequency of rain vs. snow (Knowles et al., 2006) and increased wintertime melting (Mote et al., 2005). Complicating the picture is large year-to-year variability. Innerannual variability of springtime snowpack comes largely from variability of wintertime precipitation (Cayan, 1996; Hamlet et al., 2005; Mote et al., 2008), that is in turn related to variability of key patterns of atmospheric circulation (Cayan, 1996; Mote et al., 2008; Stoelinga et al., 2009). These

---

[1] The contents of this chapter are published in Minder (2010), © 2010 American Meteorlogical Society. The published version may be found at: http://journals.ametsoc.org/doi/abs/10.1175/2009JCLI3263.1 .

natural fluctuations make it challenging to quantify trends with confidence, to extrapolate observed changes to project future climate, or to clearly discern changes in snowpack due to anthropogenic warming trends (e.g., Mote et al., 2008; Casola et al., 2009; Stoelinga et al., 2009). For instance, it is only recently that changes in western US snowpack have been has been formally detected and attributed to anthropogenic climate change, in an effort that required synthesis of extensive station observations with hundreds of years of model integrations (Pierce et al., 2008).

Other research in the western US has focused on making projections of snowpack for the coming century by using global climate models (GCMs) to force comprehensive regional models of mountain climate and hydrology(Hamlet and Lettenmaier, 1999; Leung and Qian, 2003; Vicuna et al., 2007; Salathé et al., 2008; Climate Impacts Group, 2009). However, despite the advanced techniques used, projections of future snowpack from these models are still fraught with uncertainty. Much of the uncertainty is inherited from the climate projections of the parent GCMs used to force them, while further uncertainties stem from the sensitivity of regional models to how key physical processes are parameterized.

In order to minimize the above-mentioned challenges presented by natural variability and modeling uncertainties this paper takes a different approach to understanding how climate change affects mountain snowpack. In particular, a pair of idealized, physically based models are used to simulate snowfall for the Cascade Mountains. Experiments with these models are then used to study the changes in climatological snow accumulation occurring due to local changes in temperature alone.

4.2 Focus and strategy

This paper examines the physical controls on the sensitivity of mountain snowpack to local temperature changes (e.g., Casola et al., 2009). Let Σ_t be defined as a measure of the total Snow liquid Water Equivalent (SWE) integrated over some region (e.g. the annual accumulated SWE integrated over a catchment, measured in units of volume), and T be a representative surface temperature (e.g. the mean surface temperature at sea level). The temperature sensitivity of the snowpack is then defined as:

$$\lambda \equiv \frac{1}{\Sigma_t}\frac{d\Sigma_t}{dT}. \tag{4.1}$$

Unless otherwise noted, values of λ quoted are normalized by the Σ_t associated with the control climate such that they represent percentage changes in the snowpack per degree of warming. λ can be expanded into the direct and indirect effects of warming:

$$\lambda \approx \frac{1}{\Sigma_t}\left[\frac{\partial\Sigma_t}{\partial T} + \sum_i \frac{\partial\Sigma_t}{\partial y_i}\frac{\partial y_i}{\partial T}\right]. \tag{4.2}$$

The direct sensitivity, $\frac{\partial\Sigma_t}{\partial T}$, is due to changes in precipitation phase and melting directly attributable to warming. Indirect sensitivities, $\frac{\partial\Sigma_t}{\partial y_i}\frac{\partial y_i}{\partial T}$, include changes in a related variable, y_i, that in turn affect snow accumulation (for example, changes in precipitation intensity due to warming that in turn affect snowfall). This paper only considers indirect sensitivities that are closely tied to local changes in temperature. For instance, changes in snowpack due to possible global warming induced changes in midlatitude storm tracks are neglected.

Casola et al. (2009) used three methods to determine λ for the portion of the Cascade mountains draining into Puget Sound (Figure 4.1): a simple geometrical model; daily station observations of precipitation and temperature; and a sophisticated hydrological model. In estimating the direct sensitivity ($\frac{\partial\Sigma_t}{\partial T}$, neglecting precipitation changes) all three methods yielded a remarkably similar values of between 22 and 24% loss of April 1st SWE per degree of warming. The agreement between methods suggests that λ is a robust measure that is determined largely by relatively simple controls. An alternative, observationally based, estimate of the direct sensitivity of Cascade snowpack gives a lower value of 15%°C^{-1} (Stoelinga et al., 2009). Other studies have estimated λ values between -6 and -10% °C^{-1} for the California Sierra Nevada (Howat and Tulaczyk, 2005) and equal to about -15% °C^{-1} for the Swiss Alps (Beniston et al., 2003, reported as -30% for 2°C of warming).

In examining λ, this study considers the sensitivity of mountain precipitation intensity to warming. This indirect sensitivity has not been addressed in detail in other studies of λ (e.g., Howat and Tulaczyk, 2005; Casola et al., 2009). However, significant precipitation increases may occur over many mid- and high-latitude mountains under climate warming.

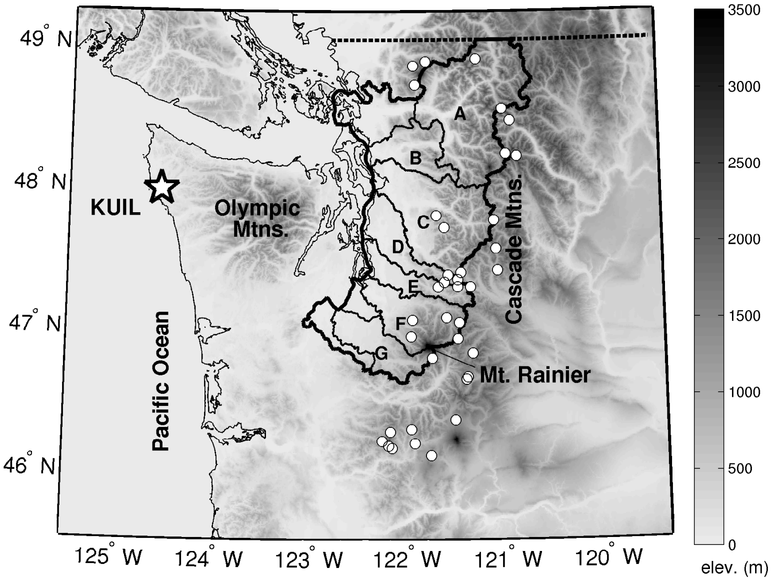
49° N
48° N
47° N
46° N
125° W
124° W
123° W
122° W
121° W
120° W
KUIL
Olympic Mtns.
Pacific Ocean
Cascade Mtns.
Mt. Rainier
A
B
C
D
E
F
G
3500
3000
2500
2000
1500
1000
500
0
elev. (m)

Figure 4.1: Map of study region. Topography of the Cascades and Olympic Mountains is shown in grayscale (maximum elevation is 4392 m at Mount Rainier). The boundary of the catchment that drains the Cascades into the Puget Sound (with the exception of a small section in Canada) is shown with a bold line. Major catchments within that basin are delineated with narrow lines (those used for Figure 4.12 are labeled A-G). The location of the Quillayute sounding (KUIL) is shown with a star, and the locations of SNOTEL stations used in Figure 4.4 are shown with white circles

.

Global climate models (GCM's) suggest that global-mean precipitation will increase by 2-3% per degree of warming (e.g., Held and Soden, 2006), and that precipitation intensity will increase throughout most of the mid- and high-latitudes (e.g., Tebaldi et al., 2006). While GCM's cannot adequately resolve the dominant scales of mountain precipitation, simple theories (e.g., Sawyer, 1956; Smith, 1979; Smith and Barstad, 2004) predict that, under neutral stratification, orographic precipitation intensity is proportional to the low-level moisture flux impinging on a mountain. This suggests that if the relative humidity

(RH) and winds do not change with warming, then low-level moisture fluxes, and hence orographic precipitation, might scale according to the Clausius-Clayperon (CC) relationship at about 6–7%°C^{-1} of warming. Using high-resolution numerical simulations, Kirshbaum and Smith (2008) show that increased temperature and moisture flux do indeed lead to robust increases in orographic precipitation. However, they also showed that precipitation does not increase with temperature as fast as the moisture flux, due to both thermodynamic and microphysical effects.

In this study a pair of idealized, physically based models of the climatology of snowpack accumulation are used to determine the controls on λ. These models are favored for their efficiency (which allows for a large number of experiments), their adaptability (which allows for substantial changes in model physics and forcing data), and their simplicity (which allows fundamental processes to be clearly diagnosed). For precisely determing the value of λ these models may not be superior to observational techniques and complex models. However, the use of simple models allows for the formulation controlled experiments and analyses to isolate controls on λ that would not be possible with other methods. This study only considers snowpack changes associated with changes in snow accumulation. This is referred to as the temperature sensitivity of the *snowfall*, λ_S. This differs from the full sensitivity of the *snowpack*, λ, because it neglects the effects of increases in temperature on snow ablation. The present study focuses on Washington state's Cascade Mountains, but will also arrive at some general lessons about mid-latitude mountain snowpack and climate.

The outline of the paper is as follows. First an intermediate complexity model of mountain snowfall is described and used to estimate λ_S for the Cascades, as well as the relative importance of precipitation and ML changes. Then a simpler model is be developed to reveal the fundamental controls on λ_S. Next a series of experiments is presented to quantify the topographic and climatic controls on changes in mountain snowfall. Finally, the main conclusions are summarized.

4.3 Linear Theory (LT) Orographic Snowfall Model

A model that accounts for many of the fundamental physical processes that shape the distribution of orographic snowfall serves as the starting point for this investigation. The model predicts snowfall on a storm-by-storm basis as a function of the characteristics of the incoming flow, and includes: 1) Spatial variability in precipitation; 2) Storm-to-storm variability in precipitation intensity; 3) The dependence of the surface rain-snow transition on the upstream ML's; 4) The temperature dependence of both orographic precipitation intensity and storm ML's. While including all of these aspects the model is also simple enough that the controls on λ_S can be clearly discerned.

4.3.1 Methods

The model for orographic snowfall presented in this section has as its foundation the linear theory (LT) model of orographic precipitation (Smith and Barstad, 2004). The LT model solves for the steady-state condensation, advection, fallout, and evaporation of water occurring in vertically integrated atmospheric columns for given uniform (horizontally and vertically) and constant impinging flow. The model assumes stable stratification and saturated conditions. It solves linearized equations of motion for flow over topography, to represent the pattern of ascent responsible for the generation of orographic clouds. It also accounts for the finite time that is required for cloud water to convert into precipitation and the time it takes for precipitation to fall to the ground, allowing for downwind drift of cloud and precipitation. Additionally, it contains a representation of lee-side evaporation that suppresses precipitation downwind of terrain.

The LT model is run by prescribing characteristic winds (speed and direction), stratification (moist stability, N_m), and low-level temperatures (which determine the specific humidity), as well as two microphysical time delay constants (τ_c and τ_f, representing timescales for the conversion of cloud to precipitation and fallout respectively), and a background precipitation rate (P_{bg}, representative of precipitation generated directly by synoptic storms). The model has a simple formulation in Fourier space, allowing for rapid computation of solutions at high spatial resolution. The LT model, when properly calibrated, has proven remarkably skillful, particularly for climatological applications (e.g., Smith et al., 2003; Barstad and Smith, 2005; Anders et al., 2007; Crochet et al., 2007). For instance, over the Olympic Mountains, just west of the Cascades (Figure 4.1), the LT model has been shown to produce realistic precipitation patterns as compared to a dense network of gauges and a high resolution atmospheric model (Anders et al., 2007).

For this study the LT model is first used to simulate the climatology of total precipitation over the Cascades. The model is run at approximately 1 km horizontal resolution, with the bottom boundary condition provided by the a National Elevation Dataset 1 arc-second Digital Elevation Model (http://ned.usgs.gov/) coarsened to 30 arc second resolution. The LT model is forced with soundings from rawindsonde measurements taken twice daily (00 and 12 UTC) at Quillayute (KUIL), Washington between 1980 and 2007 (location shown in Figure 4.1). Conditions likely to correspond to mountain precipitation events are isolated by picking out "storm" soundings, defined as soundings where the 1 to 2 km layer has average wind direction between 160 and 330 degrees and average RH greater than 85%. Temperature forcing comes from the lowest level in the sounding, and wind forcing is the vector-averaged winds from the 1–2 km layer. The moist stability forcing, N_m, is also calculated from the 1–2 km layer, by first calculating the profile of N_m^2 (using Durran and Klemp (1982)'s eq. 36), averaging it over the layer, and then taking the square root. The microphysical time delays, τ_c and τ_f, are set equal to each other (τ) following Smith and Barstad (2004). Both τ and P_{bg}, which are not directly observable, are reserved as tunable parameters.

When the flow is unstably stratified ($N_m^2 < 0$) the LT model cannot solve for the airflow dynamics. Observations (not shown) from a network of gauges in the Olympic Mountains near the KUIL sounding (described by Anders et al. (2007) and Minder et al. (2008)), show that about 25% of precipitation falls when the upstream sounding indicates unstable conditions ($N_m^2 < 0$ for the 1–2 km layer). This is taken as an indication that unstable events cannot be neglected in the climatology. Accordingly, these events are included, albeit rather crudely, by simply setting N_m equal to zero for moderately unstable soundings.

After using the LT model to predict the pattern of precipitation, the temperature structure from the KUIL sounding is used to predict the pattern of precipitation phase (rain vs. snow) on a storm-by-storm basis. For each event the sounding is used to determine the ML upwind of the mountain as the lowest elevation where the sounding temperature crosses a 1°C threshold. This threshold roughly corresponds to the temperature where 50% of the time precipitation falls as snow according to results of United States Army Corps of

Engineers (1956) and Dai (2008) for a site in the Sierra Nevada of California and for a global dataset of land observations respectively. As mentioned above, the LT model assumes a saturated sounding with uniform moist stability. For consistency with these assumptions the ML is calculated from an idealized version of the sounding, constructed with the observed 1.5 km temperature and the N_m used to force the model.

It is common for the 0°C isotherm, radar bright band, and ML to dip to lower elevations on the mountainside (sometimes exceeding 500 m displacement) as compared to in the free air upstream of the mountains (Marwitz, 1987; Medina et al., 2005; Lundquist et al., 2008). The LT snowfall model accounts for this effect by introducing a constant orographic ML depression, ΔML, the value of which is used as a tunable parameter.

To warm the LT snowfall model for climate change experiments a new idealized sounding is constructed with the 1.5 km temperature warmed by 1 °C and the same uniform N_m as used in the control simulation. This results in warming that is a function of elevation, with less warming at 0 km (on average 0.83°C instead of 1°C). This methodology is motivated by the expectation of roughly constant mid-latitude moist stability under climate change (Frierson, 2006). The surface temperature and ML's used for the warmed simulations are attained from the new sounding.

4.3.2 LT snowfall model calibration

The LT snowfall model is calibrated by comparing its output with that of an operational mesoscale weather forecast model, adjusting the τ, P_{bg}, and ΔML parameters to maximize the agreement between the two. Simulated precipitation from the MM5 modeling system run operationally by the Northwest Regional Modeling Consortium at the University of Washington (Mass et al., 2003) is used. The MM5 was run twice daily with horizontal resolution of 4 km over the Washington Cascade mountains from 1997–2008. A full listing of the model grid, initialization, and parameterization choices can be found at http://www.atmos.washington.edu/mm5rt/.

The precipitation simulated from forecast hours 24–36 of each MM5 run for the snow accumulation season of two water years (October–March of 2005-2006 and 2006-2007) was

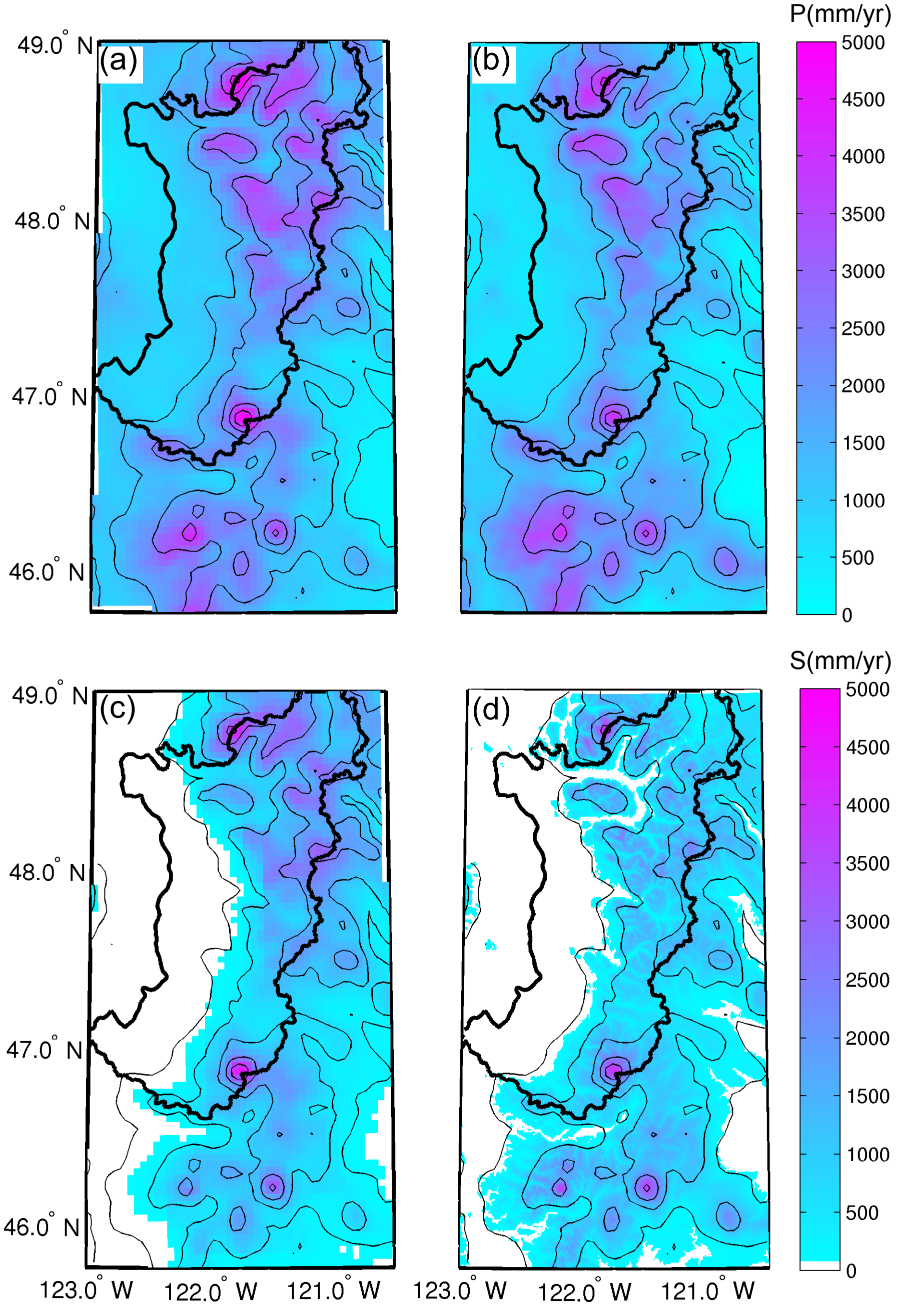
P(mm/yr)
5000
4500
4000
3500
3000
2500
2000
1500
1000
500
0
S(mm/yr)
(a)
(b)
(c)
(d)
49.0° N
48.0° N
47.0° N
46.0° N
123.0° W
122.0° W
121.0° W

Figure 4.2: Comparison of maps of precipitation, P, and snow water accumulation, S, from MM5 and LT models for Oct-Mar of 2005-2006 and 2006-2007: (a) MM5 modeled P, (b) LT modeled P, (c) MM5 modeled S, (d) LT modeled S. Thick black line shows the Puget Sound catchment. The MM5 model elevation is contoured with thin black lines every 500 m.

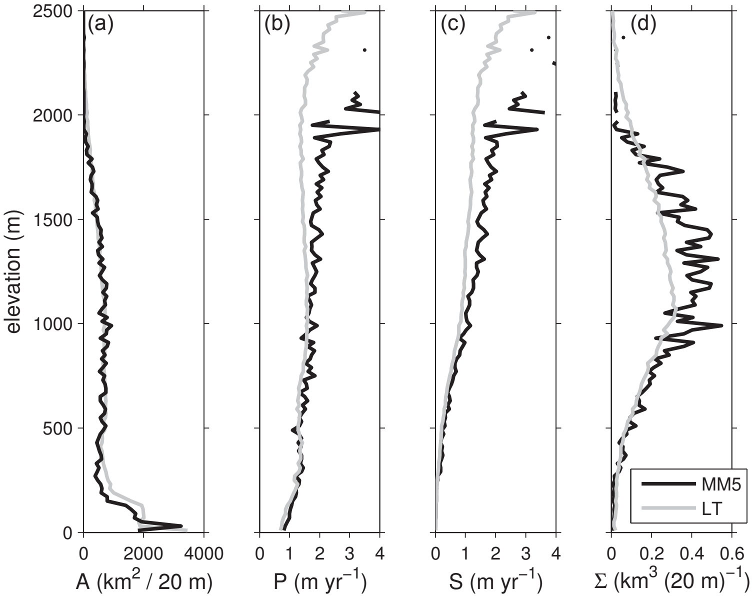

Figure 4.3: Comparison of LT model and MM5. Profiles of (a) $A(z)$, (b) $P(z)$, (c) $S(z)$, and (d) $\Sigma(z)$ from MM5 (black line) and LT snowfall model (grey line) for the accumulation seasons of water years 2006 and 2007. Profiles are evaluated for the entire domain shown in Figure 4.2.

integrated over all forecasts to find the mean precipitation (as in Anders et al., 2007; Minder et al., 2008). Figure 4.2 shows maps of mean accumulation season precipitation simulated by MM5 and the LT model, and Figure 4.3 shows vertical profiles of average precipitation as a function of elevation. A P_{bg} of 0.25 mm/hr and a τ of 1800 s were chosen by trial and error to subjectively maximize agreement between the mean precipitation profiles and maps for the two models. Figures 4.2 and 4.3 show that the vertical profile of precipitation and the basic pattern of orographic enhancement is similar between the models. Differences occur in terms of how much precipitation is simulated at mid-to-high elevations and in the northeast corner of the domain. Yet, overall the LT model produces a plausible simulation of precipitation that includes the primary features present in the MM5 forecasts.

Comparing snowfall simulated by the two models is less straightforward, since snow accumulation is not an archived field for the MM5 forecasts. To approximate MM5 snowfall the modeled 2 m temperatures are used with a 1°C temperature threshold to estimate the phase of modeled precipitation at each grid cell for each 12 hours (results shown in Figures 4.2 and 4.3). A ΔML of -200 m was chosen to match the mean snowfall profiles from the two models. The LT snowfall model reproduces the basic structure of MM5's snowfall profile. The most notable difference between the two models is less snow above 1000 m in the LT snowfall model. This is due in part to less precipitation at these elevations and in part to more rain vs snow in the LT model. However since the MM5 snowfall is only crudely estimated, and may have its own biases, it is unclear how significant this difference is. Furthermore, Appendix B shows that there does not appear to be a systematic underprediction of high elevation snow in the LT model when it is compared to station observations.

4.3.3 LT snowfall model evaluation

The LT snowfall model is evaluated by comparing its simulation of annual mean snowfall to that measured by the SNOTEL network of automated snow observations (http://www.wcc.nrcs.usda.gov/snow/). For a collection of SNOTEL stations in the model domain with long records (shown in Figure 4.1) daily observations are used to calculate the mean Oct-Apr accumulated snow, S, and precipitation, P, for the SNOTEL period of record (1980–2007). Only daily gains in snow are summed, neglecting days with snow loss, to evaluate S. For each station the LT precipitation is linearly interpolated to the station location and the actual station elevation is used with the model ML for the determination of precipitation phase. For all water years with available data, the fractional error in the simulated P and S, $(forecast - observation)/observation$, is calculated and presented as a function of elevation(Figure 4.4a-b).

The mean absolute fractional error is 0.33 for P and 0.40 for S. Spatial correlation coefficients are 0.53 for P and 0.52 for S. The errors that occur at many sites are unsurprising, since orographic precipitation has proven challenging to simulate, even with sophisticated

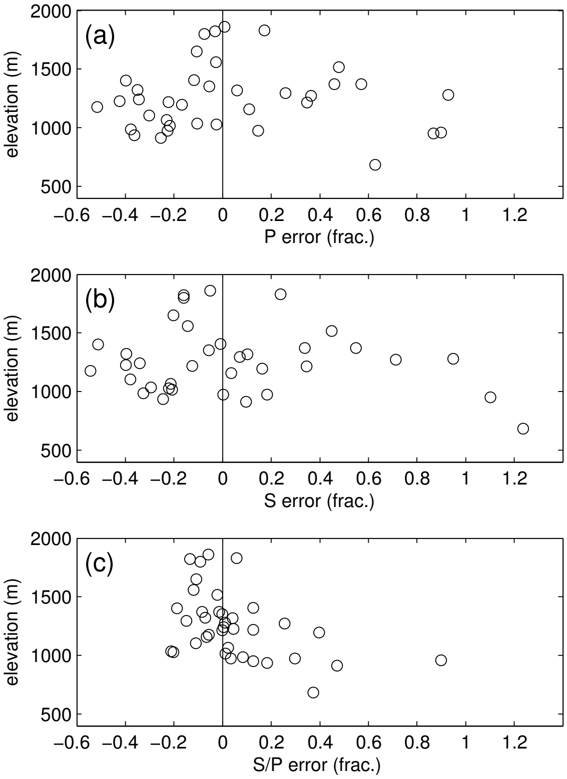

Figure 4.4: Comparison of LT snowfall model with SNOTEL observations. Average fractional error in LT modeled Oct-Apr (a) P and (b) S accumulation, and (c) S/P relative to SNOTEL stations as a function of elevation for 1980-2007.

models (e.g., Colle et al., 2000). Furthermore, the significance of the errors is unclear, since site-specific factors (e.g. vegetation, aspect) and observational biases (e.g. gauge undercatch, snow drift) may affect SNOTEL observations, and substantial errors can occur even for a perfect model when comparing grid-cell predictions to point observations (e.g., Tustison et al., 2001). Nevertheless, the absence of large systematic biases or distinct vertical structure in the error is encouraging. The possible impact of model biases on λ_S estimates is discussed in Section 4.5.1.

The ability of the LT snowfall model to reproduce the observed partitioning between rain and snow is also evaluated by calculating and comparing the average ratio of Oct-Apr accumulated S to P for model and observations (Figure 4.4c). This shows that, except for the lowest elevation stations, the model reproduces quite well the observed snowfall fraction (with a mean absolute fractional error of 0.14, and spatial correlation of 0.88), meaning that the simple model of the rain-snow transition used works reasonably well, and errors in S are primarily due to errors in P.

4.3.4 Results

The LT model is first used to simulate snowpack accumulation over the Cascades under current and warmed climate conditions for the 28 year period 1980-2007. λ_S is calculated by dividing the modeled fractional Σ_T changes by the average surface warming (0.83 °C).

Results are plotted as profiles in Figure 4.5, including the distribution with elevation of: topographic area (the derivative of the hypsometric curve), $A(z)$; average annual precipitation, $P(z)$; water equivalent snowfall, $S(z)$; and annual mean total volume of accumulated snow water, $\Sigma(z)$ $(= A(z) \times S(z))$. Note that the largest volume of snow accumulates at mid elevations where snowfall is frequent and large amounts of topographic area reside (Figure 4.5c).

In the warmed simulation precipitation increases at all elevations (Figure 4.5b), but not enough to offset the reduced frequency of snowfall due to shifts in the ML (Figure 4.5c). Maps of the change in precipitation and snowfall are plotted in Figure 4.6. The precipitation increases uniformly by about 5% $^{\circ}\mathrm{C}^{-1}$. The change in snowfall is variable is space, and is negative everywhere except the highest volcanic peaks.

Integrating the $\Sigma(z)$ curves for the control and warmed climates, and taking a fractional difference yields a λ_S of -18.1% $^{\circ}\mathrm{C}^{-1}$ (Table 1, *climo_control*). Isolating the effects of ML changes, by holding modeled precipitation constant, gives a sensitivity of -22.6% $^{\circ}\mathrm{C}^{-1}$, which will be referred to as λ_{ML}. Thus, precipitation changes reduce the magnitude of the sensitivity of snow accumulation by 4.5% $^{\circ}\mathrm{C}^{-1}$. Changes in precipitation alone give a sensitivity of 5.49% $^{\circ}\mathrm{C}^{-1}$ (about 1% $^{\circ}\mathrm{C}^{-1}$ less than the CC scaling), which will be referred to as λ_P.

Interestingly, the full sensitivity is not equal to the sum of the partial sensitivities to

Table 4.1: Sensitivity of snow accumulation to warming for various runs of LT and ML models. The top section of the table gives results for the two long simulations (1980-2007), with and without vertical structure to the warming, discussed in Sections 4.3 and 4.4. The lower section is for simulations of Oct.-Apr. of 2005-06 and 2006-07 (acc0607) used for the experiments discussed in Section 4.5. All values are in units of % change in snow accumulation per degree C of surface warming. ML model entries that are left blank have the same value as *exp_control*.

	LT model			ML model		
Run	λ_{ML}	λ_P	λ_S	λ_{ML}	λ_P	λ_S
1980–2007						
climo_control	-22.6	5.49	-18.1	-25.1	6.84	-19.8
climo_ΔTunif	-19.4	5.55	-14.8	-21.6	6.84	-16.3
acc0607						
exp_control	-20.3	5.56	-15.6	-23.2	6.90	-17.7
*exp_wdir*50	-23.4	5.76	-18.7			
*exp_tau*850	-21.3	6.03	-16.3			
*exp_ΔML_*0	-23.6	5.60	-19.0	-25.7	6.90	-20.4
*exp_ΔML_*400	-18.2	5.51	-13.4	-22.2	6.90	-16.6
*exp_Pbg*0	-20.0	6.92	-14.2			
*exp_PbgX*2	-20.6	4.47	-16.8			
exp_PbgCC	-20.3	7.14	-14.3			
*exp_z*75%	-27.8	5.21	-23.8	-30.7	6.90	-25.6
*exp_z*125%	-15.9	5.79	-10.8	-18.5	6.90	-12.7
*exp_x*75%	-20.1	5.68	-15.3			
*exp_x*125%	-20.3	5.43	-15.8			

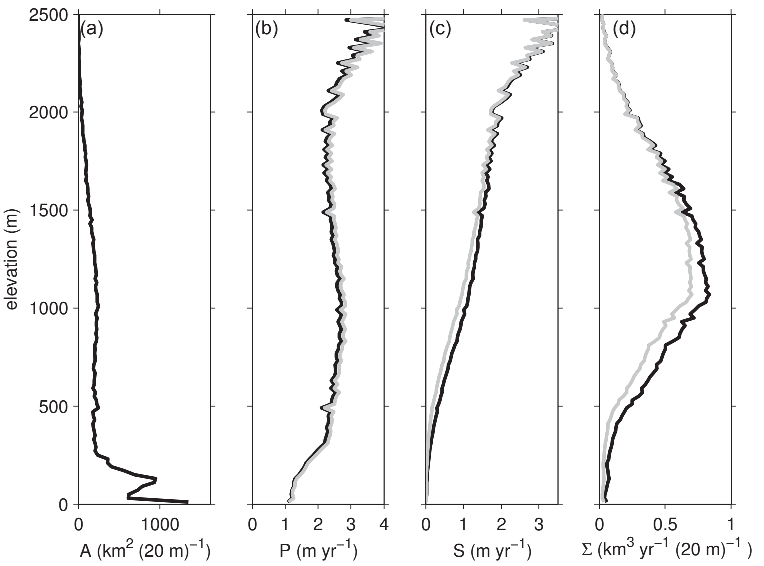

Figure 4.5: Profiles of LT snowfall model variables for the Puget Sound catchment (Figure 4.1) from the *climo_control* run: (a) topographic area, $A(z)$, (b) average accumulated precipitation, $P(z)$, (c) average snow water accumulation $S(z)$, and (d) integrated snow water accumulation $\Sigma(z)$. Control simulation is shown in black, and grey lines are for simulation with 1.5 km level warmed by 1°C (surface warming of 0.83 °C).

ML and precipitation changes ($\lambda_S \neq \lambda_{ML} + \lambda_P$): only 82% of the increased precipitation is realized as an increase in snowfall. The explanation for this is purely geometrical. While precipitation intensity for each storm is increased by several percent across the basin, some of the increase occurs in regions that receive snow in the control climate but rain in the warmed climate, meaning it is lost as runoff.

The λ_{ML} value of -22.6 % °C^{-1} from the LT snowfall model is within the range of the λ values of attained by Casola et al. (2009) when they neglected precipitation changes (-22 to -24% °C^{-1}) . However, comparison of these estimates is not entirely straightforward since this study simulates annual mean snowfall whereas Casola et al. (2009) simulates April 1st

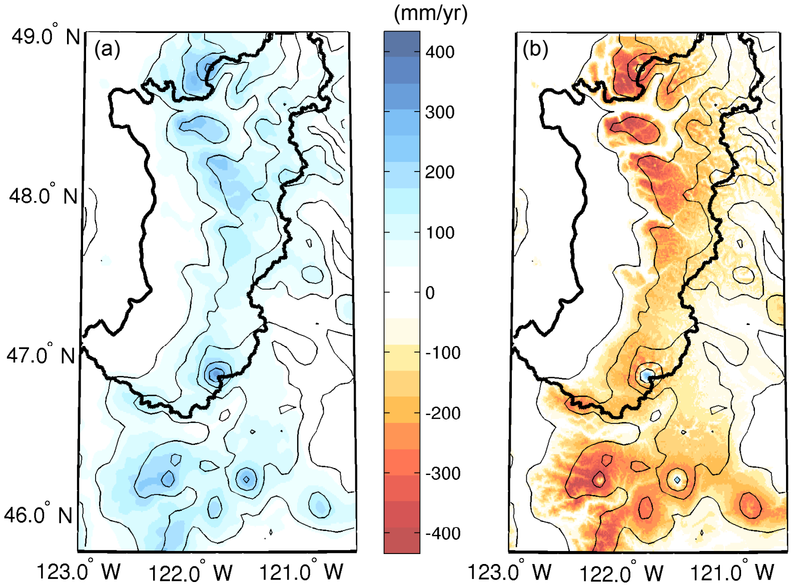

Figure 4.6: Maps of LT model change in (a) precipitation and (b) snow water accumulation for *climo_control* simulation. Smoothed topography (from the MM5 model) is contoured every 500 m.

snowpack. If increases in accumulation season melting with warming are negligible for the region (i.e. if $\lambda \sim \lambda_S$), then the models are in close agreement. However, if accumulation season melting increases substantially with warming (making λ larger in magnitude than λ_S), then the LT model underestimates the magnitude of λ, and thus implies a more sensitive snowpack than Casola et al. (2009). In terms of how precipitation increases affect snowfall accumulation the two studies agree. Casola et al. (2009) used temperature and precipitation data at a single representative station, to estimate that only 76% of increased precipitation would translate into increased snowpack. This value is similar to the 82% from the LT snowfall model, a notable agreement since these estimates were attained by very different methods.

4.3.5 Sensitivity to the vertical structure of the warming

The LT snowfall model runs have used a vertical structure to climate warming that is determined by the assumption of constant moist stability, which has consequences for λ_S. These consequences are examined by analyzing the output of another LT model simulation where a 1 °C warming that is uniform with elevation is assumed (Table 1, $climo\_\Delta Tunif$). Although uniform temperature change would result in a change in N_m, it is held constant for LT model dynamics to focus on effects of ML changes and CC scaling.

Table 1 reveals significant differences in the estimate of λ_S depending upon the vertical profile of warming that is assumed. The simulation where ΔT is a function of elevation (*climo_control*) has a λ_S value 3.3% $°C^{-1}$ larger in magnitude than when uniform warming is used ($climo\_\Delta Tunif$). This difference arises from differences in λ_{ML}. The uniform and structured warming cases have similar temperature and ML changes at mid-elevations (near 1.5 km) where the most snow accumulates, so similar amounts of snow are lost due to ML changes. However, in calculating λ the snowpack change is divided by the sea level (z=0) warming, which is smaller in the *climo_control* case, leading to a λ_{ML} of larger magnitude. λ_P is not similarly affected, since it is controlled by the same surface temperature change used in the λ calculation.

4.4 Melting-Level (ML) Model

The LT snowfall model considers a range of physical processes. To isolate those most fundamental for determining λ_S a simpler model, containing only minimal elements, is analyzed. This model just includes the distribution of topographic area with elevation and the climatological ML frequency distribution, and is referred to as the melting-level (ML) model. Comparing this model with the LT model shows that the relationship between the ML frequency distribution and the mountain hypsometry is the predominant control on λ_S.

4.4.1 Methods

The ML model is based on three major simplifying assumptions: (1) atmospheric soundings during storms are representative of steady-state conditions for the 12 hours that surround them; (2) during storms the precipitation rate is always the same constant and uniform value across the domain (i.e., there is no temporal or spatial variation in precipitation rate); and (3) the elevation at which a threshold temperature is reached in the sounding determines a uniform ML across the landscape.

The ML model has a similar degree of complexity as the geometric model of Casola et al. (2009). However, the ML model differs from Casola et al. (2009)'s model in that it requires no assumptions about the lapse rate, snow base elevation, or snow profile shape, since these all come directly from climatological observations and physical considerations.

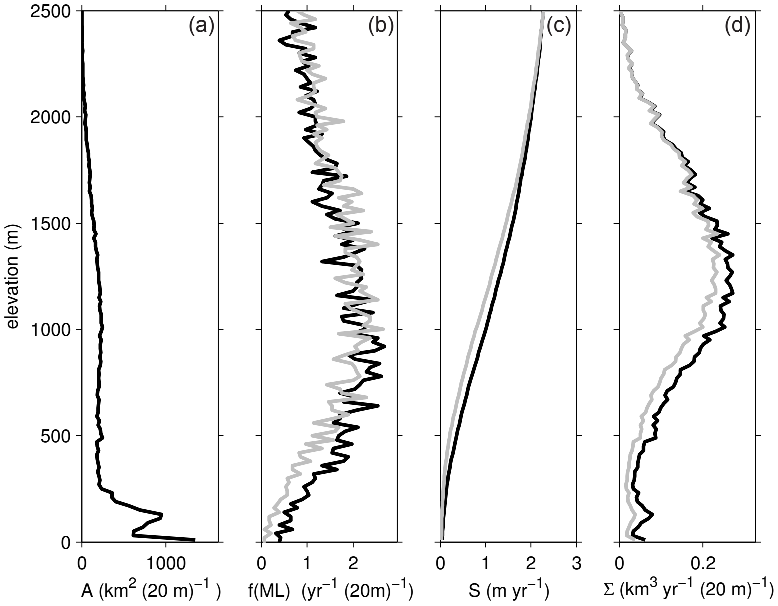

Figure 4.7: Profiles of ML model variables for the Puget Sound catchment (Figure 4.1) from the $climo\_\Delta Tunif$ run: (a) topographic area, $A(z)$, (b) ML frequency distribution, $f(ML; z)$, (c) average snow water accumulation $S(z)$, and (d) integrated snow water accumulation $\Sigma(z)$. Control simulation is shown in black, warmed simulation is in gray.

To formulate the ML model the terrain is first binned by elevation bands (of size Δz=20 m) to give the distribution of area with elevation, $A(z)$ (Figure 4.7a). The same

ML's used in the LT model simulations (including the displacement ΔML) are then used to determine the climatological frequency distribution of storm ML's, $f(ML; z)$, (Figure 4.7b). From $f(ML; z)$ and the assumption of constant and uniform precipitation (with value P_o) the profile of snowfall $S(z)$ can be found by summing over the climatological distribution of storm ML's, adding snowfall to all elevations above each ML. The corresponding expression for the climatological average snow accumulation, S, at each elevation, z_N, is:

$$S(z_N) = P_o \sum_{i=1}^{N} f(ML; z_i) \Delta z \Delta t, \tag{4.3}$$

where elevation bins are indexed with $i = 1$ at sea level, and Δt is the interval of time associated with each sounding (12 hrs). Figure 4.7c shows the resulting $S(z)$ profile attained assuming a P_o of 1 mm hr^{-1}. Multiplying $A(z)$ by $S(z)$ gives the total volume of accumulated snow water in each elevation band, $\Sigma(z)$ (Figure 4.7d).

The ML model assumes that, under climate warming, temperature increases are uniform (i.e., 1 °C at all elevations). In a warmed the model simply increases the precipitation intensity according to the CC scaling as set by the mean temperature at the sounding's lowest level (about 6.8% °C^{-1}). Profiles for the warmed climate are shown in Figure 4.7.

4.4.2 Results

Calculating λ_S for the ML model gives -16.3 % °C^{-1} (Table 1, *climo_*$\Delta Tunif$). Isolating the effects of ML changes, by holding precipitation constant, gives a λ_{ML} of -21.6 % °C^{-1}, while isolating the effect of changes in precipitation intensity gives a λ_P of 6.84 % °C^{-1} (Table 1, *climo_*$\Delta Tunif$). Note that these results do not depend on the value of P_o chosen since it cancels out in the fractional difference used to calculate the λ's. The ML model λ_S is within 2% °C^{-1} of the LT model value, and the models show a similar breakdown between λ_{ML} and λ_P (Table 1, *climo_*$\Delta Tunif$). Furthermore, in the ML model only 77% of the increased precipitation is realized as an increase in snowfall, similar to the 82% found for the LT model. An additional ML model simulation is also made using the low-level temperatures and ML's from the LT model runs where warming is a function of elevation, and the results from these simulations also agree well (Table 1, *climo_control*).

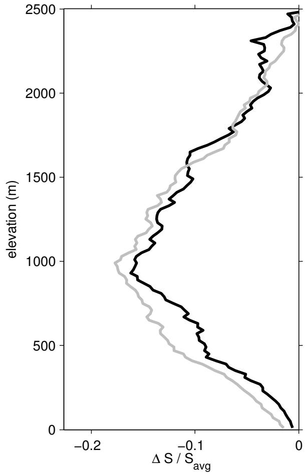

Figure 4.8: Profile of change in average snow water accumulation, $\Delta S(z)$, under climate warming from the ML model (grey) compared with LT model (black). To facilitate comparison the $\Delta S(z)$ values from each model are normalized by dividing by the average of $S(z)$ from 0-2500 m for that model.

The ML and LT models are compared in more detail by examining profiles of change in $S(z)$ under warming for the *climo_control* runs (Figure 4.8). The profiles reveal that the ML model is able to predict well the distribution of snow loss with elevation. This favorable comparison of the LT model and the very simple ML model suggests that the geometrical relationship between the ML distribution and the terrain — the only thing included in the ML model — dominates in setting the magnitude of λ_S. Spatial and temporal variations in orographic precipitation are responsible for the differences between the two models. While these variations have a quantitative impact on λ_S, they only make small modifications to the λ_S set by the elements included in the ML model.

4.5 Experiments: Controls on λ_S

Understanding how various aspects of both climate and topography control λ_S is key to understanding: past and future changes in snowpack, uncertainties in projections of mountain snowpack, and the differing responses of mountain climates of the world to climate changes. Controls on λ_S are investigated by resimulating the snow accumulation seasons (Oct.-Mar.) of water years 2006 and 2007 (hereafter acc0607) with the LT model, changing attributes of the incoming flow, model physics, and terrain. The control run for this period (Table 1, *exp_control*) uses the same configuration as *climo_control*, but produces a somewhat different λ_S, -15.6% $°\mathrm{C}^{-1}$, due to interannual variability (Table 1). While the following experiments reveal a range of ways in which climate and topography can affect λ_S, they also emphasize the importance of the relationship between mountain hypsometry and the ML climatology, since only in experiments where these are significantly altered (for instance by changing the mean temperature or the mountain height) is λ_S substantially changed.

4.5.1 Climatic controls on λ_S

Precipitation pattern

The importance of orographic precipitation patterns is quantified by making large changes to the precipitation patterns in the LT model runs. First the precipitation patterns are altered by changing the wind direction (*exp_wdir*50). The acc0607 period is resimulated with the LT snowfall model, rotating the wind direction by 50 degrees during each event for both the control and warmed case. This drastically different wind climatology changes the precipitation pattern and increases the orographic enhancement of precipitation (compare Figures 4.9a and 4.2b). The precipitation pattern is altered in a second experiment by varying the value of the microphysical time delay, τ (*exp_tau*850). The acc0607 period is resimulated with τ decreased to 850 s (compared to 1800 s from *exp_control*). Comparing Figures 4.9b and 4.2b shows large changes in precipitation pattern associated with decreasing τ, most notably increases in precipitation spatial variability and maxima.

In both of these experiments the precipitation changes substantially, but λ_S is only modestly affected (Table 1). Why do these substantial changes in the precipitation pattern fail to have a large impact on λ_S? The success of the geometric model of Casola et al. (2009) and the ML model (both essentially 1-dimensional) shows that the shape of the $S(z)$ profile is central in setting λ_S. For *exp_tau*850 the profile of precipitation with elevation is changed

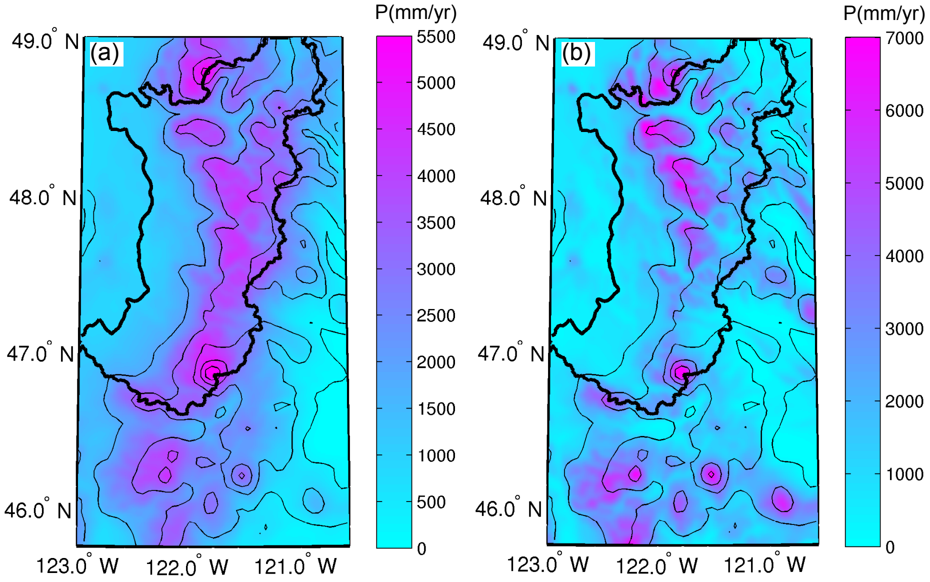
P(mm/yr)
5500
5000
4500
4000
3500
3000
2500
2000
1500
1000
500
0
(a)
49.0° N
48.0° N
47.0° N
46.0° N
123.0° W
122.0° W
121.0° W
P(mm/yr)
7000
6000
5000
4000
3000
2000
1000
0
(b)

Figure 4.9: LT model simulated precipitation patterns (mm yr^{-1}) for acc0607 period from runs with (a) more westerly wind direction ($exp\_\Delta wdir50$), and (b) decreased microphysical time delay ($exp\_\tau 850$). MM5 topography is contoured every 500 m.

very little (as shown in Figure 4.10a), and thus the snow profile (Figure 4.10b) and λ_S only changes modestly (Table 1). Larger changes to the precipitation and snow profiles occur for exp_wdir50 (Figure 4.10a-b), however these are still not enough to drastically change λ_S (Table1). Since these drastic changes in the precipitation pattern have only have small impacts on λ_S, it is unlikely that the LT model errors in precipitation (Figure 4.4a, the primary errors relative to SNOTEL observations) have large influences on the results of this study.

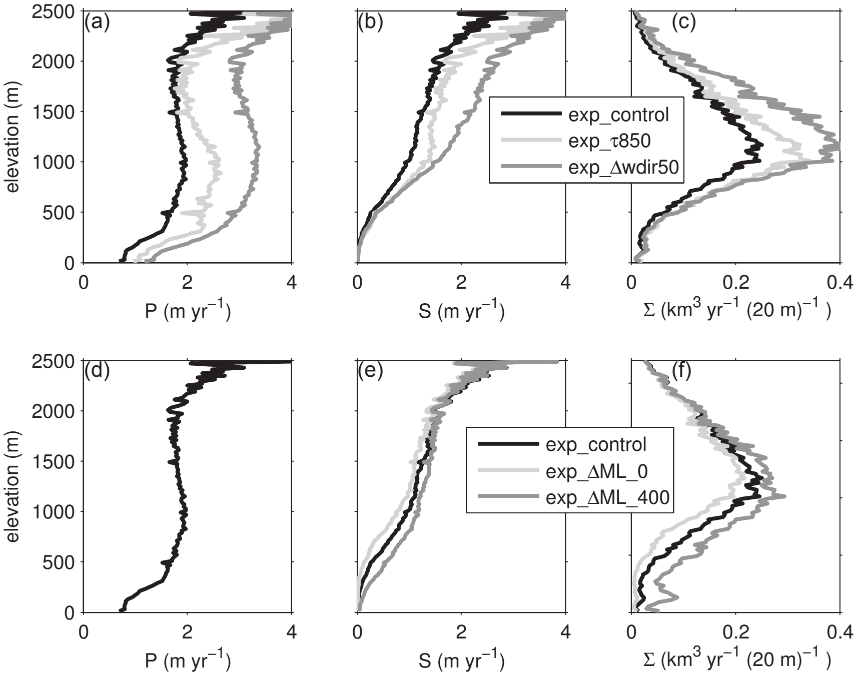

Figure 4.10: (a)-(c) Profiles of LT snowfall model $P(z)$, $S(z)$, and $\Sigma(z)$ for acc0607 period from: (black) *exp_control*, (light gray) *exp_*τ850 experiment, and (dark gray) Δ*_wdir*50 experiment. (d)-(f) same as for (a)-(c) but for: (black) *exp_control*, (light gray) *exp_*ΔML*_*0, and (dark gray) ΔML*_*400.

ML depression

The role of the distribution of snowfall, independent of the distribution of total precipitation is investigated by varying ΔML. Simulations are conducted where ΔML is changed to 0 or to -400 m, yielding λ_S values of -19.0 and -13.4% °C^{-1} respectively (Table 1, *exp_*ΔML*_*0 and *exp_*ΔML*_*400). These ML shifts have more impact than changes in precipitation patterns because they affect the base elevation of the $S(z)$ profile (Figure 4.10d-f). This implies that the apparent overprediction of lowland snow fraction (Figure 4.4c), roughly equivalent to an overprediction of $-\Delta ML$, may result in a modest underestimate of the magnitude of λ_S by the LT model.

Background Precipitation

The importance of the chosen value of background or synoptic precipitation, P_{bg}, is investigated through runs with P_{bg} set to zero and doubled (results shown in Table 1: exp_Pbg0 and exp_PbgX2). These reveal that λ_P decreases with increasing P_{bg}, causing λ_S to increase in magnitude. This results from the assumption that P_{bg} does not change with temperature. Since P_{bg} is constant with climate, larger values of P_{bg} relative to total precipitation lead to more modest fractional increases in precipitation, and larger fractional losses of snow. If, alternatively, P_{bg} is made to scale with the increasing atmospheric moisture (as determined by the CC scaling with surface temperatures; Table 1, exp_PbgCC), λ_P increases to 7.14% $^\circ\mathrm{C}^{-1}$, roughly the value for P_{bg}=0 case.

Mean temperature

The importance of mean temperature is quantified by estimating the λ_S that the Cascades would have were it subject to substantially warmer or colder climate. This is done with a series of simulations, with both models, of the acc0607 period where the incoming flow is warmed or cooled by various amounts while maintaining constant N_m. The sounding temperatures at 1.5 km are changed by ± 0.5, 1, 2, 4, 6, and 10 °C, with corresponding sea level changes of ± 0.41, 0.83, 1.66, 3.31, 4.98, and 8.33 °C. The output from these simulations is used to calculate λ_S values by taking centered fractional differences of $\Sigma_t(T)$. The results in Figure 4.11 show the range of sensitivities that would be expected for a Cascade-like mountain range in warmer and cooler climates. λ_S is about doubled in magnitude for a 4 °C warmer climate, and reduced to zero for a 7 °C cooler climate. Figure 4.11 also shows that the basic temperature dependence of λ_S is well captured by the ML model (except at much cooler temperatures where the treatment of non-orographic lowland snow causes large differences), as it is mainly determined by where the distribution of ML's lies on the mountain.

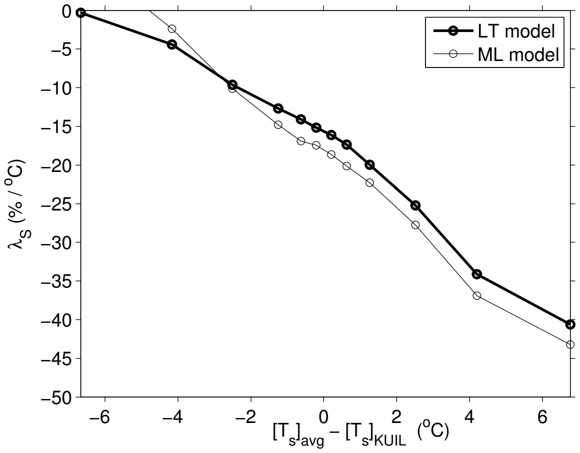

Figure 4.11: Values of λ_S estimated as a function of average sea level temperature during storms. Temperatures are relative to current KUIL climatology ($[T_s]_{avg} - [T_s]_{KUIL}$, with $[T_s]_{KUIL} = 8.5$ °C). Bold line is for LT model and thin line is for ML model.

4.5.2 Topgraphic controls on λ_S

Basin-to-basin variability

Differences in λ_S between the major catchments of the study region (distinguished in Figure 4.1) are considered. Figure 4.12 shows the values of λ_S estimated by the LT snowfall model plotted against the values estimated by the ML model. For these basins λ_S ranges from -14 to -32% $°C^{-1}$, revealing that different portions of the Cascades, subject to the same regional climate but different topography, exhibit considerable variability in their response to warming. This is due largely to the differing hypsometries of these basins relative to the ML distribution, evidenced by the ML model's ability to capture variations in λ_S. Note that basin-to-basin variability is quite large in comparison to the effects of most climate factors (e.g., the scaling of precipitation, vertical structure of the warming, ΔML).

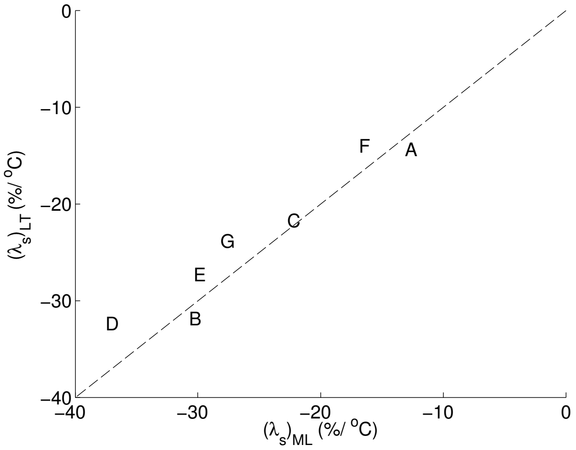

Figure 4.12: Sensitivity of snowfall to warming predicted by the LT snowfall model ($(\lambda_S)_{LT}$) versus sensitivity from the ML ($(\lambda_S)_{ML}$) for various catchments draining into Puget Sound (indicated with letters in Figure 4.1). The dashed line has a slope of unity for comparison. Note the large basin to basin variability of λ_S exhibited by both models.

Mountain height and width

To investigate the importance of mountain height the acc0607 period is resimulated with the topographic height scaled by a uniform factor of 75 or 125%. As the scale is reduced there is a decrease in orographic precipitation due to reduced lifting of the incoming flow, and also a decrease in snow vs. rain due to an increased fraction of the terrain residing below the storm ML's (Table 1: *exp_z*75% and *exp_z*125%). Unsurprisingly, the temperature sensitivity decreases in magnitude as mountain height is increased and more of the mountain is subject to cold temperatures, with λ_S going from -23.8 to -10.8% °C^{-1}. This is largely due to changes in λ_{ML}, which goes from -27.8 to -15.9% °C^{-1}. With the increased mountain height λ_P also changes, increasing from 5.21 to 5.79% °C^{-1}, and the fraction of the precipitation increase realized as snow also increases, from 77% to 88%.

The importance of mountain width is investigated by resimulating the acc0607 period using the LT model with the east-west dimensions of the model grid cells scaled by 75 or 125%. As the mountain narrows the total precipitation integrated over the windward slope decreases somewhat (due to more spillover and lee-side evaporation), but the average precipitation at each elevation increases since the rain and snowfall is distributed over a smaller area. However, these changes do little to alter the shape of the S(z) profile (not shown), and as a result barely affect the values of λ_S (Table 1, *exp_x*75% and *exp_x*125%).

4.5.3 Response to warming in excess of 1 °C

So far this study has only dealt with the changes in snowpack associated with a 1 °C warming. Results have been expressed as a percentage change in snow accumulation per degree of warming, units which imply the fractional loss of snowpack scales linearly with the amount of warming, but this may not be the case. To investigate how the magnitude of the climate warming determines the loss of snowfall, the experiments described in section 4.5.1 are used to calculate fractional changes in snow accumulation (relative to the control climate) as a function of sea-level temperature change, ΔT_s (Figure 4.13).

This analysis reveals that for surface warming up to about 4 °C the fractional loss of snow is an approximately linear function of ΔT_s, which can be estimated well from the ΔT=1 °C case (see fine-dashed line in Figure 4.13). Also shown is how the change in snowfall due to precipitation changes or ML changes alone depends on the amount of warming (gray lines in Figure 4.13). This demonstrates that the relative importance of precipitation and ML changes is a strong function of the amount of warming. Figure 4.13 also shows that for large amounts of warming, the loss of accumulation area due to ML changes dominates, and precipitation changes have a negligible effect. This is emphasized by comparison of the total loss in accumulation with the loss predicted by summing the ML and precipitation related changes (solid and dashed black lines in Figure 4.13). For modest amounts of warming these two values are similar since much of the increase in precipitation is realized as an increase in snowfall. But, for large amounts of warming the total loss of snowfall is much greater than the sum of the two effects, since much of the increase in precipitation occurs in areas where snow has been turned to rain as ML's rise. For surface warming in excess of about 2 °C, less than 50% of the precipitation increase adds to the snowpack, and for 5 °C this is reduced to less than 20%. Therefore, under substantial warming the loss of snow accumulation area provides a profound limit on how much precipitation increases may act to preserve the snowpack.

Figure 4.13 also shows the range and "best guess" of wintertime warming projected for the Northwestern US from the IPCC AR4 GCMs for the 2080's relative to the 1980's (Climate Impacts Group, 2009). Taking into account this range of projections the LT snowfall model suggests a very large uncertainty in the amount snowfall loss by late in the century: 20-75%. This range comes both from uncertainties in greenhouse gas emissions and how those emissions relate to regional climate warming. For the LT snowfall model these uncertainties appear much larger than those associated with the choice of methods and model parameters used to relate a given warming to a change in snow accumulation (note the range of λ_S values in Table 1). The loss of snowfall is substantial even at 3 °C, in the middle of the range of possible warmings, despite an almost 20 % increase in precipitation, since much of the precipitation increase is lost to runoff.

4.5.4 Response to circulation changes

The LT snowfall model may also be used to assess the importance of climate changes other than warming. It has been suggested that circulation changes associated with global warming may cause winds to impinge against the Cascades at a different angle, resulting in altered orographic enhancement of precipitation (Salathé et al., 2008; Climate Impacts Group, 2009). The importance of such circulation changes is roughly quantified by rerunning the LT snowfall model assuming that, in addition to warming, climate change includes a shift in the wind direction during storms. An experiment is conducted where the acc0607 period is resimulated with the wind directions shifted clockwise by 12° (an amount equal to twice the standard deviation of the annual mean wind direction in the 1-2 km layer of the KUIL storm soundings). This shift makes the winds more perpendicular to the Cascades and increases orographic enhancement. The increase in orographic precipitation due to the wind shift almost perfectly cancels out the loss of snow due to warming, resulting in a decrease in snowfall of only -0.5% for 1°C of surface warming (instead of -15.6% in the control case). Note, this method neglects the effect that circulation changes would have on the temperature and moisture characteristics of the incoming flow. More westerly winds would presumably be colder and drier. Thus, these results likely overestimate the impact of circulation changes, perhaps presenting an effective upper limit. If instead the wind directions are rotated counter-clockwise by 12°, there is reduced orographic enhancement and an increased snowfall loss of -29.9%. These results suggest that if regional climate change includes substantial shifts in circulation patterns, then the associated changes in orographic enhancement may be important for snowpack, possibly more important than precipitation changes directly due to warming.

4.6 Conclusions

Controls on the sensitivity of mountain snowpack accumulation to climate warming, λ_S, have been examined using experiments with a pair of idealized, physically based models: an idealized orographic snowfall model (the LT snowfall model), and a very simple melting-level (ML) model. Experiments and comparisons between the two models show that the relationship between the climatological distribution of storm ML's and the mountain hypsometry is the strong underlying determinant of λ_S.

Accounting for ML changes alone, the more sophisticated of these two models gives a temperature sensitivity of -19.4 or -22.6% $^\circ\mathrm{C}^{-1}$ of warming for the windward slopes of the Washington Cascades, depending on the vertical structure of the warming. For modest amounts of warming, increases in orographic precipitation associated with increasing atmospheric moisture may play an important role in moderating the loss of snowfall, reducing the magnitude of the Cascades sensitivity to -14.8 or -18.1 % $^\circ\mathrm{C}^{-1}$. However, for the Cascades, and presumably other temperate mountains of moderate height, once warming exceeds a few degrees physically plausible increases in orographic precipitation are unable to compete with the loss of accumulation area and have minimal effect on λ_S. Shifts in circulation patterns may also play an important role. Changes in wind direction have large impacts on the intensity of orographic precipitation, and accordingly may act to moderate or exacerbate the loss of mountain snowpack under climate change.

Since λ_S is determined mainly from the terrain and ML distribution, simple models such as the ML model and Casola et al. (2009)'s geometrical model can be quite effective tools for estimating λ_S. The ML model is computationally cheap, requires minimum input data, and compares favorably with more complex models. It thus may be useful for resource managers desiring ballpark estimates of the vulnerability of specific mountainous watersheds to climate warming. It is more generally applicable than the geometrical model of Casola et al. (2009) since it does not require assumptions about the base elevation of the snowpack, the shape of the snow profile, or the lapse rate.

By focusing on identifying the relative importance of various factors for determing λ_S, this research offers information about what models must capture to make a realistic projections of the impacts of warming on mountain snowpack. For instance, large differences in the climatological pattern of orographic precipitation were found to have only modest effects on λ_S. Thus, biases in precipitation patterns in regional climate models may not introduce large errors in projections of fractional snowpack change. In contrast, the distribution of ML's relative to the basin hypsometry is of fundamental importance. Accordingly, differences in the hypsometry of adjacent catchments in the same mountain range may lead to substantial differences in λ_S, and errors in characterizing ML's may have sizeable effects on estimates of λ_S.

Many results of this study should be broadly applicable to other mid- and high-latitude mountain ranges around the world that receive much of their precipitation during moist, stable, and relatively unblocked flow. Experiments where mountain shape and mean temperature are varied give a sense of how results may be different for mountains with different terrain geometry or mean climate. Despite these differences, the importance of hypsometry and ML climatology, and the decreasing importance of precipitation changes with increasing warming should hold true for many other regions.

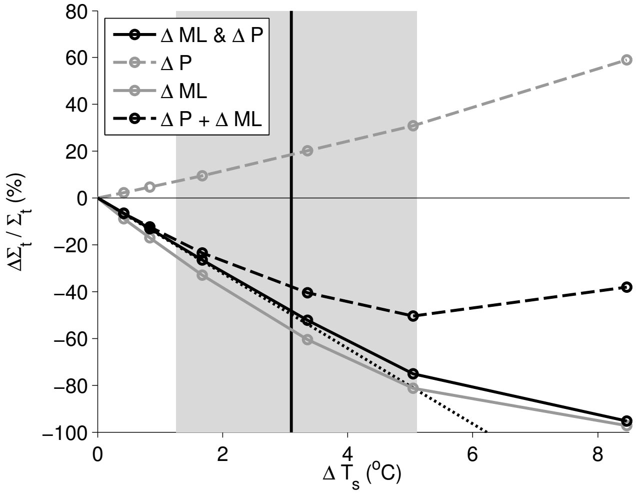

Figure 4.13: Percentage change in snow accumulation as a function of surface warming as estimated by LT snowfall model (black solid line, with circles showing individual model runs). Gray solid line and dashed lines show the changes that would occur if only ML's or precipitation intensity were to change with warming. Black dashed line shows the sum of the two gray lines. The fine dashed line show the linear extrapolation of the λ_S values calculated from the $\Delta T = 1$ °C case. The shaded region shows the range of GCM projected warmings (for 2080's minus 1980's) for the Pacific Northwest region (Climate Impacts Group, 2009). Projections come from the IPCC AR4 models with emissions scenario A1B. Vertical line shows the best GCM estimate attained from a weighted average of the AR4 models (Climate Impacts Group, 2009).

Chapter 5

MESOSCALE CONTROLS ON THE CLIMATOLOGY OF THE MOUNTAINSIDE SNOW LINE

5.1 Introduction and background

One of the most fundamental aspects of mountain weather and climate is the snow line, loosely the boundary between low elevation rainfall and high elevation snowfall. The precise location that the snow line intersects the topography during storms is central in determining the navigability of mountain roadways and railways, the risk of landslides and avalanches, and the quality of mountain recreation. The snow line is particularly important for determining the effect of storms on mountain streamflow, since snow may accumulate on the ground whereas rainfall can produce runoff much more quickly, potentially leading to flooding (White et al., 2002; Hamlet and Lettenmaier, 2007; Lundquist et al., 2008). The distribution of snow line elevations during storms also determines the seasonal accumulation of mountain snowpack (e.g., Minder, 2010). For many societies mountain snowpack is a crucial water resource (e.g., Barnett et al., 2005), and its sensitivity to climate is responsible for some of the largest impacts of climate variability and climate change (e.g., Climate Impacts Group, 2009).

For both storm runoff and climatological snowpack accumulation, changes of a few hundred meters in the snow line elevation have major impacts. For example, White et al. (2002) modeled that a rise in the snow line of about 2000 ft (610 m) during a storm would lead to a tripling of the runoff for three mountainous river basins in northern California. Minder (2010) modeled that the approximately 200 m rise in the average snow line elevation associated with 1°C of climate warming acts to reduce annual snowpack accumulation in the western Cascade mountains by about 15–18%.

Despite these large sensitivities to modest changes in snow line, forecasters and researchers often rely on simple empirical relationships to estimate mountain snow lines, relationships that do not take into account the myriad physical processes that control precipitation formation, phase change, and fallout over mountains. For instance, hydrological models often estimate the phase of precipitation based on surface temperature relationships, ignoring the impact of atmospheric processes aloft (e.g., Anderson, 1976; Westrick and Mass, 2001; Hamlet et al., 2005). Furthermore, climate studies sometimes use vertical temperature profiles from coarse resolution models— models that very poorly resolve mountainous topography— to infer trends in mountain snow lines and resulting climate impacts on systems such as mountain glaciers and snowpack (e.g., Diaz et al., 2003; Arendt et al., 2009). These relatively crude methodologies are use in part because the behavior of mountain snow lines and their physical controls are poorly understood. Motivated by the central role of the snow line in mountain weather and climate, this study aims to sharpen this understanding.

5.1.1 Terminology

In understanding the snow line, a key variable is the *0 °C isotherm elevation*, Z_{0C}, since this is where frozen precipitation starts to melt as it falls. In this study Z_{0C} is defined as the lowest elevation where the atmospheric temperature profile, $T(z)$, crosses 0°C (shown schematically in Figure 5.1a). The region below Z_{0C} where melting is occurring is referred to as the *melting layer*.

The snow line is not a discrete boundary, since both frozen, partially melted, and liquid precipitation may coexist, thus it may be defined in various ways. This study focuses on the *snow line elevation*, Z_S, defined as the elevation where 50% of the frozen hydrometeor mass (quantified by the mixing ratio of snow and graupel: (q_s+q_g)) falling through Z_{0C} has been lost, presumably by melting into rain (shown schematically in figure 5.1b). Another possible measure of the snow-rain transition is the elevation at which half of the vertical flux of hydrometeors (i.e., the precipitation rate) is frozen and half is liquid. This *rain-snow line elevation*, Z_{RS}, differs from Z_S in that in considers both frozen and liquid precipitation and in that it considers hydrometeor fluxes instead of mixing ratios. For simplicity this study will focus on Z_S, but Z_{RS} will also be briefly considered to show how the results depend on

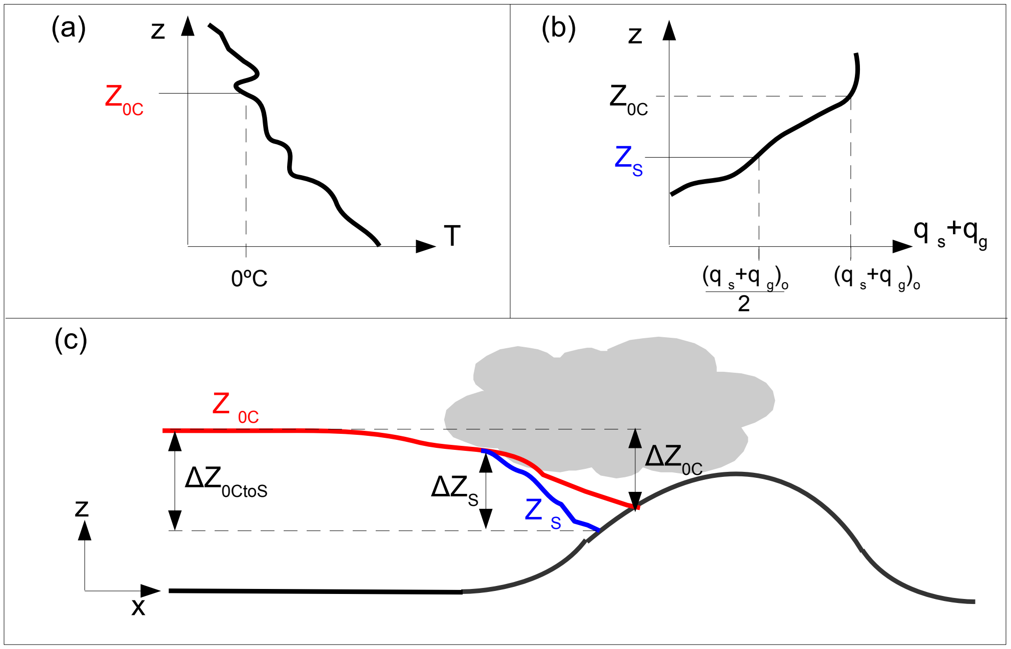

Figure 5.1: Schematic illustration of how the main quantities considered in this study are defined. (a) Determination of Z_{0C} from a temperature profile, $T(z)$. (b) Determination of Z_S from a profile of frozen hydrometeor mixing ratio , $(q_s + q_g)(z)$. (c) Determination of ΔZ_{0C}, ΔZ_S, and ΔZ_{0CtoS} from upwind and mountainside values of Z_{0C} and Z_S. Dashed lines are drawn at the elevation of the upstream Z_{0C} and the mountainside Z_S.

the choice of metric.

Directly measuring Z_S aloft is challenging and requires missions with specially equipped aircraft. Consequently, most observations of Z_S are indirect in nature, relying on remote measurements of equivalent radar reflectivity factor. During stratiform precipitation, radar reflectivities often show a strong enhancement in the region of melting. This is referred to as the radar *bright band*, BB, and occurs as a result of aggregation of hydrometeors, changes in complex index of refraction, and changes in fall speed that occur during melting (e.g., Houze, 1993). The BB is a region of finite thickness that typically begins just below the elevation of Z_{0C} and roughly coincides with the melting layer. The vertical thickness of the BB is observed to increase with increasing precipitation rate (Klaassen, 1988; Fabry and Zawadzki, 1995). The *bright band elevation*, Z_{BB}, is be defined as the elevation in this region with maximum reflectivity (following, e.g., White et al., 2002). Z_{BB} is typically the best remotely sensed proxy for Z_S available.

The focus of this study is on how Z_{0C} and Z_S are modified over the windward slopes of a mountain. This is quantified by comparing Z_{0C} and Z_S where they intersect the mountain to upstream values where orographic influences are modest or absent. The orographic influence on temperatures are quantified as ΔZ_{0C}, the displacement between the mountainside Z_{0C} and its upwind value (figure 5.1c). Likewise, the local orographic influence on the snow line is quantified as ΔZ_S, the displacement between the mountainside Z_S and its upwind value (figure 5.1c). Understanding ΔZ_S is relevant to the interpretation of radar datasets that measure Z_{BB} upwind of and over mountains (e.g., White et al., 2002; Lundquist et al., 2008). Since orographic influences on Z_{0C} may extend farther upwind than the precipitation region, the full orographic influence on the snow line is quantified as ΔZ_{0CtoS}, the displacement between the mountainside Z_S and the upwind Z_{0C} (figure 5.1c). Understanding the behavior of ΔZ_{0CtoS} is particularly important for relating upstream temperature profiles from soundings and global models to mountain snow lines (e.g., Diaz et al., 2003; Arendt et al., 2009; Minder, 2010).

5.1.2 Previous work

A comprehensive observational analysis of Z_S over mountains demands detailed mapping of the dynamic, thermodynamic, and microphysical fields above mountain slopes. Some of the earliest work to bring together and analyze such a dataset was presented by Marwitz (1983, 1987). These studies examined several orographic storms over the northern Sierra Nevada mountains using ground-based C-band radar, special soundings, and *in situ* aircraft data. Over the windward slopes during stratiform storms Z_{0C} was found to descend by at least 400 m (relative to the upstream) (Figure 5.2a, Marwitz, 1987), and the radar BB was found to increase substantially in depth as it approached the mountain (becoming as thick as 1 km) (Figure 5.2b, Marwitz, 1983).

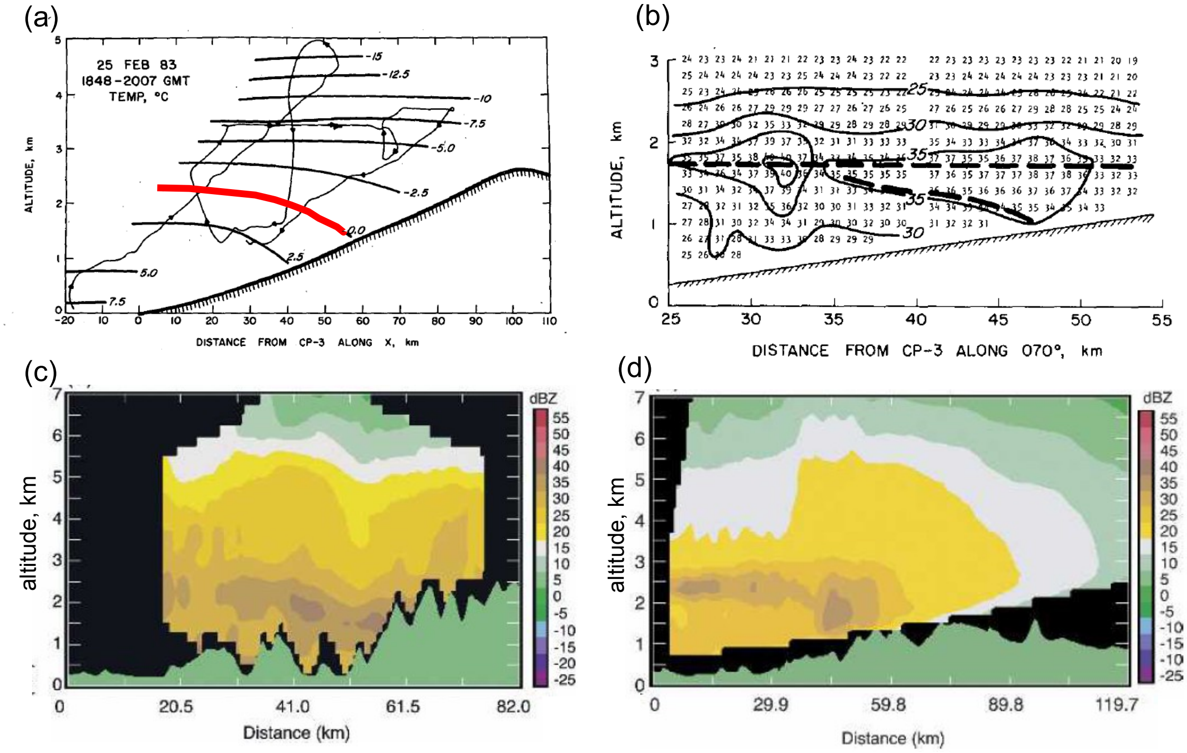

Figure 5.2: Figures from previous observational studies showing drop in Z_{0C} and Z_{BB}. (a) Isotherms (^{o}C, with Z_{0C} in red) analyzed from aircraft *in situ* measurements over the northern Sierra Nevada on 25 Feb 1983 (adapted from Marwitz, 1987). (b) Equivalent radar reflectivity (dBZ_e) from RHI scans with the NOAA CP-3 radar over the northern Sierra Nevada on 15 Feb 1980 (from Marwitz, 1983). (c) Reflectivity (dBZ_e) from P-3 airborne radar analysis over the Lago Maggiore region of the Italian Alps on 21 Oct 1999 (from Medina et al., 2005). (d) Reflectivity (dBZ_e) from RHI scans with the S-Pol radar over the Oregon Cascades on 28 Nov 2001 (from Medina et al., 2005). In all panels winds are impinging from the left.

The features in the temperature and reflectivity fields described by Marwitz (1983, 1987) are not unique to the specific storms he observed over the Sierra Nevada. This was made evident by Medina et al. (2005), who examined ground-based and airborne radar data from three stratiform precipitation events: one over the Alps (from the MAP field campaign) and two over the Oregon Cascades (from the IMPROVE-2 campaign). As shown Figure 5.2c-d, they found a similar drop in Z_{BB} of several hundred meters over the windward slopes of both of these ranges. Interestingly, the form of this drop was shown to be variable: over the Cascades the BB expanded in depth from the bottom (Figure 5.2d), whereas over the Alps both the upper and lower edge of the BB sloped downwards towards the crest of the range (Figure 5.2c).

The mesoscale modification of Z_S also appears consistently in observations of many storms, distinguishing it as a climatological feature. Lundquist et al. (2008) and Kingsmill et al. (2008) used several years of observations to characterize the spatial variability of Z_S and Z_{0C} in the same region of the northern Sierra Nevada as studied by Marwitz (1983, 1987). Lundquist et al. (2008) used 5 years of hourly radar profiler measurements to show that on average Z_{BB} drops by 73 m between a coastal site and a site at the base of the Sierra (although Z_{BB} may drop even farther between the radar and the windward slopes). Kingsmill et al. (2008) used a transect of profilers from the HMT field program (e.g., Ralph et al., 2005) to track the BB across the entire windward slope of the Sierra for three years. They found that Z_{BB} above the windward slopes is on average ∼200 m lower than upstream of the terrain. Furthermore, large storm-to-storm variability was observed: the windward Z_{BB} was found to range from 1 km lower to 200 m higher than the upstream Z_{BB} (Kingsmill et al., 2008).

5.1.3 Possible mechanisms

A number of physical mechanisms have been proposed to explain the mesoscale structure of Z_S observed over mountains.

- The first of these proposed mechanisms relies upon cooling of the air by the melting of orographically enhanced precipitation, and is based on concepts developed from studies of stratiform precipitation over flat terrain. In a classic study Findeisen (1940) observed a number of soundings through stratiform precipitation with near-freezing isothermal layers, leading him to propose a conceptual model for the profile of temperature in the melting layer: the upper portion of the melting layer is cooled to near-freezing by the uptake of latent heat during melting; then this localized cooling leads to an unstable stratification, which in turn induces convective overturning and a deepening of the layer of cooled air and melting. Subsequent studies elaborated greatly on Findeisen (1940)'s work. For instance, Stewart et al. (1984) examined *in situ* aircraft data from the melting layer of stratiform clouds and found near-isothermal 0°C layers ~200 m thick atop the melting layer and the radar BB, with unstable stratification below. Simple analytic models have been formulated— by considering the energy balance and convective adjustment of a vertical column— and used to understand how the depth of the 0°C isothermal layer increases with time and precipitation rate (Lin and Stewart, 1986; Unterstrasser and Zängl, 2006). The increase in 0°C layer thickness with precipitation rate has been cited as a cause of the observed increase in BB thickness with precipitation rate (Klaassen, 1988).

During studies of orographic storms over the Sierra, Marwitz (1983, 1987) observed soundings with deep near-isothermal layers at near-freezing temperatures. He cited this as evidence that the drop in Z_{BB} (and Z_S) over the windward slope is due to the latent cooling of air by the melting of orographically enhanced precipitation (hereafter LCpmelt); he argued that enhanced precipitation rates over the mountain slopes lead to more cooling, deeper 0°C layers, and lower Z_S, than in the air upwind. Modeling studies have also cited LCpmelt as important in determing the mesoscale structure of Z_S and Z_{0C} during stable flow over topography. Focusing on a single case, Wei and Marwitz (1996) conducted 2D simulations of an orographic blizzard over the Colorado Front Range. They showed that, in the model, substantial cooling of air over the windward slopes due to LCpmelt lead to a several hundred meter drop in Z_{0C} and the development of a mesoscale front. Also, Colle (2004) showed a drop in Z_S in a number of his simulations of flow over 2D ridges. He attributed this to LCpmelt, but did not characterize the behavior in any detail.

- Another hypothesis, not directly discussed in previous work, is that a large portion of the drop in Z_S can be explained by variations in the distance over which frozen hydrometeors melt. Since melting snowflakes of different sizes fall and melt at different rates, the distance that a melting snowflake travels below Z_{0C} before melting is a function of the snowflake size (as well as relative humidity, snow density, and atmospheric lapse rate) (Matsuo and Sasyo, 1981; Mitra et al., 1990). For example, Mitra et al. (1990) modeled that a snowflake 10 mm in diameter would descend about 100 m farther below Z_{0C} before melting than a 5 mm snowflake. Since higher precipitation rates are associated with snowflakes of larger sizes, this implies thicker melting layers (and radar BB's) for higher precipitation rates, as is observed (e.g., Klaassen, 1988; Fabry and Zawadzki, 1995).

  In the upwind side of the orographic cloud the size distribution of the frozen hydrometeors is likely to be weighted towards small diameter snowflakes, which fall slowly and melt relatively quickly. Thus, Z_S should be expected to lie near Z_{0C}. Downwind, closer to the windward slope, where vertical motion is stronger and cloud water is enhanced, snowflakes grow larger and rime into graupel. These larger snowflakes and graupel will fall more quickly and take longer to melt. Therefore, frozen hydrometeors should descend farther before melting completely, and Z_S should lie farther below Z_{0C} than in the upstream. This should be true even if the temperature profile is the same throughout the orographic cloud (i.e., even in the absence of LCpmelt).

- As noted by Medina et al. (2005) and Kingsmill et al. (2008), the process of adiabatic cooling, which occurs as parcels are forced to rise over a topographic barrier and expand, could be important. If air parcels passing over the mountainside have risen and cooled with respect to the air at the same elevation upwind, Z_{0C} and Z_S will drop.

- When impinging winds are weak relative to the atmospheric stratification and mountain height, the flow upwind of a mountain can become blocked and stagnate. If the blocked region consists of preexisting cold air that is colder that the incoming flow, this could result in a lowering of Z_{0C} and Z_S (e.g., Bousquet and Smull, 2003; Medina et al., 2005).

- Other more local factors can play a major role in determining Z_S at specific mountain locations. Steenburgh et al. (1997) showed that cold continental air can be channeled through passes in the Cascade Mountains by easterly winds, in opposition to the synoptic scale flow, resulting in a localized lowering of Z_{0C} and Z_S. Other studies have shown how the geometry of mountain valleys can amplify the tendency for LCpmelt to lower Z_S (e.g., Steinacker, 1983; Unterstrasser and Zängl, 2006).

5.1.4 Questions

As described above, previous research has made it clear that mesoscale processes over the windward slopes of mountain ranges regularly act to strongly modify Z_S relative to the upstream. On average this results in a drop of a few hundred meters in Z_S, but this behavior can be quite variable storm-to-storm. Furthermore, while a number of physical mechanisms have been suggested, no study has yet considered these mechanisms together and in depth, assessed their relative importance, examined their interactions, or used them to explain the storm-to-storm variability observed in the climatology.

This study uses a numerical model of mountain airflow and precipitation combined with theory to address the following:

1. How do various physical processes (e.g., adiabatic cooling from orographic lifting, diabatic cooling from melting precipitation, variations in hydrometeor melting distance) interact to determine Z_S on a mountainside?

2. How robust are predictions of Z_S to the choice of model configuration?

3. How do variations in upstream conditions cause the mesoscale structure of Z_S to vary storm-to-storm and with climate?

4. How do differences in topographic form cause the mesoscale structure of Z_S to vary between different mountains?

For simplicity this study focuses on mechanisms responsible for determing Z_S averaged along the length of a mountain range. Thus, local effects associated with valleys and mountain passes are disregarded.

5.2 Numerical Model

To represent the various dynamic, thermodynamic, and microphysical processes influencing Z_S requires a full mesoscale numerical weather prediction model capable of simulating all these processes and their interactions. Accordingly, the Weather Research and Forecasting (WRF) model (version 3.0.1, Skamarock et al., 2008) is employed to conduct experiments. Since these experiments are focused on isolating and understanding the physical mechanisms that control Z_S (as opposed to simulating Z_S for a specific storm) the model is used in a semi-idealized configuration, with simplified topography and incoming flow characteristics (as in studies such as, Epifanio and Durran, 2001; Jiang, 2003; Colle, 2004; Kirshbaum and Smith, 2008; Galewsky, 2008). Including only the minimum components necessary to capture the gross behavior or Z_S allows for clear diagnosis of important processes. The importance of additional layers of complexity is assessed by adding them incrementally.

The experiments simulate steady, stably-stratified, near-saturated, non-hydrostatic airflow and precipitation over a smooth mountain barrier. The simulations are initialzed with a horizontally uniform atmospheric profile. In the troposphere the temperature profile is constructed by prescribing a value for the temperature at $z = 0$, T_s, and then iteratively solving for temperatures at higher levels, using the methods outlined in Miglietta and Rotunno (2005, 2006). A uniform value of moist stability, N_m, is prescribed, and hydrostatic balance is imposed. The definition of N_m used comes from Lalas and Einaudi (1973) and Durran and Klemp (1982):

$$N_m^2 = \frac{g}{T}(\Gamma_m - \Gamma)(1 + \frac{L_v q_{vs}}{R_d T}) - \frac{g}{1 + q_w}\frac{dq_w}{dz}, \tag{5.1}$$

where T is temperature, Γ is the environmental lapse rate $(-\frac{dT}{dz})$, Γ_m is the moist-adiabatic lapse rate, L_v is the latent heat of vaporization for water, R_d is the ideal gas constant for dry air, q_{vs} is the saturated water vapor mixing ratio, q_w is the total water mixing ratio ($q_{vs} + q_L$, where q_L is the condensed water mixing ratio), and g is the acceleration due to gravity. A uniform relative humidity, RH is prescribed throughout the troposphere (with respect to ice for temperatures <0°C). The sounding has a tropopause at 8 km, above which is a stratosphere where RH is reduced to 20% and a dry stability, N, of 0.02 s^{-1} is prescribed.

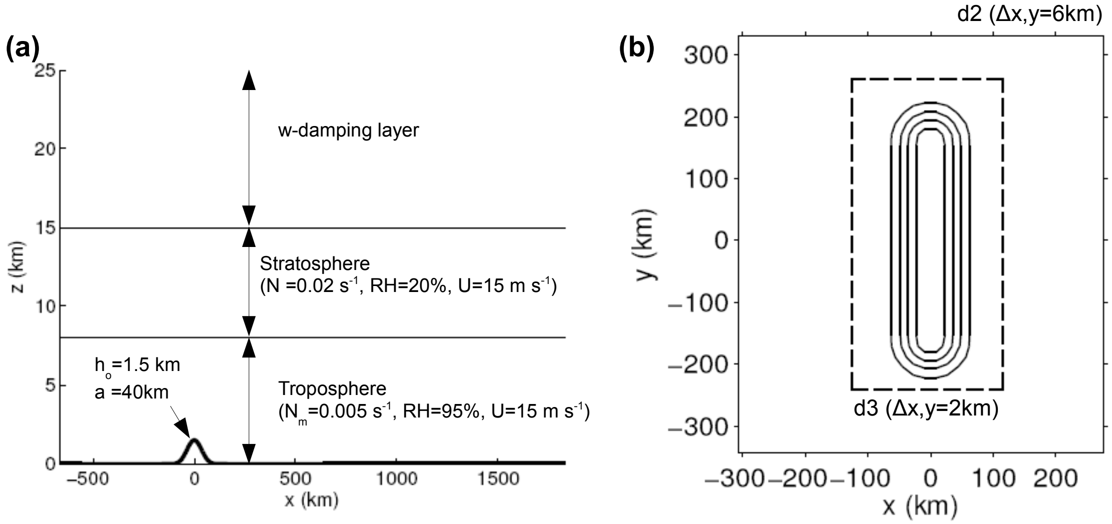
(a)
w-damping layer
Stratosphere
(N =0.02 s-1, RH=20%, U=15 m s-1)
Troposphere
(Nm=0.005 s-1, RH=95%, U=15 m s-1)
ho=1.5 km
a =40km
z (km)
25
20
15
10
5
0
-500
0
500
1000
1500
x (km)
(b)
d2 (Δx,y=6km)
d3 (Δx,y=2km)
y (km)
300
200
100
0
−100
−200
−300
−300−200−100 0 100 200
x (km)

Figure 5.3: Domains for the WRF simulations: (a) 2D simulation domain showing the terrain profile with a bold line. The location of the troposphere, stratosphere, and damping layer are denoted, as are the initial atmospheric conditions for the control simulation; (b) 3D simulation domains showing the inner two of three nested domains (d2-d3) and their horizontal grid spacing ($\Delta x, y$). The terrain elevation for the 3D control simulation is contoured every 300 m.

A first set of experiments are quasi-2D, and the terrain takes the form of a ridge that is infinitely long in the cross-wind (y) dimension and has a profile described by:

$$h(x,y) = \begin{cases} \frac{h_m}{16}[1+\cos(\pi r)]^4, & \text{if } |r| \leq 1; \\ 0, & \text{otherwise,} \end{cases} \tag{5.2}$$

where

$$r^2 = \left(\frac{x}{4a}\right)^2. \tag{5.3}$$

A mountain height, h_m, of 1.5 km and a half-width, a, of 40 km are used for most simulations, to create a terrain profile with dimensions roughly similar to the Cascade mountains (figure 5.3a). Additional fully 3D simulations are conducted where the terrain is instead described by equation 5.2 and:

$$r^2 = \begin{cases} \left(\frac{x}{4a}\right)^2 + \left(\frac{|y|-(\beta-1)a}{4a}\right)^2, & \text{if } |y| > (\beta-1)a; \\ \left(\frac{x}{4a}\right)^2, & \text{otherwise.} \end{cases} \tag{5.4}$$

A horizontal aspect ratio, β, of 5 is used in the 3D simulations.

The effects of the Earth's rotation are included in the simulations by applying the Coriolis force to the perturbations from the initial wind profile, which is assumed to be in geostrophic balance with a background pressure gradient. This is equivalent to subtracting a geostrophically balanced reference state from the governing equations, and follows Colle (2004) and Kirshbaum and Smith (2008). The f-plane approximation is made, with f=10^{-4} s^{-1}.

Third order Runge-Kutta time stepping is used, with fifth order horizontal and third order vertical advection. The boundary conditions are open in the x-direction and periodic in the y-direction for both the 2D and 3D simulations. The upper boundary condition is a constant pressure surface, with the vertical velocity damping layer described by Klemp et al. (2008) applied over the top 10 km to prevent the reflection of gravity waves off the model top (Figure 5.3a). The bottom boundary condition is free-slip. The absence of surface friction simplifies the airflow and makes the analysis more straightforward, but also may limit the realism of some results, as discussed in section 5.6.1.

For the control simulation 201 vertical levels of a terrain-following η coordinate are used with spacing, Δz, varying from 17 m near the surface, to about 450 m at the base of the damping layer, and up to 2 km at the model top at z =25 km. To reduce computational time the other simulations use 91 vertical levels, with Δz =40 m near the surface. Tests show that this change in Δz does not affect the simulated Z_S by more than $\sim$ 15%. For the 2D simulations the horizontal grid spacing, $\Delta x, y$, is 2 km, and there are 1250 gridpoints in x and 3 in y, yielding a domain 2500 km in x and 6 km in y (Figure 5.3a). For the 3D simulations there are 3 horizontally nested domains with $\Delta x, y$ =18, 6, and 2 km. The positions and dimensions of the inner domains are shown in Figure 5.3b. The outermost domain is 210×210 grid points and centered on the mountain. The domain nesting is two-way to prevent spurious wave reflections off the nested grid boundaries (e.g., Harris and Durran, 2010).

Cloud and precipitation microphysics are parameterized with the Thompson et al. scheme (Thompson et al., 2004, 2008), a bulk mixed-phase scheme that predicts the number concentration of cloud ice, and the mixing ratios of water vapor, cloud liquid water, cloud ice, rain, snow, and graupel. The scheme originated from the older Riesner2 scheme (Reisner et al., 1998). Unique features of the scheme include: a non-spherical shape assumed for snow; a snow size-distribution that is represented with the sum of exponential and gamma functions; an acceleration of snow and graupel fall speeds in the melting layer to mimic the behavior of partially melted hydrometeors. This scheme is used because it is one of the most sophisticated schemes available in WRF and its sensitivities have been extensively documented for the problem of orographic precipitation (e.g., Thompson et al., 2004, 2008; Lin and Colle, 2009). A positive-definite limiter (Skamarock and Weisman, 2009) is applied during the advection of microphysical variables in order to eliminate spurious moisture sources that can bias precipitation simulations (Skamarock and Weisman, 2009; Hahn and Mass, 2009; Lin and Colle, 2009).

Turbulent mixing is parameterized throughout the model domains using second-order diffusion in Cartesian space with spatially uniform and temporally constant eddy diffusivities. This relatively crude parameterization was used because the more sophisticated Smagorinsky first-order turbulence closure leads to numerical instabilities when used in the 3D simulations. However, tests using the Smagornisky scheme in 2D give very similar results for the fields and regions analyzed.

Cumulus convection is presumed to be resolved due to the fine grid used, thus it is not parameterized. Parameterizations for boundary layer mixing, land surface processes, and radiation are all turned off. These processes are omitted based on the hypothesis that they are not essential for producing the gross mesoscale structure of Z_S and Z_{0C}. The possible consequences of this simplification will be discussed later.

Unless otherwise stated, results presented are averages from simulation hours 36-48. By this time both the dynamical and microphysical fields reach an approximate steady state. For instance, in all but one simulation, ΔZ_{0CtoS} varies by $< \pm 5\%$ during the analysis period. Before analysis the fields are linearly interpolated from the model's terrain following coordinate onto a regular Cartesian vertical grid.

5.3 Results: physical mechanisms

Next, the results from a control simulation are presented and analyzed in detail. This analysis focuses on diagnosing and quantifying the important physical mechanisms that control Z_S and ΔZ_{0CtoS} on the mesoscale. These results provide a framework for interpreting results in subsequent sections.

5.3.1 Control simulation

For the control simulation the initial sounding is characterized by a troposphere with: vertically uniform wind, U, of 15 m s^{-1}, T_s of 15°C, N_m of 0.005 s^{-1}, and RH of 95%. A skew-T log-p plot of the control sounding is shown in Figure 5.4. The upstream Z_{0C} of this sounding is 925 m. Sounding parameters were chosen such that the moist non-dimensional mountain height, $(N_m h_m)/U$, is 0.5, small enough that the flow should be relatively unblocked and rise over the barrier (Pierrehumbert and Wyman, 1985; Jiang, 2003; Galewsky, 2008). Considering the winds and mountain width, the Rossby number, $U/(fa)$, is 3.75, indicating that rotational effects will play a role, roughly limiting the upwind influence of the topography to a deformation radius, $(N_m h_m)/f$, or about 75 km (Pierrehumbert and Wyman, 1985).

Steady-state winds and cloud water fields from the control simulation are shown in figure 5.5. Cross mountain winds, u, are decelerated as the flow approaches the barrier, and

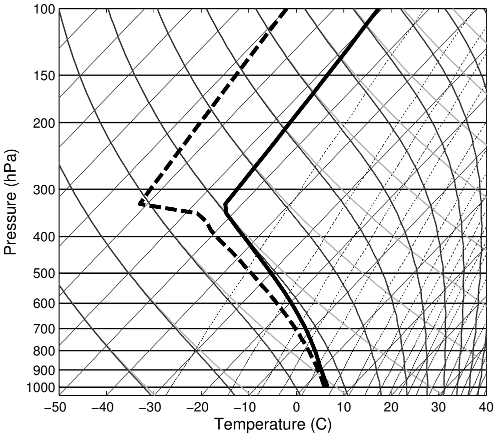

Figure 5.4: Skew-T log-p plot showing soundings of temperature (solid) and dew-point (dashed) used to initialize the control simulation.

along-mountain flow, v, develops as the winds are turned to the left due to the decreased Coriolis force (figure 5.5a). Since the ridge is infinitely long and the cross-mountain winds are everywhere positive, the flow all passes over the ridge. The lack of surface friction in the simulation allows quite strong near-surface winds (>20 m s−1) to develop. Ascent over the mountain produces vertical winds, w, exceeding 40 cm s^{-1} (figure 5.5b), which in turn lead to supersaturation and condensation of cloud liquid water through a 4 km deep layer (cloud liquid water mixing ratio, q_c, plotted in figure 5.5b).

Figure 5.6a shows the mixing ratios of various microphysical species. High above the mountain cloud ice, q_i, is generated, which grows by deposition to form snow, q_s, in the upper regions of the cloud. Note that small values of q_s are found upwind of the edge of the q_i field. This is a spurious result, occurring due to excessive diffusion on the upwind edge of the q_s field. Tests show that this feature is removed if a more sophisticated turbulence parameterization is used, however test also show this error has little impact on the structure of Z_S or Z_{0C}. In the lower 2 km, high q_c leads to riming of snow to form graupel, q_g. At low levels the snow and graupel melt to form rain, q_r. The surface precipitation rates are shown in figure 5.7, revealing that surface precipitation transitions from rain, to mostly snow and

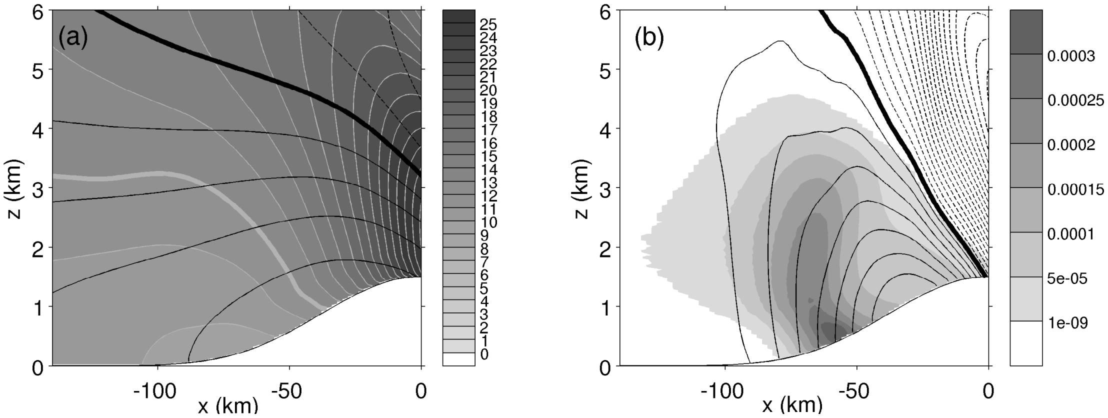

Figure 5.5: Wind and cloud for control simulation. (a) Cross-mountain winds (u, filled contours every 1 m s^{-1}, with bold grey line at $u = U$ =15 m s^{-1}) and along-mountain winds (v, contoured every 1 m s^{-1}, with bold line at v=0, and dashed lines for v <0). (b) Vertical winds (w, contoured every 10 cm s^{-1}, with bold line at w=0, and dashed lines for w <0), and cloud liquid water mixing ratio (q_c, shaded every 5×10^{-5} kg kg^{-1}).

some graupel over a few hundred meters of elevation.

The melting layer is detailed in figure 5.6b, which shows that Z_{0C}, Z_S, and Z_{RS} all descend as they approach the terrain. Although they have different structures upwind of the mountain, Z_S and Z_{RS} intersect the terrain at similar elevations. Note that Z_{RS} is not defined upwind of about $x = -100$ m because snow is sublimating into vapor and no rain is produced. As a result Z_{RS} begins some distance below Z_{0C}, whereas the upwind end of Z_S is nearly colocated with Z_{0C}. Quantitatively, the mesoscale modifications of Z_S and Z_{0C} are: ΔZ_{0C} =153 m, ΔZ_S =235 m, and ΔZ_{0CtoS} =304 m.

Figure 5.6b offers some initial insights into the mechanisms. Temperature contours reveal that isotherms both above and below Z_{0C} also descend significantly. Since this descent occurs well-away from the melting region, where air parcels have not been cooled by LCp-melt, it is clear that another process — such as adiabatic cooling — is playing a role in lowering Z_{0C}. Furthermore, the lack of a substantial modification of the temperature structure below Z_{0C} (e.g., the lack of a near-isothermal layer as found in previous observational studies) also suggests that LCpmelt is not particularly pronounced. Also of note is the much larger drop in Z_S (and Z_{RS}) as compared to Z_{0C}. Since LCpmelt and adiabatic cooling affect Z_S principally by cooling the air and lowering isotherms, the additional drop in Z_S is likely due to a mechanism that does not affect temperatures – such as spatial variations in microphysical melting distances.

The following subsections analyze the results of this simulation to further characterize and quantify the contributions from LCpmelt, adiabatic cooling, and microphysical melting distance.

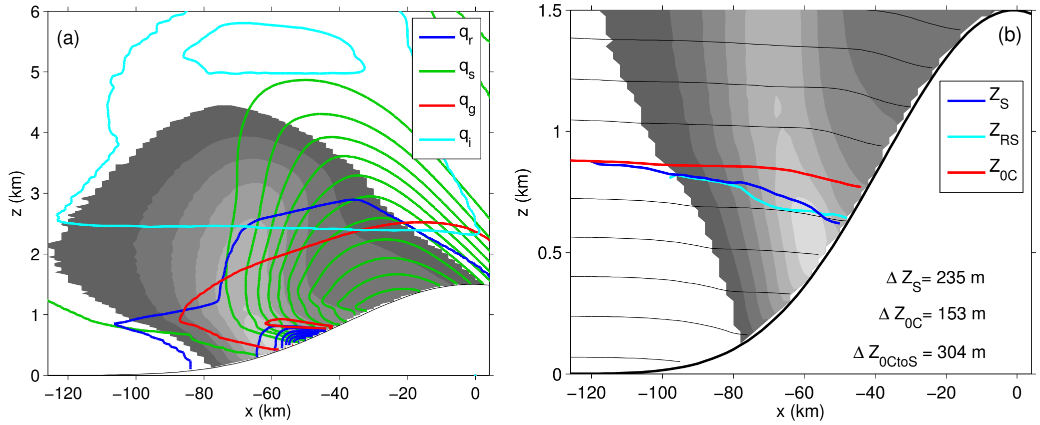

Figure 5.6: (a) Mixing ratios of cloud and hydrometeor species for control simulation. q_c is shaded every shaded every $5{\times}10^{-5}$ kg kg^{-1}. Hydrometeor mixing ratios are contoured every $5{\times}10^{-5}$ kg kg^{-1}: rain (q_r, blue), snow (q_s, green), graupel (q_g, red). Cloud ice (q_i, cyan) is contoured every $2.5{\times}10^{-6}$ kg kg^{-1}. (b) Detail of melting region. Isotherms are contoured with thin lines every 1°C. Bold lines show: Z_{0C} (red), Z_S (blue), and Z_{RS} (cyan). The mesoscale modification of Z_{0C} and Z_S are noted (ΔZ_{0C}, ΔZ_S, and ΔZ_{0CtoS}).

5.3.2 Effect of microphysical melting distance

The role of microphysics, specifically variations in frozen hydrometeor melting distance, will be quantified first. Consider a single profile through the melting layer of hydrometeor mixing

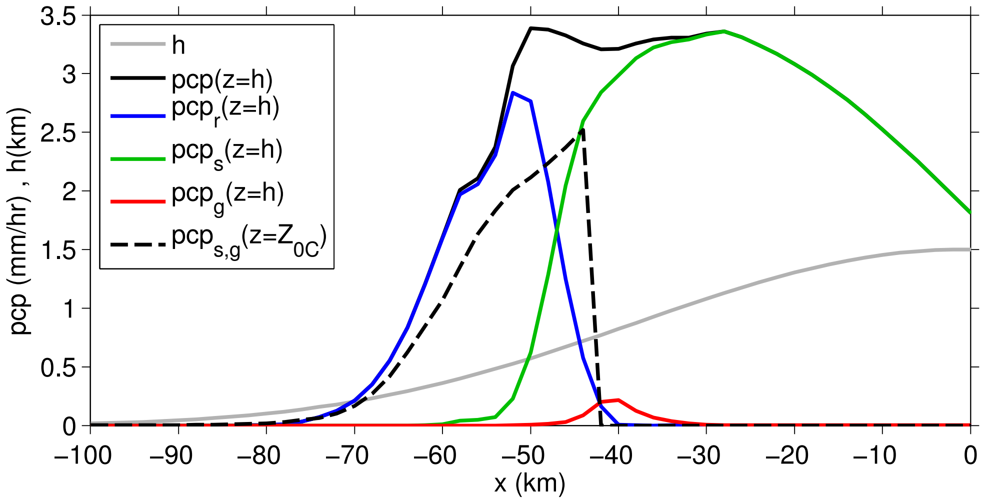

Figure 5.7: Surface precipitation rates (at $z = h$) for total precipitation (pcp), rain, (pcp_r), snow (pcp_s), and graupel (pcp_g). Also shown are the frozen precipitation rate ($pcp_{s,g}$) at $z = Z_{0C}$ and the terrain profile (h) (in gray).

ratios and precipitation rates, taken at $x = -66$ m and shown in figure 5.8. These profiles show how the concentrations of snow and graupel decrease with increasing distance below Z_{0C} as melting coverts them into rain. The vertical gradients of q_s and q_r are small at the top of the melting layer where temperatures are near 0°C, then increase quickly as melting progresses in the warmer mid-elevations, and become small again in the lower elevations. This microphysical structure is similar to that produced by more detailed models of melting layer microphysics (e.g., Szyrmer and Zawadzki, 1999). The structure of these profiles, and the distance that frozen hydrometeors descend below Z_{0C} before melting, is determined by numerous environmental conditions (e.g., temperature lapse rate, winds, humidity, cloud), that affect microphysical tendencies (via sedimentation, sublimation, melting, collection, evaporation, advection, mixing), that in turn may modify the environmental conditions (via absorption and release of latent heat).

Let us hypothesize that, for a given environmental profile, the essential processes determining the melting distance, $Z_{0C} - Z_S$, in the WRF simulations are the rates of sedimenta-

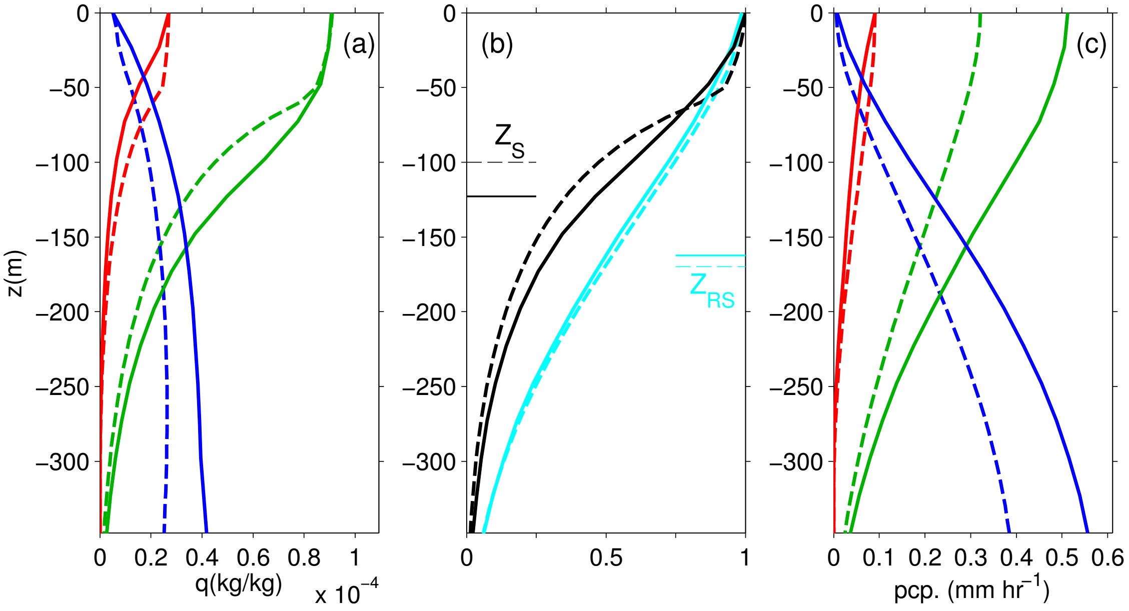

Figure 5.8: Microphysical profiles at x=-66 km from WRF control simulation (solid) and simplified column model (dashed) as a function of distance below Z_{0C}. (a) Mixing ratios: q_s (green), q_g (red), q_r (blue). (b) Fraction of frozen hydrometeor mass from Z_{0C} remaining, $\frac{(q_s+q_g)(z)}{(q_s+q_g)(z=Z_{0C})}$ (black), and ratio of frozen precipitation to total precipitation rate, $\frac{pcp_s+pcp_g}{pcp}$ (cyan). Horizontal lines denote Z_S (black) and Z_{RS} (cyan) from each model. (c) Precipitation rates: pcp_s (green), pcp_g (red), pcp_r (blue).

tion and melting of hydrometeors as determined by the flux of hydrometeors through Z_{0C} and by the mean vertical wind and temperature lapse rate below. This implies that other microphysical tendencies (e.g., collection, sublimation/deposition) and other environmental conditions (e.g., the mixing ratios of cloud ice and liquid water) are only of secondary importance.

To test this hypothesis a model of the precipitation processes acting in a single column of the melting layer is constructed. Hydrometeor mixing ratios q_s, q_g, and q_r are stepped forward in time using a simplified version of the Thompson et al. scheme. This scheme is formulated as described in (Thompson et al., 2008) and configured in WRF V3.0.1, except:

(1) all microphysical tendencies are ignored except sedimentation and the melting of q_s and q_g; (2) an exponential size distribution for snow is assumed as in (Thompson et al., 2008) (instead of a generalized gamma distribution); (3) the "boosting" of snow terminal velocity based on diagnosed degree of riming is omitted. The domain is Z_{0C} to the surface, and the vertical resolution is 10 m. The temperature profile is assumed to be steady in time and is prescribed using the mean lapse rate from the output of the control WRF run at x=-66 m (5.9°C km^{-1}). The air is assumed to be saturated with respect to water, and a uniform vertical velocity averaged from the WRF simulation (0.19 m s^{-1}) is prescribed. The initial condition is zero hydrometeor mixing ratios except at the upper boundary where the values from the WRF simulation are prescribed and held constant.

Figure 5.8 shows the output of this column model applied at $x = -66$ m after a steady state has been reached. Overall it matches the WRF profiles well. The main difference is reduced snowfall rates in the column model as compared to WRF. Additional experiments (not shown) reveal that most of this difference occurs because the column model omits the "boosting" of snow terminal fall velocity applied in the full scheme to mimic the effects of riming (Thompson et al., 2008). Still, despite this difference, the column model Z_S and Z_{RS} are very close to those from the full model.

These results support the hypothesis that, in WRF, the distance between Z_{0C} and Z_S (or Z_{RS}) is determined mainly by the melting distance associated with the precipitation that enters the melting layer. As discussed above, spatial variations in this melting distance may arise from spatial variations in the frozen hydrometeor precipitation rate at Z_{0C} caused by orographic precipitation enhancement. To illustrate the sensitivity of Z_S to precipitation rate the column model is rerun using the same environmental conditions (i.e., $w, \frac{dT}{dz}$), but different q_s and q_g prescribed at Z_{0C}. Figure 5.9 shows how the modeled Z_S and Z_{RS} vary with precipitation rate. For very weak precipitation Z_S and Z_{RS} are found just 50 m below Z_{0C}. But, as precipitation is increased to 14 mm hr^{-1}, the distance of Z_S and Z_{RS} below Z_{0C} increases to 180 m and 480 m.

Note that despite these differences between the behavior of Z_{RS} and Z_S in the column model, they intersect the mountain at approximately the same elevation in most of the subsequent experiments. This may be due to the effects of vertical air motions near the

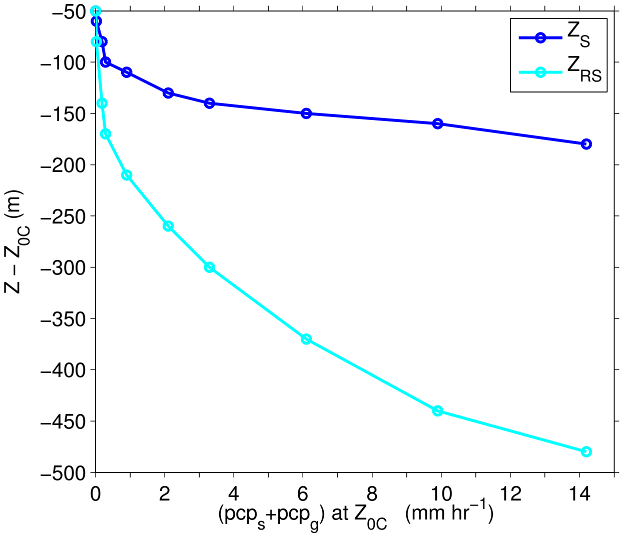

Figure 5.9: Sensitivity of column model Z_S and Z_{RS} to variations in frozen precipitation rate $(pcp_s + pcp_g)$ at Z_{0C}. All simulations use the same lapse rate and w as in Figure 5.8. Distance is measured from Z_{0C}.

mountain on fallspeeds, which have larger effects on the precipitation rates used to calculate Z_{RS} than the mixing ratios used for Z_S. For simplicity, the remaining analyses will only focus on Z_S.

In the full WRF simulation Z_S is 170 m below Z_{0C} when it intersects the terrain (figure 5.6b), and the frozen precipitation rate is 2.3 mm hr^{-1} at Z_{0C} (figure 5.7). The column model predicts a a similar (albeit smaller) distance between Z_S and Z_{0C} for the same precipitation rate (figure 5.9). In WRF Z_{0C} and Z_S are nearly colocated at the upwind edge of the snowfall where precipitation is very weak (at about $x = -120$ km in figure 5.6b). This contrasts with the 50 m distance between Z_{0C} and Z_S for weak precipitation in figure 5.9. This discrepancy is likely due to sublimation that acts as a sink for snow in the unsaturated sub-cloud region in WRF, but is neglected in the simplified column model.

Thus, it appears that, by modulating the melting distance for frozen hydrometeors, spatial variations in orographic precipitation enhancement contribute to lowering Z_S over

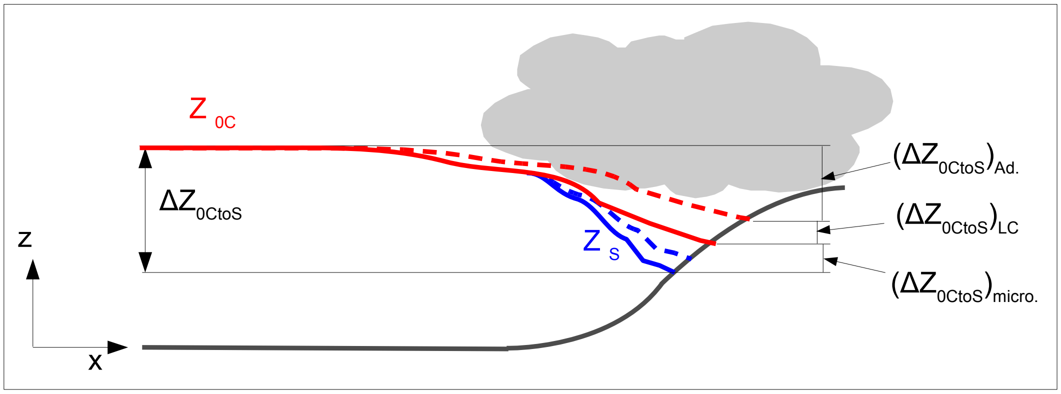

Figure 5.10: Schematic diagram showing how the contributions of various physical processes to ΔZ_{0CtoS} are quantified in the WRF simulation. Solind lines represent Z_{0C} (red) and Z_S (blue) from a control simulation, while dashed lines represent Z_{0C} and Z_S from a simulation where LCpmelt is suppressed. Denoted on the right are contributions from: microphysical melting distance, $(\Delta Z_{0CtoS})_{micro.}$; LCpmelt, $(\Delta Z_{0CtoS})_{LC}$); adiabatic cooling, $(\Delta Z_{0CtoS})_{Ad.}$.

the windward slopes. Accordingly, this "microphysical" component of ΔZ_{0CtoS} is quantified as $(\Delta Z_{0CtoS})_{micro} = \Delta Z_{0CtoS} - \Delta Z_{0C}$. This is shown schematically in Figure 5.10. Note that the geometry of the rising terrain means that Z_S intersects the terrain upwind of Z_{0C}. This limits the drop in Z_S, since lowering of Z_{0C} donwind of moutainside snow line can not affect Z_S. As defined, $(\Delta Z_{0CtoS})_{micro}$ includes this geometrical effect. For the control WRF simulation $(\Delta Z_{0CtoS})_{micro} = 151$ m.

5.3.3 Effect of latent cooling

To quantify the role of LCpmelt, another WRF simulation is conducted, the same as the control except the absorption of latent heat by melting of precipitation is removed from the thermodynamic equation. Figure 5.11 compares Z_{0C} and Z_S from this "no LCpmelt" simulation and the control simulation. ΔZ_{0C} is reduced to 104 m (a reduction of 32 %) while ΔZ_S is reduced to 205 m (a reduction of only 13%). Thus, for the control simulation, LCpmelt has an important impact on the structure of Z_{0C}, but only a relatively modest impact on Z_S. The component of ΔZ_{0CtoS} attributable to LCpmelt is quantified as $(\Delta Z_{0CtoS})_{LC} = (\Delta Z_{0C}) - (\Delta Z_{0C})_{noLC}$ (Figure 5.10). Since this definition focuses on the effects of LCpmelt on Z_{0C} it overestimates the effect of LCpmelt on Z_S, since the lowering of Z_{0C} occurring downwind of the mountainside snowline does not effect Z_S. However, since this geometrical effect depends on the behavior of Z_S, it is included in $(\Delta Z_{0CtoS})_{micro}$. For the control WRF simulation $(\Delta Z_{0CtoS})_{LC} = 49$ m.

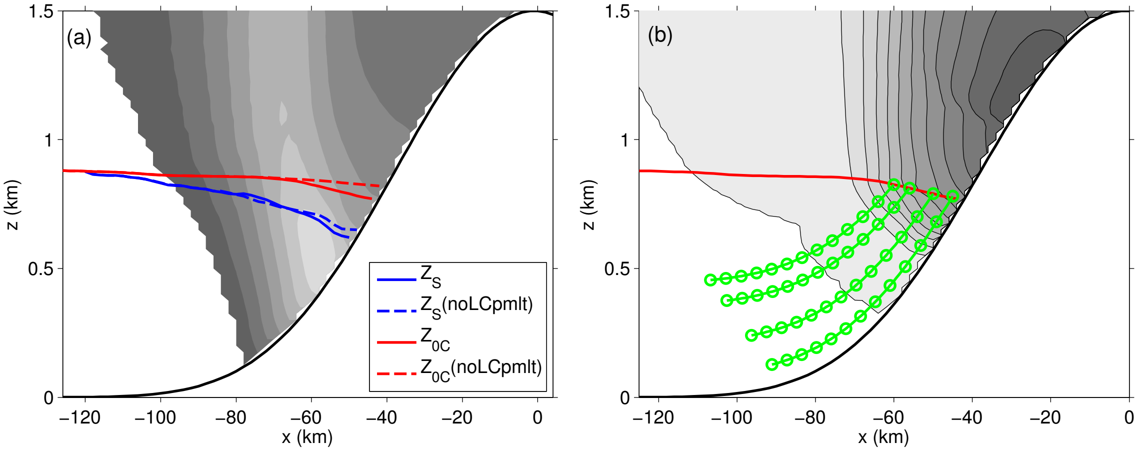

Figure 5.11: (a) As in figure 5.6, but Z_{0C} and Z_S are also shown for the experiment in which LCpmelt is suppressed (dashed lines) and Z_{RS} is omitted. (b) Back trajectory analysis for the control simulation. One-hour air parcel back trajectories ending at Z_{0C} are plotted (green lines, with circles every 5 min). Also shown are: $(q_s + q_g)$ (shaded every 1×10^{-4}) and Z_{0C} (red line)

The modest contribution of LCpmelt is notable since LCpmelt has been suggested as the principle cause for the lowering of Z_S by several previous studies (e.g., Marwitz, 1983, 1987; Colle, 2004). Why is LCpmelt ineffective in substantially lowering Z_{0C} and Z_S in this simulation? In the simple model used by Lin and Stewart (1986) and Unterstrasser and Zängl (2006) the depth of the 0°C layer formed during stratiform precipitation (over flat terrain) is a function of the snowfall rate into the melting layer, the temperature lapse rate below Z_{0C}, and the duration of the precipitation. There is no duration associated with the WRF results since they represent a steady state scenario. However, a potentially important timescale in the problem is the duration of time that an air parcel spends in the melting region, since this acts as a limitation on how much the air may be cooled by melting.

To characterize the residence time of air parcels in the melting region one-hour back trajectories are calculated for air parcels ending at various locations along Z_{0C}. These are plotted in figure 5.11b. To show the region where substantial latent cooling may be occurring, Z_{0C} and the total frozen hydrometeor mixing ratio, $(q_s + q_g)$, are also plotted, since only regions below Z_{0C} with substantial $(q_s + q_g)$ should be associated with significant melting and cooling. These trajectories reveal that, due to the strong near-surface winds, air parcels spend only about 25 min in the melting region, and even less in the region of significant $(q_s + q_g)$ (about 10 min). Apparently this is insufficient time for melting to cool the parcels substantially. In fact, for stratiform precipitation with the same environmental lapse rate and precipitation rate as in the WRF simulation, the simple model of Lin and Stewart (1986) (as modified by Unterstrasser and Zängl (2006)) predicts a very shallow $0°C$ layer of only 15 m when a 10 min precipitation duration is assumed.

5.3.4 Effect of adiabatic cooling

The effects of adiabatic cooling on Z_S are first examined by analyzing a model much simpler than the full WRF simulation: a Lagrangian air parcel model that describes how the temperature of the near surface air varies as it passes over the windward slopes of the mountain. This model assumes that flow over the topgraphic barrier is steady-state, pseudo-adiabatic, unblocked, and laminar. In this situation the lowest streamline parallels the topography. Furthermore, parcel temperatures along this streamline are determined completely by the initial temperature of the air and the amount of ascent that occurs (as determined by a the dry adiabatic lapse rate, Γ_d, until saturation occurs, and then by the moist pseudo-adiabatic lapse rate, Γ_m). Thus, if the RH and surface temperature upstream of the mountain, T_s, are known, then the mountainside value of Z_{0C} can be determined (assuming also that the mountain is tall enough to lift and cool parcels to 0^oC). If the upstream temperature profile, and thus the upstream value of Z_{0C}, is also known (e.g., by knowledge of the stratification N_m), then ΔZ_{0C} can be determined as well. This is all shown schematically in Figure 5.12a-b.

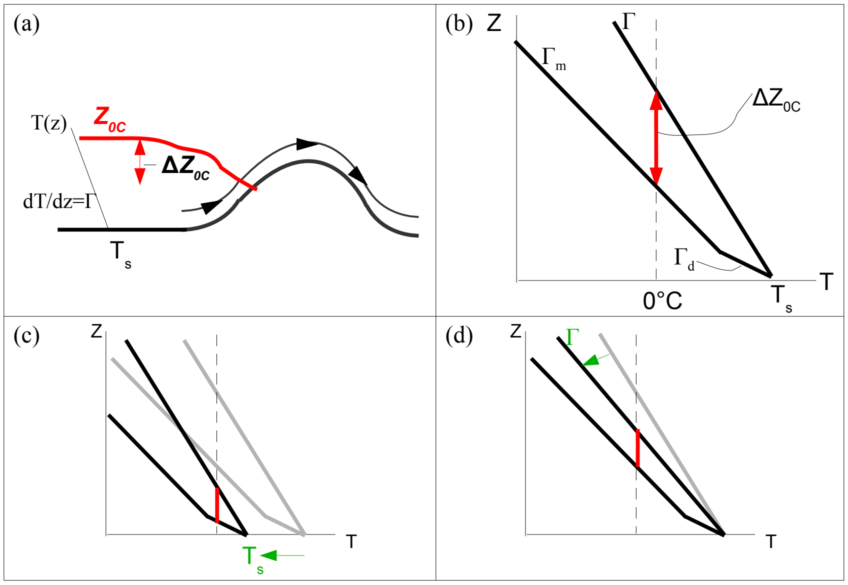

Figure 5.12: Schematics showing how ΔZ_{0C} is determined by adiabatic cooling in the parcel model. (a) $x - z$ section showing environmental temperature profile and flow along lowest streamline. (b) Idealized profiles of environmental temperature (with lapse rate Γ) and parcel temperature (with lapse rates Γ_d and Γ_m) showing how lapse rate differences lead to ΔZ_{0C} (shown in red). (c) Profiles (in black) showing how a decrease in T_s decreases ΔZ_{0C}. (d) Profiles (in black) showing how an increase in Γ (and decrease in N_m) decreases ΔZ_{0C}.

Values of ΔZ_{0C} predicted from the parcel model are shown for a range of T_s and N_m in Figure 5.13. First, note that, for nearly all values of the upstream parameters, ΔZ_{0C} is positive, indicating a drop in Z_{0C} over the windward slopes. This occurs because as long as the static stability is significantly positive the upstream environmental lapse rate, Γ, is less than Γ_m and Γ_d, so a parcel rising over the mountain reaches Z_{0C} at an elevation lower

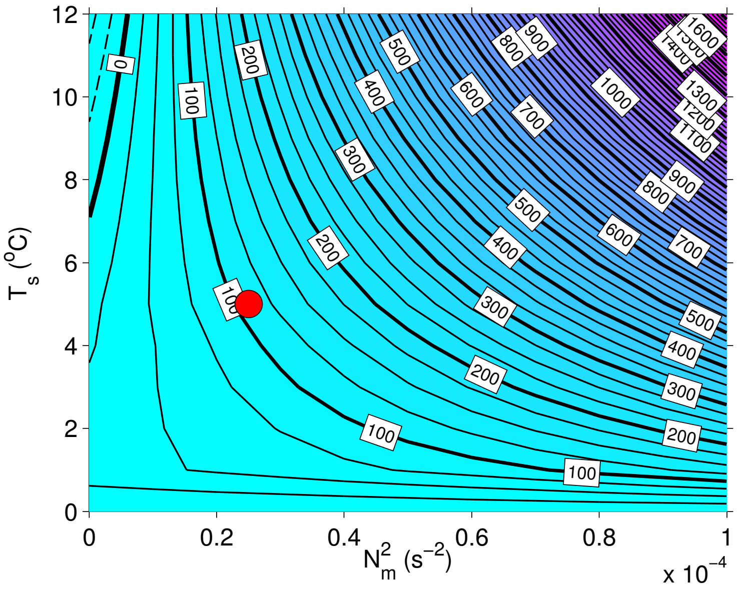

Figure 5.13: Results from idealized parcel model showing ΔZ_{0C} (contours) as a function of upstream surface temperature, T_s, and moist stability, N_m^2, for RH =95 %. Negative contours are dashed. Red dot shows the parameters used for the control WRF simulation.

than the upstream sounding (see figure 5.12b). The exception of positive ΔZ_{0C} occurs for very low values of N_m and high values of T_s, which actually correspond to environmental lapse rates that are larger than the moist pseudo-adiabatic value (note, that in equation 5.1, for $N_m = 0$ and $\frac{dq_w}{dx} < 0$, $\Gamma > \Gamma_m$). Another important prediction of this model is a monotonic increase in ΔZ_{0C} for both increases in T_s and increases in N_m^2 (except at very low N_m). The sign of these tendencies can be understood from the simple schematics in figure 5.12c-d.

Note that the parcel model neglects blocking of the incoming airflow, which could prevent surface streamlines from following the topography, particularly for high mountains and strong stability. Therefore, the regime corresponding to the upper right of Figure 5.13, where stabilities are high and a tall mountain is required to lift and cool parcels to 0^oC, is likely poorly represented by the parcel model.

The impact of adiabatic cooling is apparent at all elevations in the isotherms shown in figure 5.6b. Ascent of unsaturated air parcels, upwind of the orographic cloud, results in a downward slope of isotherms since $\Gamma_d > \Gamma$. As the air reaches saturation at the edge of the cloud condensation occurs, releasing latent heat, and air parcels begin to rise with lapse rate of Γ_m. This change in parcel lapse rate results in an abrupt change in the isotherm slope, but since Γ_m is also greater than Γ, the isotherms still slope downward, and the isotherm slope increases toward the mountain as streamlines steepen and LCpmelt also becomes important.

To relate the simple parcel model to the control WRF simulation the ΔZ_{0C} from the no LCpmelt simulation is considered, since the parcel model does not attempt to account for latent cooling. For the N_m and T_s associated with the WRF control simulation the parcel model predicts a $(\Delta Z_{0C})_{parcel}$ of 110 m (see red dot in figure 5.13). This agrees very well with the $(\Delta Z_{0C})_{noLC}$ of 104 m from WRF. Thus, the portion of ΔZ_{0C} not caused by LCpmelt appears to be entirely caused by adiabatic cooling of air parcels as they are lifted over the mountain. Accordingly, the component of ΔZ_{0CtoS} attributable to adiabatic cooling is quantified as: $(\Delta Z_{0CtoS})_{Ad.} = (\Delta Z_{0C})_{noLC}$ (Figure 5.10). Again, note that focusing on Z_{0C} overestimates the effects of adiabatic cooling on Z_S somewhat due to geometrical effects. $(\Delta Z_{0CtoS})_{Ad.} = 104$ m for the control simulation.

5.3.5 Sensitivity to microphysical parameterization

An array of studies have documented the sensitivity of orographic precipitation simulations to the microphysical parameterization (e.g., Colle and Zeng, 2004a,b; Thompson et al., 2004; Colle et al., 2005; Grubisic et al., 2005; Lin and Colle, 2009; Jankov et al., 2009). These studies have revealed that both the scheme applied and how the applied scheme is configured have major impacts on the amount, pattern, and type of precipitation simulated. A cursory analysis of how the simulation of Z_S is affected by microphysical parameterization is made by repeating the control simulation using four of the other microphysical parameterizations available in WRF. All of the schemes used are bulk schemes— with assumed size distributions for precipitation and cloud particles— that predict cloud liquid water, cloud ice, rain, snow, and graupel separately. The Purdue Lin scheme (Chen and Sun, 2002) is a single moment scheme that predicts mixing ratios of microphysical species based on Lin et al. (1983) and Rutledge and Hobbs (1984). The WSM6 scheme (Hong et al., 2004; Hong and Lim, 2006) is also single moment and similar to the Purdue Lin scheme, but with various modifications to the treatment of ice (e.g., Hong et al., 2004), and with freezing/melting calculated on the sedimentation timestep to improve accuracy of latent heating/cooling profiles. The Goddard Cumulus Ensemble scheme (Tao et al., 2003) is another single moment scheme. The Morrison et al. scheme (Morrison et al., 2005, 2009) is a double moment scheme that predicts both number concentrations and mixing ratios of all microphysical species and represents their size distributions with gamma functions. More detailed discussion of the differences between the schemes may be found in Skamarock et al. (2008); Lin and Colle (2009); Jankov et al. (2009). All schemes are employed using their default configuration in the WRF v3.0.1 release.

The top panels in figure 5.14 show the mixing ratios predicted by the various schemes. All of these schemes simulate more cloud ice aloft as compared to the Thompson et al. scheme (c.f., figure 5.6a, noting the different scale for q_i). The simulated cloud liquid water is confined to much lower levels in the WSM6 simulation, and both q_i and q_c show some spurious aliasing aloft in the Purdue Lin simulation. There are major contrasts between the relative proportion of snow and graupel predicted by the schemes. Like the Thompson et

Figure 5.14: (overleaf) Results from simulations with different microphysical parameterizations. (top) Mixing ratios (q_c,q_r,q_s,q_g, and q_i) as in figure 5.6a, except q_i is contoured every $1{\times}10^{-5}$ kg kg^{-1}. (b) Detail of melting region showing Z_{0C} (red), Z_S (blue), and q_c as in figure 5.6b.

al. scheme, the Goddard and WSM6 schemes produce a mixture of snow and graupel (with more graupel at low levels in WSM6), whereas Purdue Lin produces nearly all graupel and Morrison et al. produces all snow. These differences in the relative abundance of q_s and q_g are consistent with the results of previous studies (e.g., Lin and Colle, 2009; Jankov et al., 2009).

The lower panels of figure 5.14 show q_c, Z_{0C}, and Z_S in detail over the windward slope. All the simulations exhibit a drop in both Z_{0C} and Z_S over the windward slopes. They also all produce a similar ΔZ_{0C} to the control (to within 20%). Thus, it appears that the adiabatic and latent cooling contributions to ΔZ_{0CtoS}, which act by lowering Z_{0C}, operate similarly regardless of the details of the microphysical parameterizations. This is perhaps not surprising since these mechanisms depend mostly on airflow, thermodynamics, and gross aspects of the microphysics (condensational heating, flux of frozen precipitation into the melting region) that are similar between the simulations.

The structure of Z_S is much less consistent across the various runs. The Purdue Lin and WSM6 simulations give a larger ΔZ_S than the control simulation (23% and 15% greater). Still, both show similar Z_S structures to the control, with the distance between Z_{0C} and Z_S increasing as the mountain is approached due increased precipitation rates that increase fall speeds and melting times. In contrast, for both the Goddard and Morrison simulations Z_S does not diverge from Z_{0C} as the mountain is approached (except temporarily at the cloud edge in the Morrison simulation). Accordingly, these schemes have little microphysical contribution to ΔZ_{0CtoS}. So, in contrast to the LCpmelt and adiabatic components, the microphysical contribution to ΔZ_{0CtoS} varies widely depending upon the scheme used.

Since these schemes are different from each other in many ways, it is not straightforward to discern the cause of the simulated Z_S differences or to determine which scheme represents

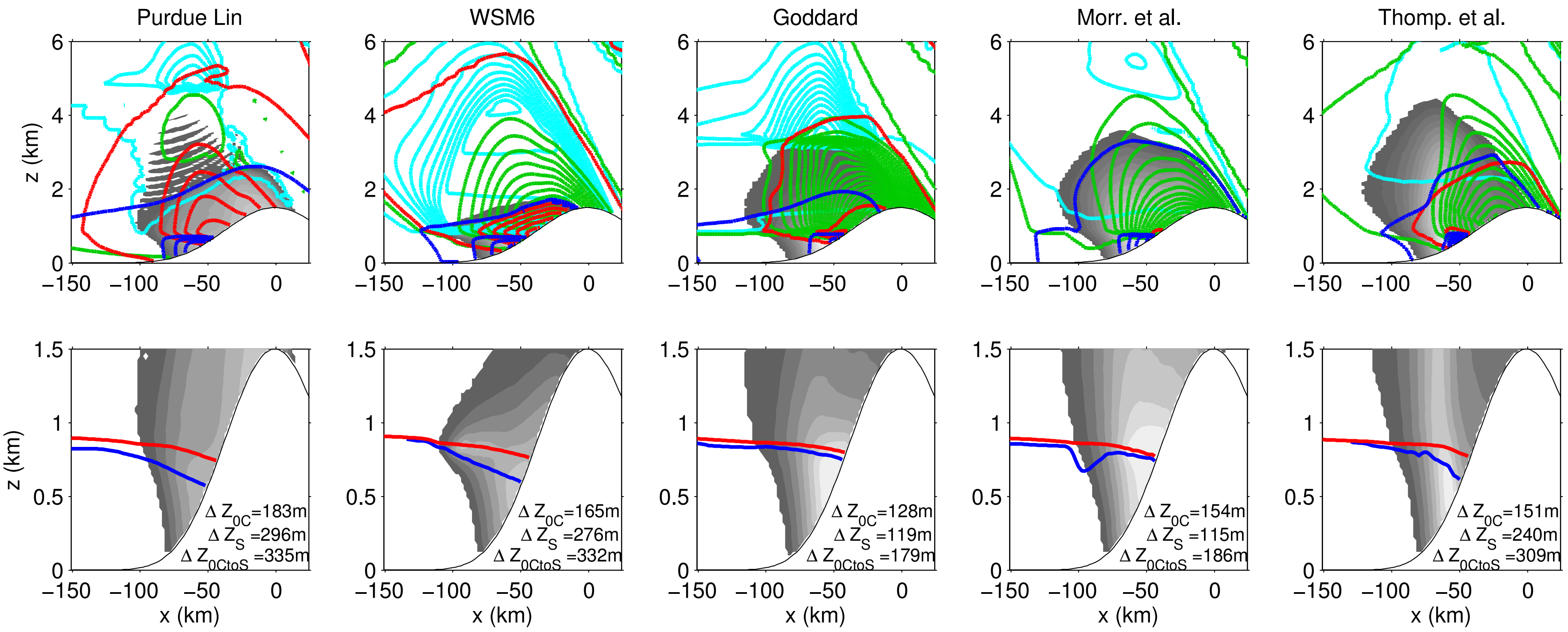
Purdue Lin
WSM6
Goddard
Morr. et al.
Thomp. et al.
z (km)
x (km)
Δ Z_{0C}=183m
Δ Z_S =296m
Δ Z_{0CtoS} =335m
Δ Z_{0C}=165m
Δ Z_S =276m
Δ Z_{0CtoS} =332m
Δ Z_{0C}=128m
Δ Z_S =119m
Δ Z_{0CtoS} =179m
Δ Z_{0C}=154m
Δ Z_S =115m
Δ Z_{0CtoS} =186m
Δ Z_{0C}=151m
Δ Z_S =240m
Δ Z_{0CtoS} =309m

Z_S most realistically; differences in assumed hydrometeor size distributions, graupel formation, and diameter-fallspeed relationships could all affect melting distances. Furthermore, some of the attributes that are common to all the schemes may severely limit their realism in the melting region. For instance, melting snowflakes have shapes, fallspeeds, and other characteristics that are distinct from that of rain or snow (e.g., Mitra et al., 1990), however none of the schemes considered treat melting snow as a separate microphysical species. Furthermore, the process of melting tends to convert the smallest snowflakes into rain first, eliminating the lower end of the snow size spectrum, however the schemes considered all have size distribution assumptions that do not allow this to occur. The Thompson et al. scheme attempts to compensate for one consequence of these deficiencies by increasing the fallspeeds of snow and graupel (to that of rain) in the melting region (Thompson et al., 2008) to make their behavior more consistent with observations (e.g., Mitra et al., 1990). Consideration of the simulated profiles from more detailed models (e.g., Szyrmer and Zawadzki, 1999) and observations (Stewart et al., 1984; Mitra et al., 1990) suggests that the very small $(Z_{0C} - Z_S)$ found in the Goddard and Morrison et al. schemes is not very realistic. However, determination of which of WRF's parameterizations most accurately simulate $(\Delta Z_{0CtoS})_{micro}$ will require more direct comparisons with models that offer a more detailed representation of melting precipitation (e.g., Szyrmer and Zawadzki, 1999; Theriault et al., 2006), and with both remote (e.g., Jankov et al., 2009) and *in situ* (e.g., Stewart et al., 1984) observations of the melting layer.

5.4 Results: 2-D sensitivity experiments

In order to understand how mesoscale controls on Z_S vary between different storms, climates, and mountain ranges a series of 2D sensitivity experiments are conducted. In each experiment the same setup as the control simulation is used, but a single aspect of either the incoming flow or the terrain geometry is altered. This study begins by focusing on 2D experiments for computational efficiency and because simpler airflow response (compared to 3D) makes the results more straightforward to interpret. Since airflow and precipitation are most similar between 2D and 3D for unblocked flows (e.g., Epifanio and Durran, 2001; Galewsky, 2008), the following experiments are designed to keep $(N_m h_m)/U \leq 1$.

5.4.1 Temperature

To test sensitivity to temperature, additional simulations are made with warmer (7°C) and colder (3°C) values of T_s, with and without LCpmelt. Figure 5.15a-b shows cross sections with q_c, Z_{0C}, and Z_S for these simulations. Since N_m is held constant, the T_s change also results in changes of the upstream Z_{0C} (from 0.56 km to 1.31 km). Figure 5.15c shows the precipitation rates associated with each T_s simulation. As T_s is increased the maximum values of q_c and *pcp* both increase due to the increased moisture flux, although these increases are moderated by microphysical effects (e.g., Kirshbaum and Smith, 2008).

Figure 5.16a shows that ΔZ_{0C}, ΔZ_S, and ΔZ_{0CtoS} all increase with increasing T_s, and figure 5.16b quantifies the contributions to ΔZ_{0CtoS} of the three physical mechanisms discussed in sections 5.3.2–5.3.4. All three physical mechanisms act to increase ΔZ_{0CtoS} as temperatures are warmed: increased adiabatic cooling results from the higher Z_{0C} (e.g., figures 5.12c and 5.13); increased LCpmelt comes from higher precipitation rates that deliver more ice into the melting layer; increased microphysical contributions come from the longer distance that the larger snow and graupel particles (associated with heavier precipitation) descend below Z_{0C}.

If this simulated dependency on T_s also exists in nature it could have important consequences for regional climate change in mountainous areas. As T_s is warmed in these simulations Z_{0C} rises by 742 m upwind of the mountains. However, the increase in ΔZ_{0CtoS} results in only a 594 m rise in the mountainside Z_S. Thus, mesoscale processes over the mountain act to buffer the impact of warming on Z_S, reducing by 20% the rise that would be expected by only considering the effects of warming on the upwind Z_{0C}.

5.4.2 Stratification

To test the effect of stratification, simulations are made with smaller ($N_m = 0.002$ s^{-1}) and larger ($N_m = 0.007$ s^{-1}) moist stabilities. Results are shown in figures 5.17 and 5.18. As N_m is increased the upwind Z_{0C} is increased since the environmental lapse rate is decreased (figure 5.17a-b). Changes in N_m affect both the upwind water vapor flux profile and the pattern of vertical motion over the mountain, and the effect on the precipitation pattern

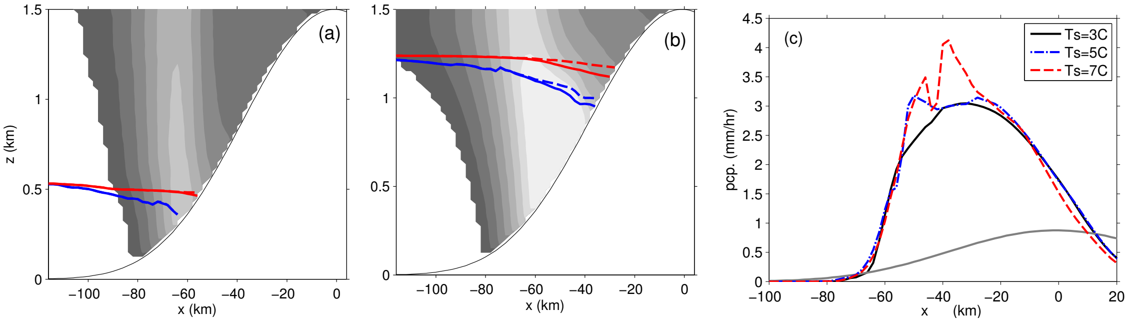

Figure 5.15: Cross-sections from T_s simulations. (a) For T_s=3°C simulation: q_c (shaded every 5×10^{-5} kg kg^{-1}), Z_{0C} and Z_S from simulations with (solid) and without (dashed) LCpmelt. (b) As in (a), but for T_s=7°C. (c) Precipitation rates (see key) and terrain profile (gray).

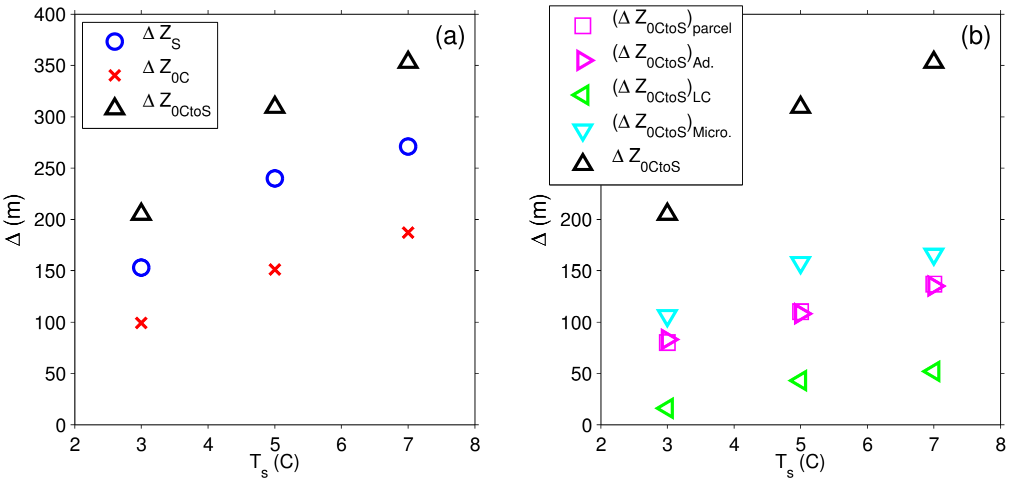

Figure 5.16: (a) ΔZ_S, ΔZ_{0C}, and ΔZ_{0CtoS} as a function of T_s (see key). (b) Contributions of mechanisms discussed in text to ΔZ_{0CtoS} as a function T_s (see key). Also included is the prediction from the parcel model discussed in section 5.3.4.

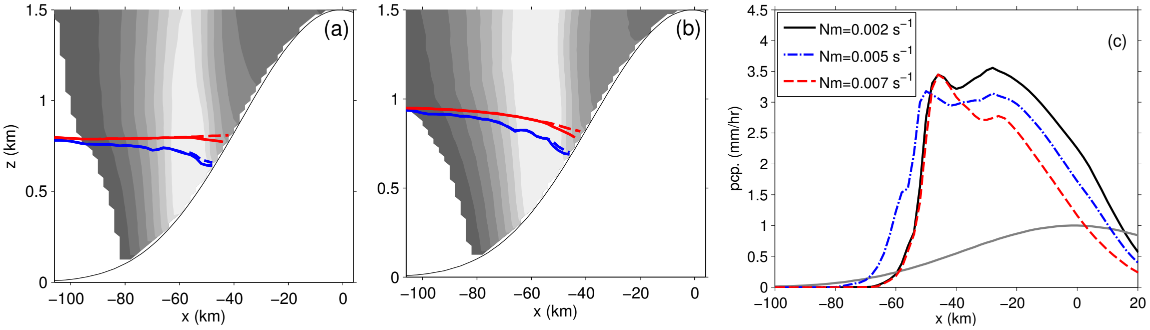

Figure 5.17: (a) As in figure 5.15a, but for $N_m = 0.002$ s^{-1} simulation. (b) As in figure 5.15a, but for $N_m = 0.007$ s^{-1}. (c) As in figure 5.15c, for N_m simulations.

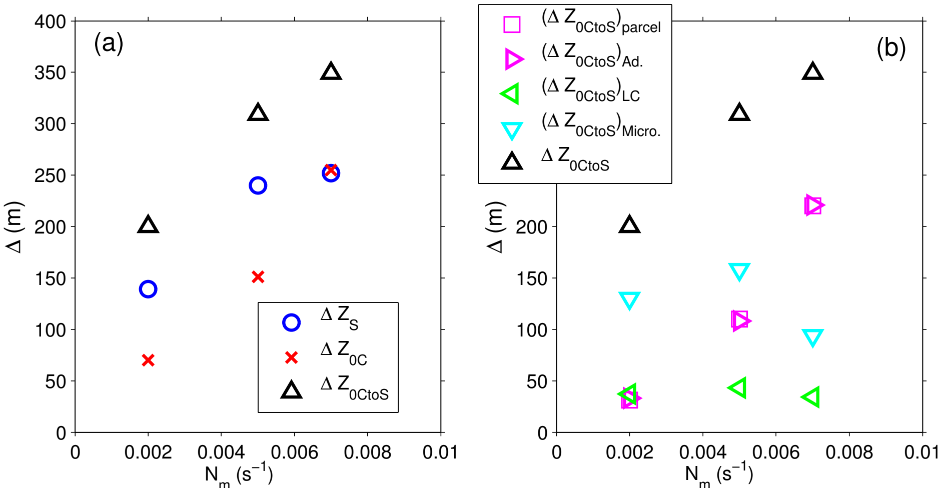

Figure 5.18: As in figure 5.16, but for N_m experiments.

is complex (figure 5.17c). The surface precipitation shifts upwind as N_m increases from $= 0.002$ to $N_m = 0.005\ \ \mathrm{s}^{-1}$, since the increase in stability causes a greater upstream tilt with height of the gravity wave vertical velocities (e.g., Smith and Barstad, 2004; Colle, 2004). However, as N_m increases from $= 0.005$ to $N_m = 0.007\ \ \mathrm{s}^{-1}$, a further increase in the upstream gravity wave tilt results in descent aloft that eliminates formation of q_i above the windward slope. This in turn acts to increase the timescale for precipitation formation, shifting the the upwind edge of the precipitation back downstream (figure 5.17c).

Figure 5.18 shows that ΔZ_{0CtoS} increases with N_m. This increase is predicted well by the parcel model, and analysis of the WRF output indicates that variations in $(\Delta Z_{0CtoS})_{Ad.}$ are largely responsible for the N_m dependence (figure 5.18b). N_m has a more complicated relationship to $(\Delta Z_{0CtoS})_{micro}$ due to the manner in which precipitation rates change at Z_{0C}. Decreases in $(\Delta Z_{0CtoS})_{micro}$ act to counteract increases in $(\Delta Z_{0CtoS})_{Ad.}$ as N_m increases from $N_m = 0.005\ \mathrm{s}^{-1}$ to $N_m = 0.007\ \mathrm{s}^{-1}$. $(\Delta Z_{0CtoS})_{LCpmelt}$ has very weak dependence on N_m.

5.4.3 Wind speed

To test the effect of wind speed, simulations are made with smaller ($U = 10\mathrm{m\ s}^{-1}$) and larger ($U = 20\mathrm{m\ s}^{-1}$) cross mountain winds. Results are shown in figures 5.19 and 5.20. Since the moisture flux scales with U, changes in windspeed have a large impact on precipitation intensity, with larger winds yielding heavier precipitation rates (figure 5.19c). Increasing U from 10 to 15 m s^{-1} increases precipitation everywhere. In contrast, as U is increased further, to 20 m s^{-1}, the timescale associated with cross-mountain advection becomes comparable with the microphysical timescales required for precipitation formation and fallout, resulting in a downwind shift of the precipitation pattern, and decreases in intensity over the lower windward slopes (e.g., Jiang and Smith, 2003; Smith and Barstad, 2004; Colle, 2004; Roe and Baker, 2006).

Increasing U from 10 to 15 m s^{-1} results in a modest increase in ΔZ_{0CtoS}, but increasing U from 15 to 20 m s^{-1} leads to a sharp decline in ΔZ_{0CtoS} (figure 5.20a). $(\Delta Z_{0CtoS})_{PA}$ shows almost no U dependence, as predicted by the parcel model (figure 5.20b). $(\Delta Z_S)_{LCpmelt}$ is

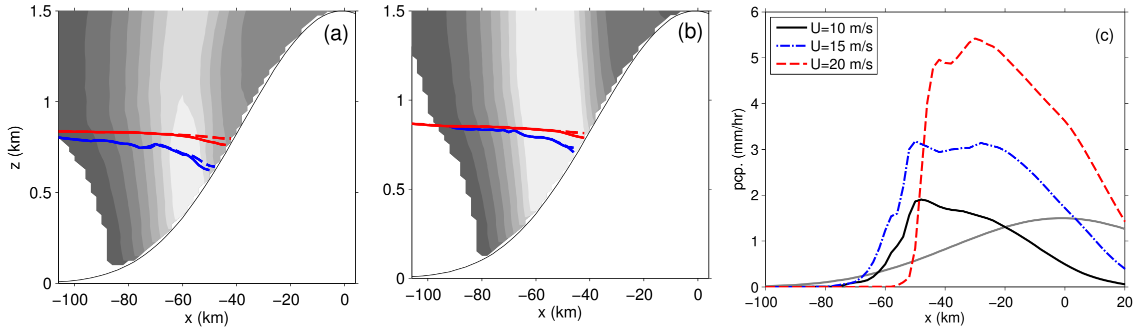

Figure 5.19: (a) As in figure 5.15a, but for $U = 10$ m s^{-1} simulation. (b) As in figure 5.15a, but for $U = 20$ m s^{-1}. (c) As in 5.15c, but for U simulations.

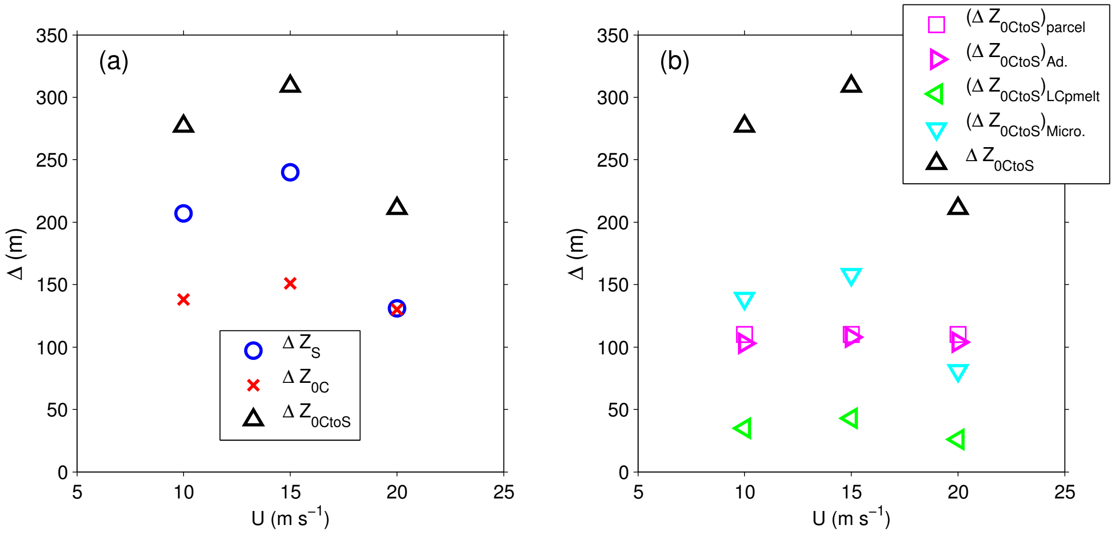

Figure 5.20: As in figure 5.16, but for U experiments.

also constant with U, since the increased melting due to heavier precipitation rates is almost perfectly compensated for by the decreased residence time of faster moving air parcels in the melting region (figure 5.20b). Thus, the dependency on U is almost completely due to microphysical effects.

As U is increased from 10 to 15 m s^{-1} the precipitation rates at Z_{0C} are increased, resulting in a modest increase in $(\Delta Z_{0CtoS})_{micro}$. However as U is increased to 20 m s^{-1}, despite the increase in peak surface precipitation rate, the flux of frozen precipitation at Z_{0C} is decreased everywhere upwind of $x = -47$ km. In the last few kilometers, between x=-47 km and where Z_S intersects the mountain, Z_S cannot drop drastically due to strong vertical motion (which are enhanced in the U=20 m s^{-1} case) that acts to slow the descent of falling precipitation. As a result $(\Delta Z_{0CtoS})_{micro}$ is reduced at high windspeeds.

5.4.4 Relative Humidity

To test the effect of relative humidity, simulations are made with RH ranging from 85–98%. Results are shown in figures 5.21 and 5.22. As RH is increased both the extent and intensity of precipitation increase, since the moisture flux is increased and less lifting is required to cool the air to saturation (figure 5.21c).

Increasing RH leads to decreases in ΔZ_{0C}, whereas ΔZ_S initially increases, then is only weakly affected (figure 5.22a). ΔZ_{0CtoS} is largely unchanged as RH increases from 85 to 90%, but then decreases with further increases in RH (figure 5.22a). All three mechanisms contribute significantly to this behavior (figure 5.22b). $(\Delta Z_{0CtoS})_{Ad.}$ increases with decreasing RH because air parcels rise and cool dry adiabatically longer at lower RH, resulting in larger lapse rate differences between the parcel and the upwind temperature profile. In contrast, $(\Delta Z_{0CtoS})_{micro.}$ and $(\Delta Z_{0CtoS})_{LC}$ both increase with RH due to increases in precipitation rates that accompany the moister flow. At low values of RH (85–90%), these changes largely compensate and ΔZ_{0CtoS} is only weakly affected, whereas at higher RH (90–98%) decreases in $(\Delta Z_{0CtoS})_{Ad.}$ dominate and ΔZ_{0CtoS} decreases with RH.

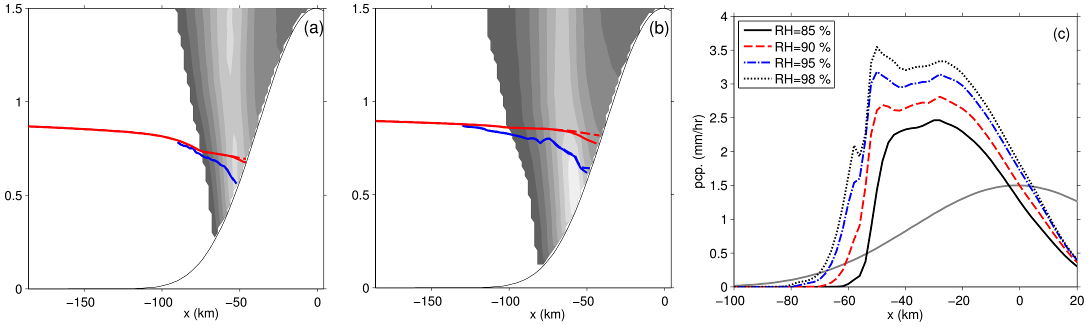

Figure 5.21: (a) As in figure 5.15a, but for $RH = 85\%$ simulation. (b) As in figure 5.15a, but for $RH = 98\%$. (c) As in figure 5.15c, but for RH simulations.

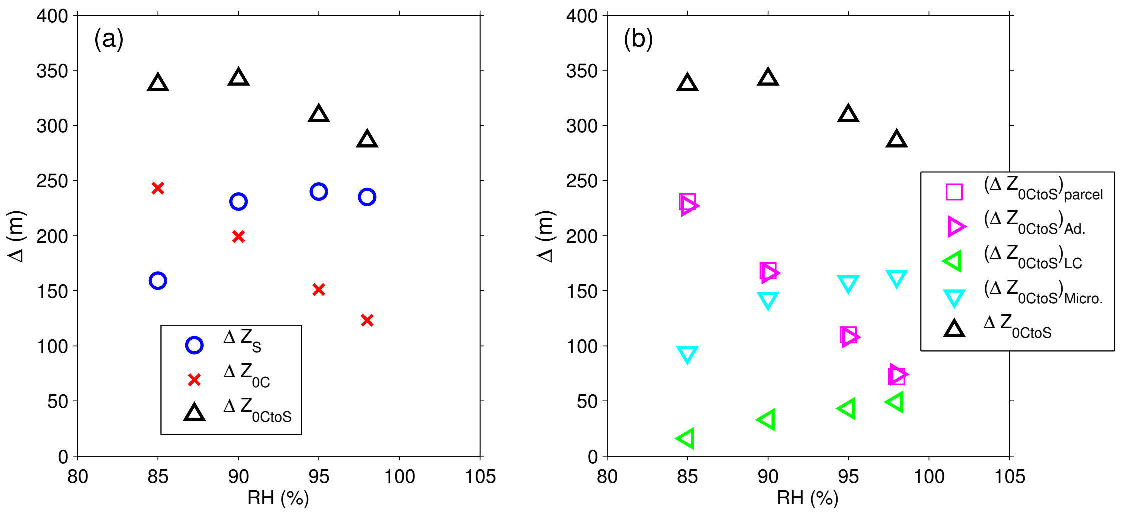

Figure 5.22: As in figure 5.16, but for RH experiments.

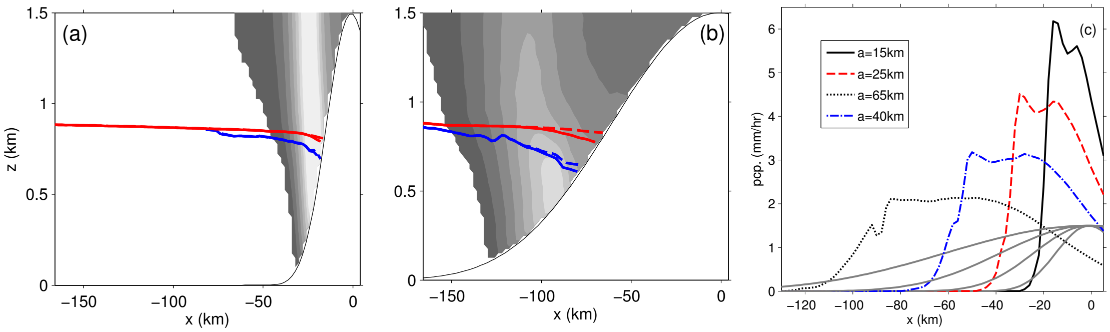

Figure 5.23: (a) As in figure 5.15a, but for $a = 15$ km simulation. (b) As in figure 5.15a, but for $a = 65$ km. (c) As in figure 5.15c, but for a simulations.

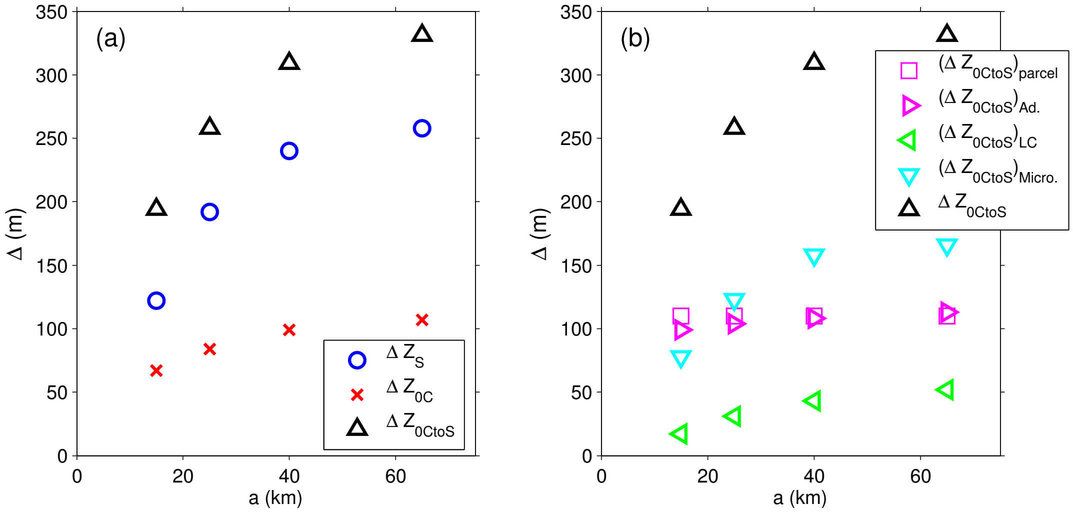

Figure 5.24: As in figure 5.16, but for a experiments.

5.4.5 Mountain width

To test the effect of mountain width, simulations are made with a ranging from 15 km to 65 km. Results are shown in figures 5.23 and 5.24. As the mountain becomes wider the precipitation becomes more widely distributed and less intense (figures 5.23c). Although the peak intensity decreases, the total precipitation over the windward slopes increases by about 55% as a varies from 15 km to 65 km. This larger precipitation efficiency occurs because the increased timescale for cross mountain advection (relative to microphysical conversion and sedimentation timescales) allows more water vapor to form precipitation and fallout before being advected into the lee (e.g., Jiang and Smith, 2003; Smith and Barstad, 2004; Colle, 2004; Roe and Baker, 2006).

Figures 5.23a-b and 5.24 show that ΔZ_S, ΔZ_{0C}, and ΔZ_{0CtoS} all increase with a, particularly for relatively narrow ridges (e.g., as a increases from 15 to 25 km). The a dependency of ΔZ_{0CtoS} is largely due to $(\Delta Z_{0CtoS})_{micro}$ (figure 5.24b). As the ridge becomes narrower the region of intense precipitation is shifted downwind, away from the melting region and the vertical velocities become strong over the windward slope. This is analogous to what happens as U is increased in the earlier experiment. As with increasing U, decreasing a results in a decrease in $(\Delta Z_{0CtoS})_{micro}$. As predicted by the parcel model, $(\Delta Z_{0CtoS})_{Ad.}$ has almost no dependence on a (figure 5.24b). The broadening of the precipitation with increasing a acts to increase the residence time of air parcels in the melting region. Accordingly, $(\Delta Z_{0CtoS})_{LCpmelt}$ increases with a (figure 5.24b).

5.4.6 Mountain height

To test the effect of mountain height simulations are made with h_m ranging from 1.5 km to 3 km (values of $h_m \leq 1$ km are not used because they result in no surface snowfall). Results are shown in figures 5.25 and 5.26. As the mountain becomes taller the precipitation becomes more intense (figures 5.25c) due to increased lifting of the incoming flow. As h_m reaches 3 km, and $(N_m h_m)/U$ reaches 1, the low-level flow becomes more decelerated and blocked, and ascent over the blocked air increases the upstream extent of lifting and precipitation (e.g., Colle, 2004; Galewsky, 2008).

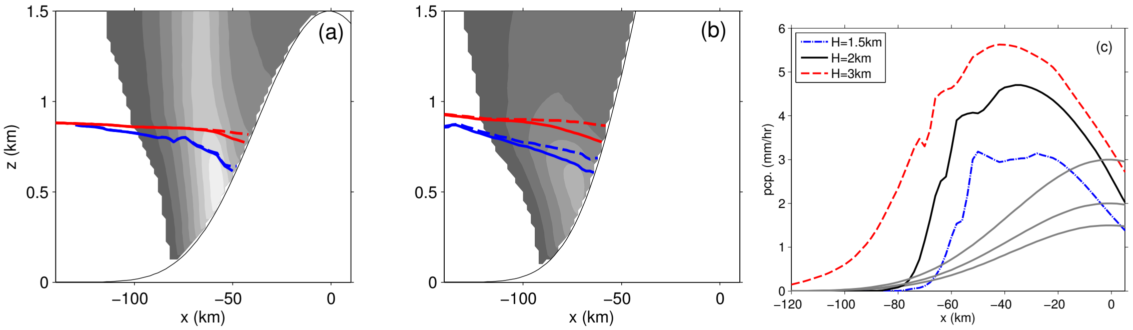

Figure 5.25: (a) As in figure 5.15a. (b) As in figure 5.15a, but for $h_m = 3$ km. (c) As in figure 5.15c, but for h_m simulations.

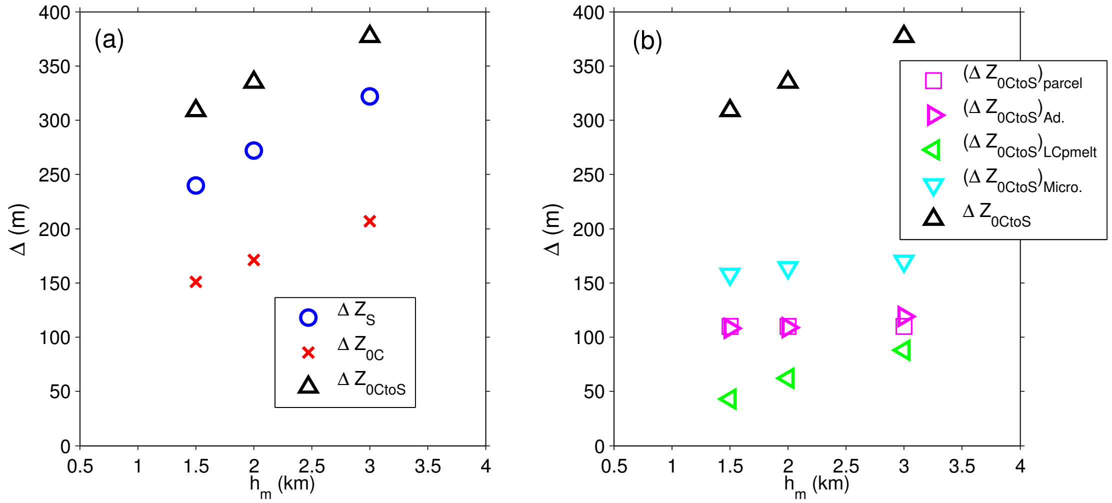

Figure 5.26: As in figure 5.16, but for h_m experiments.

As h_m is increased ΔZ_S, ΔZ_{0C}, ΔZ_{0CtoS} all increase (figures 5.25a-b and 5.26a). This occurs mainly due to increases in $(\Delta Z_{0CtoS})_{LC}$ (figure 5.26b). As h_m increases, the combination of the decrease in u and the widened precipitation region increases the residence time of air parcels in the melting region by about 30% for the h_m =3 km case relative to the control. This increased residence time together with increased precipitation rate account for the increase in $(\Delta Z_{0CtoS})_{LC}$ with h_m. The increased precipitation rates also act to increase $(\Delta Z_{0CtoS})_{micro.}$ slightly (figure 5.26b). $(\Delta Z_{0CtoS})_{Ad.}$ changes little with h_m, again as predicted by the parcel model (figure 5.26b).

5.5 Results: 3D effects

5.5.1 Control: $(N_m h_m)/U = 0.5$

To quantify the effect of finite ridge length and fully 3D structure, the control simulation is repeated, but with a 3D domain and a finite length ridge with $\beta = 5$ (see figure 5.3b). This ridge-length is chosen because it is long enough to produce an airflow response similar to much longer ridges (Epifanio and Durran, 2001), but short enough to minimize computational expense associated with the model's horizontal grid size. The resulting near-surface winds and surface precipitation rate in the horizontal plane are shown in figure 5.27a. The flow diverges as it approaches the mountain and some flow passes around the ridge, but most flow at low levels is still directed across the ridge. Some asymmetry in the precipitation pattern occurs in the cross-wind direction due to the influence of the Coriolis force (e.g., Galewsky, 2008).

$x - z$ cross-sections at $y = 0$ are shown in figure 5.28. In the 3D simulation the depth and strength of the upward motion over the windward slopes is reduced compared to 2D (compare figure 5.28a and 5.5b). As a result the depth of the orographic cloud is reduced and no cloud ice is initiated aloft (compare figure 5.28b and 5.6a). The combination of reduced ascent and the lack of q_i aloft to seed the orographic cloud leads to a reduction of peak precipitation rates in 3D of about one-third (figure 5.28d).

The Z_{0C} and Z_S from the 3D case are shown in figure 5.28c. ΔZ_{0C}, ΔZ_S, and ΔZ_{0CtoS} are all reduced as compared to the 2D case, and the reduction in ΔZ_{0CtoS} is 28% (figure

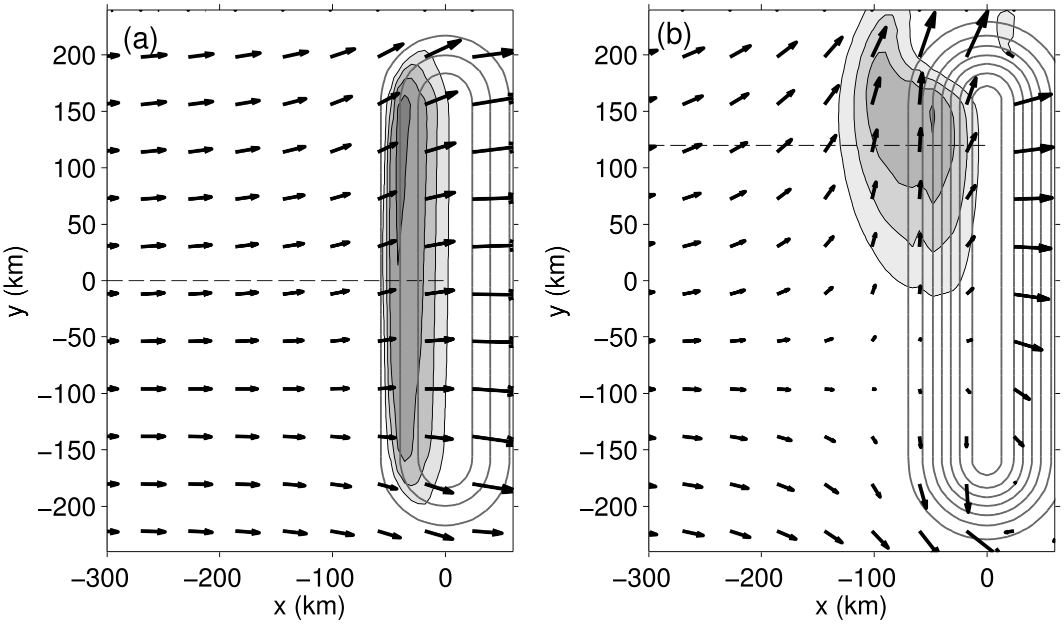

Figure 5.27: Horizontal winds at lowest model level (vectors), precipitation rate (filled contours), and terrain height (gray contours, every 300 m) from intermediate domain ($\Delta x, y$ =6 km) for 3D experiments: (a) for control case (precipitation contoured every 0.5 mm h^{-1}), (b) for blocked case (precipitation contoured every 0.1 mm h^{-1}). Dashed lines show locations of the cross sections shown in figures 5.28 and 5.29

5.28c). A 51 m reduction in $(\Delta Z_{0CtoS})_{micro.}$, caused by reduced precipitation rates, make the largest contribution to the reduction in ΔZ_{0CtoS}. However, the other mechanisms also play a role; the reduced precipitation rates moderate $(\Delta Z_{0CtoS})_{LC}$ by 19 m, and $(\Delta Z_{0CtoS})_{Ad.}$ is reduced by 15 m.

Thus, for the unblocked control case, while 3D effects reduce the magnitude of ΔZ_{0CtoS} somewhat, the fundamental processes remain the same as in 2D (albeit with some change in their relative importance). This suggests that the 2D results from the previous section should still provide useful insights into the more complex 3D problem.

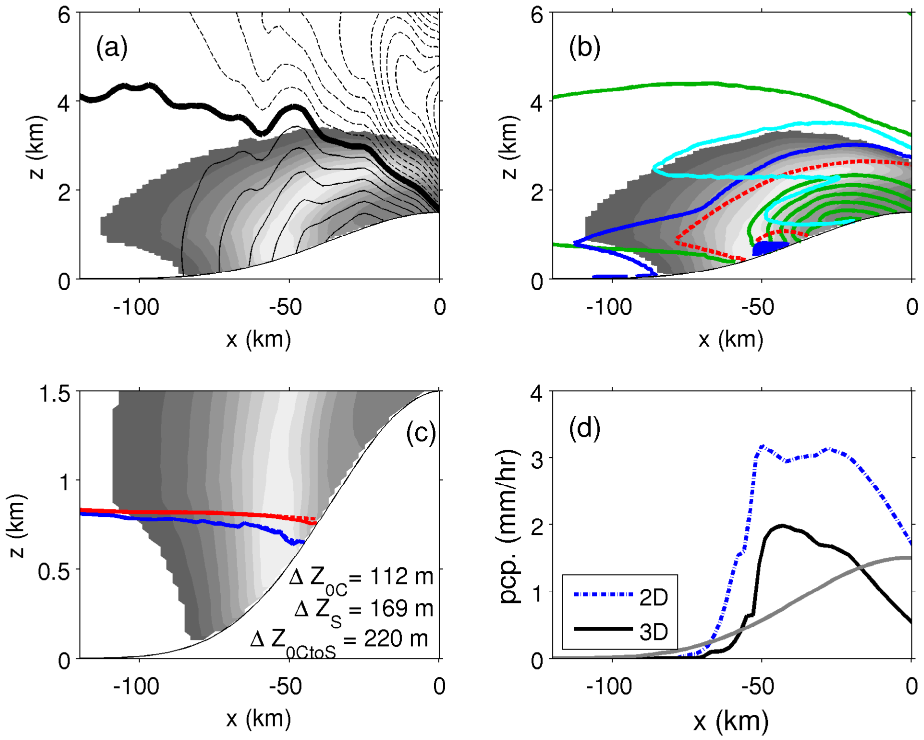

Figure 5.28: Cross sections at $y = 0$ for 3D version of control simulation: (a) w (contoured) and q_c (shaded), as in figure 5.5b; (b) Mixing ratios: q_r, q_s, q_g, and q_i (contoured) and q_c (shaded), as in figure 5.6a; (c) Z_{0C} (red) and Z_S (blue), with (solid) and without (dashed) LCpmelt, and q_c (shaded), as in figure 5.11a; (d) surface precipitation rate compared between 3D and 2D control simulations (see key) with terrain profile (gray).

5.5.2 Blocked: $(N_m h_m)/U = 2$

Since 2D simulations poorly represent airflow and precipitation associated with blocked flows over ridges of finite length (e.g., Epifanio and Durran, 2001; Galewsky, 2008), the 2D simulations presented in this study were mainly restricted to scenarios with $(N_m h_m)/U < 1$. An initial investigation of the effects of blocking on Z_{0C} and Z_S is made by simulating fully 3D flow over a $h_m = 3$ km ridge with aspect ratio $\beta = 5$. To encourage blocking a sounding with strong stability (N_m=0.007 s^{-1}) and weak winds (U=10 m s^{-1}) is used, yielding

$(N_m h_m)/U = 2.1$.

The near-surface horizontal winds and surface precipitation from this case are shown in figure 5.27b. The winds at the lowest levels do not rise over the topography. Instead there is a stagnation point near $y = -60$ km where the cross-mountain flow reaches zero and airflow splits around the mountain. By limiting the lifting of air and condensation of water this deflection of blocked flow around the mountian— an inherently 3D phenomena— severely limits the intensity of the precipitation produced (e.g., Jiang, 2003; Galewsky, 2008). Maximum precipitation rates are about one-fifth of the values in the unblocked 3D-control simulation (figure 5.27). Blocking also has a large impact on the spatial pattern of precipitation. For example, a strong northward deflection of the blocked flow results in enhanced precipitation to the north and no precipitation to the south. Since the incoming flow rises over the decelerated air at low levels, vertical motion and precipitation extend much farther upwind of the mountain as compared to the unblocked case (Galewsky, 2008).

$x - z$ cross-sections through the middle of the precipitating region (y = 120 km) are shown in figure 5.29. Very weak vertical velocities are found at low level, leading to less condensation of cloud water than in the unblocked case (figure 5.29a). Lifting and cloud that extend much farther upwind, since the blocked air effectively increases the width of the barrier. This yields a precipitation pattern more similar to the a=65 km case in 2D (compare figure 5.29d and 5.23c). The hydrometeor mixing ratios are modest (compare figures 5.29d and 5.6a). Both Z_{0C} and Z_S gradually descend over windward slope. The values of ΔZ_{0C}, ΔZ_S, and ΔZ_{0CtoS} are all increased relative to the unblocked 3D case (figure 5.29c).

As in the unblocked case, microphysics make the largest contribution to the lowering of Z_S: $(\Delta Z_{0CtoS})_{micro.}$ =124 m. This large microphysical contribution occurs even with relatively weak precipitation rates, due in part to the weak vertical velocities that allow snow to descend farther below Z_{0C} before melting. Due to higher N_m the adiabatic contribution is increased compared to the unblocked case: $(\Delta Z_{0CtoS})_{Ad.}$ =136 m. However, since splitting of the blocked flow prevents the lowest streamline from surmounting the mountain, $(\Delta Z_{0CtoS})_{Ad.}$ is significantly less than predicted by the parcel model: $(\Delta Z_{0CtoS})_{parcel}$=220 m. Despite the weak precipitation, the contribution from LCpmelt is

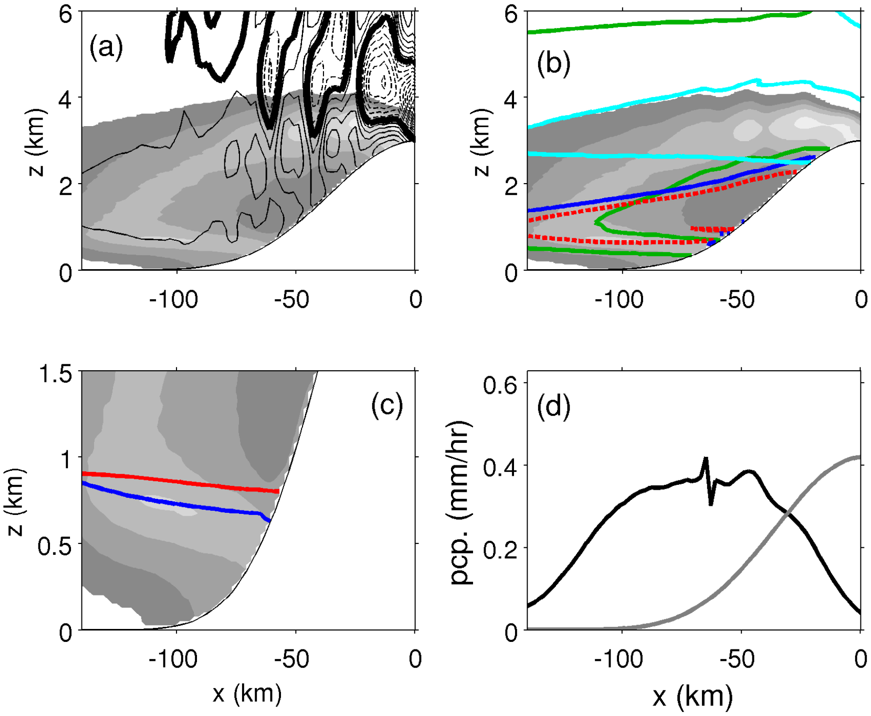

Figure 5.29: $x - z$ cross sections from blocked simulation. As in figure 5.28, but vertical velocities in (a) are contoured every 2 cm s^{-1}.

slightly increased relative to the unblocked case: $(\Delta Z_{0CtoS})_{LC}$ =30 m. Although the flux of frozen hydrometeors through Z_{0C} is reduced with blocking, the increased horizontal extent of the melting region and weak cross-mountain flow increase the residence time of air parcels in the melting layer enough to keep LCpmelt significant.

This initial analysis of the blocked flow regime suggests somewhat larger magnitudes of ΔZ_{0CtoS} but similar physical causes as in the unblocked case. However, it is still unclear how the sensitivity to terrain geometry and atmospheric conditions may differ between 2D and 3D. Further experiments will be required to investigate this issue, and other aspects of the blocked regimes (such as along-ridge variations in the mountainside Z_S, and sensitivity to terrain geometry and degree of blocking).

5.6 Discussion

5.6.1 Limitations

The framework used for experiments in this study has some limitations that present challenges for relating the results to real cases of orographic snowfall. Furthermore, while the semi-idealized WRF simulations produce mesoscale drops in Z_S similar to the climatological mean values observed in the Sierra (Kingsmill et al., 2008), the various WRF simulations fail to produce the extremely large drops (∼1 km) occasionally found in the climatology (Kingsmill et al., 2008) and in case studies (e.g., Medina et al., 2005). This may be an indication that an important process responsible for the behavior of Z_S has been neglected in this study.

Two potentially important components omitted from these simulations are surface fluxes and the effects of boundary layer (BL) mixing. BL's often have near-neutral stratification, so the presence of a BL could reduce $(\Delta Z_{0CtoS})_{Ad.}$. BL's also influence the pattern and intensity of orographic precipitation (e.g., Smith, 2007), and thus could influence $(\Delta Z_{0CtoS})_{micro.}$ and $(\Delta Z_{0CtoS})_{LC}$. Additionally, the use of a free-slip bottom boundary condition results in the simulation of low-level winds that are are much stronger than would occur in nature. More realistic low-level winds could result in larger residence time of air parcels in the melting layer, and potentially much larger $(\Delta Z_{0CtoS})_{LC}$. Unrealistically fast advection of air parcels through the melting region may be responsible for the absence of the often-observed 0°C near-isothermal layer in the current simulations. The effects of surface friction and BL mixing will be investigated in future simulations.

Another limitation stems from the absence of synoptically generated precipitation in the above simulations. Since all the modeled precipitation is generated by orographic lifting, there is no precipitation far upwind of the mountain. In reality, mid-latitude orographic precipitation events are usually associated with synoptic-scale disturbances that do generate precipitation far upwind of a mountain barrier (e.g., Smith, 2006). With finite upwind precipitation, Z_S should be located some distance below Z_{0C} upwind of the barrier. Furthermore, synoptic forcing may increase precipitation intensities, both by the direct generation of precipitation and by the collection of orographic cloud water and ice by synopticaly generated hydrometeors.

In the simulations presented, microphysical variations have often made the largest contribution to ΔZ_{0CtoS} and have played a central role in explaining the sensitivity of the snow line to atmospheric conditions and terrain geometry. Unfortunately, $(\Delta Z_{0CtoS})_{micro.}$ is the component that is simulated with the least confidence, since it depends strongly upon the choice of microphysical parameterization and since none of the schemes in WRF contain detailed representations of the effects of melting on the size distribution and fallspeeds of hydrometeors. Studies examining more sophisticated models of the melting layer and observations suggest that distance from Z_{0C} to Z_S (and thus $(\Delta Z_{0CtoS})_{micro.}$) simulated here is not unreasonable (e.g., Szyrmer and Zawadzki, 1999). Still, simulations with more complete microphysics and observations within orographic melting layers are required to build confidence in the magnitude and sensitivities of $(\Delta Z_{0CtoS})_{micro.}$.

Some other components of real orographic storms that have been omitted include: the transient forcing of vertical motion by fronts, the presence of pre-existing cold air against the mountain, and terrain with small scale variability (i.e., ridges, valleys, passes). Although these may play important roles in nature, the above results demonstrate that substantial mesoscale modifications of Z_S, modifications similar in magnitude to those observed in the climatological mean, may occur without such features.

5.6.2 Implications for mesoscale modeling

The simulation by WRF of ΔZ_S values comparable with observations (e.g., Lundquist et al., 2008; Kingsmill et al., 2008) offers an initial suggestion that current mesoscale models are capable of predicting the mesoscale controls on Z_S. The results of this study suggest that $(\Delta Z_{0CtoS})_{Ad}$ and $(\Delta Z_{0CtoS})_{LC}$ should be well simulated by models that capture the upwind temperature profile, airflow over the windward slopes, and gross pattern of precipitation. Successfully simulating $(\Delta Z_{0CtoS})_{micro.}$ appears to depend on the details of how microphysical processes are parameterized, making it a potentially larger challenge. Future work should quantify the skill of models at representing Z_S over mountains by comparing simulations, using various model configurations, with detailed observations.

5.6.3 Implications for regional climate change

Figure 5.16 suggests that mesoscale processes may play an important role in shaping the impacts of climate warming on mountain snowfall. For instance, if ΔZ_{0CtoS} increases with warming as shown, then the accumulation of mountain snowpack will decrease significantly less than would be suggested by only considering the upwind rise in Z_{0C}. If present in nature, such a mesoscale buffering of climate change may help to reconcile the results of recent studies that have focused on the sensitivity of Cascade snowpack to climate warming. The observationally based results of Stoelinga et al. (2009) estimate a 11% loss of region-averaged spring snowpack per degree Celsius of warming, whereas, using idealized models, Casola et al. (2009) and Minder (2010) estimated values of $16\%\mathrm{C}^{-1}$ and $15\text{-}18\%\mathrm{C}^{-1}$ for Cascade snowpack and snow accumulation sensitivity. The neglect of temperature dependent mesoscale structures in Z_S and Z_{0C} could act to bias the model results towards high snowpack sensitivities and explain the discrepancy between the model and observation based estimates.

Furthermore, if ΔZ_{0CtoS} depends strongly on other aspects of climate (e.g., stability, windspeed/direction) it may be important to go beyond the effect of warming when assessing future climate impacts. The important role for various mesoscale processes in controlling the snow line argues for the use of high resolution dynamical models in investigations regional climate. For instance, hydrological models that investigate changes in snowpack based on regionally uniform warming and surface temperature thresholds for snow accumulation (e.g., Hamlet and Lettenmaier, 1999; Casola et al., 2009; Climate Impacts Group, 2009) may miss important mesoscale influences on mountain snowfall. Further insight into the potential role of mesoscale processes in determing the response of mountainside Z_S to climate change may be gained by examining the behavior of Z_S and Z_{0C} in mesoscale model simulations of regional climates (e.g., Salathé et al., 2008), and by the use of simple models for mountain snow fall (e.g., Minder, 2010).

5.7 Summary and Conclusions

Observations show that a mesoscale lowering of Z_{0C} and Z_S over the windward slopes appears as a pervasive feature of mountain weather and climate (Marwitz, 1987; Medina et al., 2005; Lundquist et al., 2008; Kingsmill et al., 2008). The magnitude of the phenomena is large enough to have important implications for mountain hydroclimate. A number of physical mechanisms appear to be responsible for this behavior. Two of these mechanisms act by lowering Z_{0C}, and consequently Z_S, while the third acts by displacing Z_S farther below Z_{0C}: 1) for stable stratification adiabatic cooling of rising air results in colder temperatures, and lower Z_{0C}, over the mountain than upwind; 2) orographic enhancement of precipitation over the windward slopes results in a localized cooling of the air by melting of frozen hydrometeors that also lowers Z_{0C} relative to the upwind; 3) orographic enhancement of precipitation over the windward slopes results in larger frozen hydrometeors that descend farther below Z_{0C} before melting into rain than in the upwind.

This study has used semi-idealized simulations with a mesoscale numerical atmospheric model to diagnose the processes responsible for determing Z_S on the mesoscale, quantify their relative importance, and investigate their sensitivities to atmospheric conditions and terrain geometry. These simulations have reproduced a mesoscale lowering of Z_S similar to that found in observations. Results reveal that all three of the above processes may play an important role in determing ΔZ_{0CtoS}. The microphysical parameterizations chosen has a large impact on the simulated contribution from spatial variations melting distance, however the adiabatic and latent cooling contributions are only weakly affected.

Contribution from the various processes change depending on the mountain, storm, or climate. 2D simulations suggest that flows with moderate winds, strong stratification, and warm temperatures impinging against tall and wide mountains produce the largest ΔZ_{0CtoS}. While air with strong winds, less stable stratification, and cold temperatures impinging on low and narrow mountains produces relatively small ΔZ_{0CtoS}. Taken together, the simulated sensitivities to atmospheric conditions help to explain the large variability in ΔZ_S observed in the climatology (Kingsmill et al., 2008). Of particular interest is the simulated increase in ΔZ_{0CtoS} with temperature, since such an effect could act to buffer against the impacts of climate warming on mountain hydroclimate.

3D simulations suggest finite ridge length may act to moderate ΔZ_{0CtoS} somewhat for relatively unblocked scenarios by reducing precipitation rates. Under blocked conditions ΔZ_{0CtoS} is still substantial — even increased relative to the unblocked case— despite the reductions in precipitation that occur due to flow splitting and reduced lifting. This is explained by increased residence times for air parcels in the melting region, weak vertical velocities that allow for larger melting distances, and strong adiabatic cooling effects associated with high upwind stability. Additional work is required to better understand the effects of 3D terrain geometry and blocking on Z_S.

The semi-idealized nature of these simulations means that it remains unclear how closely the results represent the behavior of real orographic storms. Inclusion of additional realism, such as boundary layer friction and turbulence, may be required to represent the full range behavior found in reality (such as kilometer-scale drops in Z_S). Nonetheless, this study presents a framework for how the various mesoscale controls on Z_S can be quantified and understood even in more complex scenarios. Using this as a foundation, future work will add additional layers of realism to the simulations and synthesize models results with field observations to give a more complete understanding of the climatology of the rain-snow transition over mountains.

Chapter 6

SUMMARY AND CONCLUSIONS

The climatology of mid-latitude orographic precipitation is important for a range of natural and human systems. It determines the susceptibility of regions to hazards such as flooding and landslides while also cotrolling the volume and timing of streamflow and fresh water resources. The climatological study of orographic precipitation is made challenging by the small spatial scales that must be observed or simulated for successful characterization of patterns and processes. Remote, rugged terrain, computational limitations, and the wide range of important physical processes, contribute to making this a challenging task. This thesis has used a synthesis of numerical models, theory, and field observations, loosely focused on the Cascade and Olympic Mountains of Washington State, to investigate in detail a number of general aspects of mid-latitude orographic precipitation. These include: ridge-valley scale patterns of accumulation, impacts of precipitation patterns on landslide susceptibility, the sensitivity of mountain snowpack to climate warming, and the mesoscale processes controlling the mountainside snow line climatology.

The climatology of small-scale patterns of mountain precipitation is poorly constrained, yet important for applications ranging from natural hazard assessment to understanding the geologic evolution of mountain ranges. Synthesizing four rainy seasons of high-resolution precipitation observations and mesoscale model output (from the MM5 model), reveals a persistent small-scale pattern of precipitation over the ∼10 km wide, ∼800 m high ridges and valleys of the Western Olympic Mountains. This pattern is characterized by a 50-70 % excess accumulation over the ridge crests relative to the adjacent valleys in the annual mean. While the model shows excellent skill in simulating these patterns at seasonal time scales, major errors exist for individual storms.

Investigation of a range of storm events reveals the following mechanism for the climatological pattern. Regions of enhanced condensation of cloud water are produced by ascent in stable flow over the windward slopes of major ridges. Synoptically generated precipitation grows by collection within these clouds, leading to enhanced precipitation, which is advected by the prevailing winds. Instances of atypical patterns of precipitation suggest that under certain conditions (during periods with low freezing-levels, or convective cells) fundamental changes in small-scale patterns may occur. However, case studies and composite analysis suggest that departures from the pattern of ridge-top enhancement are rare; the basic patterns and processes appear robust to changes in temperature, winds, and background rainfall rates.

The effect of spatial patterns in climatological mountain rainfall, such as those found in the Olympics, on shallow landslide susceptibility are examined by forcing a physically based model of slope stability (SHALSTAB) with the rainfall pattern produced by the MM5 over the western Olympic Mountains of Washington state. Results suggest that, for two small basins in the Olympics, 10 km scale variations in rainfall have a non-trivial effect on landslide susceptibility. Assuming uniform rainfall equal to the average rainfall over the basins results in a moderate underestimate of landslide susceptibility. If climatological data from a lowland station is used to characterize the rainfall over the basins a substantial underestimate of susceptibility occurs. The effect of spatial variability in rainfall on variations in stability is comparable with the effect of moderate-to-large variability in soil parameters (such as ±30% variations in soil thickness). At a practical level, these results imply that accounting for persistent patterns of rainfall may aid in discerning regions within the same watershed where similar land use practices will lead to differing landslide risk.

Controls on the sensitivity of mountain snowpack accumulation to climate warming, λ_S, are also investigated. This is accomplished using two idealized, physically based models of mountain snowfall to simulate snowpack accumulation for the Cascade Mountains under current and warmed climates. Both models are forced from sounding observations. The first model uses the Linear Theory (LT) model of orographic precipitation to predict precipitation as a function of the incoming flow characteristics, and uses the sounding temperatures to estimate the elevation of the rain-snow boundary, called the melting level (ML). The second "ML model" uses only the ML from the sounding, and assumptions of uniform and constant precipitation.

Both models simulate increases in precipitation intensity and elevated storm ML's under climate warming. The LT model predicts a 14.8-18.1% loss of Cascade snowfall per degree of warming, depending on the vertical structure of the warming. The loss of snowfall is significantly greater, 19.4-22.6%, if precipitation increases are neglected. Comparing the two models shows that the predominant control on λ_S is the relationship between the distribution of storm ML's and the distribution of topographic area with elevation. While increases in precipitation due to warming may act to moderate λ_S, the loss of snow accumulation area profoundly limits the ability of precipitation increases to maintain the snowpack under substantial climate warming (beyond 1-2°C). Circulation changes may act to moderate or exacerbate the loss of mountain snowpack under climate change, via impacts on orographic precipitation enhancement.

One of the most fundamental aspects of mountain weather and climate is the snow line, the boundary between lowland rainfall and mountain snowfall. Precise knowledge of the snow line is of value, since modest changes of 100-200 m in the elevation of the snow line can have major impacts on snowpack accumulation and flooding. Perhaps the simplest expectation is that the mountainside snow line will reside at about the elevation of the 0°C isotherm upwind of a mountain. However, as air passes over a mountain the temperature and distribution of precipitation is profoundly altered; as a result, on the mountainside the snow line is often located at an elevation hundreds of meters different from its elevation in the free air upwind of the mountain. This mesoscale modification of the snow line is poorly understood, is not resolved by global models, and is large enough to have major impacts on a variety of natural and human systems.

Semi-idealized simulations with a mesoscale numerical weather prediction model (WRF) are used to simulate the rain-snow boundary over mountains for stably stratified orographic precipitation. These simulations allow the identification of the physical mechanisms responsible for mesoscale structure of the snow line. Results reveal that spatial variations in latent cooling from melting precipitation, adiabatic cooling from vertical motion, and the melting distance of frozen hydrometeors all play important roles. The simulated role of hydrometeor melting distance is sensitive to the choice of microphysical parameterization. The identified mechanisms can account for drops in the snow line of the magnitude observed in the climatological mean.

The relative importance of the identified mechanisms for lowering the snow line depends on the properties of the incoming flow and the terrain geometry. Temperature, wind speed, stability, relative humidity, terrain height, and terrain width all play an important role in determing the mesoscale structure of the snow line. The simulated sensitivities to atmospheric conditions help to explain the variability in the snow line drop observed in climatologies. One sensitivity of particular interest is the simulated increase with temperature of the mountainside snowline's displacement below the upstream 0°C level. If such a relationship exists in nature it could act to buffer mountain hydroclimates against the impacts of climate warming.

Three-dimensional airflow dynamics, associated with ridges of finite length and blocked flows, have important impacts on the mesoscale processes that control the snow line. Initial analyses show that certain blocked flows can be associated with even larger drops in the snow line than unblocked flows. Further work examining the snow line in blocked regimes and in the presence of surface friction and boundary layer mixing, as well as syntheses of modeling and observations, are required to expand understanding of the behavior of the snow line over mountains.

BIBLIOGRAPHY

Alpert, P., H. Shafir, and W. Cotton, 1994: Prediction of meso-γ scale orographic precipitation. *Trends in Hydrology*, **1**, 403–441.

Anders, A. M., G. Roe, D. Montgomery, and B. Hallet, 2008: Influence of precipitation phase on the form of mountain ranges. *Geology*, **36 (6)**, 479–482, doi:10.1130/G24821A.1.

Anders, A. M., G. H. Roe, D. R. Durran, and J. R. Minder, 2007: Small-scale spatial gradients in climatological precipitation on the Olympic Peninsula. *Journal of Hydrometeorology*, **8 (5)**, 1068–1081.

Anders, A. M., G. H. Roe, B. Hallet, D. R. Montgomery, N. Finnegan, and J. Putkonen, 2006: Spatial patterns of precipitation and topography in the Himalaya. *Tectonics, Climate, and Landscape Evolution: Geological Society of America Special Paper 398*, S. Willett, N. Hovius, M. Brandon, and D. Fisher, Eds., Boulder, CO, 39–53.

Anderson, E. A., 1976: A point energy and mass balance model of a snow cover. NOAA technical report 19, US Dept. of Commerce, 150 p pp., Silver Spring, MD.

Arendt, A., J. Walsh, and W. Harrison, 2009: Changes of glaciers and climate in northwestern North America during the late twentieth century. *Journal of Climate*, **22 (15)**, 4117–4134, doi:10.1175/2009JCLI2784.1.

Baeza, C. and J. Corominas, 2001: Assessment of shallow landslide susceptibility by means of multivariate statistical techniques. *Earth Surface Processes and Landforms*, **26 (12)**, 1251–1263.

Banta, R., 1990: The role of mountain flows in making clouds. *Atmospheric Processes Over Complex Terrain: Meteorological Monographs vol. 23, no. 45*, W. Blumen, Ed., Boston, MA.

Barnett, T. P., J. C. Adam, and D. P. Lettenmaier, 2005: Potential impacts of a warming climate on water availability in snow-dominated regions. *Nature*, **438 (7066)**, 303–309, doi:10.1038/nature04141.

Barstad, I. and R. B. Smith, 2005: Evaluation of an orographic precipitation model. *Journal of Hydrometeorology*, **6 (1)**, 85–99.

Beniston, M., F. Keller, B. Koffi, and S. Goyette, 2003: Estimates of snow accumulation and volume in the Swiss Alps under changing climatic conditions. *Theoretical and Applied Climatology*, **76 (3–4)**, 125–140, doi:10.1007/s00704-003-0016-5.

Bergeron, T., 1960: Operation and results of 'Project Pluvius'. *Physics of Precipitation*, 152–157.

Bergeron, T., 1968: On the low-level distribution of atmospheric water caused by orography. *Int. Cloud Phys. Conf.*, Toronto, 96–100.

Biswas, A. K. and K. O. L. F. Jayaweera, 1976: NOAA-3 satellite-observations of thunderstorms in Alaska. *Monthly Weather Review*, **104 (3)**, 292–297.

Bond, N. A., et al., 1997: The Coastal Observation and Simulation with Topography (COAST) experiment. *Bulletin of the American Meteorological Society*, **78 (9)**, 1941–1955.

Bougeault, P., et al., 2001: The MAP special observing period. *Bulletin of the American Meteorological Society*, **82 (3)**, 433–462.

Bousquet, O. and B. F. Smull, 2003: Observations and impacts of upstream blocking during a widespread orographic precipitation event. *Quarterly Journal of the Royal Meteorological Society*, **129 (588)**, 391–409, doi:10.1256/qj.02.49.

Browning, K. A., F. F. Hill, and C. W. Pardoe, 1974: Structure and mechanism of precipitation and effect of orography in a wintertime warm sector. *Quarterly Journal of the Royal Meteorological Society*, **100 (425)**, 309–330.

Bruintjes, R. T., T. L. Clark, and W. D. Hall, 1994: Interactions between topographic air-flow and cloud / precipitation development during the passage of a winter storm in Arizona. *Journal of the Atmospheric Sciences*, **51 (1)**, 48–67.

Caine, N., 1980: The rainfall intensity-duration control of shallow landslides and debris flows. *Geografiska Annaler Series A-physical Geography*, **62 (1)**, 23–27.

Campbell, R., 1975: Remote rainfall sensing for landslide hazard analysis. *U.S. Geological Survey Open-File Report 75-851.*

Carruthers, D. J. and T. W. Choularton, 1983: A model of the feeder seeder mechanism of orographic rain including stratification and wind-drift effects. *Quarterly Journal of the Royal Meteorological Society*, **109 (461)**, 575–588.

Casadel, M., W. E. Dietrich, and N. L. Miller, 2003: Testing a model for predicting the timing and location of shallow landslide initiation in soil-mantled landscapes. *Earth Surface Processes and Landforms*, **28 (9)**, 925–950, doi:10.1002/esp.470.

Casola, J., L. Cuo, B. Livneh, D. Lettenmaier, M. Stoelinga, P. Mote, and J. Wallace, 2009: Assessing the impacts of global warming on snowpack in the Washington Cascades. *Journal of Climate*, **22 (10)**, 2758–2772, doi:10.1175/2008JCLI2612.1.

Cayan, D. R., 1996: Interannual climate variability and snowpack in the western United States. *Journal of Climate*, **9 (5)**, 928–948.

Chang, K., S. Chiang, and F. Lei, 2008: Analysing the relationship between typhoon-triggered landslides and critical rainfall conditions. *Earth Surface Processes and Landforms*, **33 (8)**, 1261–1271, doi:10.1002/esp.1611.

Chen, S. H. and W. Y. Sun, 2002: A one-dimensional time dependent cloud model. *Journal of the Meteorological Society of Japan*, **80 (1)**, 99–118.

Choularton, T. W. and S. J. Perry, 1986: A model of the orographic enhancement of snowfall by the seeder-feeder mechanism. *Quarterly Journal of the Royal Meteorological Society*, **112 (472)**, 335–345.

Climate Impacts Group, 2009: *Washington Climate Change Impacts Assesment: Evaluating Washington's Future in a Changing Climate*. University of Washington, Seattle, Washington.

Colle, B. A., 2004: Sensitivity of orographic precipitation to changing ambient conditions and terrain geometries: An idealized modeling perspective. *Journal of the Atmospheric Sciences*, **61 (5)**, 588–606.

Colle, B. A., 2007: Two-dimensioal idealized simulations of the impact of multiple windward ridges on orographic precipitation. *Journal of Atmospheric Science*, submitted.

Colle, B. A., M. F. Garvert, J. B. Wolfe, C. F. Mass, and C. P. Woods, 2005: The 13–14 December 2001 IMPROVE-2 event. Part III: Simulated microphysical budgets and sensitivity studies. *Journal of the Atmospheric Sciences*, **62 (10)**, 3535–3558.

Colle, B. A. and C. F. Mass, 1996: An observational and modeling study of the interaction of low-level southwesterly flow with the Olympic mountains during COAST IOP 4. *Monthly Weather Review*, **124 (10)**, 2152–2175.

Colle, B. A., C. F. Mass, and K. J. Westrick, 2000: MM5 precipitation verification over the Pacific Northwest during the 1997–99 cool seasons. *Weather and Forecasting*, **15 (6)**, 730–744.

Colle, B. A. and S. E. Yuter, 2007: The impact of coastal boundaries and small hills on the precipitation distribution across southern Connecticut and Long Island, New York. *Monthly Weather Review*, **135 (3)**, 933–954.

Colle, B. A. and Y. G. Zeng, 2004a: Bulk microphysical sensitivities within the MM5 for orographic precipitation. Part I: The Sierra 1986 event. *Monthly Weather Review*, **132 (12)**, 2780–2801.

Colle, B. A. and Y. G. Zeng, 2004b: Bulk microphysical sensitivities within the MM5 for orographic precipitation. Part II: Impact of barrier width and freezing level. *Monthly Weather Review*, **132 (12)**, 2802–2815.

Conway, H. and C. F. Raymond, 1993: Snow stability during rain. *Journal of Glaciology*, **39 (133)**, 635–642.

Crochet, P., T. Johannesson, T. Jonsson, O. Sigurdsson, H. Bjonsson, F. Palsson, and I. Barstad, 2007: Estimating the spatial distribution of precipitation in Iceland using a linear model of orographic precipitation. *Journal of Hydrometeorology*, **8 (6)**, 1285–1306, doi:10.1175/2007JHM795.1.

Dai, A. G., 2008: Temperature and pressure dependence of the rain-snow phase transition over land and ocean. *Geophysical Research Letters*, **35 (12)**, doi:10.1029/2008GL033295.

Daly, C., W. P. Gibson, G. H. Taylor, G. L. Johnson, and P. Pasteris, 2002: A knowledge-based approach to the statistical mapping of climate. *Climate Research*, **22 (2)**, 99–113.

Daly, C., M. Halbleib, J. Smith, W. Gibson, M. Doggett, G. Taylor, J. Curtis, and P. Pasteris, 2008: Physiographically sensitive mapping of climatological temperature and precipitation across the conterminous United States. *International Journal of Climatology*, **28 (15)**, 2031–2064, doi:10.1002/joc.1688.

Diaz, H. F., J. K. Eischeid, C. Duncan, and R. S. Bradley, 2003: Variability of freezing levels, melting season indicators, and snow cover for selected high-elevation and continental regions in the last 50 years. *Climatic Change*, **59 (1–2)**, 33–52.

Doyle, J. D. and Q. F. Jiang, 2006: Observations and numerical simulations of mountain waves in the presence of directional wind shear. *Quarterly Journal of the Royal Meteorological Society*, **132 (619)**, 1877–1905.

Dudhia, J., 1989: Numerical study of convection observed during the winter monsoon experiment using a mesoscale two-dimensional model. *Journal of the Atmospheric Sciences*, **46 (20)**, 3077–3107.

Durran, D. R. and J. B. Klemp, 1982: On the effects of moisture on the Brunt-Väisälä frequency. *Journal of the Atmospheric Sciences*, **39 (10)**, 2152–2158.

Epifanio, C. C. and D. R. Durran, 2001: Three-dimensional effects in high-drag-state flows over long ridges. *Journal of the Atmospheric Sciences*, **58 (9)**, 1051–1065.

Fabry, F. and T. Zawadzki, 1995: Long-term radar observations of the melting layer of precipitation and their interpretation. *Journal of the Atmospheric Sciences*, **52 (7)**, 838–851.

Findeisen, W., 1940: The formation of the 0 degree C isothermal layer in fractocumulus and nimbostratus. *Meteorologische Zeitschrift*, **57**, 49–54.

Frei, C. and C. Schär, 1998: A precipitation climatology of the Alps from high-resolution rain-gauge observations. *International Journal of Climatology*, **18 (8)**, 873–900.

Frierson, D. W., 2006: Robust increases in midlatitude static stability in simulations of global warming. *Geophysical Research Letters*, **33 (24)**, doi:10.1029/2006GL027504.

Fuhrer, O. and C. Schär, 2005: Embedded cellular convection in moist flow past topography. *Journal of the Atmospheric Sciences*, **62 (8)**, 2810–2828.

Galewsky, J., 2008: Orographic clouds in terrain-blocked flows: An idealized modeling study. *Journal of the Atmospheric Sciences*, **65 (11)**, 3460–3478, doi:10.1175/2008JAS2435.1.

Garvert, M. F., B. Smull, and C. Mass, 2007: Multiscale mountain waves influencing a major orographic precipitation event. *Journal of the Atmospheric Sciences*, **64 (3)**, 711–737.

Giorgi, F., J. W. Hurrell, M. R. Marinucci, and M. Beniston, 1997: Elevation dependency of the surface climate change signal: A model study. *Journal of Climate*, **10 (2)**, 288–296.

Giovannettone, J. and A. Barros, 2009: Probing regional orographic controls of precipitation and cloudiness in the central Andes using satellite data. *Journal of Hydrometeorology*, **10 (1)**, 167–182, doi:10.1175/2008JHM973.1.

Gorsevski, P. V., P. E. Gessler, J. Boll, W. J. Elliot, and R. B. Foltz, 2006: Spatially and temporally distributed modeling of landslide susceptibility. *Geomorphology*, **80 (3–4)**, 178–198, doi:10.1016/j.geomorph.2006.02.011.

Grell, G., J. Dudhia, and D. Stauffer, 1995: Description of the fifth-generation Penn State/NCAR mesoscale model (MM5). NCAR tech. note NCAR/TN-398 1 STR, National Center for Atmospheric Research, 122 pp., Boulder, CO.

Groisman, P. Y. and D. R. Legates, 1994: The accuracy of United-States precipitation data. *Bulletin of the American Meteorological Society*, **75 (2)**, 215–227.

Grubisic, V., R. K. Vellore, and A. W. Huggins, 2005: Quantitative precipitation forecasting of wintertime storms in the Sierra Nevada: Sensitivity to the microphysical parameterization and horizontal resolution. *Monthly Weather Review*, **133 (10)**, 2834–2859.

Gupta, R. and B. Joshi, 1990: Landslide hazard zoning using the GIS approach - a case-study from the Ramganga catchment, Himalayas. *Engineering Geology*, **28 (1–2)**, 119–131.

Guzzetti, F., S. Peruccacci, M. Rossi, and C. Stark, 2008: The rainfall intensity-duration control of shallow landslides and debris flows: an update. *Landslides*, **5 (1)**, 3–17, doi: 10.1007/s10346-007-0112-1.

Hack, J. J., B. A. Boville, B. P. Briegleb, J. T. Kiehl, P. J. Rasch, and D. L. Williamson, 1993: Description of the NCAR Community Climate Model (CCM2). *NCAR Technical Note, NCAR/TN-382+STR*, 120 pp.

Hahn, R. and C. Mass, 2009: The impact of positive-definite moisture advection and low-level moisture flux bias over orography. *Monthly Weather Review*, **137 (9)**, 3055–3071, doi:10.1175/2009MWR2873.1.

Hamlet, A. F. and D. P. Lettenmaier, 1999: Effects of climate change on hydrology and water resources in the Columbia River basin. *Journal of the American Water Resources Association*, **35 (6)**, 1597–1623.

Hamlet, A. F. and D. P. Lettenmaier, 2007: Effects of 20th century warming and climate variability on flood risk in the western U.S. *Water Resources Research*, **43 (6)**, doi: 10.1029/2006WR005099.

Hamlet, A. F., P. W. Mote, M. P. Clark, and D. P. Lettenmaier, 2005: Effects of temperature and precipitation variability on snowpack trends in the western United States. *Journal of Climate*, **18 (21)**, 4545–4561.

Harris, L. and D. Durran, 2010: An idealized comparison of one-way and two-way grid nesting. *Monthly Weather Review*, in press.

Held, I. M. and B. J. Soden, 2006: Robust responses of the hydrological cycle to global warming. *Journal of Climate*, **19 (21)**, 5686–5699.

Hill, F. F., K. A. Browning, and M. J. Bader, 1981: Radar and rain-gauge observations of orographic rain over South-Wales. *Quarterly Journal of the Royal Meteorological Society*, **107 (453)**, 643–670.

Hobbs, P., L. Radke, A. Fraser, and R. Weiss, 1971: The Cascade Project: A study of winter cyclonic storms in the Pacific Northwest. *Proc. Int. Conf. on Weather Modification*, Canberra, Australia.

Hobbs, P. V., 1975: Nature of winter clouds and precipitation in cascade mountains and their modification by artificial seeding. Part 1: Natural conditions. *Journal of Applied Meteorology*, **14 (5)**, 783–804.

Hobbs, P. V., 1978: Organization and structure of clouds and precipitation on mesoscale and microscale in cyclonic storms. *Reviews of Geophysics*, **16 (4)**, 741–755.

Hobbs, P. V., R. C. Easter, and A. B. Fraser, 1973: Theoretical study of flow of air and fallout of solid precipitation over mountainous terrain: Part II. microphysics. *Journal of the Atmospheric Sciences*, **30 (5)**, 813–823.

Hohenegger, C., P. Brockhaus, and C. Schar, 2008: Towards climate simulations at cloud-resolving scales. *Meteorologische Zeitschrift*, **17 (4)**, 383–394, doi:10.1127/0941-2948/2008/0303.

Hong, S. and J. Lim, 2006: The WRF Single-Moment 6-class microphysics scheme (WSM6). *Journal of the Korean Meteorological Society*, **42**, 129–151.

Hong, S. Y., J. Dudhia, and S. H. Chen, 2004: A revised approach to ice microphysical processes for the bulk parameterization of clouds and precipitation. *Monthly Weather Review*, **132 (1)**, 103–120.

Hong, S. Y. and H. L. Pan, 1996: Nonlocal boundary layer vertical diffusion in a medium-range forecast model. *Monthly Weather Review*, **124 (10)**, 2322–2339.

Hong, Y., R. Adler, and G. Huffman, 2006: Evaluation of the potential of NASA multi-satellite precipitation analysis in global landslide hazard assessment. *Geophysical Research Letters*, **33 (L22402)**, 54–68.

Houze, R., 1993: *Cloud Dynamics*. Academic Press, San Diego, CA.

Houze, R. A., C. N. James, and S. Medina, 2001: Radar observations of precipitation and airflow on the Mediterranean side of the Alps: Autumn 1998 and 1999. *Quarterly Journal of the Royal Meteorological Society*, **127 (578)**, 2537–2558.

Houze, R. A. and S. Medina, 2005: Turbulence as a mechanism for orographic precipitation enhancement. *Journal of the Atmospheric Sciences*, **62 (10)**, 3599–3623.

Howat, I. M. and S. Tulaczyk, 2005: Climate sensitivity of spring snowpack in the Sierra Nevada. *Journal of Geophysical Research-earth Surface*, **110 (4)**, doi:10.1029/2005JF000356.

Huff, F. A., S. A. Changnon, and D. M. A. Jones, 1975: Precipitation increases in low hills of southern Illinois. Part 1: Climatic and network studies. *Monthly Weather Review*, **103 (9)**, 823–829.

Iverson, R., 2000: Landslide triggering by rain infiltration. *Water Resources Research*, **36 (7)**, 1879–1910.

James, C. and R. Houze, 2005: Modification of precipitation by coastal orography in storms crossing Northern California. *Monthly Weather Review*, **133**, 3110–3130.

Jankov, I., J. Bao, P. Neiman, P. Schultz, H. Yuan, and A. White, 2009: Evaluation and comparison of microphysical algorithms in ARW-WRF model simulations of atmospheric river events affecting the California coast. *Journal of Hydrometeorology*, **10 (4)**, 847–870, doi:10.1175/2009JHM1059.1.

Javier, J. R. N., J. A. Smith, J. England, M. L. Baeck, M. Steiner, and A. A. Ntelekos, 2007: Climatology of extreme rainfall and flooding from orographic thunderstorm systems in the upper Arkansas River basin. *Water Resources Research*, **43 (10)**, doi:10.1029/2006WR005093.

Jiang, Q. F., 2003: Moist dynamics and orographic precipitation. *Tellus Series A-dynamic Meteorology and Oceanography*, **55 (4)**, 301–316.

Jiang, Q. F. and R. B. Smith, 2003: Cloud timescales and orographic precipitation. *Journal of the Atmospheric Sciences*, **60 (13)**, 1543–1559.

Kain, J. S., 2004: The Kain-Fritsch convective parameterization: An update. *Journal of Applied Meteorology*, **43 (1)**, 170–181.

Kalnay, E., et al., 1996: The NCEP/NCAR 40-year reanalysis project. *Bulletin of the American Meteorological Society*, **77 (3)**, 437–471.

Kingsmill, D., A. White, D. Gottas, and P. Neiman, 2008: Spatial variability of the snow level across the northern California Sierra Nevada. *Proceedings of the 13th AMS Conference on Mountain Meteorology*, American Meteorlogical Society.

Kirshbaum, D. and R. Smith, 2008: Temperature and moist-stability effects on midlatitude orographic precipitation. *Quarterly Journal of the Royal Meteorological Society*, **134 (634)**, 1183–1199, doi:10.1002/qj.274.

Kirshbaum, D. J., G. Bryan, R. Rottuno, and D. R. Durran, 2007: The triggering of orographic rainbands by small-scale topography. *Journal of the Atmospheric Sciences*, in press.

Kirshbaum, D. J. and D. R. Durran, 2004: Factors governing cellular convection in orographic precipitation. *Journal of the Atmospheric Sciences*, **61 (6)**, 682–698.

Kirshbaum, D. J. and D. R. Durran, 2005: Observations and modeling of banded orographic convection. *Journal of the Atmospheric Sciences*, **62 (5)**, 1463–1479.

Kitchen, M. and R. M. Blackall, 1992: Orographic rainfall over low hills and associated corrections to radar measurements. *Journal of Hydrology*, **139 (1)**, 115–134.

Klaassen, W., 1988: Radar observations and simulation of the melting layer of precipitation. *Journal of the Atmospheric Sciences*, **45 (24)**, 3741–3753.

Klemp, J., J. Dudhia, and A. Hassiotis, 2008: An upper gravity-wave absorbing layer for NWP applications. *Monthly Weather Review*, **136 (10)**, 3987–4004, doi:10.1175/2008MWR2596.1.

Klemp, J. B. and D. R. Durran, 1983: An upper boundary-condition permitting internal gravity-wave radiation in numerical mesoscale models. *Monthly Weather Review*, **111 (3)**, 430–444.

Knowles, N., M. D. Dettinger, and D. R. Cayan, 2006: Trends in snowfall versus rainfall in the Western United States. *Journal of Climate*, **19 (18)**, 4545–4559.

Kuo, J. and H. Orville, 1973: A radar climatology of convective clouds in the Black Hills. *Journal of Applied Meteorology*, **12**, 359–368.

Lalas, D. P. and F. Einaudi, 1973: Stability of a moist atmosphere in presence of a background wind. *Journal of the Atmospheric Sciences*, **30 (5)**, 795–800.

Lee, S., J. H. Ryu, K. D. Min, and J. S. Won, 2003: Landslide susceptibility analysis using GIS and artificial neural network. *Earth Surface Processes and Landforms*, **28 (12)**, 1361–1376, doi:10.1002/esp.593.

Leung, L. R. and Y. Qian, 2003: The sensitivity of precipitation and snowpack simulations to model resolution via nesting in regions of complex terrain. *Journal of Hydrometeorology*, **4 (6)**, 1025–1043.

Leung, L. R., Y. Qian, and X. D. Bian, 2003a: Hydroclimate of the western United States based on observations and regional climate simulation of 1981-2000. Part I: Seasonal statistics. *Journal of Climate*, **16 (12)**, 1892–1911.

Leung, L. R., Y. Qian, X. D. Bian, and A. Hunt, 2003b: Hydroclimate of the western United States based on observations and regional climate simulation of 1981-2000. Part II: Mesoscale ENSO anomalies. *Journal of Climate*, **16 (12)**, 1912–1928.

Leung, L. R., Y. Qian, X. D. Bian, W. M. Washington, J. G. Han, and J. O. Roads, 2004: Mid-century ensemble regional climate change scenarios for the western United States. *Climatic Change*, **62 (1–3)**, 75–113.

Lin, C. A. and R. E. Stewart, 1986: Mesoscale circulations initiated by melting snow. *Journal of Geophysical Research-atmospheres*, **91 (12)**, 3299–3302.

Lin, Y. and B. Colle, 2009: The 4-5 December 2001 IMPROVE-2 event: Observed microphysics and comparisons with the Weather Research and Forecasting model. *Monthly Weather Review*, **137 (4)**, 1372–1392, doi:10.1175/2008MWR2653.1.

Lin, Y. L., R. D. Farley, and H. D. Orville, 1983: Bulk parameterization of the snow field in a cloud model. *Journal of Climate and Applied Meteorology*, **22 (6)**, 1065–1092.

Lingley, L., 1999: Geology: Chapter 2 modular reports. *Quinault River watershed analysis: Quinault Indian Nation*, Quinault Indian Nation, U.S. Forest Service, U.S. Geological Survey, and others, Vol. 1.

Lundquist, J., J. Minder, P. Neiman, and E. Sukovich, 2010: Relationships between barrier jet heights, precipitation distributions, and streamflow in the norhtern Sierra Nevada. *Water Resources Research*, **Accepted**.

Lundquist, J., P. Neiman, B. Martner, A. White, D. Gottas, and F. Ralph, 2008: Rain versus snow in the Sierra Nevada, California: Comparing Doppler profiling radar and surface observations of melting level. *Journal of Hydrometeorology*, **9 (2)**, 194–211, doi:10.1175/2007JHM853.1.

MacLeod, A., 2006: Coupling meteorological data with hydrologic and slope stability models to constrain controls on shallow landsliding. M.S. thesis, University of Oregon.

Marwitz, J. D., 1983: The kinematics of orographic air-flow during Sierra storms. *Journal of the Atmospheric Sciences*, **40 (5)**, 1218–1227.

Marwitz, J. D., 1987: Deep orographic storms over the Sierra-Nevada Part I: Thermodynamic and kinematic structure. *Journal of the Atmospheric Sciences*, **44 (1)**, 159–173.

Mass, C., 1981: Topographically forced convergence in western washington state. *Monthly Weather Review*, **109 (6)**, 1335–1347.

Mass, C. F., et al., 2003: Regional environmental prediction over the Pacific Northwest. *Bulletin of the American Meteorological Society*, **84 (10)**, 1353–1366.

Matsuo, T. and Y. Sasyo, 1981: Melting of snowflakes below the freezing level in the atmosphere. *Journal of the Meteorlogical Society of Japan*, **59 (1)**, 10–24.

McCaughey, W. W. and P. E. Farnes, 1996: Measuring winter precipitation with an antifreeze based tipping bucket gauge, Bend, OR. 130–136.

Medina, S. and R. A. Houze, 2003: Air motions and precipitation growth in Alpine storms. *Quarterly Journal of the Royal Meteorological Society*, **129 (588)**, 345–371.

Medina, S., B. F. Smull, R. A. Houze, and M. Steiner, 2005: Cross-barrier flow during orographic precipitation events: Results from MAP and IMPROVE. *Journal of the Atmospheric Sciences*, **62 (10)**, 3580–3598.

Medina, S., E. Sukovich, and R. A. Houze, 2007: Vertical structures of precipitation in cyclones crossing the Oregon Cascades. *Monthly Weather Review*, **135 (10)**, 3565–3586, doi:10.1175/MWR3470.1.

Miglietta, M. M. and R. Rotunno, 2005: Simulations of moist nearly neutral flow over a ridge. *Journal of the Atmospheric Sciences*, **62 (5)**, 1410–1427.

Miglietta, M. M. and R. Rotunno, 2006: Further results on moist nearly neutral flow over a ridge. *Journal of the Atmospheric Sciences*, **63 (11)**, 2881–2897.

Minder, J., 2010: The sensitivity of mountain snowpack accumulation to climate warming. *Journal of Climate*, **23 (10)**, 2634–2650.

Minder, J., D. Durran, G. Roe, and A. Anders, 2008: The climatology of small-scale orographic precipitation over the Olympic Mountains: Patterns and processes. *Quarterly Journal of the Royal Meteorological Society*, **134 (633)**, 817–839, doi:10.1002/qj.258.

Minder, J. and G. Roe, 2010: Orographic precipitation. *The Encyclopedia of Snow, Ice, and Glaciers*, V. P. Singh, P. Singh, and U. K. Haritashya, Eds., Springer.

Minder, J., G. Roe, and D. Montgomery, 2009: Spatial patterns of rainfall and shallow landslide susceptibility. *Water Resources Research*, **45**, doi:10.1029/2008WR007027.

Mitra, S. K., O. Vohl, M. Ahr, and H. R. Pruppacher, 1990: A wind-tunnel and theoretical-study of the melting behavior of atmospheric ice particles. Part 4: Experiment and theory for snow flakes. *Journal of the Atmospheric Sciences*, **47 (5)**, 584–591.

Montgomery, D., K. Schmidt, H. Greenberg, and W. Dietrich, 2000: Forest clearing and regional landsliding. *Geology*, **28 (4)**, 311–314.

Montgomery, D. R. and W. E. Dietrich, 1994: A physically-based model for the topographic control on shallow landsliding. *Water Resources Research*, **30 (4)**, 1153–1171.

Montgomery, D. R., K. Sullivan, and H. M. Greenberg, 1998: Regional test of a model for shallow landsliding. *Hydrological Processes*, **12 (6)**, 943–955.

Morrison, H., J. A. Curry, and V. I. Khvorostyanov, 2005: A new double-moment microphysics parameterization for application in cloud and climate models. Part I: Description. *Journal of the Atmospheric Sciences*, **62 (6)**, 1665–1677.

Morrison, H., G. Thompson, and V. Tatarskii, 2009: Impact of cloud microphysics on the development of trailing stratiform precipitation in a simulated squall line: Comparison of one- and two-moment schemes. *Monthly Weather Review*, **137 (3)**, 991–1007, doi:10.1175/2008MWR2556.1.

Morrissey, M., G. Wieczorek, and B. Morgan, 2004: Transient hazard model using radar data for predicting debris flows in Madison County, Virginia. *Environmental & Engineering Geoscience*, **10 (4)**, 285–296.

Mote, P., A. Hamlet, and E. Salathé, 2008: Has spring snowpack declined in the Washington Cascades? *Hydrology and Earth System Sciences*, **12 (1)**, 193–206.

Mote, P. W., 2006: Climate-driven variability and trends in mountain snowpack in western North America. *Journal of Climate*, **19 (23)**, 6209–6220.

Mote, P. W., A. F. Hamlet, M. P. Clark, and D. P. Lettenmaier, 2005: Declining mountain snowpack in western North America. *Bulletin of the American Meteorological Society*, **86 (1)**, 39–49.

Neiman, P., F. Ralph, G. Wick, Y. Kuo, T. Wee, Z. Ma, G. Taylor, and M. Dettinger, 2008: Diagnosis of an intense atmospheric river impacting the Pacific Northwest: Storm summary and offshore vertical structure observed with COSMIC satellite retrievals. *Monthly Weather Review*, **136 (11)**, 4398–4420, doi:10.1175/2008MWR2550.1.

Neiman, P., M. Ralph, E. Sukovich, and M. Hughes, 2010: A seven-year wind profiler-based climatology of the windward barrier jet along california's northern sierra nevada. *Monthly Weather Review*, **In press**.

Neiman, P. J., F. M. Ralph, A. B. White, D. E. Kingsmill, and P. O. G. Persson, 2002: The statistical relationship between upslope flow and rainfall in California's coastal mountains: Observations during CALJET. *Monthly Weather Review*, **130 (6)**, 1468–1492.

Neiman, P. J., G. A. Wick, F. M. Ralph, B. E. Martner, A. B. White, and D. E. Kingsmill, 2005: Wintertime nonbrightband rain in California and Oregon during CALJET and PACJET: Geographic, interannual, and synoptic variability. *Monthly Weather Review*, **133 (5)**, 1199–1223.

Pierce, D., et al., 2008: Attribution of declining western US snowpack to human effects. *Journal of Climate*, **21 (23)**, 6425–6444, doi:10.1175/2008JCLI2405.1.

Pierrehumbert, R. T. and B. Wyman, 1985: Upstream effects of mesoscale mountains. *Journal of the Atmospheric Sciences*, **42 (10)**, 977–1003.

Pike, R. J. and S. Sobieszczyk, 2008: Soil slip/debris flow localized by site attributes and wind-driven rain in the San Francisco Bay region storm of January 1982. *Geomorphology*, **94 (3–4)**, 290–313, doi:10.1016/j.geomorph.2006.09.024.

Ralph, F. M., et al., 2005: Improving short-term (0-48 h) cool-season quantitative precipitation forecasting - Recommendations from a USWRP workshop. *Bulletin of the American Meteorological Society*, **86 (11)**, 1619–+, doi:10.1175/BAMS-86-11-1619.

Randall, D., et al., 2006: Climate models and their evaluation. *Climate Change 2007: The Physical Science Basis. Contribution of Working Group I to the Fourth Assessment Report of the Intergovernmental Panel on Climate Change*, S. Solomon, D. Qin, M. Manning, Z. Chen, M. Marquis, K. Averyt, M. Tingnor, and H. Miller, Eds., Cambridge University Press, Cambridge, UK, 39–53.

Reisner, J., R. M. Rasmussen, and R. T. Bruintjes, 1998: Explicit forecasting of supercooled liquid water in winter storms using the MM5 mesoscale model. *Quarterly Journal of the Royal Meteorological Society*, **124 (548)**, 1071–1107.

Roe, G. H., 2005: Orographic precipitation. *Annual Review of Earth and Planetary Sciences*, **33**, 645–671.

Roe, G. H. and M. B. Baker, 2006: Microphysical and geometrical controls on the pattern of orographic precipitation. *Journal of the Atmospheric Sciences*, **63 (3)**, 861–880.

Roe, G. H., D. R. Montgomery, and B. Hallet, 2002: Effects of orographic precipitation variations on the concavity of steady-state river profiles. *Geology*, **30 (2)**, 143–146.

Rotunno, R. and R. Houze, 2007: Lessons on orographic precipitation fro the mesoscale alpine programme. *Quarterly Journal of the Royal Meteorlogical Society*, **133**, 811–830.

Rutledge, S. A. and P. V. Hobbs, 1984: The mesoscale and microscale structure and organization of clouds and precipitation in midlatitude cyclones XII: A diagnostic modeling study of precipitation development in narrow cold-frontal rainbands. *Journal of the Atmospheric Sciences*, **41 (20)**, 2949–2972.

Saha, A. K., R. P. Gupta, I. Sarkar, M. K. Arora, and E. Csaplovics, 2005: An approach for GIS-based statistical landslide susceptibility zonation - with a case study in the himalayas. *Landslides*, **2 (1)**, 61–69, doi:10.1007/s10346-004-0039-8.

Salathé, E., R. Steed, C. Mass, and P. Zahn, 2008: A high-resolution climate model for the US Pacific Northwest: Mesoscale feedbacks and local responses to climate change. *Journal of Climate*, **21 (21)**, 5708–5726, doi:10.1175/2008JCLI2090.1.

Sawyer, J., 1956: The physical and dynamical problems of orographic rain. *Weather*, **11**, 375–381.

Schmidt, J., G. Turek, M. Clark, M. Uddstrom, and J. Dymond, 2008: Probabilistic forecasting of shallow, rainfall-triggered landslides using real-time numerical weather predictions. *Natural Hazards and Earth System Sciences*, **8 (2)**, 349–357.

Schmidt, K. M., J. J. Roering, J. D. Stock, W. E. Dietrich, D. R. Montgomery, and T. Schaub, 2001: The variability of root cohesion as an influence on shallow landslide susceptibility in the Oregon Coast Range. *Canadian Geotechnical Journal*, **38 (5)**, 995–1024.

Schuler, T., P. Crochet, R. Hock, M. Jackson, I. Barstad, and T. Johannesson, 2008: Distribution of snow accumulation on the Svartisen ice cap, Norway, assessed by a model of orographic precipitation. *Hydrological Processes*, **22 (19)**, 3998–4008, doi:10.1002/hyp.7073.

Serreze, M. C., M. P. Clark, R. L. Armstrong, D. A. McGinnis, and R. S. Pulwarty, 1999: Characteristics of the western United States snowpack from snowpack telemetry (SNOTEL) data. *Water Resources Research*, **35 (7)**, 2145–2160.

Serreze, M. C., M. P. Clark, and A. Frei, 2001: Characteristics of large snowfall events in the montane western United States as examined using snowpack telemetry (SNOTEL) data. *Water Resources Research*, **37 (3)**, 675–688.

Shutts, G. J., 1998: Stationary gravity-wave structure in flows with directional wind shear. *Quarterly Journal of the Royal Meteorological Society*, **124 (549)**, 1421–1442.

Sinclair, M. R., D. S. Wratt, R. D. Henderson, and W. R. Gray, 1997: Factors affecting the distribution and spillover of precipitation in the southern Alps of New Zealand - a case study. *Journal of Applied Meteorology*, **36 (5)**, 428–442.

Skamarock, W. and M. Weisman, 2009: The impact of positive-definite moisture transport on NWP precipitation forecasts. *Monthly Weather Review*, **137 (1)**, 488–494, doi:10.1175/2008MWR2583.1.

Skamarock, W., et al., 2008: A description of the advanced research WRF version 3. NCAR tech. note NCAR/TN-475+STR, National Center for Atmospheric Research, 113 pp pp., Boulder, CO.

Smith, R., 2006: Progress on the theory of orographic precipitation. *Tectonics, Climate, and Landscape Evolution: Geological Society of America Special Paper 398*, S. Willett, N. Hovius, M. Brandon, and D. Fisher, Eds., Boulder, CO.

Smith, R. B., 1979: The influence of mountains on the atmosphere. *Advances in geophysics*, **21**, 87–230.

Smith, R. B., 2007: Interacting mountain waves and boundary layers. *Journal of the Atmospheric Sciences*, **64 (2)**, 594–607.

Smith, R. B. and I. Barstad, 2004: A linear theory of orographic precipitation. *Journal of the Atmospheric Sciences*, **61 (12)**, 1377–1391.

Smith, R. B., Q. F. Jiang, M. G. Fearon, P. Tabary, M. Dorninger, J. D. Doyle, and R. Benoit, 2003: Orographic precipitation and air mass transformation: An Alpine example. *Quarterly Journal of the Royal Meteorological Society*, **129 (588)**, 433–454.

Stauffer, D. R. and N. L. Seaman, 1990: Use of 4-dimensional data assimilation in a limited-area mesoscale model: Part I experiments with synoptic-scale data. *Monthly Weather Review*, **118 (6)**, 1250–1277.

Steenburgh, W. J., C. F. Mass, and S. A. Ferguson, 1997: The influence of terrain-induced circulations on wintertime temperature and snow level in the Washington Cascades. *Weather and Forecasting*, **12 (2)**, 208–227.

Steinacker, R., 1983: Diagnose und prognose der schneefallgrenze (Diagnosing and predicting the snowline). *Wetter und Leben*, **35**, 81–90.

Stewart, R. E., J. D. Marwitz, J. C. Pace, and R. E. Carbone, 1984: Characteristics through the melting layer of stratiform clouds. *Journal of the Atmospheric Sciences*, **41 (22)**, 3227–3237.

Stoelinga, M. T., M. Albright, and C. Mass, 2009: A new look at snowpack trends in the Cascade Mountains. *In Press – Journal of Climate*.

Stoelinga, M. T., et al., 2003: Improvement of Microphysical Parameterization through Observational Verification Experiment. *Bulletin of the American Meteorological Society*, **84 (12)**.

Stolar, D., G. Roe, and S. Willett, 2007: Controls on the patterns of topography and erosion rate in a critical orogen. *Journal of Geophysical Research-earth Surface*, **112 (4)**, doi:10.1029/2006JF000713.

Szyrmer, W. and I. Zawadzki, 1999: Modeling of the melting layer. Part I: Dynamics and microphysics. *Journal of the Atmospheric Sciences*, **56 (20)**, 3573–3592.

Tao, W. K., et al., 2003: Microphysics, radiation and surface processes in the Goddard Cumulus Ensemble (GCE) model. *Meteorology and Atmospheric Physics*, **82 (1–4)**, 97–137, doi:10.1007/s00703-001-0594-7.

Tebaldi, C., K. Hayhoe, J. M. Arblaster, and G. A. Meehl, 2006: Going to the extremes. *Climatic Change*, **79 (3–4)**, 185–211, doi:10.1007/s10584-006-9051-4.

Theriault, J. M., R. E. Stewart, J. A. Milbrandt, and M. K. Yau, 2006: On the simulation of winter precipitation types. *Journal of Geophysical Research-atmospheres*, **111 (18)**, doi:10.1029/2005JD006665.

Thompson, G., P. Field, R. Rasmussen, and W. Hall, 2008: Explicit forecasts of winter precipitation using an improved bulk microphysics scheme. Part II: Implementation of a new snow parameterization. *Monthly Weather Review*, **136 (12)**, 5095–5115, doi:10.1175/2008MWR2387.1.

Thompson, G., R. M. Rasmussen, and K. Manning, 2004: Explicit forecasts of winter precipitation using an improved bulk microphysics scheme. Part I: Description and sensitivity analysis. *Monthly Weather Review*, **132 (2)**, 519–542.

Torn, R. D. and G. J. Hakim, 2007: Ensemble-based sensitivity analysis. *Monthly Weather Review*, accepted.

Tustison, B., D. Harris, and E. Foufoula-Georgiou, 2001: Scale issues in verification of precipitation forecasts. *Journal of Geophysical Research-atmospheres*, **106 (11)**, 11 775–11 784.

United States Army Corps of Engineers, 1956: *Snow Hydrology: Summary report of the snow investigations*. North Pacific Division, U.S. Army Corps of Engineers.

Unterstrasser, S. and G. Zängl, 2006: Cooling by melting precipitation in Alpine valleys: An idealized numerical modelling study. *Quarterly Journal of the Royal Meteorological Society*, **132 (618)**, 1489–1508, doi:10.1256/qj.05.158.

Vicuna, S., E. P. Maurer, B. Joyce, J. A. Dracup, and D. Purkey, 2007: The sensitivity of California water resources to climate change scenarios. *Journal of the American Water Resources Association*, **43 (2)**, 482–498, doi:10.1111/j.1752-1688.2007.00038.x.

Walser, A. and C. Schär, 2004: Convection-resolving precipitation forecasting and its predictability in Alpine river catchments. *Journal of Hydrology*, **288 (1)**, 57–73.

Wang, J. H., H. L. Cole, D. J. Carlson, E. R. Miller, K. Beierle, A. Paukkunen, and T. K. Laine, 2002: Corrections of humidity measurement errors from the vaisala RS80 radiosonde - application to TOGA COARE data. *Journal of Atmospheric and Oceanic Technology*, **19 (7)**, 981–1002.

Wei, Y. L. and J. Marwitz, 1996: The Front Range blizzard of 1990. Part III: Numerical simulations of melting effects. *Monthly Weather Review*, **124 (11)**, 2483–2496.

Westrick, K. J. and C. F. Mass, 2001: An evaluation of a high-resolution hydrometeorological modeling system for prediction of a cool-season flood event in a coastal mountainous watershed. *Journal of Hydrometeorology*, **2 (2)**, 161–180.

White, A. B., D. J. Gottas, E. T. Strem, F. M. Ralph, and P. J. Neiman, 2002: An automated brightband height detection algorithm for use with Doppler radar spectral moments. *Journal of Atmospheric and Oceanic Technology*, **19 (5)**, 687–697.

Wieczorek, G. F., H. McWreath, and C. Davenport, 2001: Remote rainfall sensing for landslide hazard analysis. *U.S. Geological Survey Open-File Report 01-339.*

Willett, S. D., 1999: Orogeny and orography: The effects of erosion on the structure of mountain belts. *Journal of Geophysical Research-solid Earth*, **104 (12)**, 28 957–28 981.

Wilson, J. W. and M. A. Atwater, 1972: Storm rainfall variability over Connecticut. *Journal of Geophysical Research*, **77 (21)**, 3950–&.

Wu, W. M. and R. C. Sidle, 1995: A distributed slope stability model for steep forested basins. *Water Resources Research*, **31 (8)**, 2097–2110.

Yang, D. Q., B. E. Goodison, J. R. Metcalfe, V. S. Golubev, R. Bates, T. Pangburn, and C. L. Hanson, 1998: Accuracy of NWS 8 inch standard nonrecording precipitation gauge: Results and application of WMO intercomparison. *Journal of Atmospheric and Oceanic Technology*, **15 (1)**, 54–68.

Zängl, G., 2005: The impact of lee-side stratification on the spatial distribution of orographic precipitation. *Quarterly Journal of the Royal Meteorological Society*, **131 (607)**, 1075–1091.

Zängl, G., 2007: Interaction between dynamics and cloud microphysics in orographic precipitation enhancement: A high-resolution modeling study of two North Alpine heavy-precipitation events. *Monthly Weather Review*, **135 (8)**, 2817–2840.

Zängl, G., 2008: The temperature dependence of small-scale orographic precipitation enhancement. *Quarterly Journal of the Royal Meteorological Society*, **134 (634)**, 1167–1181, doi:10.1002/qj.267.

VITA

Justin Minder was born in Glens Falls, New York in 1982 and raised in the foothills of the Adirondack Mountains. He received a B.A. from Vassar College in 2004, with a double-major in Geology and Physics. During his undergraduate years he dabbled in research involving observations of submarine-landslides and tsunamis, numerical modeling and field monitoring of stream hydrology, and laboratory modeling of mantle dynamics (in a vat of corn syrup). He came to Seattle to study at the University of Washington in September of 2004. He will begin as a Flint Postdoctoral Fellow at Yale University working with Professor Ronald Smith in the fall of 2010 (after a summer hiking, climbing, and generally savoring the mountains of the Pacific Northwest). He will miss Seattle and the associated friends, food, trees, water, music, etc.